STRATOSPHERIC GEOENGINEERING WITH BLACK CARBON AEROSOLS

by

BENJAMIN S. KRAVITZ

A Dissertation submitted to the

Graduate School-New Brunswick

Rutgers, The State University of New Jersey

in partial fulfillment of the requirements

for the degree of

Doctor of Philosophy

Graduate Program in Atmospheric Science

written under the direction of

Professor Alan Robock

and approved by

_____

_____

_____

_____

New Brunswick, New Jersey

May, 2011

ABSTRACT OF THE DISSERTATION

Stratospheric Geoengineering with Black Carbon Aerosols

By BENJAMIN S. KRAVITZ

Dissertation Director:
Professor Alan Robock

I use a general circulation model of Earth's climate to simulate stratospheric
geoengineering with black carbon aerosols, varying the altitude of injection,
initial particle size, and whether the deposited black carbon modifies ground
albedo. 1 Tg of black carbon aerosols injected into the stratosphere each year will
cause significant enough surface cooling to negate anthropogenic warming if the
aerosols are small (r=0.03 μm) or if the aerosols are injected into the middle
stratosphere, although using small aerosols causes large regional cooling effects
that would be catastrophic to agriculture. The aerosols cause significant
stratospheric heating, resulting in stratospheric ozone destruction and circulation
changes, most notably an increase in the Northern Hemisphere polar jet, which
forms an Arctic ozone hole and forces a positive mode of the Arctic Oscillation.
The hydrologic cycle is perturbed, specifically the summer monsoon system of
India, Africa, and East Asia, resulting in monsoon precipitation collapse. Global
primary productivity is decreased by 35.5% for the small particle case. Surface
cooling causes some sea ice regrowth, but not at statistically significant levels.
All of these climate impacts are exacerbated for small particle geoengineering,

with high altitude geoengineering with the default particle size (r=0.08 µm) causing a reasonable amount of cooling, and large particle (r=0.15 µm) geoengineering or particle injection into the lower stratosphere causing few of these effects. The modification of ground albedo by the soot particles slightly perturbs the radiative budget but does not cause any distinguishable climate effects. The cheapest means we investigated for placing 1 Tg of black carbon aerosols into the stratosphere by diesel fuel combustion would cost $1.4 trillion initially and $541 billion annual, or 2.0% and 0.8% of GDP, respectively. The additional carbon dioxide released from combusting diesel to produce these aerosols is about 1% of current emissions, but the additional NO_x would be 17% of current sources and could further reduce the total ozone column by up to 10%. Geoengineering with carbon black, if technically feasible, would be much cheaper, costing approximately $1 billion initially and $1.3 billion annually, with few troublesome emissions factors.

ACKNOWLEDGMENTS

This section would go on forever if I allowed myself to spend the time, as there are so many people who have contributed to this great step in my career and my life. To any potential reader I've forgotten to thank: I've tried my best to mention everyone, but if you're not in here, yet you feel you deserve to be mentioned, you probably do.

I begin by thanking the members of my thesis committee: Professors Alan Robock, Mark Miller, and Tony Broccoli, and Dr. Drew Shindell. Your patience with me through this project, and my studies in general, is much more appreciated than I know how to put in words, and I could not have done this without your help. Your wisdom, insight, and experience have helped shape this effort, and all who look closely will see your indelible mark and influence on much of the work contained here.

I would like to especially thank Dr. Robock for being a tremendous advisor—perhaps the best for whom I could have hoped. I cannot list the lessons you've taught me, but they all amount to ensuring I will become a good scientist. I hope to make you proud I was your student, and even more, when I have my own students, I plan to pass on the lessons I've learned from you.

I thank the faculty of the atmospheric science program at Rutgers University. I've often enjoyed knocking on people's doors to indulge my curiosity about any number of things, and I've always been met warmly and enthusiastically. Very often, I walked away with more questions than answers,

which is exactly how it should be. Professors Barb Turpin and Ann-Marie Carlton deserve special mention, as they kindly devoted their time and significant expertise to this project. This welcoming experience is also true of many of the faculty of the Institute for Marine and Coastal Sciences, with whom I have had frequent interaction. Professor Gera Stenchikov also deserves special mention. My close work with him for the first two years of my graduate career helped shape my interests and contributed significantly to my choice in this project. Dr. Virendra Ghate was always ready with offers for much valued help, sympathies, and lots of humor to help me get through this entire process.

I additionally wish to acknowledge many people without whom this project would not be successful. Dr. Luke Oman taught me how to use the climate model and nursemaided me through the whole process. His code still lives on in my simulations. Dr. Andy Lacis of NASA GISS kindly devoted his time and assistance to my understanding of the project. Much of my experiment design, as well as my hypotheses, are based on his work. This project would not at all have been possible without model development by the scientists and staff at NASA GISS, led by Dr. Gavin Schmidt, as well as their generous devotion of computer time to my research. My simulations were conducted at NASA GSFC, so their assistance with computer time, as well as the staff to maintain it, deserve my thanks. Professor Martin Bunzl, our co-investigator on the project, was always encouraging and eager, as well as ready with good ideas and helpful arguments against bad ones. The work on this project, as well as our other work on geoengineering, is stronger for his involvement. I also thank Phil Rasch and

this list, but you're still kind enough to read this dissertation anyway, then you really deserve to be.

Above all, I owe a great debt of gratitude to my family, especially my parents, Robert and Cathy, and my sister, Molly. Your love and support throughout these years was more important than I'm capable of consciously understanding.

And finally, I thank anyone who's reading this. You make this all worthwhile.

TABLE OF CONTENTS

LIST OF TABLES

LIST OF FIGURES

CHAPTER 1: INTRODUCTION

The large amount of attention given to the climate effects of anthropogenic greenhouse gases in recent years [e.g., *Solomon et al.*, 2007] has prompted a flurry of study on potential means of ameliorating dangerous levels of climate change. Due to the very long lifetime of atmospheric carbon dioxide [*Solomon et al.*, 2009], which is the primary driver of climate change, the only permanent solution to this intimidating problem is mitigation of greenhouse gas emissions.

However, much attention has been given to alternate means of alleviating dangerous climate consequences, especially in recent years with the publication by *Crutzen* [2006], who bravely asserted a lack of confidence in humanity's ability to properly react to the changing climate in time. Although the idea of geoengineering is not new, as we describe in Section 2.1, *Crutzen* gave it legitimate scientific credibility and thrust it forward into mainstream climate research.

1.1 WHAT IS GEOENGINEERING?

Perhaps the most satisfying definition of geoengineering is "the deliberate modification of the climate to counteract anthropogenic global warming." Use of the term "global warming" is no longer in vogue due to the adoption of the phrase "climate change," but in this case, use of the original term is more apt for geoengineering. The purpose of geoengineering, when viewed at its most simplistic level, is not to reverse climate change due to increasing greenhouse gas

concentrations, although some particular schemes classified as Carbon Dioxide

Removal (CDR), which we address in Section 2.2, would indeed cause this

reversal. The vast majority of geoengineering schemes have as their primary

goal a reduction of globally averaged surface air temperature, and most other

consequences are treated as side effects. Therefore, when discussing

geoengineering, we prefer the term "global warming."

1.2 WHY RESEARCH GEOENGINEERING?

The debate regarding how to research geoengineering is ongoing, but an

even more basic question is why one would research geoengineering. Perhaps

the most revealing answer comes from a short exchange[1] between David Keith,

who is one of the foremost researchers in geoengineering [e.g., *Keith*, 2000], and

Paul Crutzen, the Nobel Prize winner who reignited the study of geoengineering

after a long stagnancy and gave it formal legitimacy in the scientific community

[*Crutzen*, 2006]:

> Keith: Do you think we'll ever have to do it?
> Crutzen: I'm afraid, yes.

One of the most compelling reasons to research geoengineering is out of possible

necessity. *Lawrence* [2006] argues that society may someday need geoengineering

as a last resort. *Dickinson* [1996] asserts that as anthropogenic climate change

becomes more prevalent in the public eye, calls for geoengineering solutions will

become increasingly persistent. Should society need to quickly and temporarily

---

[1] Exchange took place at Governing Climate Engineering - A Transdisciplinary Summer School, Max Planck Institute for Comparative Law, Heidelberg, Germany, 16 July 2010.

reduce global surface temperatures to prevent dire consequences from anthropogenic climate change, geoengineering can serve that purpose.[2] Indeed, *Washington et al.* [2009] argue that, in some circumstances, mitigation alone is not enough for society to avoid all future climate change. Therefore, reason dictates society should invest in a strong geoengineering research program, allowing us to investigate, evaluate, and resolve as many potential untoward negative effects as possible. Although some of the potential negative effects have been addressed [e.g., *Robock*, 2008], further research is greatly needed.

Bunzl [2009], as well as others, addresses some of the problems with researching geoengineering. These include that researching geoengineering detracts from the real problem of mitigating greenhouse gas emissions, it does not actually fix the problem of climate change due to these anthropogenic greenhouse gases and would have to be conducted indefinitely, and it could actually discourage people from addressing the issue of mitigation, believing they have a "quick fix" for the problem of climate change. Therefore, geoengineering research invites many interesting ethical arguments which also need to be resolved, if possible.

Strangely, a seldom mentioned reason to research geoengineering is that it provides a clear, replicable way of perturbing the climate system to study its response. However, this addresses the point that climate model experiments are the only means by which large scale geoengineering research can be conducted safely. In order to perturb the climate enough to measure effects that emerge

---

[2] From J. Shepherd and S. Rayner, untitled figure presented at Asilomar International Conference on Climate Intervention Technologies, 22-26 March 2010, Pacific Grove, CA.

from the noise of natural variability, geoengineering must be performed at scale and for a sufficient length of time [*Robock et al.*, 2009, 2010]. Although one small field experiment has been conducted [*Izrael et al.,* 2009], it was performed at such a small scale, both in the amount of aerosols created and over a small space, that the conclusions which can be drawn from it are unclear. However, this experiment does detail some of the measures a geoengineering campaign would need to take should actual implementation be desired.

CHAPTER 2: LITERATURE REVIEW

Restricting a literature review to geoengineering with stratospheric black carbon aerosols would be overly simplistic, as there has been only one study performed on this topic, which has not been published [*Lacis et al.*, unpublished], even though using black carbon aerosols has been repeatedly mentioned throughout the geoengineering literature [e.g., *Crutzen*, 2006; *Teller et al.*, 1997, 2002; *Lane et al.*, 2007]. Despite this lack of direct study, we can discuss geoengineering research in general, with a specific focus on geoengineering with stratospheric aerosols, on which a great deal of work has been done. Despite being a relatively new field, *Fleming* [2007, 2010] has compiled a large amount of material on the history of geoengineering. There have also been several summary papers of the state of geoengineering knowledge [e.g., *NAS*, 1992; *Keith*, 2000; *Shepherd et al.*, 2009], and even a review paper [*Rasch et al.*, 2008b]. Simulations of geoengineering with black carbon are sparse, but we do have some analogues which are helpful in illustrating why this means of climate modification is likely to be successful in reducing surface temperatures, albeit with side effects.

The question of how one could geoengineer has been of great concern in the past [e.g., *NAS*, 1992; *Keith*, 2000; *Robock et al.*, 2009]. However, as we wish to maintain our focus on physical science, we do not delve into discussions of feasibility and logistics in this chapter. Chapter 6 is devoted to a study of the practicality of geoengineering specifically with black carbon aerosols. We also

exclude, except in brief mentions, discussions of legality, politics, economics, or ethics of geoengineering. Although such discussions are interesting, not only are they covered in other works [e.g., *Keith*, 2000; *Fleming*, 2006; *Barrett*, 2008; *Bunzl*, 2008, 2009; *Turco*, unpublished], but they are tangent to our central purpose.

2.1 HISTORY OF GEOENGINEERING

The first mention of deliberate climate modification in modern literature was by *von Neumann* [1955] in *Fortune* magazine as an opinion piece. The idea then received sporadic attention until mention by *Budkyo* [1974], who performed detailed scientific calculations as to how much hypothetical intervention would be required for a specific amount of deliberate climate change. Budyko's thoughts were later summarized in a book [*Budyko*, 1977] which devotes an entire section to the subject of "climate modification." Demonstrating great foresight, Budyko predicted that a need for geoengineering, specifically with stratospheric sulfate aerosols, would arise in the 21st century when human economic activity and an increase in anthropogenic greenhouse gases would warrant a counteraction, and he made a broad call for research into this topic to determine any possible untoward consequences.

The term *geoengineering* was introduced soon after by *Marchetti* [1977], a paper which also mentioned dissolving carbon dioxide in the ocean as a means of counteracting anthropogenic climate change. The field progressed slowly with small studies conducted sporadically, resulting in no more than a handful of papers in any given year. Of particular note is *NAS* [1992], which outlined all of

the means of geoengineering which had been proposed up to that point, but little action was taken regarding actual scientific analysis of impacts. This was followed by the second assessment report by the IPCC, which included a mention of geoengineering [*Leemans et al.*, 1995]. A subsequent summary was written by *Flannery et al.* [1997], and a similar report was produced by *Khan et al.* [2001], which included *Dickinson's* [1996] primitive estimates as to the magnitude of geoengineering that would be required to cool the planet, based on the eruption of Pinatubo in 1991. It also included the work of *Teller et al.* [1999], in which some of the preliminary ideas were presented for future study. The first model simulations of geoengineering were conducted by *Govindasamy and Caldeira* [2000], in which they reduced the solar constant by a prescribed amount. *Khan et al.* [2001] published concurrently with a survey report by *Schneider and Keith* [2001], which included a diagram containing many of the proposed geoengineering means that had been proposed up to that point.

The idea of geoengineering only recently gained large amounts of attention with *Crutzen's* [2006] reintroduction of it. Since then, there has been a great deal of study by multiple modeling groups and several reports [e.g., *Lane et al.*, 2007; *Shepherd et al.*, 2009]. *Robock et al.* [2008] was the first paper written under an NSF-funded geoengineering grant and the first set of simulations of geoengineering to use a fully coupled atmosphere-ocean general circulation model. There is also work on a coordinated geoengineering research project called The Geoenginering Model Intercomparison Project (GeoMIP) which is already underway [*Kravitz et al.*, 2011b].

2.2 CLASSIFICATION OF GEOENGINEERING SCHEMES

As the myriad ways of geoengineering have been increasingly mentioned, there has been some attempt to classify the various schemes [e.g., *Keith*, 2000; *Lenton and Vaughan*, 2009; *Shepherd et al.*, 2009]. Recently, two categories have been accepted by the mainstream scientific community researching geoengineering: Solar Radiation Management (SRM) and Carbon Dioxide Removal (CDR).

2.2.1 SOLAR RADIATION MANAGEMENT

SRM is the term broadly applied to any means of geoengineering that seeks to reduce the amount of incident solar radiation at the surface, which ultimately makes it a modification of shortwave radiation. This can be accomplished by either extraterrestrial or terrestrial means.

Despite the large amount of work done on this idea, there is essentially only one suggested means of extraterrestrial SRM. First proposed by *Early* [1989], the solar constant would be reduced by placing reflectors at the Lagrange L1 point so they would be orbitally stable. This idea was repeated by *NAS* [1992], which was succeeded by a small amount of later work [e.g., *Angel*, 2006; *Pearson et al.*, 2006]. Due to its relative simplicity, the earliest climate model simulations of geoengineering were of this particular scenario [e.g., *Govindasamy and Caldeira*, 2000; *Govindasamy et al.*, 2002, 2003; *Bala et al.*, 2008; *Caldeira and Wood*, 2008]. The Geoengineering Model Intercomparison Project (GeoMIP) also has two scenarios which replicate this idea [*Kravitz et al.*, 2011b].

Terrestrial SRM is significantly more complicated, involving numerous possibilities, all of which generally seek to increase the planetary albedo. Due to the nature of these schemes, all of them involve direct interaction with the climate system in some form, which has the potential to increase side effects. For example, *Rasch et al.* [2008b] have shown that geoengineering with stratospheric aerosols, a terrestrial SRM scheme, will result in stratospheric heating due to absorption of solar radiation by the aerosols, which in turn can cause stratospheric ozone depletion.

This subcategory contains the two most viable [*Lenton and Vaughan*, 2009] and most studied geoengineering schemes: stratospheric aerosols and marine cloud brightening. We discuss stratospheric aerosols in much greater detail in Section 2.3, as it has direct bearing on this project.

Marine stratocumulus clouds cover approximately 25% of the ocean surface [*Charlson et al.*, 1987], and they have an albedo of between 0.3 and 0.7 [*Schwartz and Slingo*, 1996]. Therefore, modifying the albedo of these clouds, especially those which have an albedo on the lower end of the range reported by *Schwartz and Slingo*, could certainly have a strong impact on the radiative budget of the planet. *Salter et al.* [2008] state that a global albedo increase of 1.1% will produce a sufficient radiative forcing to counteract the forcing that would result from a doubling of carbon dioxide concentrations.

Due to the first indirect effect as originally described by *Twomey* [1977], it has been postulated that the albedo of marine stratocumulus clouds can be increased by seeding the clouds with aerosols that can serve as cloud

condensation nuclei [*Stevens and Feingold*, 2009]. The first mention of this idea was by *Wigley* [1989] and *Latham* [1990], concurrent with a study by *Slingo* [1990] reporting on the sensitivity of these marine stratocumulus clouds to changes in albedo.

Various aspects of this idea were investigated in later years [e.g., *Charlson et al.*, 1992; *Latham*, 2002; *Ackerman et al.*, 2004; *Bower et al.*, 2006], including an appearance in *NAS* [1992]. Preliminary simulations with a general circulation model showed that this scheme can result in a reduction of globally averaged surface air temperature which would counteract the warming due to anthropogenic climate change [*Latham et al.*, 2008]. Additional simulations by *Jones et al.* [2009] showed that up to 35% of the radiative forcing due to current levels of greenhouse gases could be offset by marine stratocumulus brightening, which would result in a delay of global warming by about 25 years. However, *Jones et al.* also found that seeding marine stratocumulus clouds would result in a catastrophic decrease in precipitation over the Amazon. Despite this strong drawback, this scheme does have the advantage that should it cease, the climate system would be restored to its previous state within a few days [*Latham et al.*, 2008].

One additional postulated means is enhancing ocean production of dimethyl sulfide, which is a natural product of marine phytoplankton [e.g., *Niki et al.*, 2000; *Simó et al.*, 2002]. Dimethyl sulfide is a major source of cloud condensation nuclei over the oceans [*Charlson et al.*, 1987]. *Wingenter et al.* [2007] have proposed a means by which ocean iron fertilization (see Section 2.2.2 below)

will enhance phytoplankton production of dimethyl sulfide, which would serve as additional cloud condensation nuclei. The theory says that this, in turn, would brighten marine stratocumulus clouds via the aerosol indirect effect [*Twomey*, 1977], thus increasing the planetary albedo.

Other possible techniques of reducing the amount of insolation that is absorbed by Earth's surface can involve increasing the albedo of the surface. Such methods include, for example, albedo modification of deserts and grasslands [e.g., *Hamwey*, 2007], croplands [*Ridgwell et al.*, 2009], and urban areas [*Akbari et al.,* 2009], including the somewhat notorious idea of painting roofs white. *NAS* [1992] also provided the suggestion of lofting a large number of aluminized balloons to provide a reflection screen.

2.2.2 CARBON DIOXIDE REMOVAL

CDR aims to modify the climate by removing carbon dioxide from the atmosphere and sequestering it. Unlike some of the potential negative consequences of SRM, CDR would actually reverse anthropogenic climate change. Since greenhouse gases increase the residence time of outgoing longwave radiation in the atmosphere, CDR is effectively a longwave geoengineering solution.

One of the most commonly discussed means of conducting CDR is ocean iron fertilization (OIF). The idea, as discussed by *Falkowski* [1997], is to supplement certain regions of the ocean that are nutrient limited in order to spur phytoplankton blooms. These nutrients can be in the form of fixed nitrogen

[*Falkowski*, 1997; *Lampitt et al.*, 2008], phosphorus [*Lampitt et al.*, 2008], or, in the case of OIF, iron. *NAS* [1992] and *Shepherd et al.* [2009], both reviews of existing work, also discussed OIF as a means of geoengineering. *Boyd et al.* [2005] conducted a field experiment in which they managed to induce a phytoplankton bloom. However, this does not seem a particularly attractive solution, since conducting fertilization across the global ocean for 100 years would reduce CO_2 concentrations by approximately 33 ppm [*Aumont and Bopp*, 2006], which is insufficient for a permanent solution to the climate change problem and would have disastrous ecological consequences.

Another idea which has recently gained attention is ambient capture of carbon dioxide from the air, with implied sequestration of the carbon from the atmosphere. Some of the earliest work on this was done by *Lackner et al.* [1996] and *Keith* [2000]. Work on this idea has continued [e.g., *Zeman and Lackner*, 2004; *Keith et al.*, 2006; *Zeman*, 2007], including an actual prototype capture module [*Lackner*, 2009]. Much of the work on carbon capture was included in a special report by the IPCC on carbon dioxide capture and storage [*IPCC*, 2005].

Generally, carbon sequestration sites are assumed to be underground [e.g., *Ehlig-Economides and Economides*, 2010]. However, another place to sequester CO_2 is in the ocean, as the ocean will naturally dissolve atmospheric CO_2. Enhancing ocean upwelling to accelerate this natural process has been mentioned in the past [e.g., *Salter*, 2009]. However, this will actually worsen the problem of ocean acidification that is already occurring under climate change [e.g., *Raven et al.*, 2005; *Matthews et al.*, 2009].

The summary report by *Shepherd et al*. [2009] included several other carbon dioxide removal schemes. One such option is afforestation, which was mentioned by *NAS* [1992] and is treated as a mitigation option in the IPCC Fourth Assessment Report [*Solomon et al.*, 2007]. *Ornstein et al*. [2009] used GISS ModelE, a general circulation model of Earth's atmosphere and ocean developed by the NASA Goddard Institute for Space Studies [*Schmidt et al.*, 2006], and the same one we use for our simulations (Section 3.3), to investigate afforestation of deserts to sequester carbon dioxide. They found that afforestation of the Sahara and the Australian outback could more than offset CO_2 emissions from current fossil fuel burning. However, if the trees used in afforestation are later harvested, the only true CO_2 offset is the carbon stored below ground or in long-lived lumber products.

Another technology mentioned by *NAS* [1992] is accelerating the carbonation of rock minerals [e.g., *Lackner*, 2003]. Peridotite naturally absorbs carbon dioxide from the atmosphere and converts it to carbonates, so this process could be amenable to carbon capture and sequestration if the time scale over which it operates could be reduced [*Kelemen and Matter*, 2008]. Additionally, implementation of biochar can offset fossil fuel emissions and serve as a carbon sink [*Lehmann et al.*, 2006; *Lehmann*, 2007].

2.3 GEOENGINEERING WITH STRATOSPHERIC AEROSOLS

Geoengineering with stratospheric aerosols, which falls under the category of SRM, is likely the most famous geoengineering scheme, and it has

also received the most attention by climate researchers. Indeed, when researchers discuss SRM, or geoengineering in general, they are most often referring to geoengineering with stratospheric sulfate aerosols. The future of geoengineering research is likely to continue with this scheme, due to its relative ease of simulation and feasibility of implementation [*Kravitz et al.*, 2011b].

Geoengineering with stratospheric aerosols was first suggested by *Budyko* [1974, 1977], using volcanic eruptions as an analogue. During the year following the eruption of Mount Pinatubo in 1991, the stratospheric sulfate aerosols created resulted in a reduction of globally averaged surface air temperature by approximately 0.5°C [*Lacis and Mishchenko*, 1995]. *Hansen et al.* [2005] found that the radiative forcing at the tropopause (in units of W m^{-2}) due to a large tropical volcanic eruption such as Pinatubo, after allowing stratospheric temperatures to adjust, is approximately -23τ, where τ is the aerosol optical depth of the created sulfate aerosols, measured at 550 nm. However, although volcanic eruptions are a useful analogue, due to the thermal inertia of the ocean, surface cooling under geoengineering would be greater than under a single injection of sulfur, as would happen under a volcanic eruption [e.g., *Lane et al.*, 2007]. Therefore, simulations of volcanic eruptions cannot serve as a perfect analogue for simulations of geoengineering.

The simplest study of this particular geoengineering scenario was conducted by *Wigley* [2006]. Using an energy balance model with a climate sensitivity of 3°C for a doubling of carbon dioxide concentrations, he performed experiments by specifying radiative forcing due to sulfate aerosols for injection

scenarios of one Pinatubo every year (10 Tg of sulfur per year), one every two years, and one every four years. In running his model for 1000 years, he was able to achieve a steady state, for which he calculated that one Pinatubo every 2 years would result in a sustained radiative forcing of -3 W m^{-2}. Of perhaps even more significance, he showed that the climate warms rapidly once geoengineering is ceased, much more so than would be experienced under warming due to anthropogenic greenhouse gases.

Teller was a strong proponent of using scatterers to increase planetary albedo [e.g., *Teller et al.*, 1997]. However, unlike much of the geoengineering research performed by other researchers, *Teller et al.* [1999] proposed using microscopic aluminum particles or a carefully-engineered "self-lofting blue/UV chaff." They later published a few more articles on these manufactured "resonant scatterers" which would be optimized for maximal backscattering of solar radiation [*Teller et al.*, 2002; *Lane et al.*, 2007]. This idea has recently been revisited by *Keith* [2010].

NAS [1992] suggested using dust aerosols in the stratosphere. However, they also mention this could result in stratospheric heating and catalytic destruction of ozone. Moreover, most dust aerosols are much larger than sulfate aerosols, so their atmospheric lifetime will be significantly less than other more commonly discussed types.

There has been some work on how these aerosols or aerosol precursors would be placed in the stratosphere [e.g., *NAS*, 1992; *Rasch et al.*, 2008b; *Robock et al.*, 2009]. However, most of the studies of the climate effects of stratospheric

geoengineering with sulfate aerosols have assumed full conversion of these precursors, giving a maximum effect for a given amount of injection of sulfur-bearing gas. According to *Turco* [unpublished], this may not be a valid assumption. He argues, with confirmation by *Pierce et al.* [2010], that there is no evidence that injection of sulfate aerosols or aerosol precursors will in fact result in the geoengineering aerosol layer dispersion predicted by the general circulation models that have been used to date.

Another problem with geoengineering with stratospheric aerosols is an insufficient observing system to monitor these aerosols. In the past, the best means available of observing these aerosols was a limb scanner, most notably SAGE II, which was in operation for 21 years [*Russell and McCormick*, 1989]. The only limb scanner currently in operation is the Optical Spectrograph and InfraRed Imaging System (OSIRIS) [*Llewellyn et al.*, 2004], but not only is this just a single instrument and therefore cannot be deemed an observation system, this instrument is still somewhat untested and has certain issues that need to be addressed before it is deemed reliable enough for the means that would be required [*Kravitz et al.*, 2010a, 2011a].

Although many modeling experiments have been performed to simulate geoengineering with stratospheric aerosols, *Robock et al.* [2008] performed the first simulations which used a coupled atmosphere-ocean general circulation model. They performed two experiments: an injection of 5 Tg of SO_2 per year into the tropical lower stratosphere and an injection of 3 Tg of SO_2 per year into the Arctic lower stratosphere. They found that the former resulted in globally

averaged cooling by approximately 0.5°C, or a cooling to 1980 surface air temperature levels, and the latter resulted in 0.2°C of cooling to approximately 2000 levels. Conversely, *Rasch et al.* [2008a] found that 1.5 Tg of sulfur per year (approximately 3 Tg of SO_2) would counteract the radiative forcing from a doubling of CO_2, which is a far greater effectiveness than the results of *Robock et al. Jones et al.* [2010] found a similar result to *Robock et al.*, in that a tropical injection of 5 Tg a^{-1} of SO_2 causes a delay in warming of 30-35 years under the IPCC fourth assessment report's A1B scenario [*Solomon et al.*, 2007].

Determining which group's results are most accurate is not straightforward. *Rasch et al.* [2008b] addressed these multiple experiments and explained how they vary in aerosol precursor, the assumed aerosol size distribution, and the amount and location of the injection. *Jones et al.* [2010] is the first study in which two modeling groups conducted experiments that were similar enough to be comparable. One upcoming remedy to this problem is GeoMIP, which serves as a coordination of geoengineering simulation, allowing the geoengineering community to achieve robust results [*Kravitz et al.*, 2011b].

One possible reason for these differing results is variation in the assumed aerosol properties. *Rasch et al.* [2008a] note that if particle sizes are too large, geoengineering is less effective, due to both reduced scattering efficiency and increased gravitational deposition of the particles. Also, while smaller sulfate particles do not have a prominent effect in the longwave, larger sulfate particles do [*Stenchikov et al.*, 1998]. In fact, *Lacis et al.* [unpublished] showed that if the aerosol effective radius is greater than 2.2 μm, which would result from

coagulation of the particles, the sulfate aerosols would result in net warming instead of net cooling. The results obtained by *Rasch et al.* used an effective radius of approximately 0.1 μm, which they calculated to be the size that would result in the most efficient scattering, and a similar size was confirmed to be most efficient by *Lacis et al.* The simulations of *Robock et al.* [2008] used a slightly larger aerosol effective radius of 0.30-0.35 μm. However, as the injection rate increases, aerosol particles are likely to grow due to condensation of water onto the particle and coagulation of particles [*Pinto et al.*, 1989]. *Heckendorn et al.* [2009] used a model with sophisticated microphysics to conduct similar simulations. They found that particle sizes are expected to grow to larger sizes than any of the previous studies due to coagulation and a fresh supply of sulfuric acid, thus having a reduced albedo and increased sedimentation. *Pierce et al.* [2010] have suggested a means of overcoming this obstacle by directly emitting sulfuric acid which would condense into sufficiently small droplets, but this idea is, as of yet, untested.

Unlike simulations of the eruption of Pinatubo [*Stenchikov et al.*, 1998], the simulations of *Robock et al.* [2008] showed both summer and winter cooling. However, as was found in these simulations, as well as simulations of other large volcanic eruptions [*Robock and Liu*, 1994], there was a disruption of the summer monsoonal system in India, East Asia, and the Sahel. This study, as well as the study by *Bala et al.* [2008], confirmed the predicted effects on the hydrological cycle by *Trenberth and Dai* [2007].

Robock [2008] reported that one potential problem for geoengineering could be additional acid rain as a result of wet deposition of the sulfate aerosols. However, *Kravitz et al.* [2009, 2010b] showed that the resulting increase in acid deposition due to geoengineering with sulfate aerosols would have a minimal and probably undetectable impact.

A noted problem of geoengineering with stratospheric aerosols would be the destruction of stratospheric ozone, a process which has happened after large volcanic eruptions. *Hofmann and Solomon* [1989] found that the eruption of El Chichón, which injected 3-5 Tg of sulfur into the stratosphere, caused a 16% reduction in ozone at an altitude of 20 km. Mount Pinatubo, which injected 10 Tg of sulfur, resulted in a global column ozone loss of 2.5% [*Kinnison et al.*, 1994]. Additionally, *Solomon* [1999] reported that enhancing levels of stratospheric sulfate aerosols suppresses stratospheric NOx, leading to enhanced halogen-catalyzed ozone depletion. This in turn results in a delayed recovery of the ozone hole.

Simulations of Pinatubo and of geoengineering using the Whole Atmosphere Community Climate Model version 3, based on the Community Atmospheric Model developed by the National Center for Atmospheric Research [*Kiehl et al.*, 1998], showed that an injection of sulfur large enough to compensate for the surface warming that would result from a doubling of carbon dioxide concentrations would cause a strong decrease in arctic ozone during cold winters and would delay the recovery of the Antarctic ozone hole by 30-70 years [*Tilmes et al.*, 2008, 2009]. *Heckendorn et al.* [2009] further evaluated the destruction of

ozone globally by showing that stratospheric geoengineering would result in an increase in the amount of water entering the stratosphere by heating the tropical cold point tropopause. This in turn would increase catalytic ozone destruction by HO_x cycle interactions.

Another effect of geoengineering with sulfate aerosols would be modification of the quality of radiation received at the surface. *Gu et al.* [2003] showed that the eruption of Pinatubo increased the amount of diffuse radiation received at the surface, which increased photosynthesis across most of the globe. *Murphy* [2009] quantified this, showing that stratospheric aerosols reduce direct sunlight by about four watts for every watt reflected to outer space, with the balance becoming diffuse radiation. This implies that geoengineering would significantly affect concentration of solar energy for use in solar power plants. However, this increase in diffuse radiation would aid the problem of global warming by increasing the biosphere carbon sink. The 1991 eruption of Mount Pinatubo greatly increased the amount of diffuse radiation which promoted plant growth, resulting in a carbon sink of 1.13 Pg a^{-1} in 1992 and 1.53 Pg a^{-1} in 1993 [*Mercado et al.*, 2009]. *Mercado et al.* also concluded the land carbon sink has increased as a result of global dimming. This implies that terrestrial shortwave geoengineering would also have a geoengineering component in the longwave as a result of interaction with the biosphere.

2.4 CLIMATE EFFECTS OF BLACK CARBON AEROSOLS

Geoengineering with black carbon aerosols has never been performed, so the potential climate effects are, strictly speaking, largely unknown. Moreover, modeling studies of this idea are sparse [*Lacis et al.*, unpublished], so the scientific community is not yet sure of the robustness of the results that have been obtained. Nevertheless, geoengineering with black carbon has real-world and modeling analogues from which we can draw some conclusions, namely studies of forest fires and simulations of nuclear winter.

Robock [1988] investigated surface air temperatures in Northern California and Southern Oregon underneath a forest fire smoke cloud that was trapped in a valley by an inversion. He found that daily maximum temperatures were over 15°C cooler than normal for a period of 1 week and over 5°C cooler than normal for the three week period over which the inversion lasted. In a later study, *Robock* [1991] analyzed several other instances of large fires for which there were available meteorological data. He found similar results, i.e., the reduced amount of solar radiation reaching the surface, combined with the radiative cooling of the surface, resulted in reduced surface air temperatures.

Crutzen and Birks [1982] were the first to suggest that the fires from nuclear war would modify the atmosphere by causing global cooling, a suggestion that was inspired by the cooling that results from large forest fires. However, the term *nuclear winter* was invented in the famous TTAPS paper [*Turco et al.*, 1983], which simulated the climatic impact of the large fires that would result from the explosion of nuclear weapons in urban areas. These results were soon replicated

by *Aleksandrov and Stenchikov* [1983] and further appraised in *Pittock et al.* [1986] and *Turco et al.* [1990].

Covey et al. [1984] were the first to use an atmospheric general circulation model to study nuclear winter to verify the rudimentary calculations performed by *Turco et al.* [1983]. *Robock et al.* [2007b] continued this study using a modern state-of-the-art general circulation model. *Robock et al.* showed that 5 Tg of soot injected into the lower stratosphere would result in a reduction of globally averaged surface air temperature by up to 1.5°C, with point values reaching up to 6°C. This is the result of a direct aerosol radiative forcing of up to -20 W m^{-2}. This would undoubtedly have a strongly negative effect on world agriculture, sharply reducing the growing season in many of the food producing areas of the world [*Toon et al.*, 2007]. The aerosol forcing also resulted in a reduction of globally averaged precipitation of up to 9%. In addition, the aerosol layer caused stratospheric heating by up to 50°C higher than normal. This would undoubtedly have deleterious effects on ozone [e.g., *Mills et al.*, 2008], although the model simulations in this experiment were not conducted with the stratospheric chemistry that would be necessary to properly assess the results.

An additional study [*Robock et al.*, 2007a] analyzed the climate effects of 50 and 150 Tg injections of black carbon into the stratosphere. However, the temperature reductions due to such scenarios would be so drastic and disastrous, with globally averaged surface air temperature dipping well below 4°C for even the 50 Tg case, that injection values of this magnitude are infeasible for the experiments we discuss in the following chapter.

CHAPTER 3: EXPERIMENTS AND HYPOTHESES

Geoengineering with black carbon has not yet been conducted, so we have no observational record available for analysis. Therefore, we have designed climate model experiments to allow us to assess the potential effects. In this chapter, we describe the questions we plan to answer with our experiments, and we explain our experiment setup in more detail.

3.1 WHY BLACK CARBON?

The simplest reason for researching black carbon geoengineering is that, although having been suggested repeatedly in the past [e.g., *Crutzen*, 2006; *Teller et al.*, 1997, 2002; *Lane et al.*, 2007], it has not received nearly the same attention as sulfate aerosols. We were able to find only one past suite of simulation experiments of black carbon geoengineering. *Lacis et al.* [unpublished] performed simplified studies of black carbon geoengineering using a radiative-convective model. They additionally performed their simulations with a general circulation model, but their results are not available in the scientific literature. Therefore, our research has an important role in the scientific community which will add to the very small current knowledge base.

Another compelling reason is to consider black carbon as part of a radiative spectrum study. Much research has been on geoengineering with stratospheric sulfate aerosols [e.g., *Rasch et al.*, 2008b], and sulfate aerosols backscatter nearly perfectly, while black carbon aerosols are excellent absorbers

[*Haywood and Boucher*, 2000]. Considering these as two ends of a single scattering albedo spectrum, any aerosol actually chosen for geoengineering will fall between these two choices. The scattering end of the spectrum has been quite well discussed, and this study will provide results for the absorbing end of the spectrum. Interpolating between these two extremes is imperfect due to nonlinearities and feedbacks, but this idea is useful as a low order approximation.

Additionally, black carbon aerosols are easy to produce ubiquitously. Due to their small size and self-lofting capability due to solar heating [*Pueschel et al.*, 2000; *Rohatschek*, 1996], their atmospheric lifetime is much longer than sulfate aerosols, as we discuss below in Section 3.2.1, meaning a smaller mass of black carbon would need to be used to achieve the same effect as a certain amount of sulfate aerosols. This makes black carbon very attractive from a practicality standpoint.

Finally, and perhaps most importantly, stratospheric geoengineering with black carbon aerosols will likely cool the planet's surface. As we discussed in Section 2.4, this means of geoengineering has several analogues, all of which resulted in surface cooling. Therefore, we have reason to suspect large amounts of black carbon placed in the stratosphere will also cause cooling.

3.2 EXPERIMENT OBJECTIVES AND HYPOTHESES

The main question we would like to address is how the climate system will respond to a controlled stratospheric injection of black carbon aerosols. We

use the term "controlled" since, although the amount injected will be large, it will not be so large as to be comparable with the injection amount and resulting climate effects of nuclear winter.

The potential topics of investigation these experiments could pursue are myriad and varied, and we cannot possibly answer all of them. However, we have determined what we feel are the most important questions, which we subdivide into the following categories.

3.2.1 EFFECTIVENESS

Our first concerns in this project are basic questions of effectiveness, i.e., will black carbon geoengineering cause a reduction in global average surface air temperature? However, embedded in this question is the idea of regional impacts. *Ricke et al.* [2010], furthering the results of *Robock et al.* [2008], showed that geoengineering will result in regional inequalities, possibly meaning certain regions will be worse-off under geoengineering on top of climate change than due to climate change alone. In our analysis, we include assessments of regional effects, particularly relating to the hydrologic cycle.

We also evaluate atmospheric lifetimes of the soot particles. This has consequences for not only the mass of black carbon that must be injected each year, but also the potential reversibility of geoengineering should governing powers decide to terminate deployment.

Black carbon aerosols will stay in the stratosphere much longer than much larger sulfate aerosols. The simulations of *Robock et al.* [2008] show that a tropical

injection of sulfur dioxide results in an *e*-folding lifetime for the aerosols of approximately 1 year, assuming an aerosol effective radius of 0.30-0.35 μm. However, *Lacis et al.* [unpublished] estimate a fall speed of 0.1 km a^{-1} for soot particles with an effective radius of 1 nm. Due to coagulation of the soot particles, as well as the possibility of the particles to become hydrophilic, the atmospheric lifetime in our experiments will probably be less than the findings of *Lacis et al. Robock et al.* [2007a] found an *e*-folding lifetime of soot aerosols to be 4.6 years for an assumed soot aerosol radius of 0.1 μm, which is similar to the lifetime we discuss in Chapter 4, since the model we use is similar. This means the amount of black carbon we must use to get a particular radiative forcing is indeed less than the amount of sulfur for an equivalent forcing, but also that the effects of geoengineering with black carbon will have a longer relaxation time once injection ceases.

3.2.2 CLIMATE EFFECTS

Introducing a large amount of absorbing aerosols into the atmosphere will undoubtedly have climate effects. The most important effects black carbon geoengineering will have on the climate are radiative effects. The stratospheric aerosol layer will reduce the incident solar radiation at the surface, but black carbon aerosols are highly absorbing, which will introduce a strong longwave component. We thoroughly analyze the perturbations to the radiative budget caused by geoengineering.

Assuming the aerosols were injected into the stratosphere, one of the major concerns regarding this particular means of geoengineering is stratospheric heating due to strong absorption of shortwave radiation. In their nuclear winter studies, *Robock et al*. [2007a, 2007b] found that the stratospheric temperature would be dramatically increased by an introduction of black carbon aerosols into the stratosphere. *Mills et al*. [2008] confirmed these results, showing an increase in stratospheric temperature by 30-60°C from nuclear winter simulations, as did *Lacis et al*. [unpublished] who showed that the temperature in the middle atmosphere would be raised by up to 50°C from black carbon aerosol geoengineering. Because nuclear winter levels of soot injection would cause too much surface cooling, the amount of soot we would inject for geoengineering would be less, resulting in pronounced stratospheric heating but by a smaller amount.

One of the potential effects of this heating is a large reduction in stratospheric ozone. As *Mills et al*. [2008] reported, the Chapman reactions which catalyze ozone destruction are temperature sensitive. They also found that the heating due to a single 5 Tg injection of soot into the stratosphere would allow a huge pulse of water vapor to enter the stratosphere, as well as N_2O-rich air which provides extra NO_x, which could further catalyze ozone destruction, as we discuss in Section 6.2.2. *Mills et al*. found that the global ozone column would be depleted by 20-25% for five years after the injection. The continuous injection experiments of *Lacis et al*. [unpublished] also showed local decreases in ozone concentrations, but total column ozone would remain relatively constant due to

compensating recovery below. They found that the ozone layer self-heals, in that the destruction of ozone allows more ultraviolet radiation into the lower atmosphere, which results in an increase in lower altitude oxygen photolysis. However, the results of *Lacis et al.* were performed with a one-dimensional radiative convective model, so explicit modeling of the involved dynamics and chemistry would be required to adequately assess these mechanisms. We include both of these features in our simulations.

Stratospheric heating also has strong dynamic effects. *Mills et al.* [2008] found that in their nuclear winter simulations, the Brewer-Dobson circulation is slowed to half of its rate for several years after the initial injection of black carbon. This delay would likely be sustained in the continuous presence of a soot layer in the stratosphere, albeit at a possibly lower magnitude than was found by *Mills et al.* We include an assessment of the changes to atmospheric circulation in our experiments, including the zonal wind and the Arctic Oscillation.

Simulations and observations of past volcanic eruptions show that large perturbations to insolation can disrupt monsoonal precipitation [e.g., *Robock and Liu*, 1994; *Oman et al.*, 2006]. We would similarly expect effects on the hydrologic cycle from geoengineering, and arguments to this effect can be made from both modeling [*Robock et al.*, 2008] and observational [*Trenberth and Dai*, 2007] perspectives. As part of our analysis, we calculate the major terms in the water budget as represented by the model. Specifically, we include precipitation, evaporation, soil moisture, and runoff.

The surface cooling from geoengineering, as well as the circulation changes, could cause a regrowth of sea ice. We will evaluate the effects of black carbon geoengineering on the cryosphere.

3.2.3 DEPOSITION

In placing a large amount of black carbon in the stratosphere, the aerosols must eventually deposit onto the surface. Based on the results of *Kravitz et al.* [2009], the most likely locations for these aerosols to deposit in appreciable numbers is mid-latitude storm tracks and at the poles.

This addresses two potential problems. The first is that many large population centers, as well as many agricultural regions, are in the mid-latitudes. Black carbon is known to have adverse effects on human health [e.g., *CDC*, 1999; *Baan et al.*, 2006], so evaluating deposition is important in determining potential levels of exposure to harmful substances.

The second problem could also occur in the mid-latitudes in snowy regions but is more likely to be significant in polar regions where there is a large amount of snow. The albedo of fresh snow is reduced if black carbon deposits on it [*Vogelmann et al.*, 1988], which is commonly termed the "dirty snow effect." The climate model we plan to use, discussed in Section 3.3, has a feature dedicated to calculating this particular effect, and we address the results of this calculation in our analysis in Section 5.7.

As the aerosols pass through the troposphere, they will cause local heating. We determine the degree of tropospheric heating, as well as the model's evaluation of the potential consequences.

3.2.4 SENSITIVITY STUDY

Determining the climate effects of geoengineering by black carbon aerosols is our primary concern, but in doing so, we must make certain assumptions. For example, our model has a default initial aerosol size for black carbon aerosols. However, deliberately producing aerosols of a particular size may not be feasible, and as *Lacis et al.* [unpublished] suggest, one particular aerosol size may produce more desirable effects than another.

Additionally, as both *Lacis et al.* and *Ban-Weiss et al.* [2011] show, changing the altitude of insertion will change the resulting surface temperature pattern. One particularly striking result is that if the aerosols remain too low in the stratosphere, the longwave emission from the aerosol layer can actually result in surface warming, and there is an optimal altitude at which the aerosol layer can cause the most cooling. However, black carbon aerosols are heated by the sun and self-loft [*Pueschel et al*, 2000; *Rohatschek*, 1996], which could mean black carbon geoengineering is insensitive to the altitude of injection.

In light of these concerns, we include a sensitivity study in our analysis, in which we test the degree to which particular values of three parameters influence our results. The parameters we test are initial aerosol size, altitude of injection, and the perturbations solely due to the dirty snow effect.

3.3 MODEL DESCRIPTION

The climate model simulations are performed using ModelE, a general circulation model of Earth's climate, which was developed by the National Aeronautics and Space Administration's (NASA) Goddard Institute for Space Studies (GISS) [*Schmidt et al.*, 2006]. The version of the model used is run at 2° latitude by 2.5° longitude horizontal resolution (144×90 grid boxes). It has 40 vertical layers, including a completely resolved stratosphere, with a model top of 0.1 mb (approaching 80 km), and an additional three layers used specifically for the radiative transfer code. Table B.1 lists the pressure levels of the individual layers used in this resolution. The dynamical core uses a 3.75 minute leap frog time step, the model physics uses a 30 minute time step, and the radiation is calculated every 5th physics time step, or every 2.5 hours.

Greenhouse gases, natural and anthropogenic aerosols, and other radiatively important factors are fixed at the year 2000 concentrations and distributions. We used fixed sea surface temperatures, which are an average of the Hadley Centre's HadISST over the period 1996-2005 [*Rayner et al.*, 2003]. Sea ice is also prescribed climatologically by this data set and year range.

The radiation scheme in the shortwave is governed by a *k*-distribution divided into 16 intervals (Table B.3) which cover 6 spectral intervals (Table B.2). Cloud and aerosol Mie scattering parameters and surface albedos are averaged over these intervals. Additionally, one of the 16 *k*-distribution intervals governs UV ozone absorption in the approximate wavelength range 200-360 nm. The radiation scheme in the longwave is also governed by a *k*-distribution scheme

divided into 33 intervals. The radiatively important gases considered specifically by the *k*-distribution are H_2O, CO_2, O_3, CH_4, N_2O, NO, and CFCs.

The black carbon aerosols are inserted into the model as radiatively active tracers, as described by *Koch et al.* [2006]. The aerosols grow according to the ambient relative humidity per the formulas of *Tang* [1996] and are transported via the model's circulation. Soot aerosols are sorted into 25 different bins by relative humidity, which is a proxy for aerosol size (spanning sizes between 1 nm and 5.0 μm), and Mie parameters in the solar and thermal spectra are prescribed by a lookup table for these bins. Every radiation time step, radiative heating due to the aerosols is added to the existing model temperatures. Heterogeneous chemical reactions do not occur on the surfaces of the aerosols, which could affect our results, as we discuss in Section 7.2. However, current understanding of these processes and their potential effects is limited.

The aerosol interactions with clouds are limited to changes in heating rates that possibly affect cloud droplet condensation/evaporation. The aerosol indirect effects on clouds are deactivated for the experiments discussed in the next section, although the model is capable of representing these processes.

Model chemistry involves 113 reactions, including OH, ozone, HO_x, NO_x, methane, isoprene, and halogens. We note this includes heterogeneous chlorine chemistry, which accounts for Antarctic polar ozone depletion in the austral spring. The chemical reactions are also fully resolved in the stratosphere. Photolysis in the stratosphere is included and varies dynamically as a function of temperature, pressure, solar output, cloudiness, albedo, and ozone concentration.

Ozone and methane are computed at the model's resolution and are radiatively interactive with model tracers, meaning they modify heating rates and are chemically active. Other important aerosols, gases, and other tracers which are both radiatively and chemically active include dust, terpenes, biogenic isoprene, and nitrate aerosols. Secondary organic aerosol processes are not included in this version of the model.

ModelE has an option to allow black carbon deposition to modify the albedo of snow. We have selectively included this parameter as part of our sensitivity study, as we described in Section 3.2.4. Dry deposition and gravitational settling of the aerosols is described by a calculation of the bulk surface resistance, which depends upon the land surface type, temperature, and planetary boundary layer depth. This is also modified by upward cumulus mass flux. Once the aerosol comes into contact with a water droplet, the particle is advected as water and becomes involved in the convection, condensation, and cloud schemes present in the model.

3.4 EXPERIMENT DESIGN

To study the climate effects of geoengineering with stratospheric aerosols, we performed multiple ensembles of simulations in which we injected black carbon aerosols into the tropical lower stratosphere. The injections were performed at every model time step at 0° longitude, were distributed across a latitude band spanning 10°S to 10°N (see Figure 3.1), and, as our default case, through layers 24-26 of the model, roughly spanning the 100-150 mb layer, which
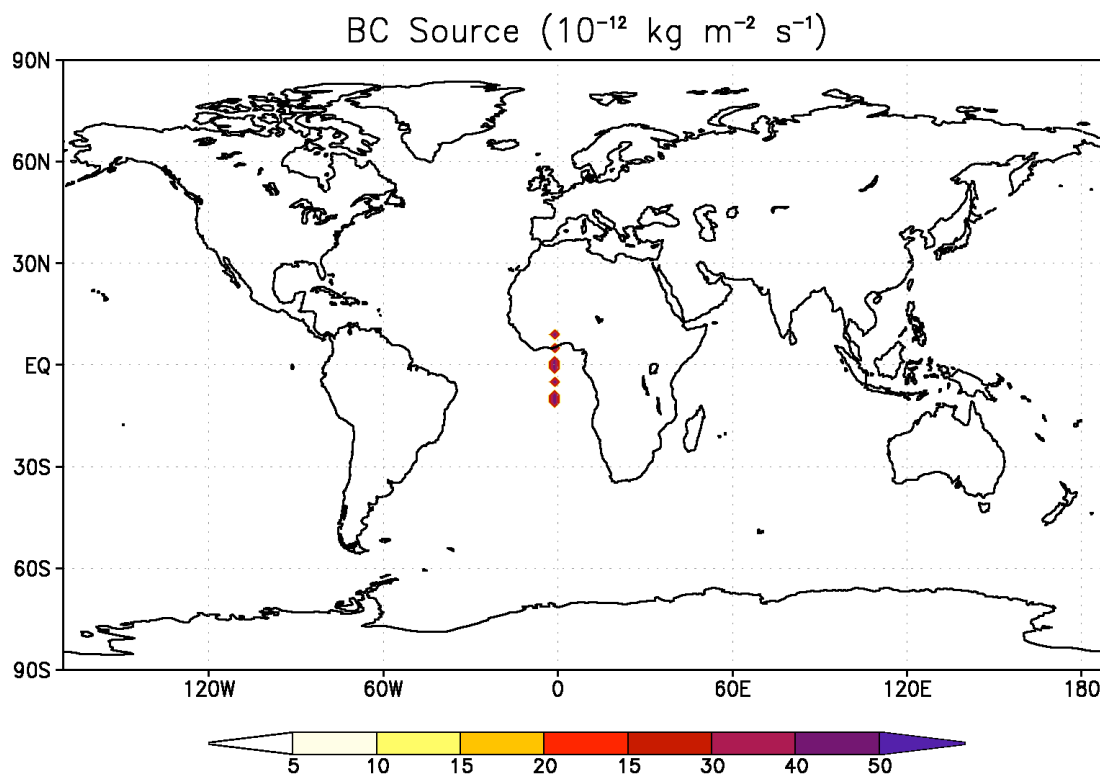
FIGURE 3.1. Spatial map of the black carbon aerosol source. Aerosols were added at these locations at every model time step through the layers appropriate to each experiment, as specified in Table 3.1.

the model designates as the lower most levels of the stratosphere. We chose to inject them across a latitude band, as the concentrations from injecting them at one point were too high for the chemistry code to perform its calculations, resulting in model blowup. Each ensemble is comprised of three 10-year model runs.

The central purpose of geoengineering in general is to reduce global average temperature by a controlled amount. Therefore, in conducting this experiment, we certainly want to use less soot than in a nuclear winter simulation. *Robock et al.* [2008] found that in their version of ModelE, in conducting simulations of stratospheric geoengineering with sulfate aerosols, a cooling of globally averaged surface air temperature by 0.5°C, or back to 1980 levels, requires a radiative forcing at the surface of -1.9 W m^{-2}. Therefore, in these experiments, as an initial goal, we wish to inject enough black carbon into the stratosphere to cause a radiative forcing of -2 W m^{-2}, which should result in similar cooling.

Translating this into a specific amount of black carbon is not straightforward. *Lacis et al*. showed that for soot particles with an effective radius of 1 nm, to cause a radiative forcing of -1 W m^{-2} would require 0.15 Tg of soot at 44-50 km in altitude or 0.23 Tg of soot at 27-29 km. This corresponds to an aerosol optical depth of 0.0047 and 0.0096, respectively. However, the default dry radius of black carbon aerosols in ModelE is 0.08 μm, nearly two orders of magnitude larger than what *Lacis et al.* used. Although the aerosol size used in

our simulations is more realistic in terms of the aerosols we are likely to create via the means described in Chapter 6 [*Rose et al.*, 2006], as *Lacis et al.* discuss, changing aerosol size will also change the optical properties.

For simplicity, we choose to inject the round number of 1 Tg per year of black carbon into the lower stratosphere, which is a similar order of magnitude to the simulations of *Lacis et al. Lacis et al.* obtained model results that were measurable above the level of natural variability, giving us confidence this amount is sufficient to surpass problems in obtaining a sufficient signal-to-noise ratio. It is one fifth the total amount used in past nuclear winter simulations [*Robock et al.*, 2007a; *Mills et al.*, 2008], although those were one-time injections, so continuous injections could result in similar atmospheric burdens. We use this same amount in our determination of practicality in Chapter 6.

To determine the sensitivity of the results to certain parameters, as we described in Section 3.2, we performed multiple ensembles of experiments. The details of these ensembles are given in Table 3.1. One parameter we tested was varying the altitude of the injection. In contrast to our standard case of injection into model layers 24-26, we injected into layers 29-31, which corresponds to the 31-57 mb pressure level, or approximately 23-28 km in altitude. Another parameter is the radius of the aerosols. By default in ModelE, the radius is 0.08 μm. After *Rose et al.* [2006], we simulated aerosol sizes of 0.03 and 0.15 μm. The final parameter we analyzed is the dirty snow effect, which can be turned on or off by specifying a model pre-processor flag. By default, we have turned off the dirty snow effect, but we do include it in two ensembles.

TABLE 3.1. A summary of the model experiments in this project. All ensembles are comprised of three 10-year runs. With the exception of the control runs, all ensembles involved continuous injections of black carbon into the tropical lower stratosphere in the amount of 1 Tg per year.

Ensemble Name	Description	Particle Radius (μm)	Altitude of Injection (Model Layers)	Dirty Snow Effect	Additional Comments
Con	Control	Control run (constant 2000 conditions)			
Def	Default	0.08	24-26	off	Default setup upon which the other runs are based.
HA	High Altitude	0.08	29-31	off	
SmR	Small Radius	0.03	24-26	off	
LgR	Large Radius	0.15	24-26	off	
DefDS	Default + Dirty Snow	0.08	24-26	on	
HASmR	High Altitude, Small Radius	0.03	29-31	off	Resulted in model blowup
HALgR	High Altitude, Large Radius	0.15	29-31	off	
HADS	High Altitude + Dirty Snow	0.08	29-31	on	

We have no results for ensemble HASmR, in which injection occurred at a higher altitude and with a smaller initial radius than the default case. For this particular ensemble, the ozone destruction was so excessive in certain locations that it created unphysical dynamic conditions, resulting in model blowup.

For our simulations, we chose to use fixed sea surface temperatures. Even though our runs are only ten years long, this assumption will certainly affect the degree of realism of our temperature, hydrologic cycle, and sea ice responses, as well as the degree to which the dirty snow effect is represented in our model. At each relevant point, we discuss the impacts this assumption had on our results. Despite this drawback, using fixed sea surface temperatures is advantageous to our set of experiments. It allows the system to equilibrate more rapidly, giving us a better idea of the relative importance of the sensitivity parameters we described above. It also considerably cuts down the amount of required computer time, which is advantageous, given that we have a total of 240 model years of simulation in our set of ensembles. As we describe in Section 7.5, the next step for investigating black carbon geoengineering is to use a dynamic ocean with a focus on the important sensitivity parameters. Additionally, many coupled chemistry-climate models use a fixed ocean for their simulations [*SPARC CCMVal*, 2010], which will allow comparability of results should the chemistry-climate models wish to conduct simulations similar to these experiments, as is suggested in Section 7.6.

CHAPTER 4: CLIMATE EFFECTS

We now analyze the climate effects of geoengineering as calculated by the model. The effects we analyze can be broadly divided into five categories. The first is effectiveness, in which we look at whether geoengineering actually cools the surface, including a discussion of surface temperature and the radiation budget. In the section on mass burden and deposition, we explore what happens to the aerosols once they are injected into the stratosphere. The next section explores the largely negative consequences of the effects of stratospheric heating. The following section looks at perturbations to the hydrologic cycle, with a focus on the Indian, African, and East Asian summer monsoon system. Finally, we look at perturbations to the cryosphere, including the potential for regrowth of Arctic sea ice due to decreased radiation and cooler temperatures.

4.1 EFFECTIVENESS

The most important question we can ask about our simulations is whether geoengineering with black carbon would actually work, i.e., whether it indeed cools the surface. As expected, according to our simulations, the answer depends upon the choice of parameters.

Figure 4.1 shows globally averaged surface air temperature anomalies for each of the ensembles.   Since sea surface temperatures are fixed, this figure actually shows land area averaged surface air temperature anomalies. However, dividing the values by 0.3 (the approximate fraction of Earth's surface covered by
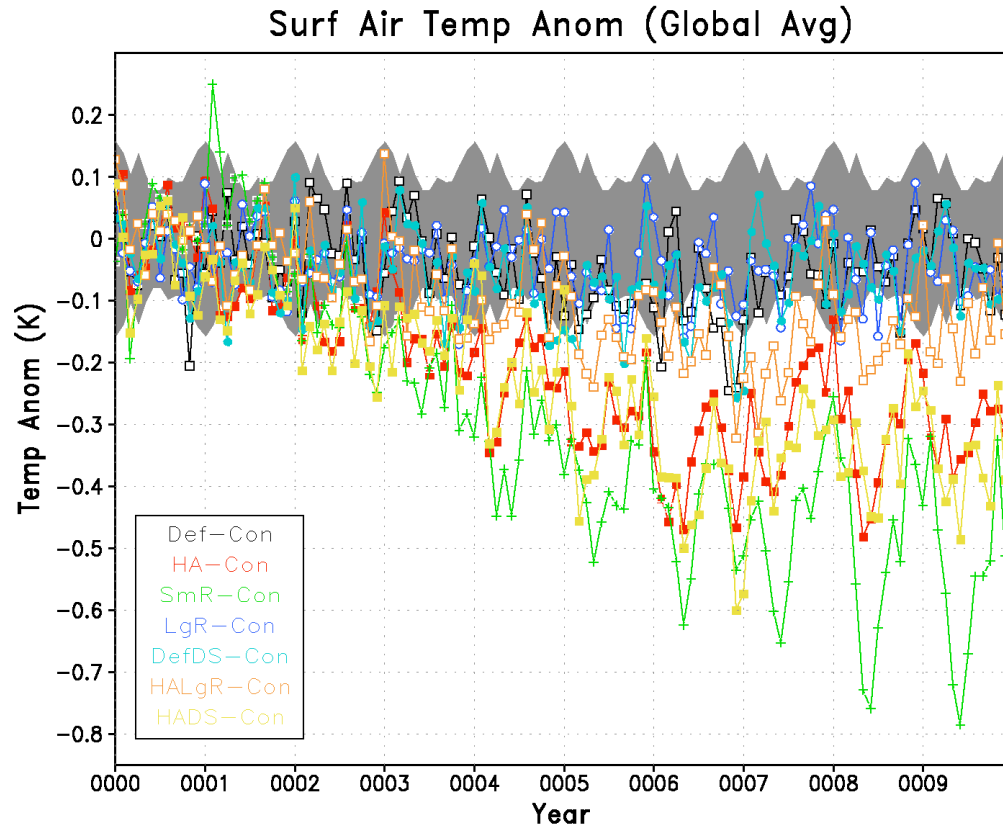
FIGURE 4.1. Globally averaged surface air temperature anomalies for each of the geoengineering ensembles. Ensemble descriptions are given in Table 3.1. Grey shading denotes ±1.96σ of the variability of the seasonal cycle of the control ensemble, averaged over the entire 10 year simulation.

land) is not a suitable estimate of what the surface air temperature anomalies would be if a dynamic ocean were used, as dynamical effects would affect the surface temperature field. Therefore, we refer to these values as globally averaged surface air temperature anomalies.

All ensembles show some degree of cooling, although Def, DefDS, and LgR show cooling that is mostly statistically insignificant when compared to the natural variability of the control ensemble. This suggests that geoengineering with a particle radius of 0.08 μm or larger in the lower stratosphere would not be particularly effective in general. However, HALgR shows some statistically significant cooling results, mostly in the boreal summer where the natural variability is lowest.

The ensembles that cause the most cooling are either higher altitude injections or injections using small particles. Using a high altitude injection (HA and HADS) appears to cause a reasonable amount of cooling by 0.3-0.4°C from the year 2000 temperatures, or back to approximately 1980 levels (land-ocean temperature index and land average only) [*Hansen et al.*, 2010]. SmR causes cooling by up to 0.8°C, or back to approximately 1880 levels (land-ocean temperature index and land average only). However, these values are for stratospheric injections of 1 Tg of black carbon per year, so this can be adjusted by varying the amount of injection. The actual cooling values would likely be larger if sea surface temperatures were allowed to vary.

From this figure, it appears that experiment HA causes the most reasonable value of cooling, and its temperature results are similar to the 5 Tg per

year experiment in *Robock et al.* [2008]. Therefore, in our discussion of the climate

effects of black carbon geoengineering, which constitutes the bulk of this

chapter, we will concentrate on this particular scenario. Figure 4.2 shows a

spatial map of the cooling due to ensemble HA. Due to this version of the model

having fixed sea surface temperatures, most of the significant anomalies are

confined to land areas. The temperature anomalies are reminiscent of volcanic

cooling patterns [*Robock*, 2000], with large areas of cooling over the Northern

Hemisphere continents, which is expected due to land's low heat capacity and

consequent responsiveness to radiative perturbations.

Analyzing in more detail, Figure 4.3 shows surface air temperature

anomalies divided into JJA and DJF averages. These also show typical volcanic

cooling patterns and are reminiscent of the *Robock et al.* [2008] results for

stratospheric sulfate geoengineering. With the exception of the Indian

subcontinent and the Tibetan Plateau, all of the continents show cooling in the

boreal summer, sometimes exceeding 5°C. The warming of the Tibetan Plateau

can be attributed to longwave emission from the absorbing aerosol layer, as we

discuss in Section 4.4. The anomaly over India is likely due to perturbations in

cloud cover and are related to a disruption of the monsoon. We discuss the

hydrologic cycle impacts in Section 4.5, but we refrain from analysis of the

impacts of geoengineering on cloud cover, as we do not have enough

information to attribute changes in clouds to any specific forcing or process. The

anomalies over Antarctica are not statistically significant and are likely due to

natural variability, which is higher in the winter. The DJF averages show a
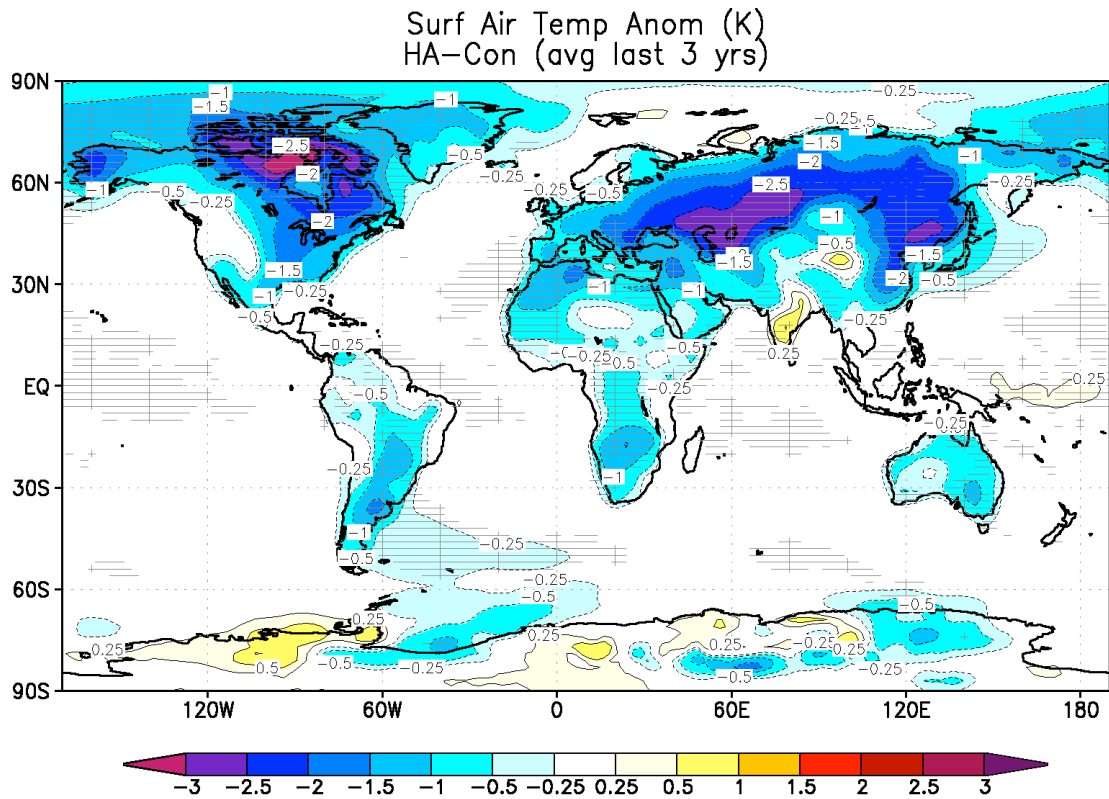
FIGURE 4.2. Surface air temperature anomaly for middle stratospheric geoengineering (ensemble HA as described in Table 3.1), averaged over the last three years of simulation. Grey hatching denotes values that are statistically significant at the 95% confidence level as calculated by an unpaired two sample Student's *t* test.
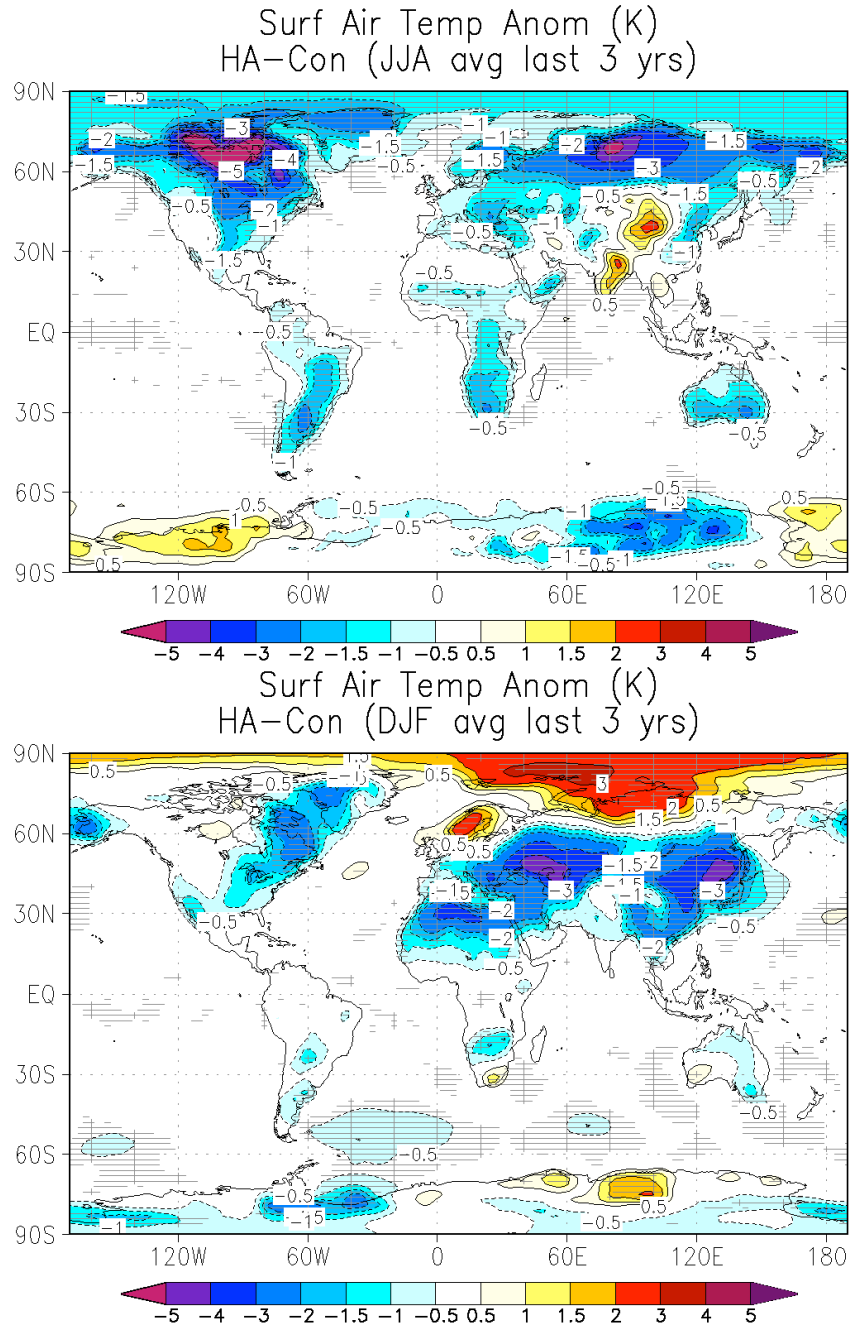
FIGURE 4.3. Surface air temperature anomalies for middle stratospheric geoengineering (ensemble HA as described in Table 3.1), averaged over the last three summers (boreal in top panel, austral in bottom panel) of simulation. Grey hatching denotes values that are statistically significant at the 95% confidence level as calculated by an unpaired two sample Student's *t* test.

strong amount of winter warming over the Arctic, which is a typical dynamical response of large volcanic eruptions [e.g., *Robock*, 2000]. This is a result of a forced positive mode of the Arctic Oscillation, as we discuss later in Section 4.4. Cooling is still pronounced over most of the Northern Hemisphere continental area.

Figure 4.4 shows aerosol optical depth and shortwave radiative forcing due to the black carbon aerosol layer. From this figure, it appears a ten year simulation was insufficient to allow the aerosol layer to reach equilibrium. After ten years, aerosol optical depth (visible) has reached a peak value of approximately 0.11. This is similar to nuclear winter simulations involving a 5 Tg pulse of black carbon injected into the stratosphere, which reached a peak zonally averaged optical depth of 0.1 one year after the eruption [*Robock et al.*, 2007b]. As we discuss in Chapter 5, the peak aerosol mass burdens are similar in this experiment and the nuclear winter simulations. For comparison, *Robock et al.* [2008] obtained a radiative forcing of -3 W m^{-2} in the summer from their tropical stratospheric sulfate geoengineering experiments, which, according to the results of *Kravitz and Robock* [2011] who used the same model, corresponds to a sulfate aerosol optical depth of approximately 0.07.

From this comparison, it appears that black carbon is much more radiatively effective than sulfur, reaching a peak value of 20 W m^{-2} after ten years. This is similar to the radiative forcing anomalies obtained by *Robock et al.* [2007b], which reached a peak of approximately -25 W m^{-2}. However, these values are perhaps not directly comparable to the sulfate geoengineering
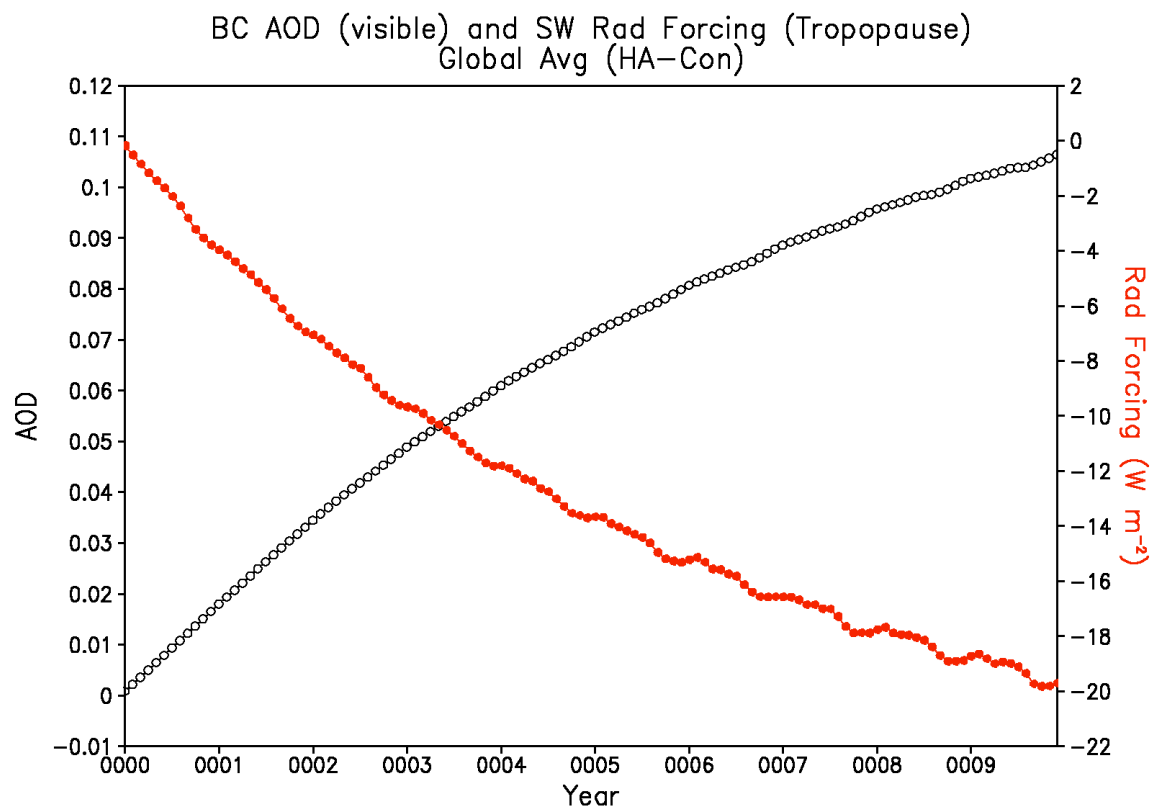
FIGURE 4.4. Globally averaged black carbon aerosol optical depth (visible spectrum) and shortwave radiative forcing at the tropopause for middle stratospheric geoengineering (ensemble HA as described in Table 3.1).

experiments, as this is a measure of instantaneous radiative forcing instead of adjusted radiative forcing [*Hansen et al.*, 2005], i.e., the stratospheric temperatures are not allowed to adjust for these calculations. For most forcing agents, the instantaneous forcing provides a good approximation to the adjusted forcing [*Hansen et al.*, 1981], which is generally considered the measure that is relevant to climate change [*Hansen et al.*, 2005]. However, for certain stratospheric species, such as ozone and stratospheric black carbon, which we have injected in large amounts, the instantaneous and adjusted forcings can be vastly different [*Hansen et al.*, 1997]. As we clearly see here, the instantaneous radiative forcing due to stratospheric geoengineering with black carbon aerosols is not a good measure of the resulting climate impacts, since such a huge radiative perturbation, more than five times the 3.7 W m^{-2} reported forcing for a doubling of CO_2 [*Solomon et al.*, 2007], results in a modest temperature perturbation. Converting these instantaneous forcings into adjusted forcings is not simple, so we do not undertake such a calculation here and instead caution the reader to properly interpret our findings regarding radiative forcing.

In the zonal averages of these fields, as in Figure 4.5, both optical depth and shortwave radiative forcing have a clear seasonal cycle, with optical depth peaking in spring at approximately 50-60° in latitude and peak radiative forcing lagging the peak in optical depth by 2-3 months. This is due to a relatively low black carbon deposition rate following peak deposition in the winter, as is seen in Figure 4.6, allowing the aerosol layer to accumulate and reach high optical depths of up to 0.15. The peak in radiative forcing, sometimes reaching 30 W m^{-2},
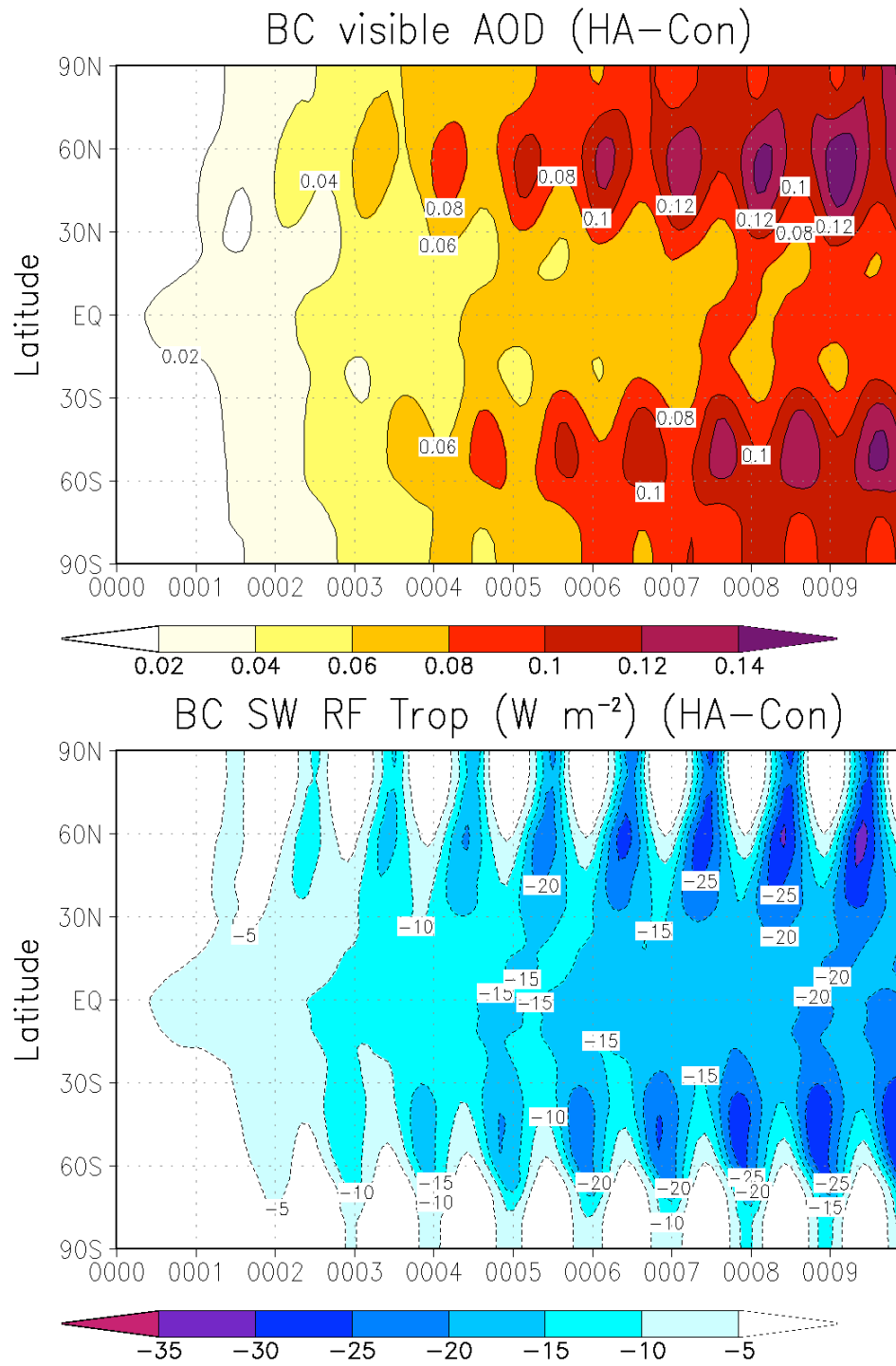
FIGURE 4.5. Zonally averaged black carbon aerosol optical depth (visible spectrum) and shortwave radiative forcing at the tropopause for middle stratospheric geoengineering (ensemble HA as described in Table 3.1).

results from the optimal combination of high optical depth and sufficient sunlight, which occurs in late spring to early summer. Average insolation at 60°N at this time of year is approximately 460 W m^{-2} [*Wallace and Hobbs*, 2006], meaning the black carbon forcing results in a loss of 6.5% of incident solar radiation reaching the tropopause.

An unusual feature of Figure 4.6 is that the black carbon deposition rate appears to increase as time progresses, particularly in the polar winter. The Northern Hemisphere midlatitudes also show an increase. The anomalies are all positive, so this is unlikely due to noise or ensemble variability. We discuss this feature in more detail in the following section.

Figure 4.7 shows this in more detail by dividing the radiation anomalies into solar and thermal components. Net radiation is calculated as down minus up, so the positive anomaly in solar radiation at TOA suggests the planet is retaining approximately 18 W m^{-2} more solar energy by the end of the tenth year of simulation. However, thermal radiation back to space at TOA increases by 25 W m^{-2}, showing a net loss of radiation by approximately 7 W m^{-2}.

Both the tropopause and the surface show reductions in total global average radiation from geoengineering. The amount of reduction in solar radiation is comparable for both the tropopause and the surface, with a value of approximately -20 W m^{-2} after ten years. However, the total tropopause anomaly of -45 W m^{-2} is much larger in magnitude than the total surface anomaly of -15 W m^{-2}, which is due to the difference in thermal radiation.
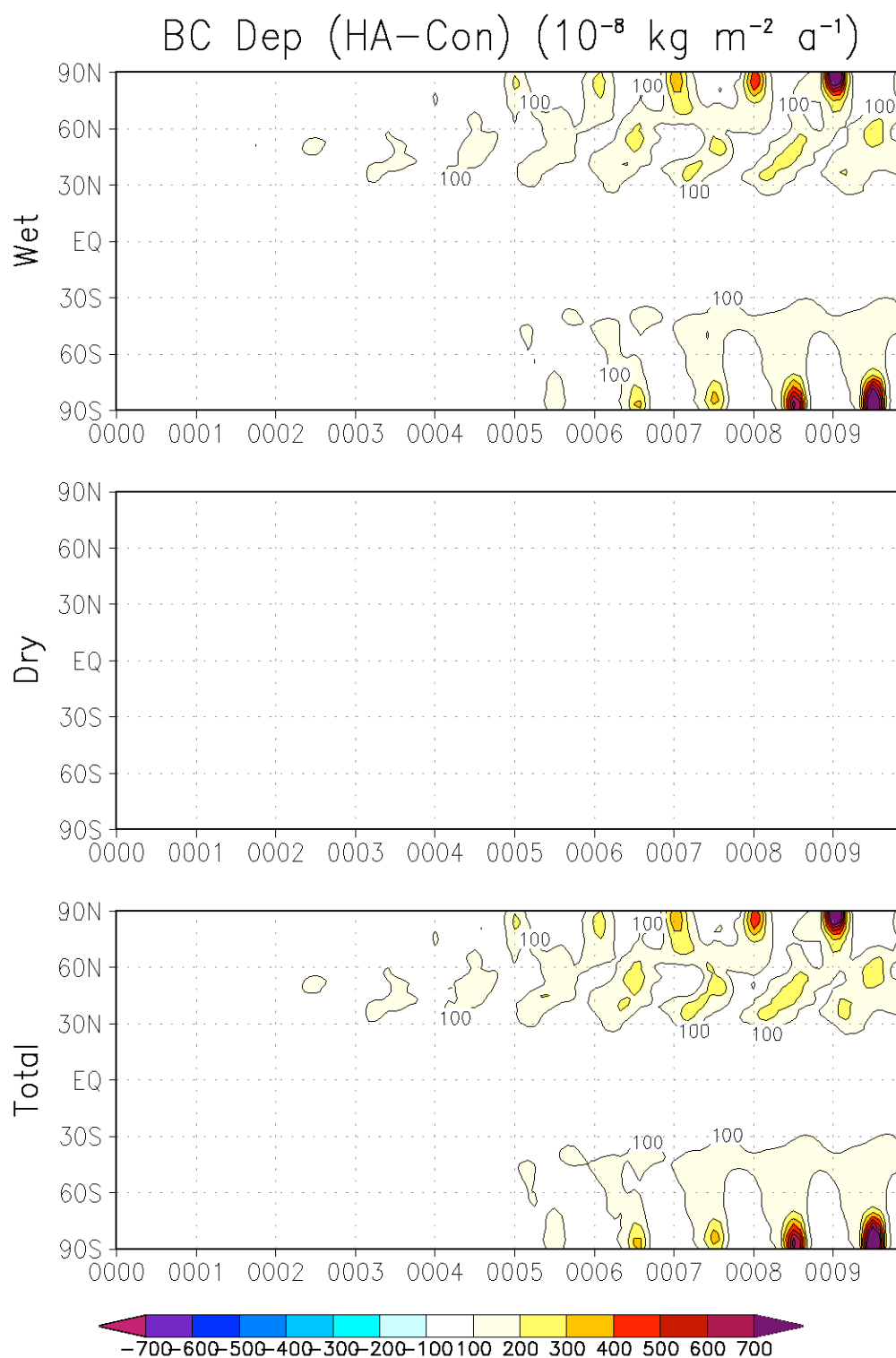
FIGURE 4.6. Zonally averaged total deposition (wet plus dry) for middle

stratospheric geoengineering (ensemble HA as described in Table 3.1).
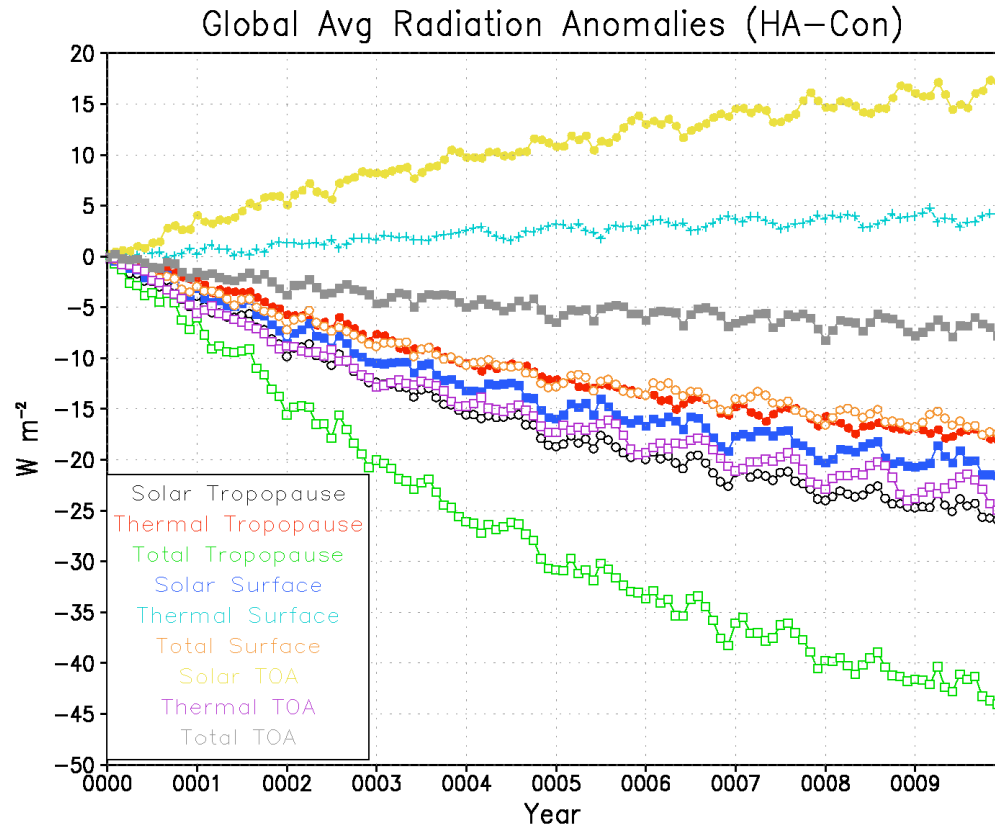
FIGURE 4.7. Globally averaged net radiation (down minus up) anomalies for middle stratospheric geoengineering (ensemble HA as described in Table 3.1). Values are calculated at the tropopause, surface, and top of atmosphere (TOA). Total anomaly is the sum of the solar and thermal anomalies.

Figures 4.8 and 4.9 show the same but zonally averaged instead of globally averaged. Solar radiation anomalies are the greatest at the poles during summer due to ozone destruction and the consequential perturbation to the shortwave budget. Indeed, Figures 4.10 and 4.11 show polar summer anomalies in TOA ozone shortwave radiative forcing of up to 3 W m^{-2} in magnitude. These quantities are calculated as downwelling minus upwelling, so a negative value in these figures indicates more upwelling shortwave radiation, which means that shortwave was not absorbed by the atmosphere. This makes sense in the context of ozone destruction, as ozone is a greenhouse gas and a strong absorber of ultraviolet radiation, which comprises a large portion of the insolation spectrum. We discuss perturbations to stratospheric ozone in more detail in Section 4.4.

Returning to Figures 4.8 and 4.9, thermal radiation anomalies follow the spatial and temporal patterns of insolation, which would be expected from an absorbing aerosol, as more solar heating of the particles will result in more thermal radiation. Since solar radiation is mostly transparent to the atmosphere, and the aerosol layer is above the tropopause, the solar radiation panels for the tropopause and the surface look similar. However, the aerosol layer is quite close to the tropopause and is far removed from the surface, which explains why the thermal radiation panels show an anomaly at the tropopause but none (or any anomalies are smaller in magnitude than 10 W m^{-2}) for the surface. In the totals, the summers appear to show the greatest radiative imbalance due to geoengineering, most prominently at the tropopause due to the large amount of nearby absorbing aerosol affecting the thermal radiation. Figures 4.12 and 4.13

Radiation Anomalies (W m^{-2})
HA–Con (zonal avg)
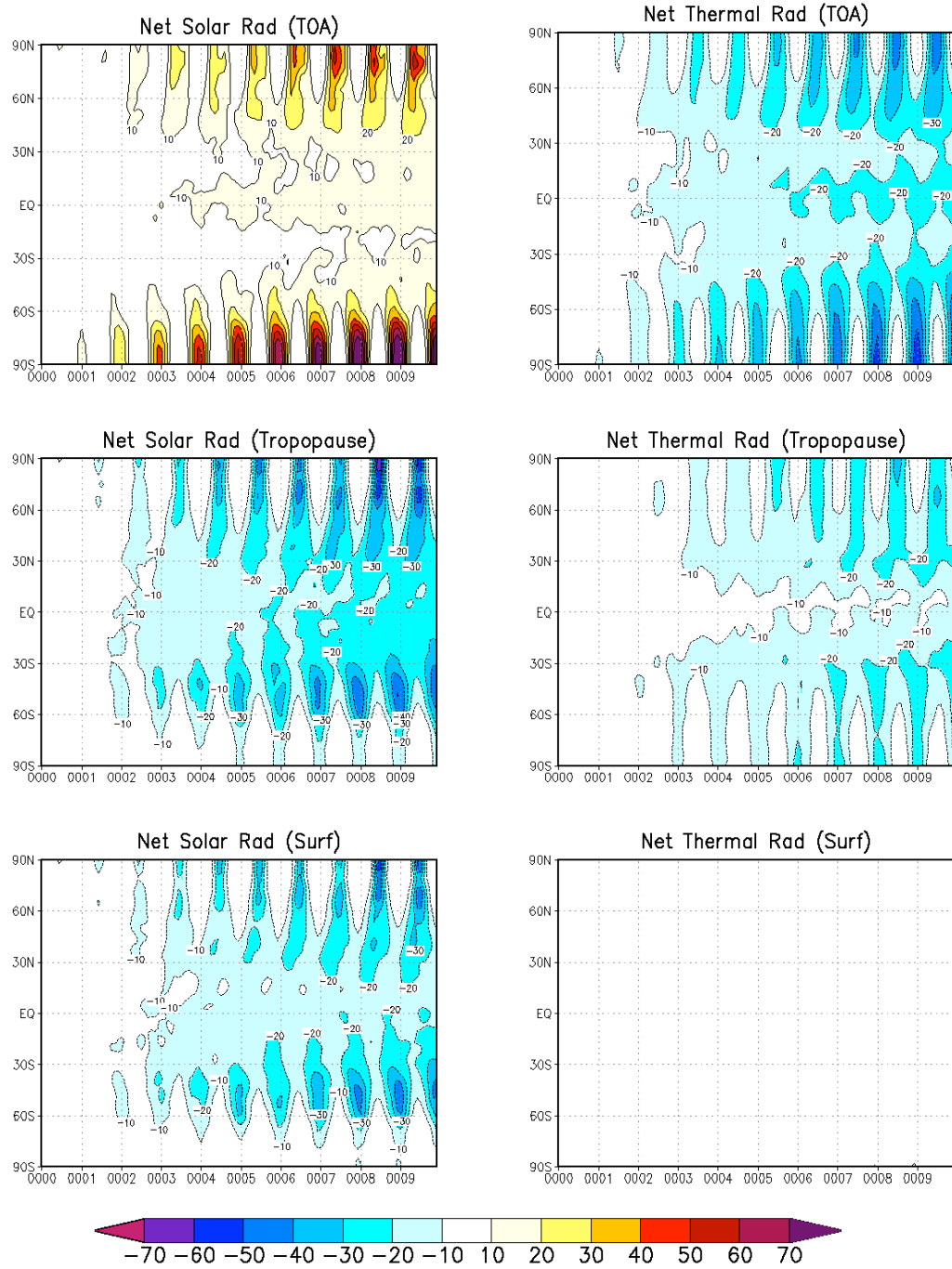
FIGURE 4.8. Zonally averaged net radiation (down minus up) anomalies for middle stratospheric geoengineering (ensemble HA as described in Table 3.1). Values are calculated at the tropopause, surface, and top of atmosphere (TOA).
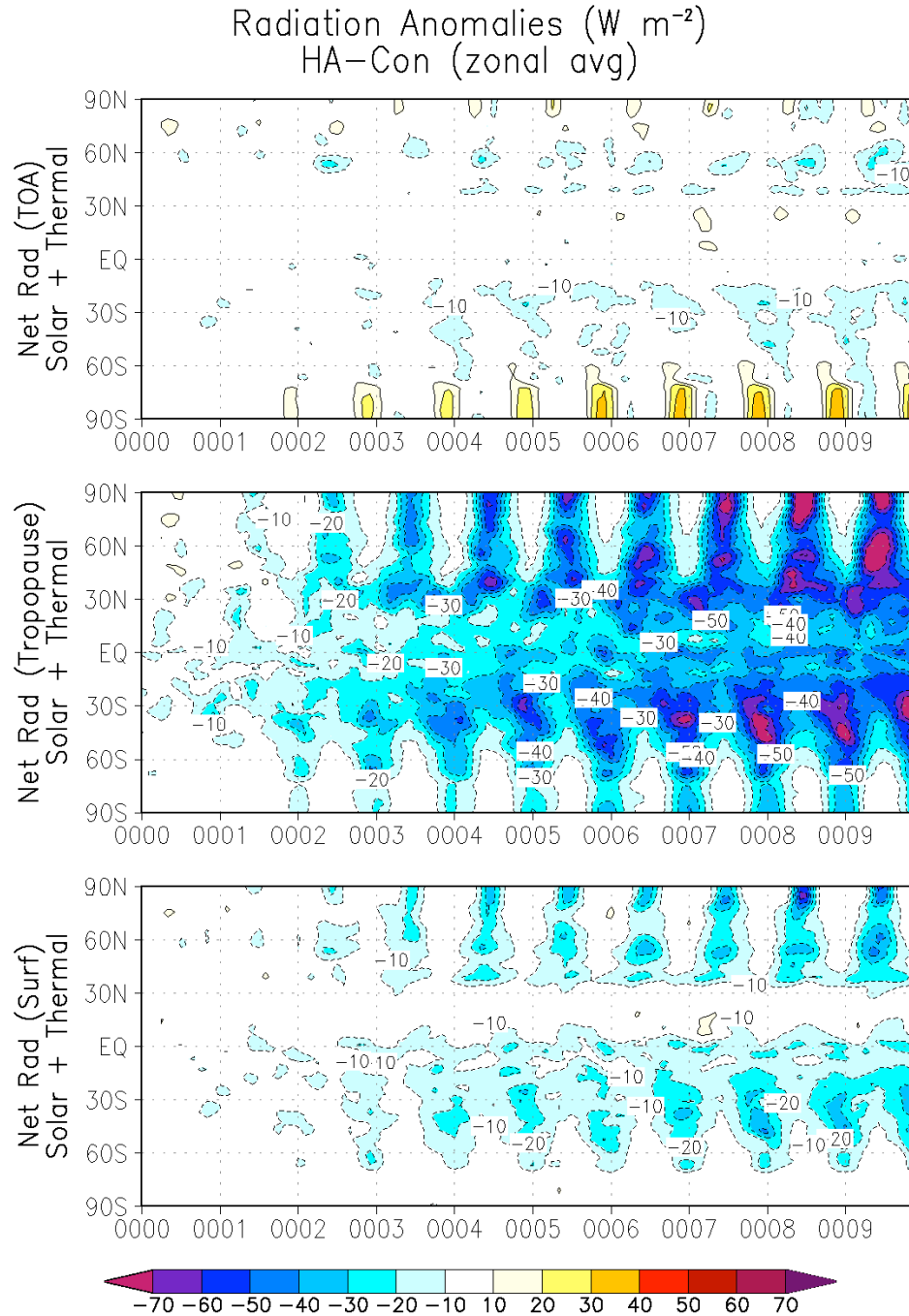
FIGURE 4.9. Zonally averaged total (solar + thermal) net radiation (down minus up) anomalies for middle stratospheric geoengineering (ensemble HA as described in Table 3.1). Values are calculated at the tropopause, surface, and top of atmosphere (TOA).
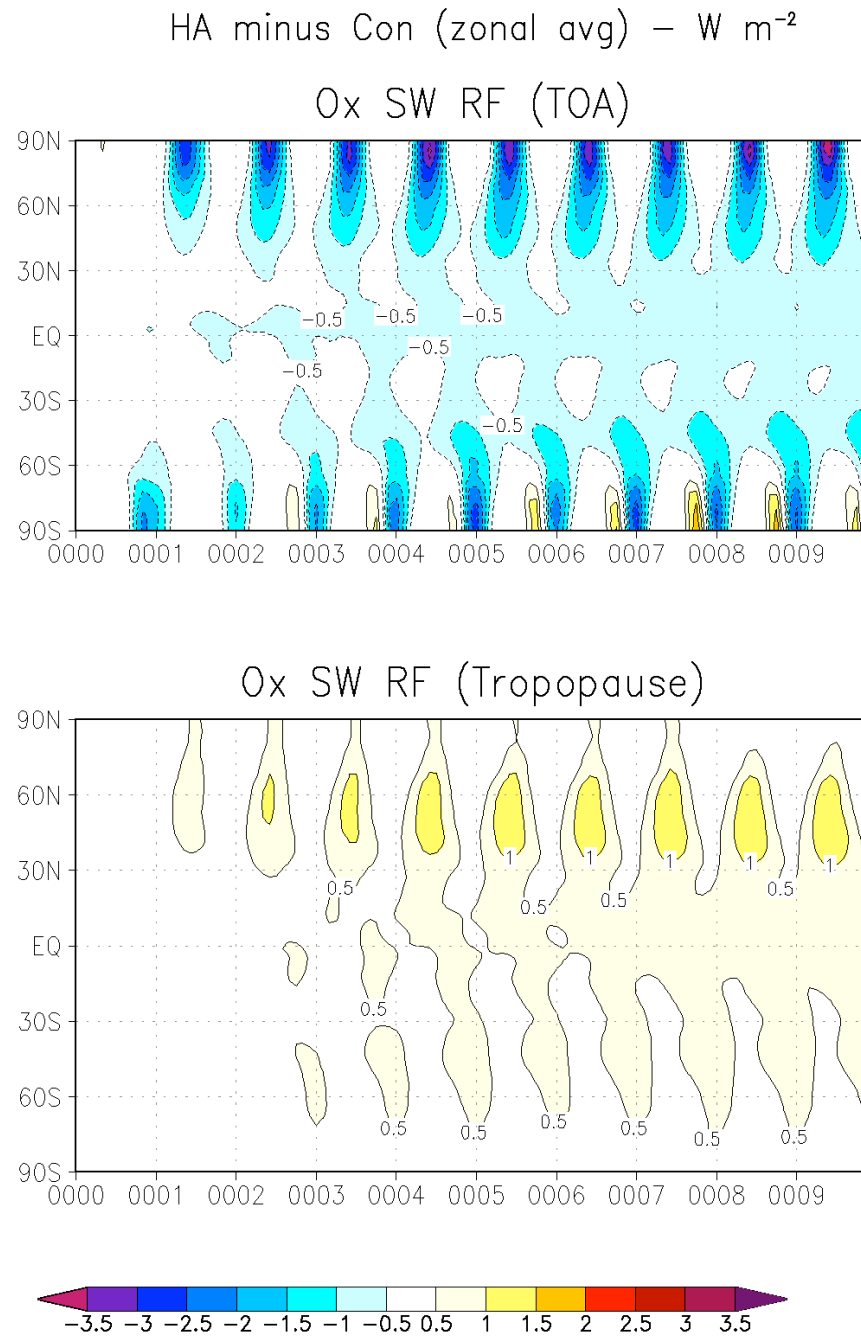
FIGURE 4.10. Zonally averaged ozone shortwave radiative forcing (down minus up) anomalies for middle stratospheric geoengineering (ensemble HA as described in Table 3.1). Values are calculated at the top of the atmosphere (TOA) and the tropopause.
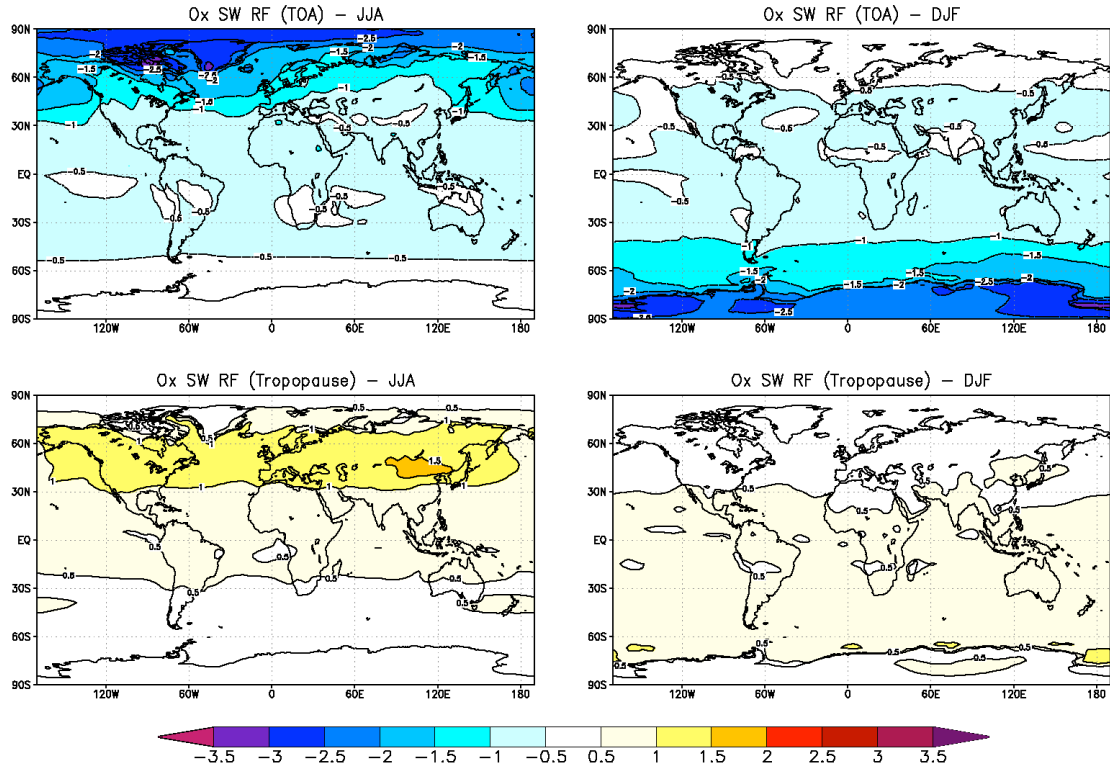
FIGURE 4.11. Spatial maps of ozone shortwave radiative forcing (down minus up) anomalies for middle stratospheric geoengineering (ensemble HA as described in Table 3.1). Values are calculated at the top of the atmosphere (TOA) and the tropopause. Time averaging is performed over the last three Northern Hemisphere summers (left panels) and Northern Hemisphere winters (right panels) of simulation.

FIGURE 4.12. Spatial maps of net radiation (down minus up) anomalies for middle stratospheric geoengineering (ensemble HA as described in Table 3.1), averaged over the last three years of simulation. Values are calculated at the tropopause, surface, and top of atmosphere (TOA).
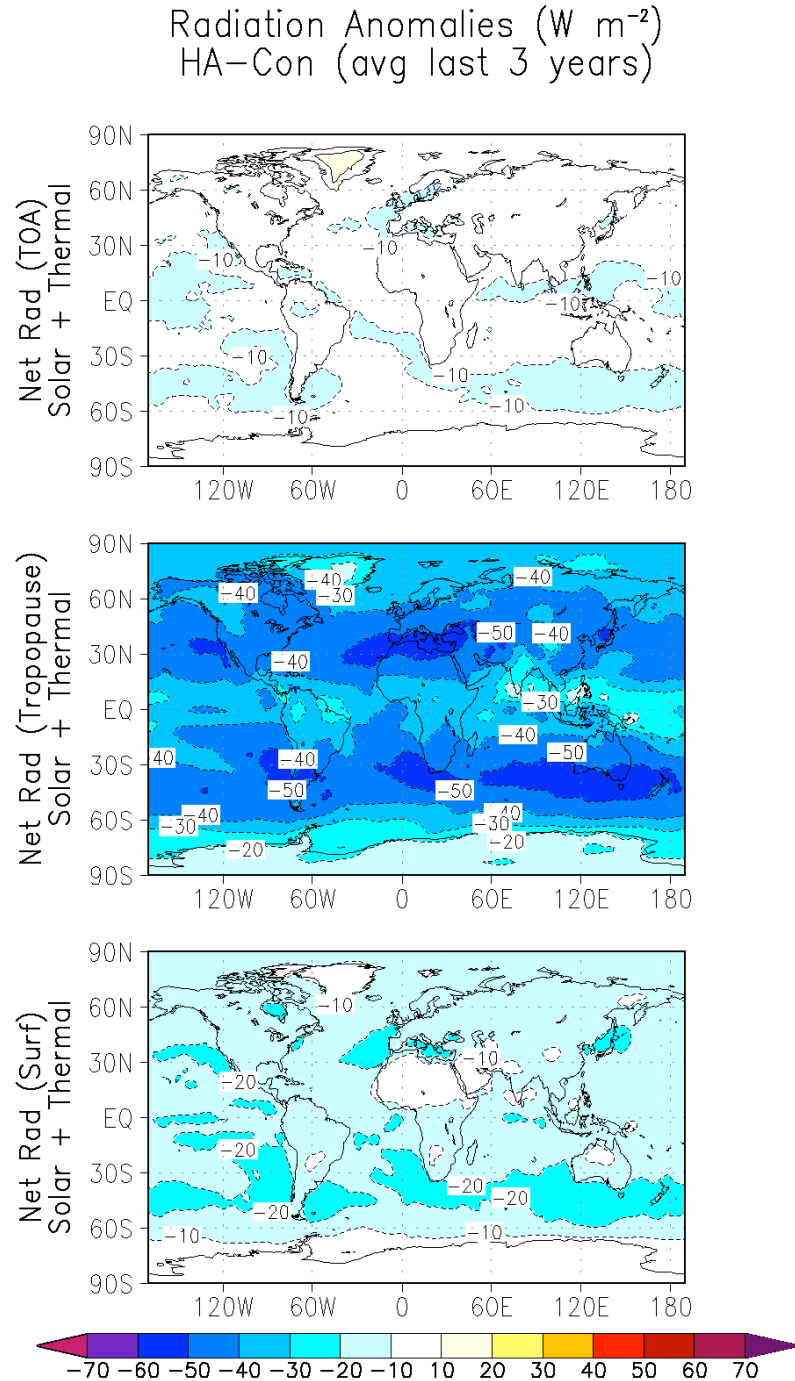
FIGURE 4.13. Spatial maps of total (solar + thermal) net radiation (down minus up) anomalies for middle stratospheric geoengineering (ensemble HA as described in Table 3.1), averaged over the last three years of simulation. Values are calculated at the tropopause, surface, and top of atmosphere (TOA).

show the same fields spatially, averaged over the last three years of simulation. These fields generally reiterate the information shown in the zonal averages, showing no distinctive regional patterns that cannot be ascertained from Figures 4.9 and 4.10.

The radiative forcing calculations, as shown in Figures 4.14-4.16 show similar results to the analysis of the radiation budget. Radiative forcing at the tropopause shows similar patterns and values to surface radiative forcing. The radiative forcing values are approximately 2.5 times smaller than the radiation values, reaching a maximum shortwave radiative forcing at the tropopause of -20 W m^{-2} in the global average and up to -30 W m^{-2} as point values. Longwave radiative forcing values are quite small, remaining less than 1 W m^{-2}. Radiative forcing peaks in the mid latitudes instead of the poles, paralleling the aerosol distribution patterns instead of the insolation patterns. Again, we note these values are calculations of instantaneous radiative forcing, not adjusted radiative forcing, so these plots have limited applicability to determining climate response.

4.2 MASS BURDEN AND DEPOSITION

Figure 4.17 shows the mass burden of black carbon as a result of geoengineering for ensemble HA. After ten years, the globally averaged mass burden is approximately 8×10^{-6} kg m^{-2}. The continuing upward trend at the end of the ten years of simulation suggests the experiments were not conducted for a long enough period of time to allow the mass burden to reach equilibrium.
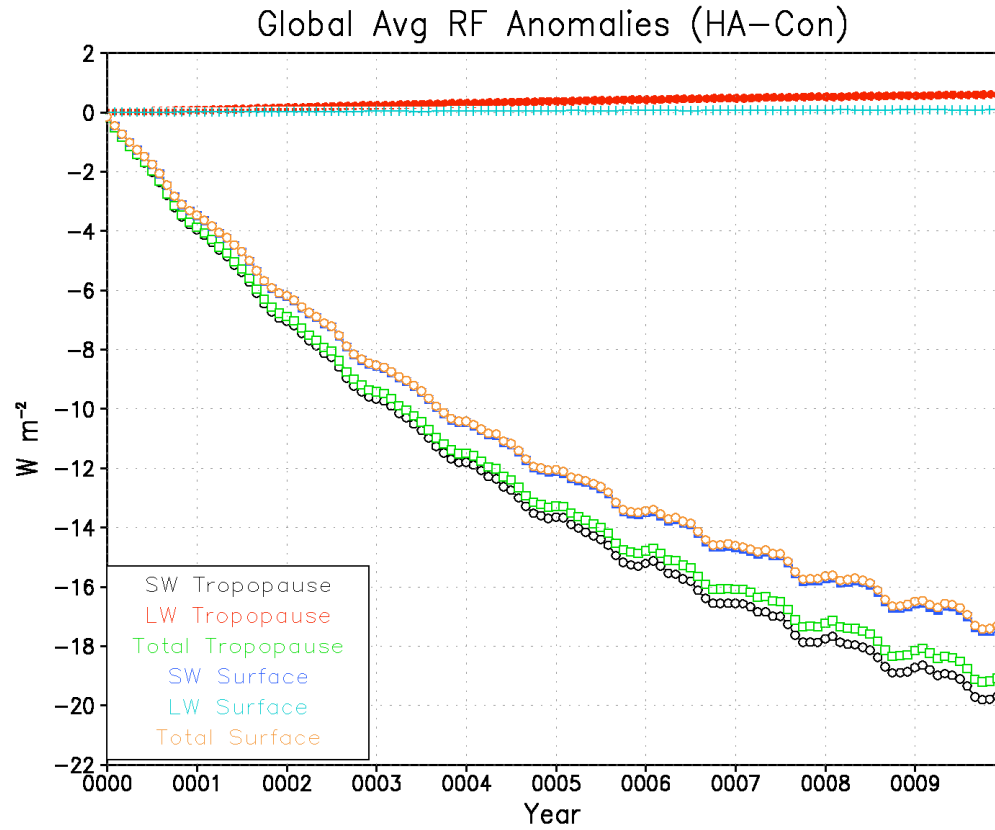
FIGURE 4.14. Globally averaged radiative forcing anomalies for middle stratospheric geoengineering (ensemble HA as described in Table 3.1). Total anomaly is the sum of the solar and thermal anomalies.
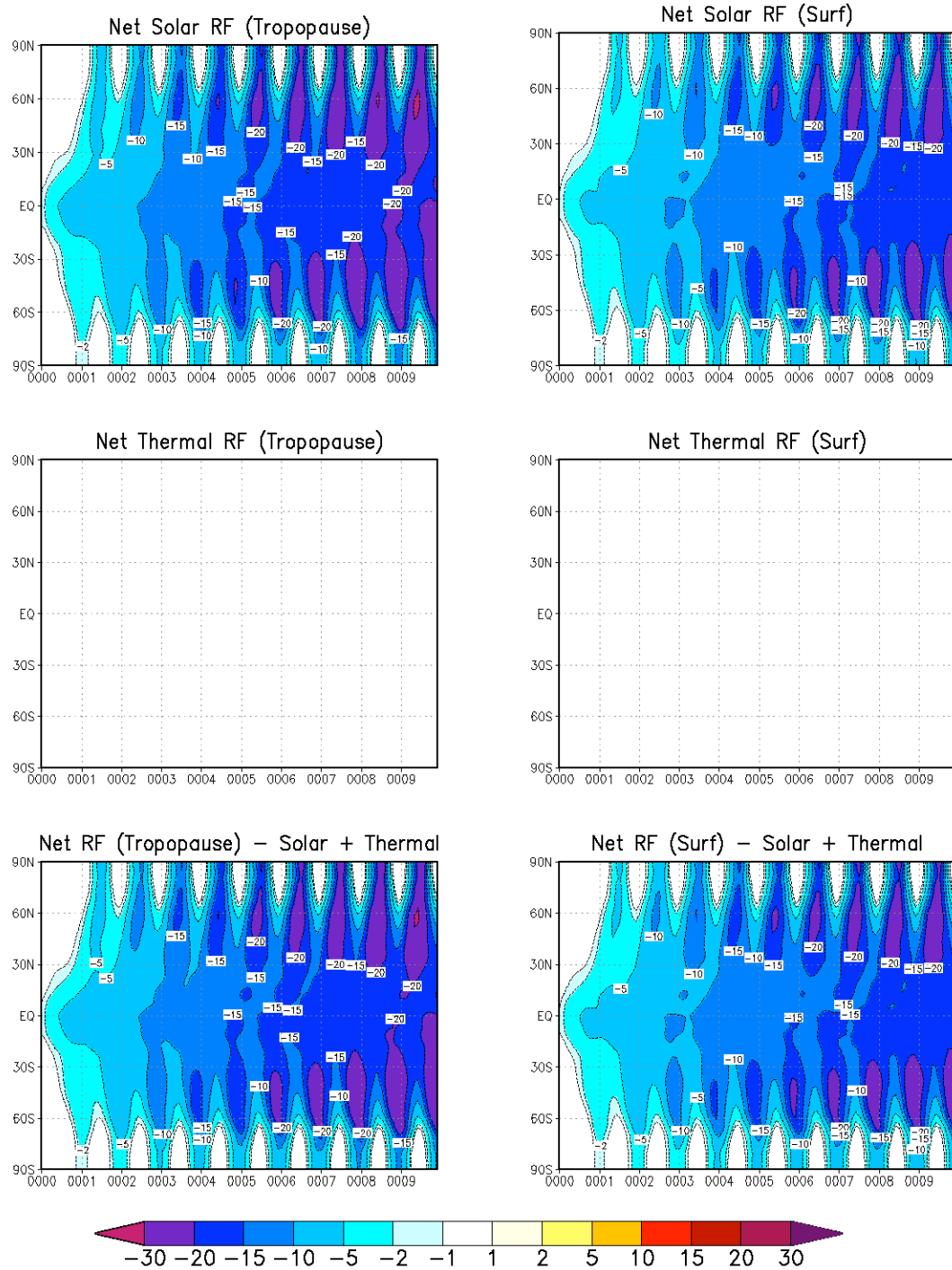
FIGURE 4.15. Zonally averaged radiative forcing anomalies for middle

stratospheric geoengineering (ensemble HA as described in Table 3.1).
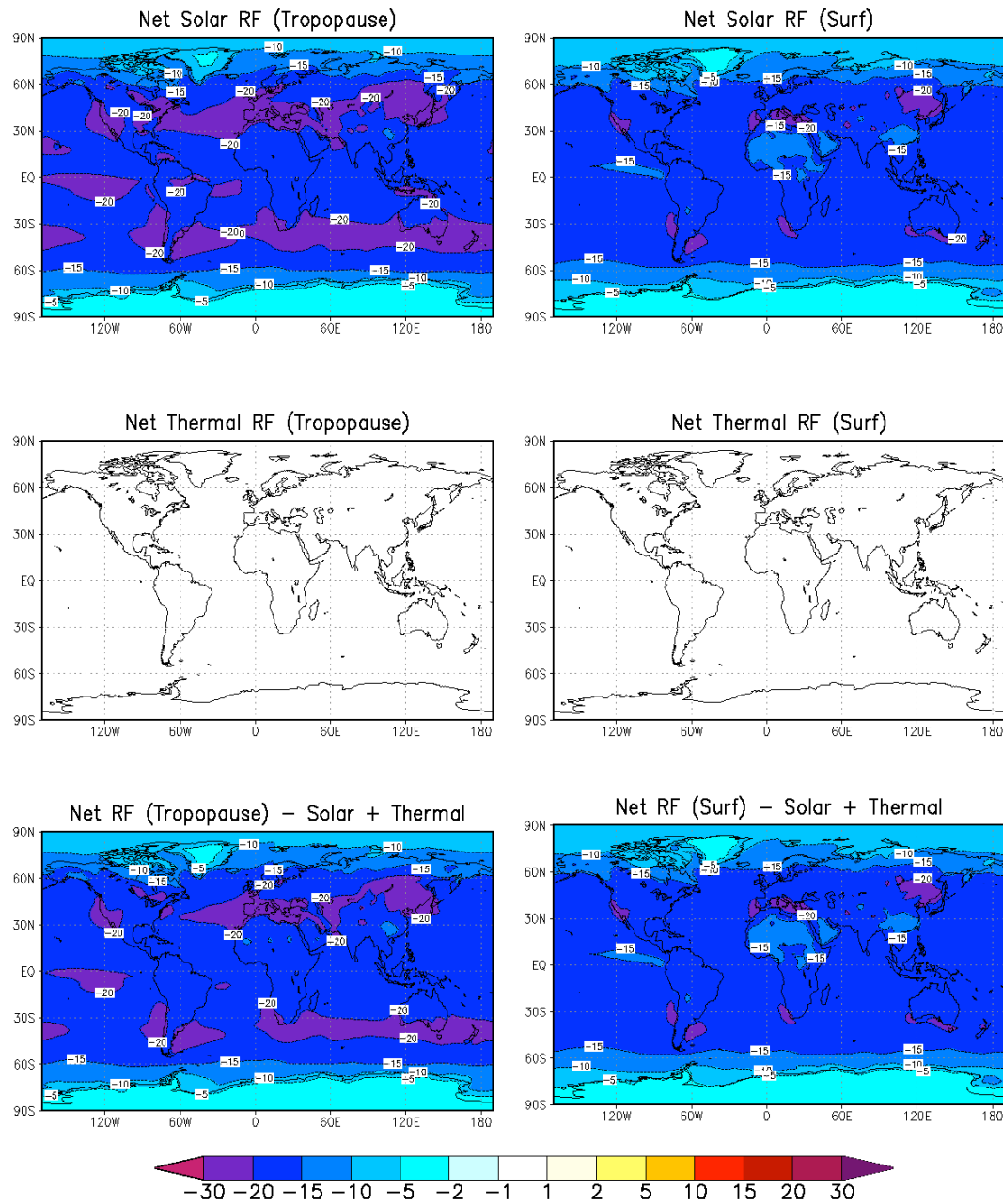
FIGURE 4.16. Spatial maps of radiative forcing anomalies for middle

stratospheric geoengineering (ensemble HA as described in Table 3.1), averaged

over the last three years of simulation.
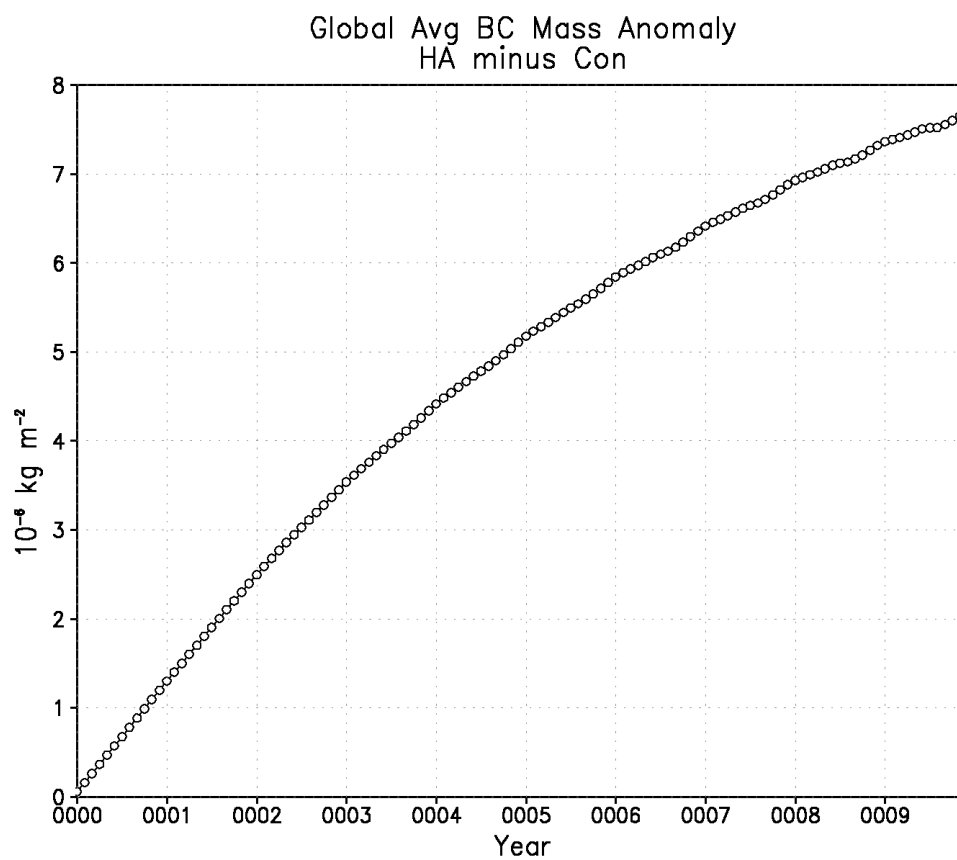
FIGURE 4.17. Globally averaged black carbon mass burden for middle

stratospheric geoengineering (ensemble HA as described in Table 3.1).

Multiplying this peak value by the surface area of the earth, approximately

5×10^{14} m^2, gives a total mass burden of approximately 4 Tg black carbon.

Inserting these values into the mass balance equation given in Section A.1 and

solving, we obtain an *e*-folding lifetime of approximately 4.5 years and an

equilibrium mass burden of 4.5 Tg black carbon. This lifetime is nearly identical

to the one found by *Robock et al.* [2007a]. After ten years, the simulations for this

particular ensemble have reached ~89% of their equilibrium mass burden. This

also explains why the optical depth and radiative forcing values in our

simulations are similar to the results of *Robock et al.* [2007b], as the spatial

distribution of the aerosols and the atmospheric mass burden are similar in both

studies.

Showing more spatial resolution, Figure 4.18 gives mass burden as a

function of height. Black carbon injection for this ensemble was through the

31-57 mb range. Due to gravitational settling, we expect to find black carbon

below this level. However, peak black carbon mass occurs above this level, and

there are significant amounts of black carbon extending up to the top of the

model. Since aerosols were not injected this high, it must be due to heating of

the aerosol particles and subsequent self-lofting [*Pueschel et al.*, 2000; *Rohatschek*,

1996]. This is further evidenced by the clear seasonal cycle in mesospheric black

carbon mass, peaking twice a year for summer in each hemisphere. Figure 4.19

shows the spatial distribution of black carbon, averaged over the last three years

of simulation. There is a clear poleward migration of the particles, following the

atmospheric general circulation, with the tropics having the lowest column mass
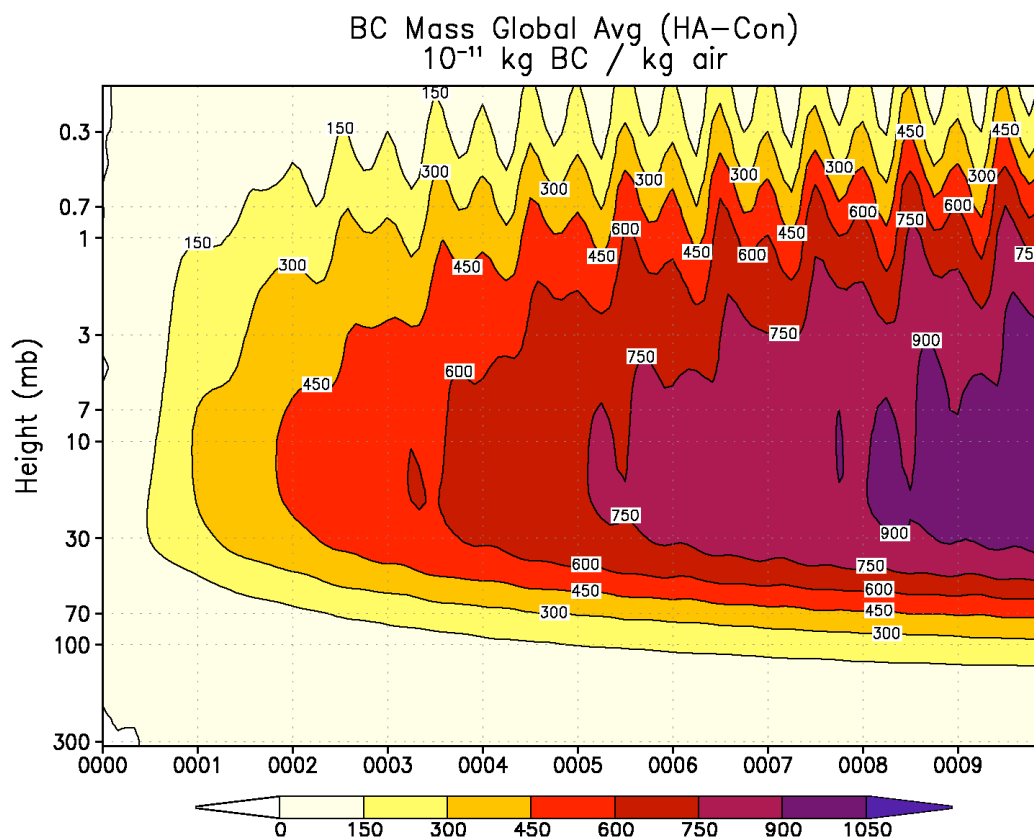
FIGURE 4.18. Globally averaged black carbon mass burden as a function of height for middle stratospheric geoengineering (ensemble HA as described in Table 3.1).
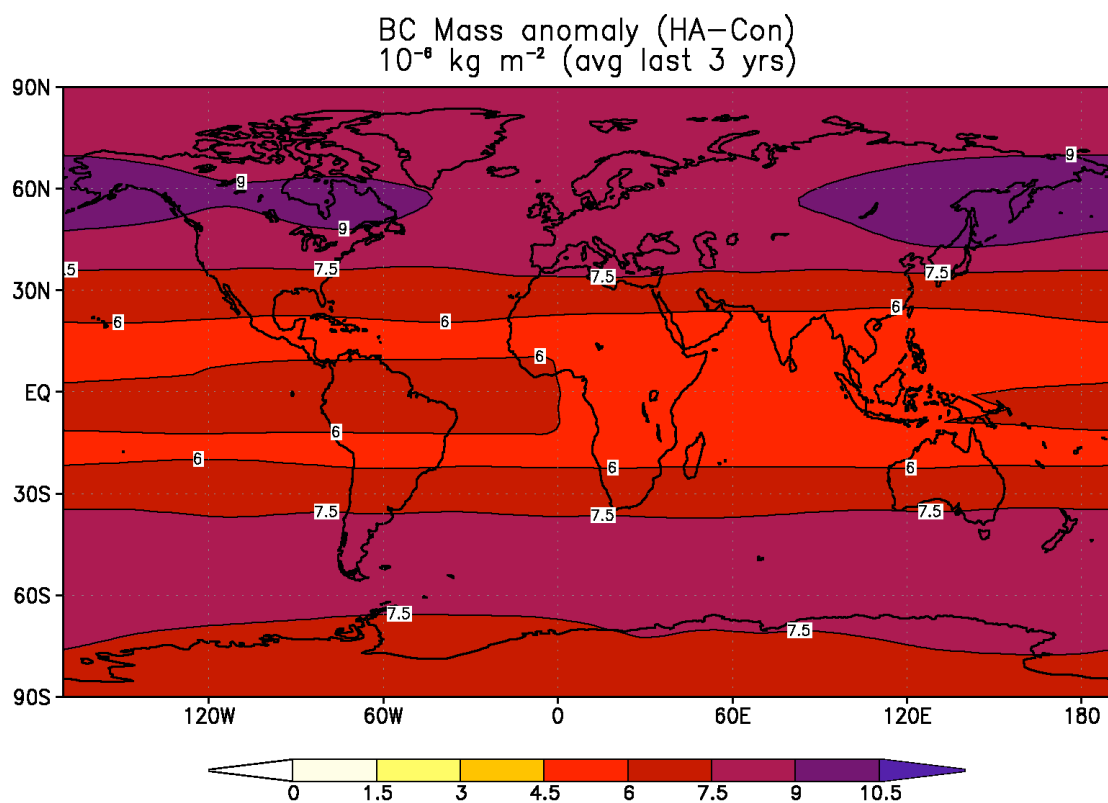
FIGURE 4.19. Spatial map of black carbon mass burden averaged over the last

three years of simulation for middle stratospheric geoengineering (ensemble HA

as described in Table 3.1).

and the mid to high latitudes having the highest. Therefore, the seasonal cycle of self-lofting is expected, as the particles in the hemisphere with the most insolation will be heated and loft the most.

Similarly, deposition rates show a clear seasonal cycle, as in Figure 4.20. This shows that wet deposition is dominant, constituting over 90% of the total amount of deposition. In contrast, deposition from sulfate aerosol geoengineering is approximately 67% wet and 33% dry [*Kravitz et al.*, 2009]. The deposition patterns in this figure show only one strong peak each year in the boreal summer, with a much smaller peak in the boreal spring, which is further reinforced by Figure 4.21, showing the average seasonal cycle. This suggests the wet deposition is strongly dominated by one hemisphere. Figure 4.6 shows that deposition rates are highest in the winter, so this implies that Southern Hemisphere deposition is larger than Northern Hemisphere deposition. This is also shown by the larger contours in the Southern Hemisphere than the Northern Hemisphere in Figure 4.6.

Figure 4.22 shows a spatial map of deposition, averaged over the last three years of simulation. Most of the deposition patterns occur in the mid-latitude storm tracks, over the poles, and over the industrialized regions of the North American East coast, Western Europe, and Southeast Asia. Deposition over the storm tracks is expected, as this is the primary means of wet deposition in the troposphere. Deposition in the industrial regions is entirely in the Northern Hemisphere, but in the zonal average, as is seen in Figure 4.6, this source is not as significant in the aggregate as at the poles.
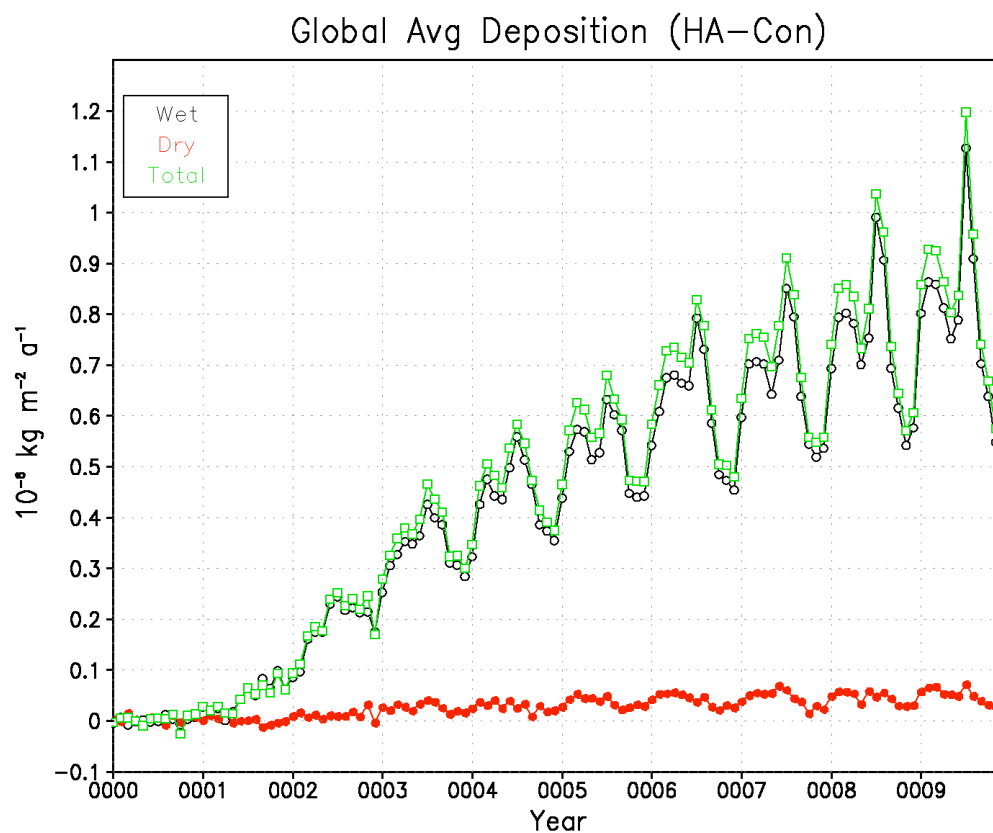
FIGURE 4.20. Globally averaged annual deposition rates for middle stratospheric geoengineering (ensemble HA as described in Table 3.1). Total deposition is the sum of wet and dry deposition.
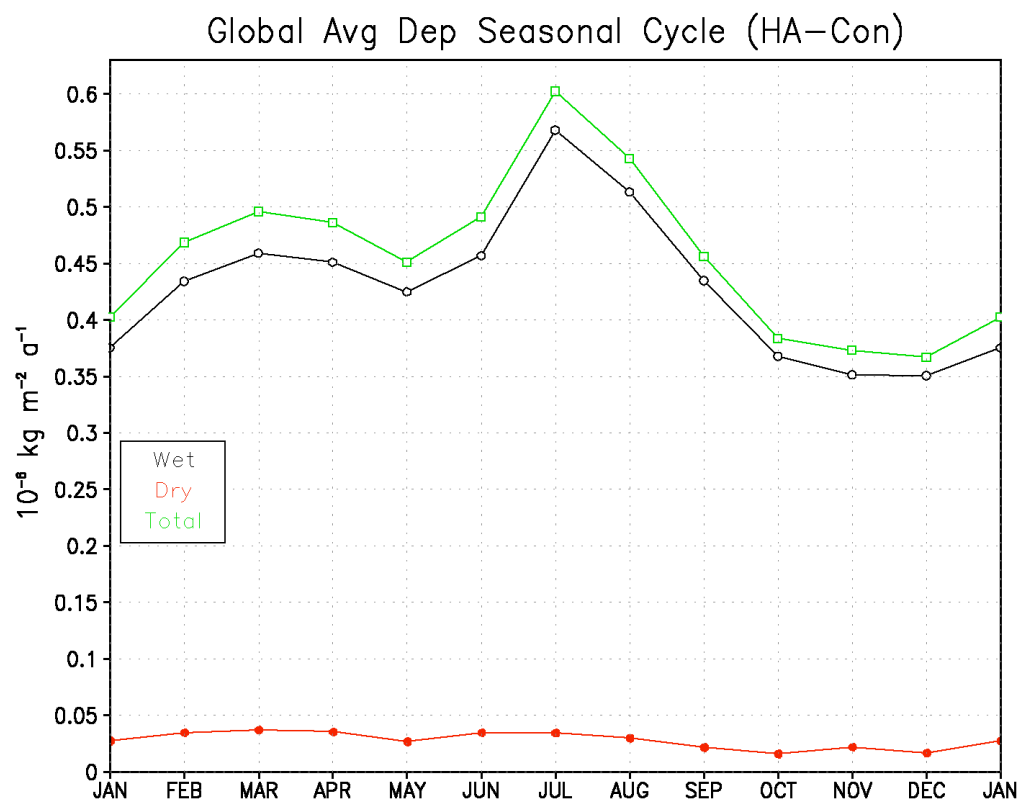
FIGURE 4.21. Globally averaged ten year average seasonal cycle of annual

deposition rates for middle stratospheric geoengineering (ensemble HA as

described in Table 3.1). Total deposition is the sum of wet and dry deposition.
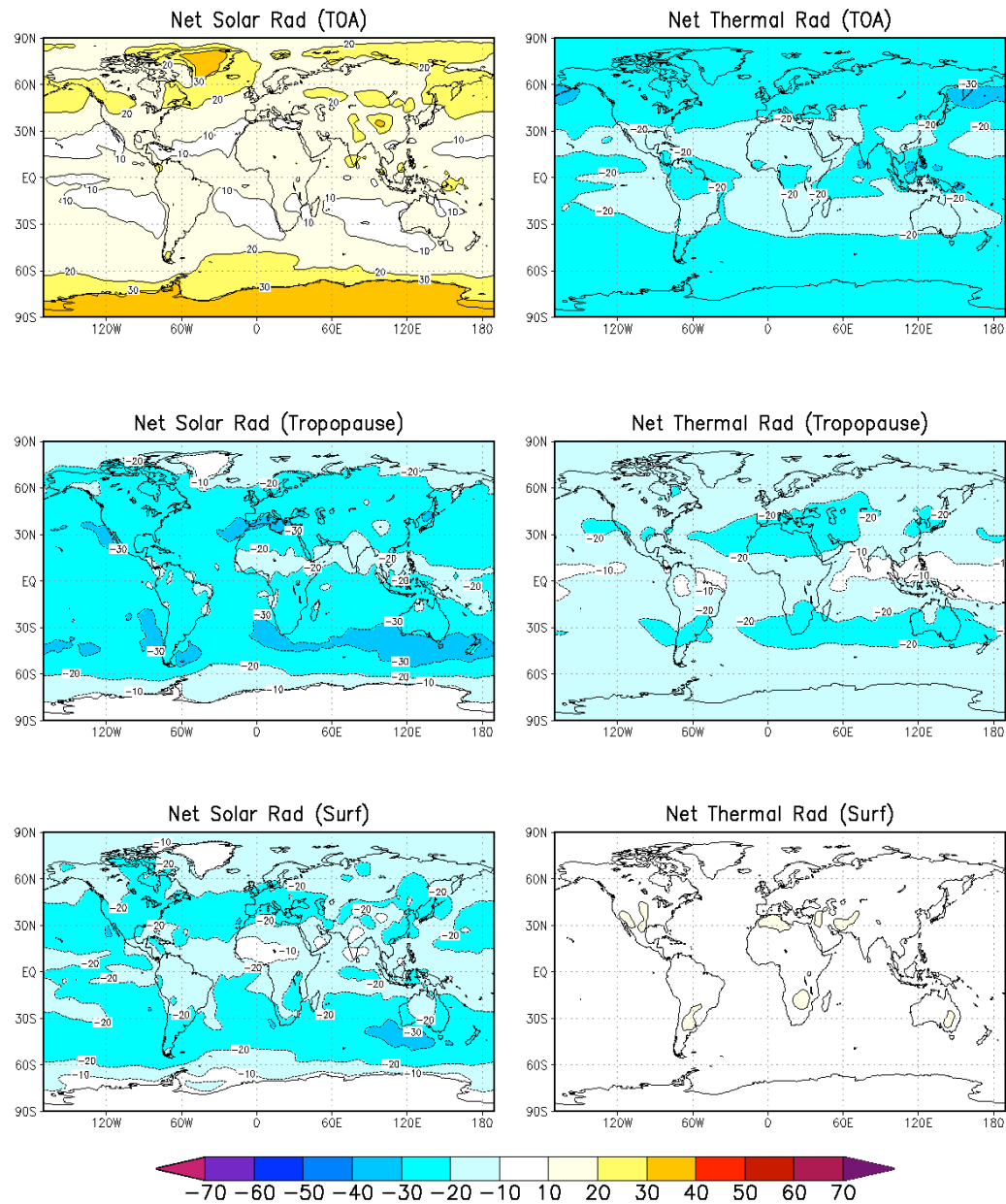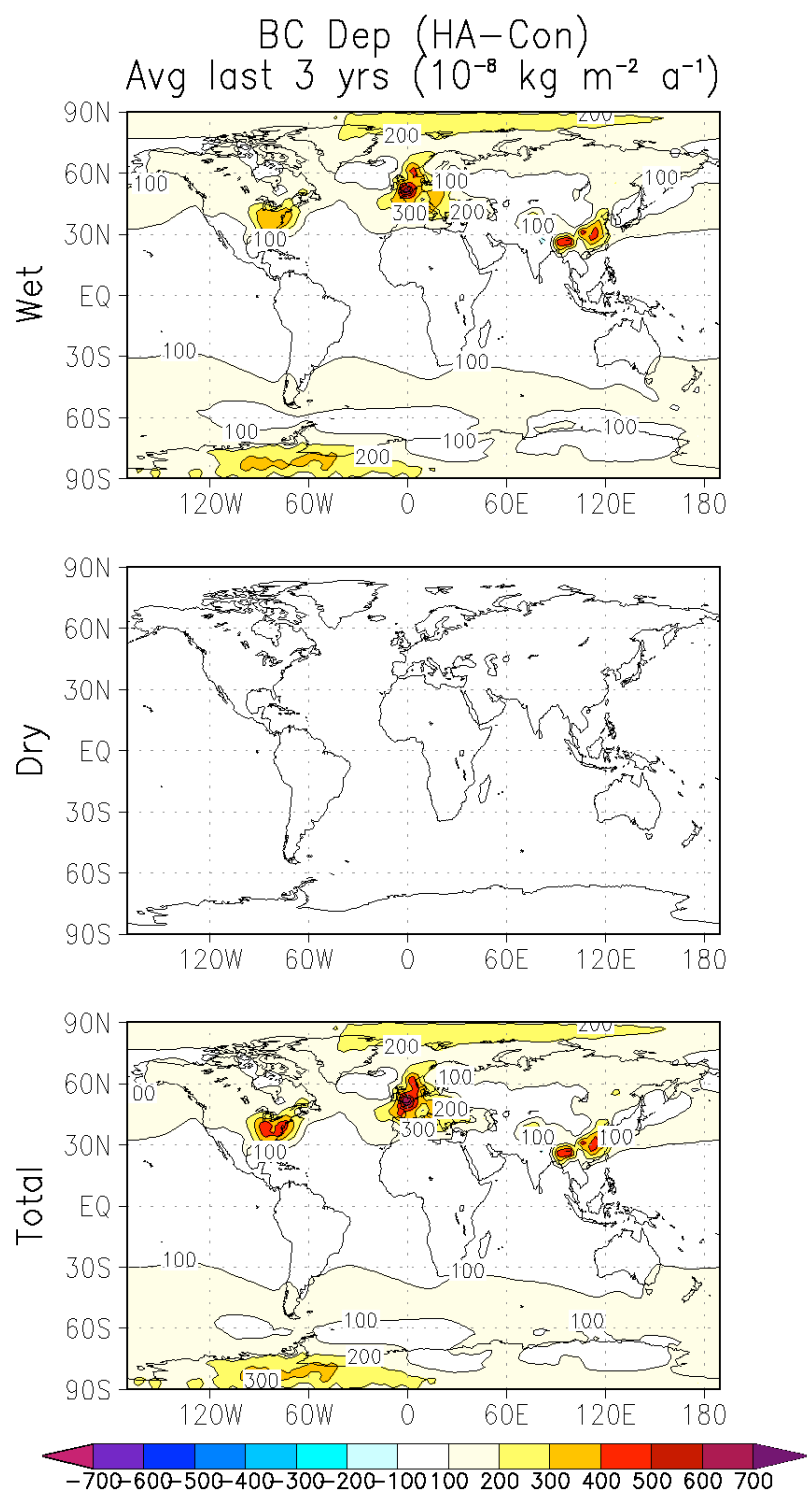
FIGURE 4.22. Spatial maps of annual deposition rates for middle stratospheric geoengineering (ensemble HA as described in Table 3.1), averaged over the last three years of simulation. Total deposition is the sum of wet and dry deposition.

At first glance, a likely candidate for these anomalies over industrialized regions is differences in weather between the geoengineering and control ensembles. However, this is unlikely, as if the anomalies were solely due to noise, the figures would show both positive and negative anomalies, and we see only positive anomalies. This suggests that black carbon geoengineering has somehow changed deposition rates in the model. We are unsure of the exact mechanisms involved, but a possible explanation is a modification of convective mass flux.

The seasonal deposition cycle seen in Figure 4.6 appears to be caused by wet deposition over the winter pole, which is also seen in Figure 4.22. As we discuss in Section 4.4 below, we do not see a significant increase in polar winter precipitation. Also, as we discuss in Section 5.3 in the next chapter, this feature of polar wet deposition occurs in other geoengineering ensembles, so it appears to be a robust feature of geoengineering with black carbon aerosols. We are unsure of the exact mechanisms that causes this large increase, but we postulate it is due to the introduction of a strong Arctic polar vortex. We describe the reasons for the amplification of this vortex in the following section. Once black carbon aerosols enter this vortex, we suspect they remain trapped and cannot mix with air from lower latitudes, meaning every time the Arctic has a precipitation event, a large amount of the aerosols are scavenged.

4.3 STRATOSPHERIC HEATING AND CONSEQUENCES

One of the prominent consequences of placing a large amount of absorbing aerosol in the stratosphere is local heating. Figure 4.23 shows the degree of stratospheric heating from this geoengineering scenario as calculated by the model. Peak heating in the stratosphere reaches over 40°C, with heating by up to 20°C extending down into the troposphere. The mesosphere, up through the model top, is also heated by at least 5°C. As in Figure 4.18, we see a clear seasonal cycle with summer peaks for each hemisphere. This is also due to self-lofting, as the particles become heated in the months of maximum insolation and ascend to higher altitudes, resulting in warmer regions of high altitude in the summer. The boreal summer appears to have a larger temperature spike than the austral summer, which makes sense in light of Figure 4.19, which shows the latitudes with the most black carbon mass are in the Northern Hemisphere. As the simulations reach the end of the ten year period, the mesospheric temperature spikes appear to lessen in magnitude, reaching below 5°C of warming in the austral summer. However, as is seen in Figure 4.18, the amount of black carbon aerosols at these altitudes actually increases over the simulation period, so this change in high altitude temperature anomalies is not due to a relaxation of the self-lofting feature of the aerosols. At this time, we are unable to diagnose a reason for this phenomenon.

A concern resulting from this stratospheric heating is the resulting warming that extends down into the troposphere. If this warming due to longwave emission is sufficient, it can negate the cooling effects of the reduction
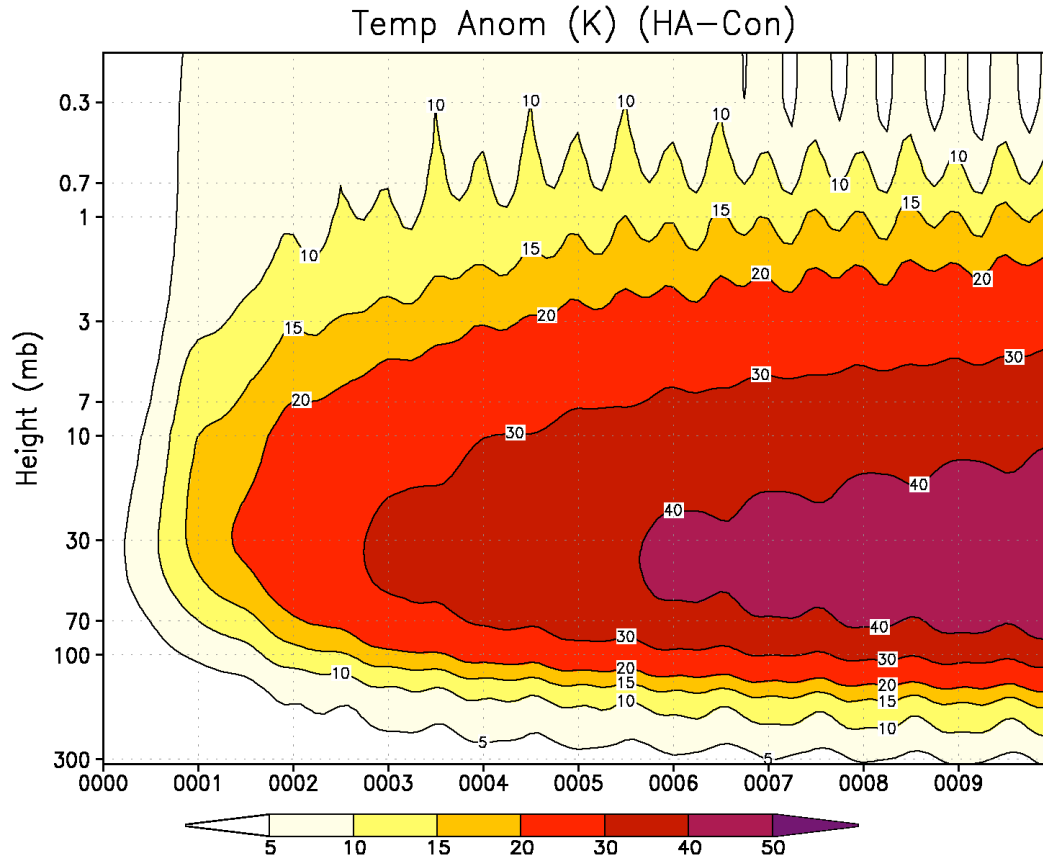
FIGURE 4.23. Stratospheric heating that would result from middle stratospheric geoengineering (ensemble HA as described in Table 3.1). Temperature anomalies are global averages as a function of height.

in radiation and can even exacerbate the surface warming due to anthropogenic greenhouse gases. Figure 4.24 shows the same field as Figure 4.23 but with the vertical extent of the plot restricted to the troposphere to highlight this warming. Heating by over 0.25°C is common in the troposphere, even into the second year of simulation, and eventually extends down to the 700 mb level. This is approximately the amount of global average cooling due to this particular geoengineering scenario, as was seen in Figure 4.1. The heating is possibly due to evaporation of clouds, but as we described previously, we refrain from discussion of the impact of black carbon geoengineering on clouds in this document.

Figure 4.25 shows the zonal distribution of stratospheric heating, averaged over the last three years of simulation. Stratospheric heating is highly asymmetric, showing a disproportionately large amount of heating at the South Pole near the tropopause by over 60°C and extending well into the troposphere. The North Pole also shows a large amount of heating of over 40°C, but only far aloft, near the stratopause (~1 mb). Heating between 30°S and 30°N is more symmetric, with heating mostly staying above the tropical tropopause and reaching a peak of over 50°C.

This significant stratospheric heating has many prominent effects on the climate. One such effect is catalytic destruction of stratospheric ozone, due to the temperature sensitivity of the Chapman reactions [e.g., *Mills et al.*, 2008]. Figure 4.26 shows total column ozone reduction for this scenario, in both absolute and percent change. Globally averaged total column ozone destruction reaches 30%
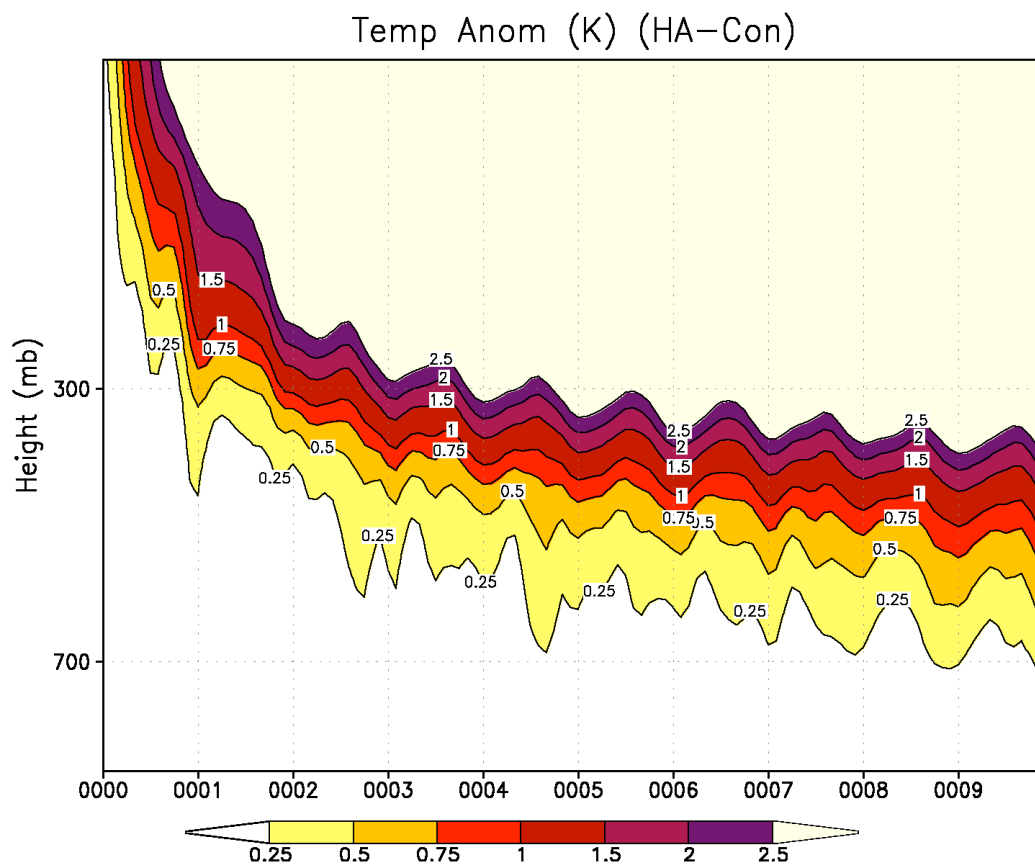
FIGURE 4.24. Tropospheric warming due to longwave emission from the aerosol layer that would result from middle stratospheric geoengineering (ensemble HA as described in Table 3.1). Temperature anomalies are global averages as a function of height.
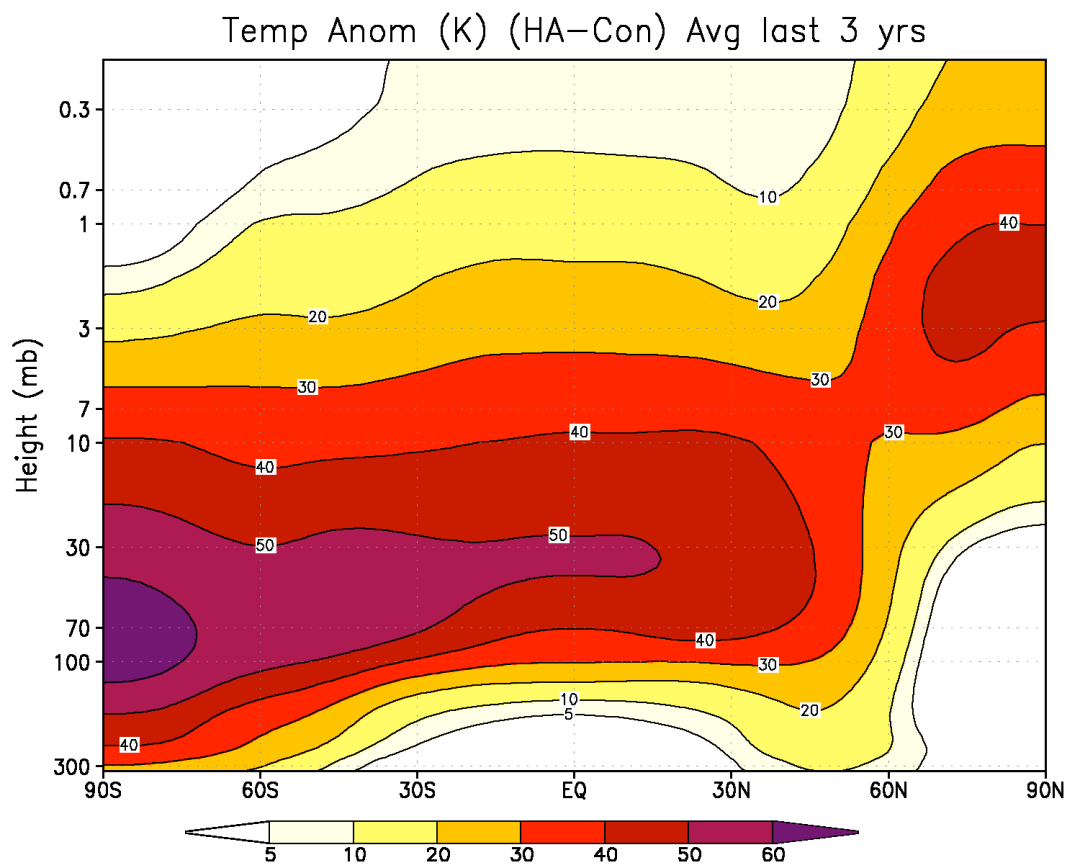
FIGURE 4.25. Zonal averages of stratospheric heating that would result from middle stratospheric geoengineering (ensemble HA as described in Table 3.1). Temperature anomalies are global averages as a function of height.
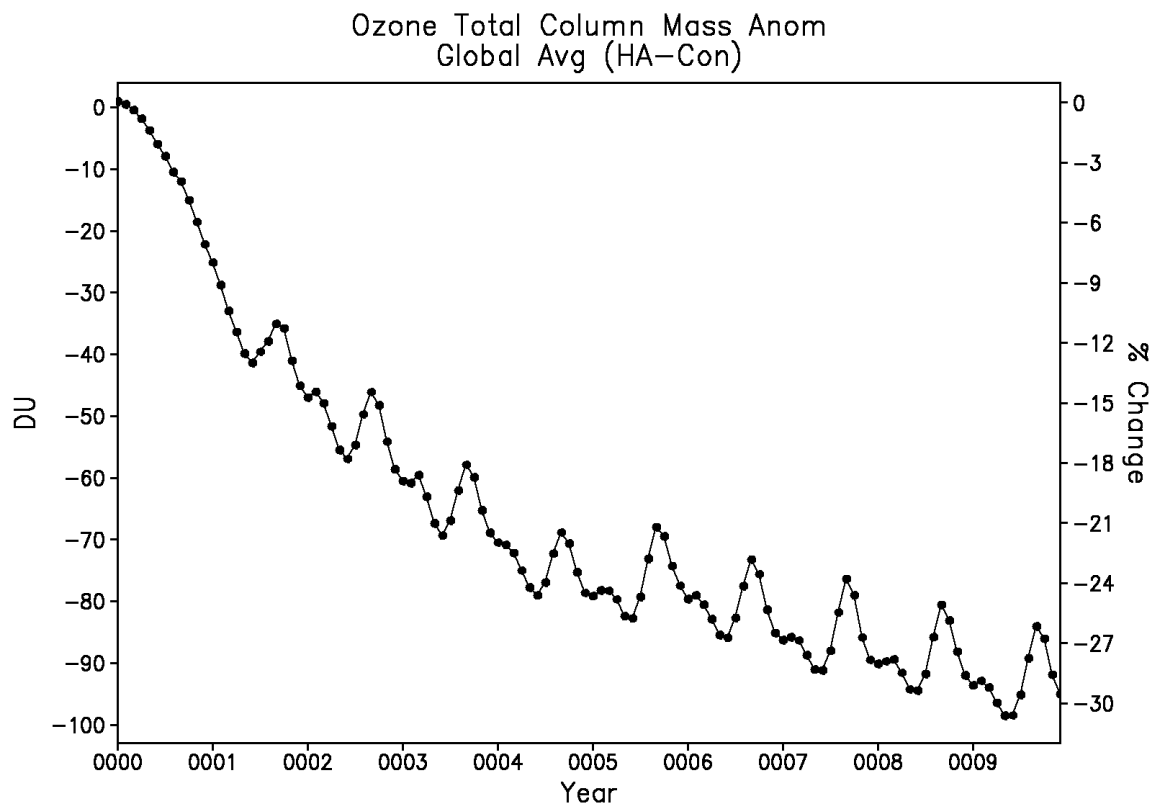
FIGURE 4.26. Globally averaged ozone total column mass anomalies for middle stratospheric geoengineering (ensemble HA as described in Table 3.1). Absolute and percent change values are given.

(compared to the control ensemble) by the tenth year of simulation, with an interseasonal variability of approximately 4%. In the zonal average (Figure 4.27), the largest amount of ozone destruction occurs nearly uniformly in the Northern Hemisphere high latitudes of over 30% in the summer and reaching over 50% in the winter. The Antarctic shows a much larger variability, with large losses in ozone of over 40% in the summer but increases of over 40% in the spring, which is normally the peak season of the Antarctic ozone hole. These results show the development of an Arctic ozone hole and a recovery of the Antarctic ozone hole due to black carbon geoengineering.

In the vertical structure of ozone changes (Figure 4.28), at the height of the bulk of the stratospheric ozone layer, there is massive depletion (on the global average) by over 35%. However, this depletion allows more ultraviolet energy to penetrate to lower altitudes. This high energy radiation causes photolysis of oxygen atoms near the polar tropopause [*Seinfeld and Pandis*, 2006], which serves to create a secondary ozone layer at lower altitudes, as is seen in Figure 4.28. Figure 4.29 shows that stratospheric destruction of ozone is relatively uniform at all latitudes, not exceeding 50%, although the largest absolute amount of destruction due to geoengineering is in the tropics. In the troposphere and lower stratosphere, there is a large increase in the tropics by over 200%, and there is a large decrease in the Northern Hemisphere high latitudes by over 50%. The Antarctic shows little additional ozone destruction due to geoengineering at these altitudes. This suggests the low altitude recovery of the ozone hole is mostly confined to the tropics.
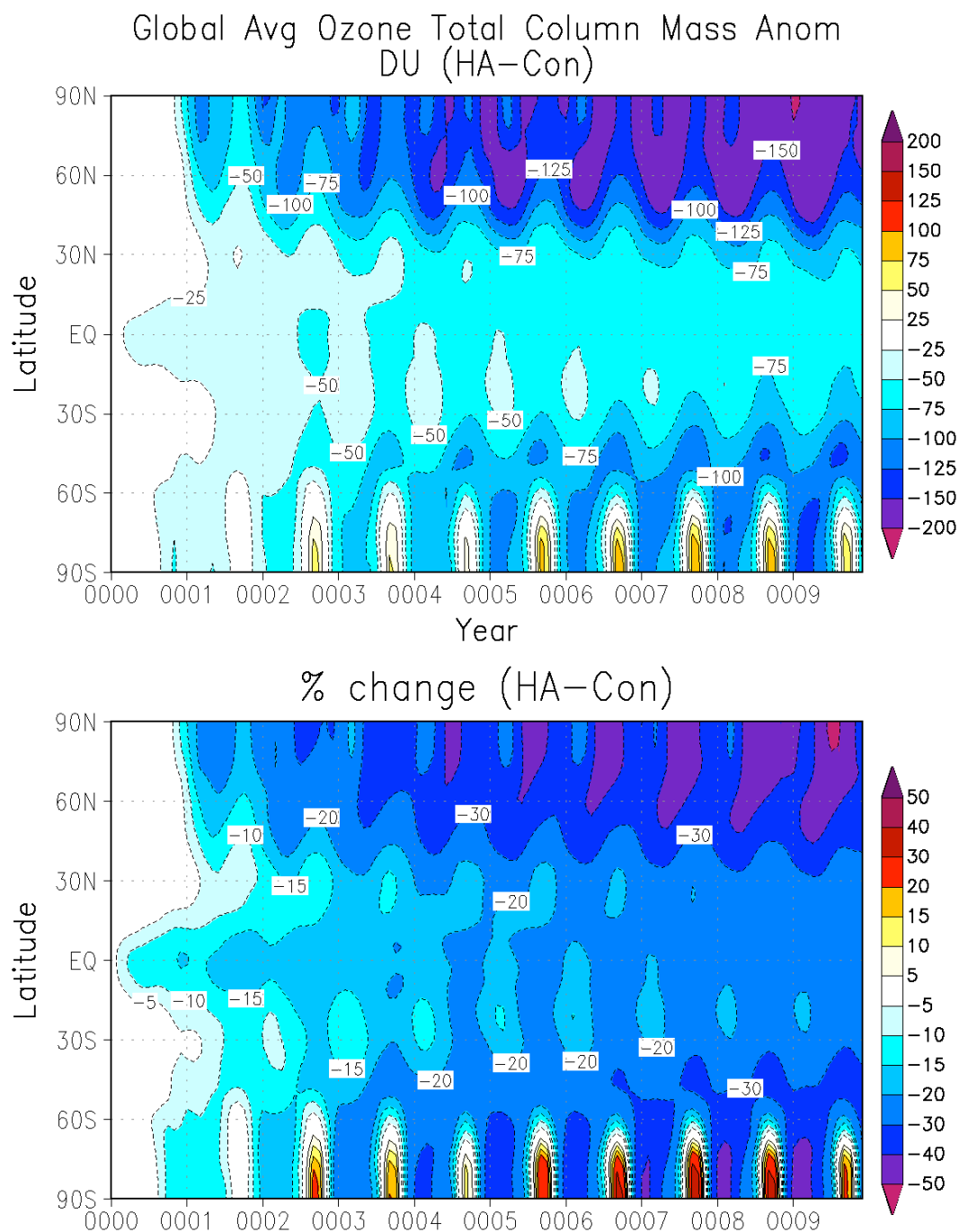
FIGURE 4.27. Zonally averaged ozone total column mass anomalies for middle stratospheric geoengineering (ensemble HA as described in Table 3.1). Absolute and percent change values are given.
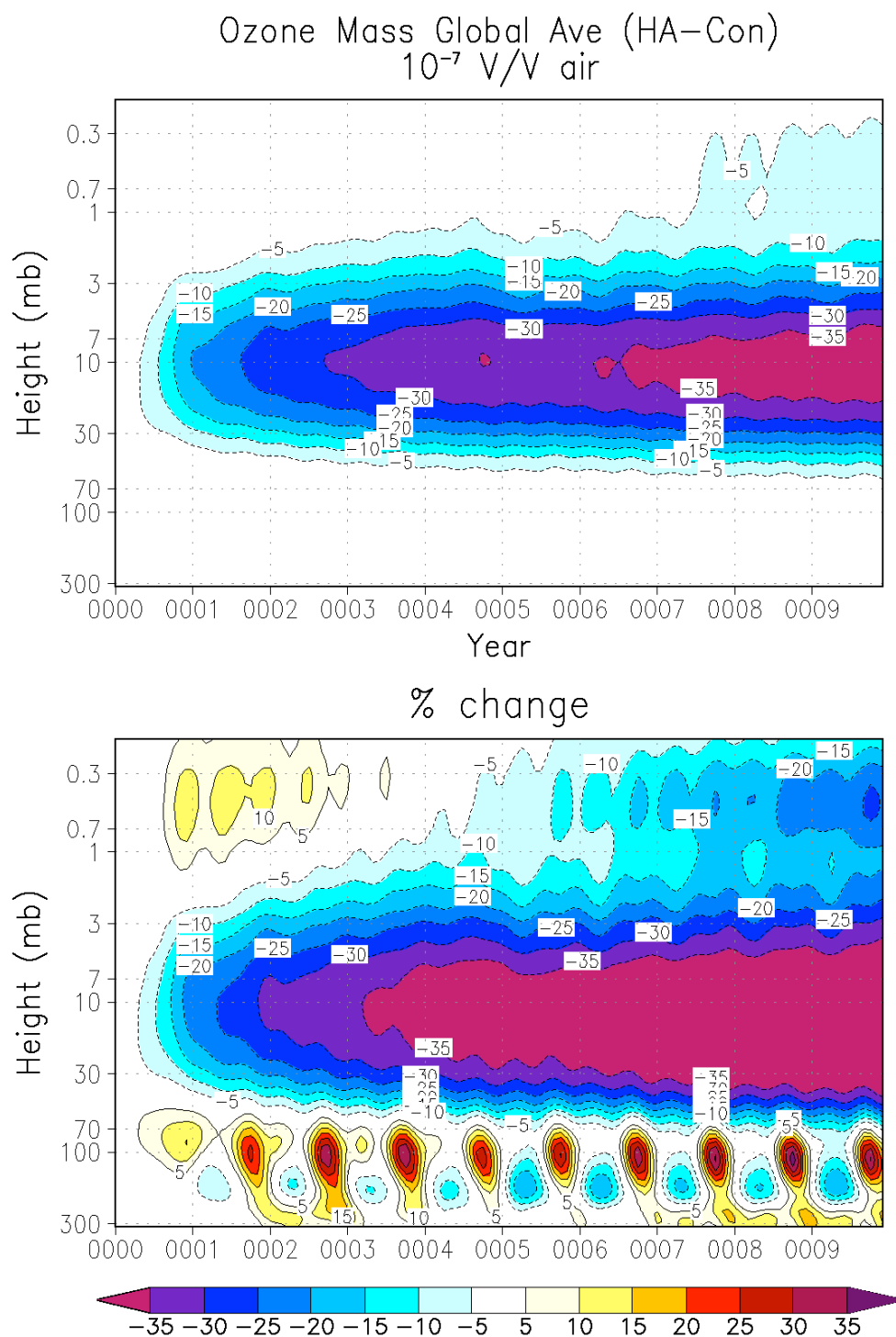
FIGURE 4.28. Ozone mixing ratio for middle stratospheric geoengineering (ensemble HA as described in Table 3.1). Values given are global averages as a function of height.
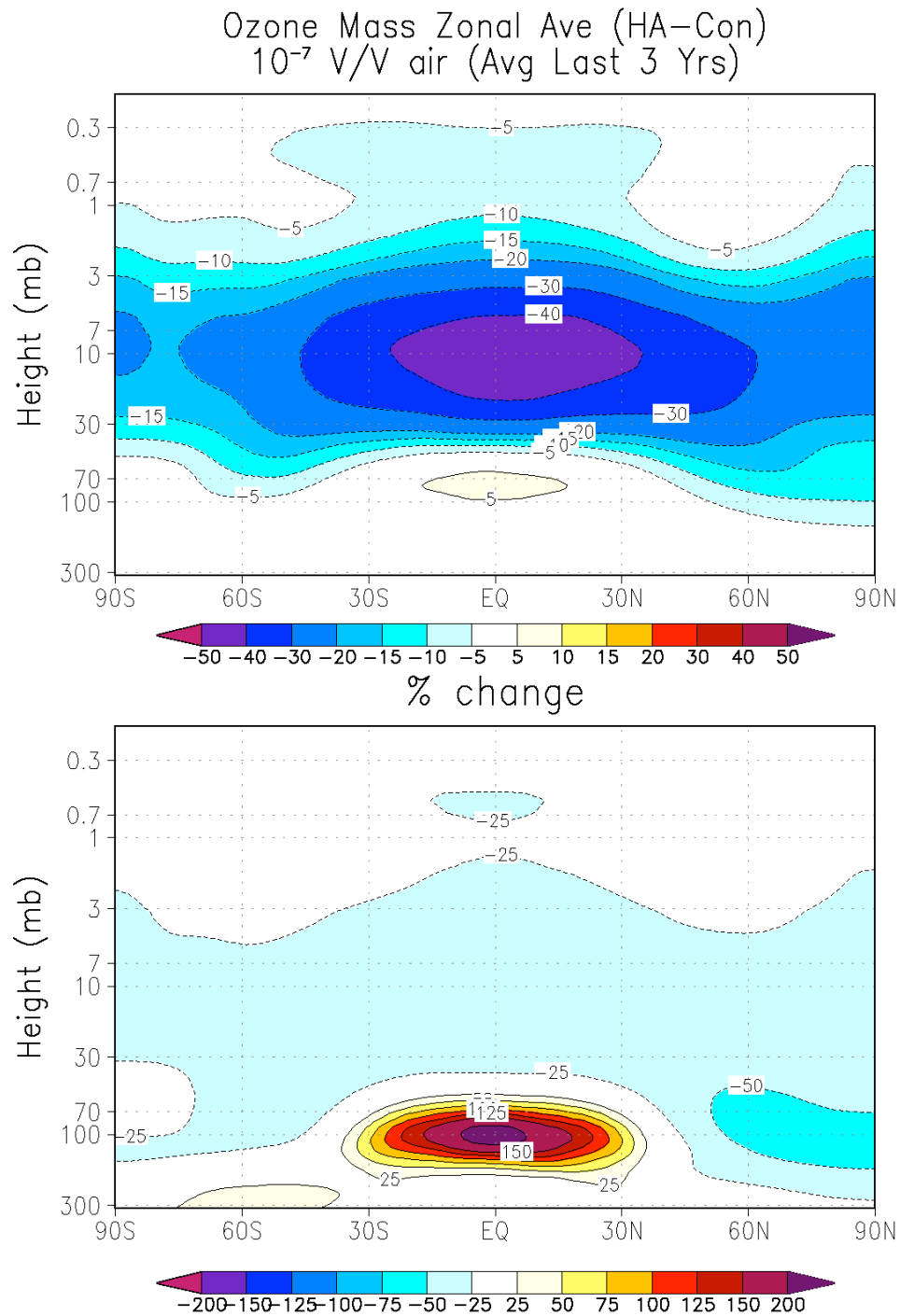
FIGURE 4.29. Ozone mixing ratio for middle stratospheric geoengineering (ensemble HA as described in Table 3.1), zonally averaged and time averaged over the last three years of simulation. Values given are global averages as a function of height.

We can explain the partial recovery of the Antarctic ozone hole by stratospheric heating, which reduces the amount of polar stratospheric clouds, meaning there are fewer surfaces on which catalytic ozone destruction can occur. Explaining the formation of the Arctic ozone hole is relatively straightforward, as the same mechanism is responsible for the creation of the Antarctic ozone hole. The Antarctic ozone hole exists because of a strong circumpolar winter jet which traps the ozone at the pole and prevents it from mixing with air at lower latitudes. This vortex creates a region of very cold temperatures, allowing polar stratospheric clouds to form, which provides surfaces for destruction of the trapped ozone over the Antarctic by free chlorine radicals [*Solomon*, 1999]. Therefore, if black carbon geoengineering caused a strong Arctic circumpolar jet, the same mechanism could apply in the Arctic, introducing an ozone hole in the spring and summer, as is seen in Figure 4.27. There is reason to believe geoengineering would cause such a circulation change. After large tropical volcanic eruptions, the sulfate aerosol layer heats the stratosphere, lifting the tropical isobars and increasing the equator-to-pole temperature gradient, causing a stronger polar jet [*Stenchikov et al.*, 1998; *Robock*, 2000]. An absorbing aerosol such as black carbon would amplify this effect, causing an even stronger jet than is seen after large tropical volcanic eruptions.

Figure 4.30 shows a climatology (control ensemble only) of the zonal wind. In comparison, Figure 4.31 shows zonal wind anomalies due to black carbon geoengineering. Stratospheric winds are strengthened in both the summer and winter, suggesting the circulation changes we predicted are
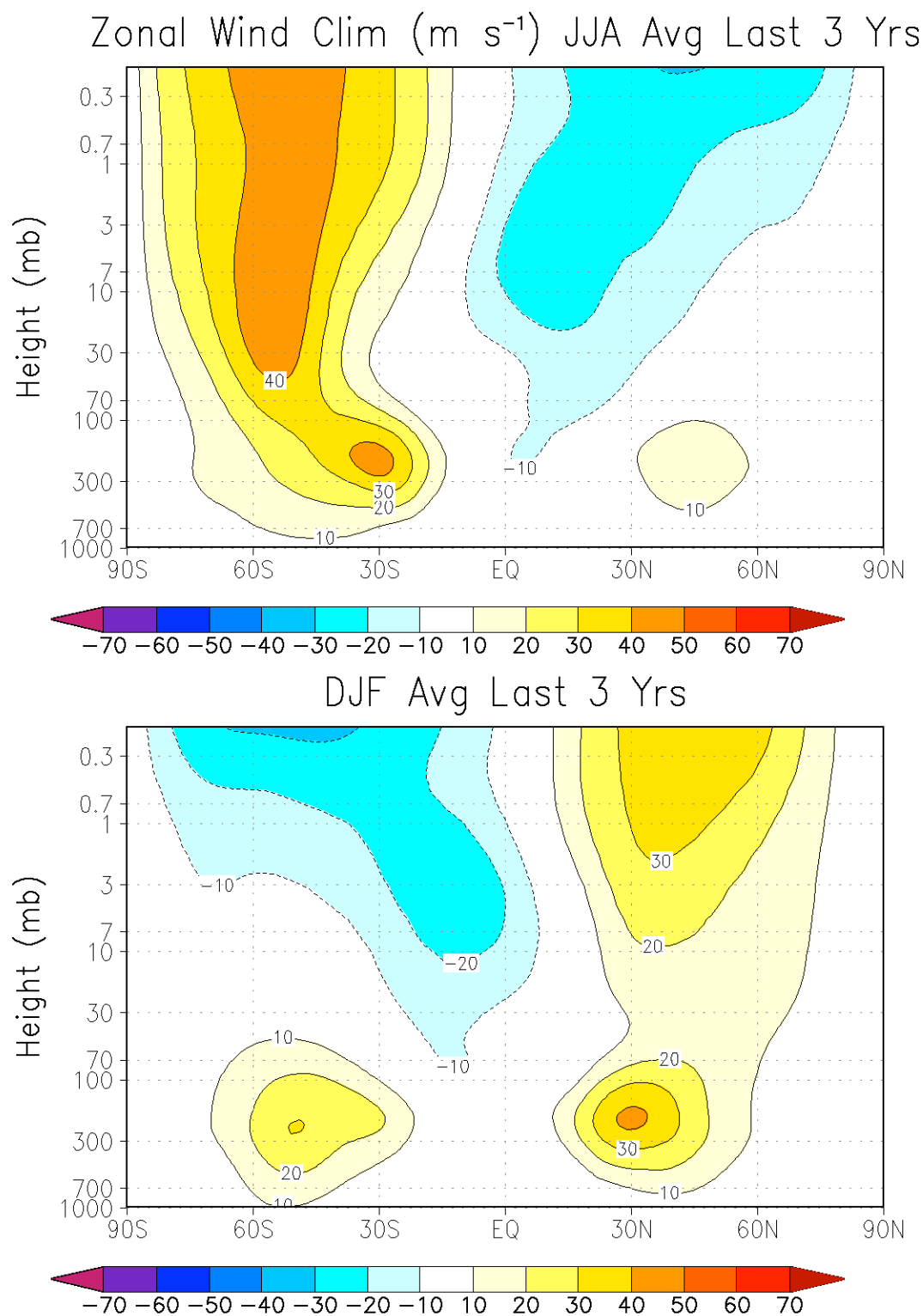
FIGURE 4.30. Climatology (Con only) of zonal wind, averaged over the last

three years of simulation for JJA and DJF.
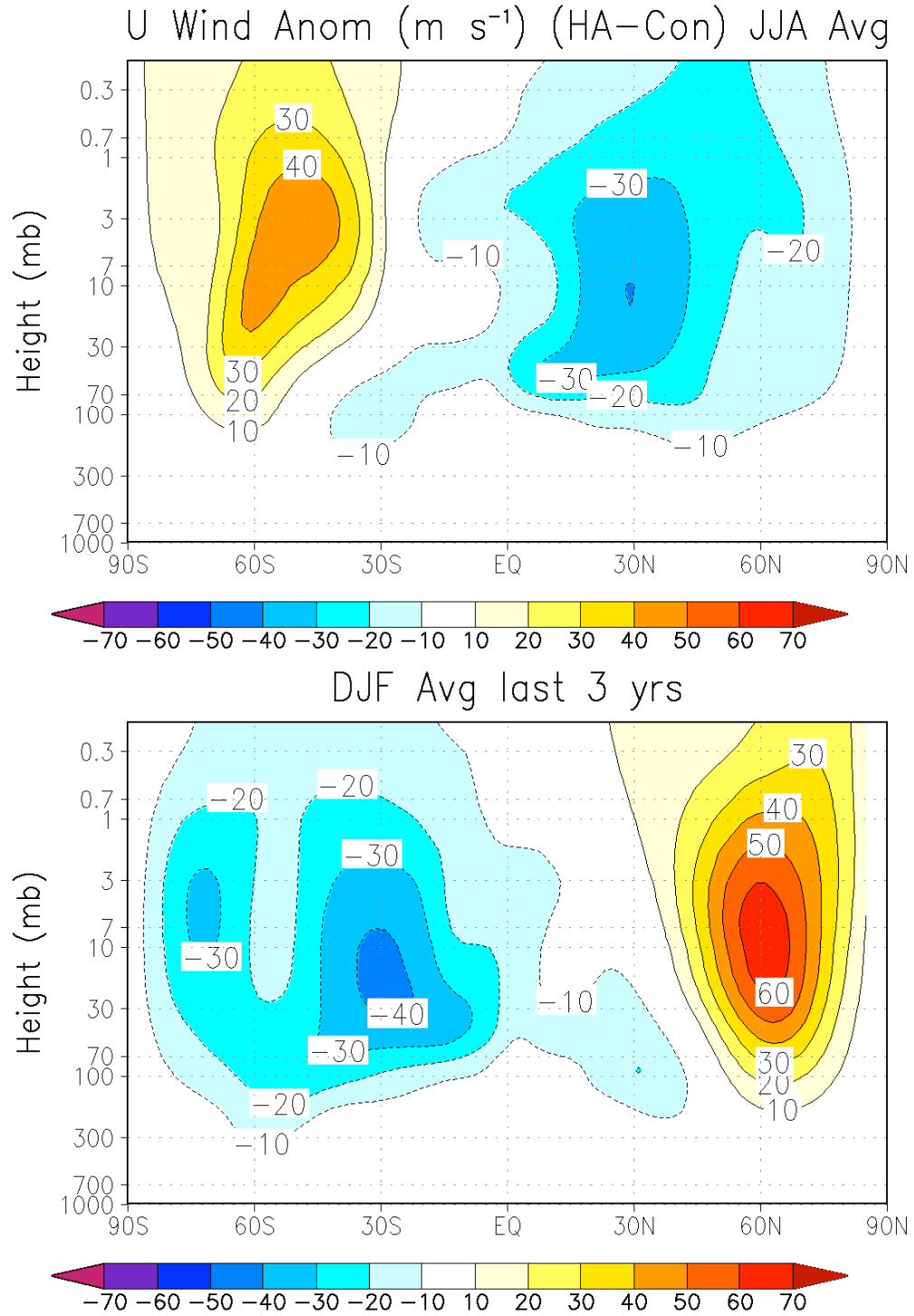
FIGURE 4.31. Zonal wind anomaly for middle stratospheric geoengineering (ensemble HA as described in Table 3.1). Values shown are averaged over the last three years of simulation for JJA and DJF.

occurring. Indeed, there is a strong induced Arctic jet which leads us to suspect this mechanism is responsible for the formation of the Arctic ozone hole.

In the case of large tropical volcanic eruptions, these circulation changes can also force a positive mode of the Arctic Oscillation [*Stenchikov et al.*, 1998; *Shindell et al.*, 2001]. Figure 4.32 shows sea level pressure anomalies over the North Pole. This is a classic positive mode pattern of the Arctic Oscillation, and many of the anomalies shown are statistically significant at the 95% confidence level. This lends further credence to our explanation for black carbon geoengineering inducing circulation changes which cause Arctic ozone destruction.

4.4 EFFECTS ON THE HYDROLOGIC CYCLE

The traditional explanation of the driving force behind the Indian summer monsoon is that summer heating of the Tibetan Plateau creates a land-ocean temperature contrast, inducing a thermally direct circulation of moist air over the Indian subcontinent [e.g., *Manabe and Terpstra*, 1974; *Hahn and Manabe*, 1975; *Held*, 1983]. More recently, *Boos and Kuang* [2010] refined this idea to show that the Tibetan Plateau is not the primary factor, and instead, direct heating of the Indian subcontinent, combined with insulation of the subcontinent from cold, dry extratropical air by the Himalayas, is responsible for inducing the monsoon circulation. They also showed that instead of temperature driven circulation, which is the more traditional view, a monsoon circulation will emerge in the presence of strong meridional gradients of below-cloud entropy and moist static
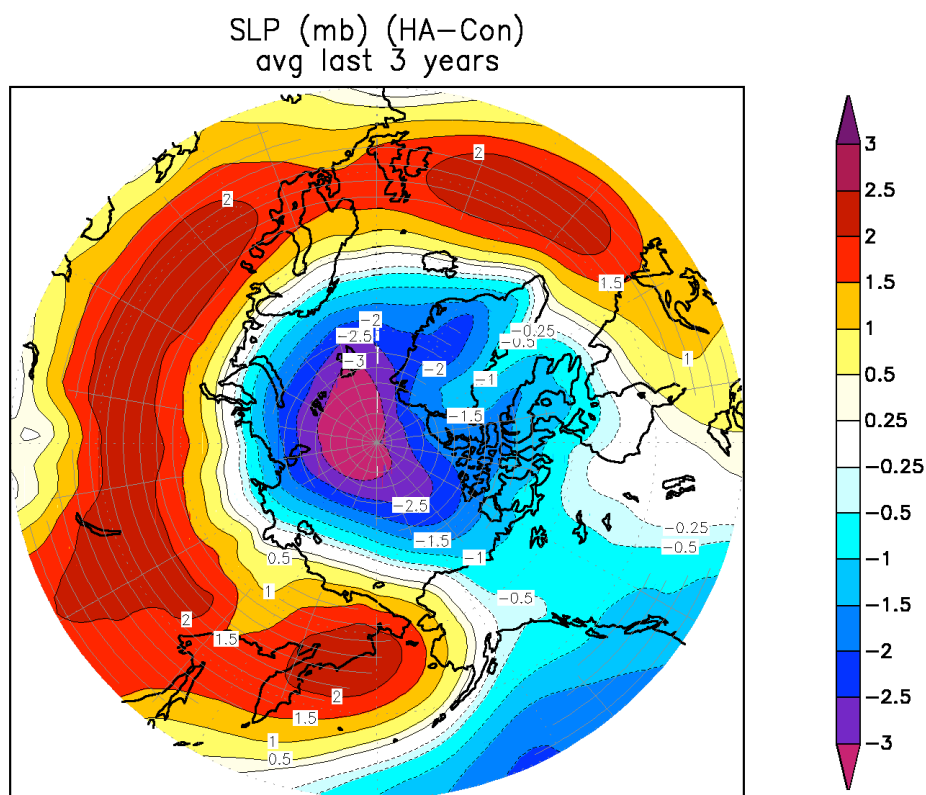
FIGURE 4.32. North polar stereographic projection of sea level pressure anomaly for middle stratospheric geoengineering (ensemble HA as described in Table 3.1), averaged over the last three years of simulation. Grey hatching denotes values that are statistically significant at the 95% confidence level as calculated by an unpaired two sample Student's *t* test.

energy between the Indian subcontinent and the Indian Ocean, suggesting the most important feature in creating a monsoon is how much energy can be drawn out of the ocean [*Molnar et al.*, 2010]. We note that this new interpretation of the monsoon plays the dominant role, but the more traditional view is not entirely replaced by it.

Both the traditional and the more refined explanations describe why a reduction in summer monsoon precipitation would be expected from geoengineering with stratospheric aerosols. In the traditional view, an aerosol cloud would blanket both the tropics and the extratropics, resulting in cooling. However, due to the lower heat capacity of land as compared to ocean, the Asian continent will cool more than the Indian Ocean, reducing the land-ocean temperature gradient, thus decreasing the thermally direct circulation which drives the monsoon [e.g., *Kravitz et al.*, 2010a]. In the new view, this mechanism is still important, but the dominant reason for reduction of the monsoon is reduced incoming radiation over the Indian Ocean, which reduces latent heat and evaporation, resulting in a reduced meridional gradient of moist static energy. Regardless of the reason, monsoonal disruptions have been shown in both simulations and observations of large stratospheric injections of aerosols. The observation record after the eruption of Mount Pinatubo shows a strong disruption to the hydrologic cycle, in reduced monsoon precipitation, reduced runoff, and increased drought [*Trenberth and Dai*, 2008]. In their geoengineering simulations, *Robock et al.* [2008] showed a large reduction in monsoon precipitation over India, East Asia, and the Sahel. Therefore, we would expect

stratospheric geoengineering with black carbon aerosols to show a disruption of the monsoon as well.

Figure 4.33 shows precipitation anomalies resulting from geoengineering. Globally averaged precipitation is vastly reduced on both an annual and interannual basis, well outside the realm of natural variability. By the tenth year of simulation, globally averaged precipitation is approximately 0.25 mm day^{-1} lower than in the control case, with reductions occurring nearly equally across all seasons. From the figure, it appears most of this reduction occurs over the oceans, as the values of reduction in land average precipitation are ~25% of the global average values. However, land precipitation is reduced by statistically significant amounts, particularly in the boreal summer months, which suggests a perturbation to the summer monsoon.

Evaporation values, as shown in Figure 4.34, are similar to the results for precipitation in Figure 4.33. The land average variability appears to be smaller for evaporation than precipitation, so more of the evaporation values show a statistically significant reduction due to geoengineering. Globally averaged values for this field are difficult to interpret, as sea surface temperatures were prescribed, but the land average values clearly show a reduction in evaporation, particularly in the boreal summer months.

One possible interpretation is that to balance the reduction in radiation at the surface, the amount of energy available for latent heating is reduced, which manifests itself as reduced evaporation. This is plausible, since latent heat involves a phase change of water, which does not require a change in
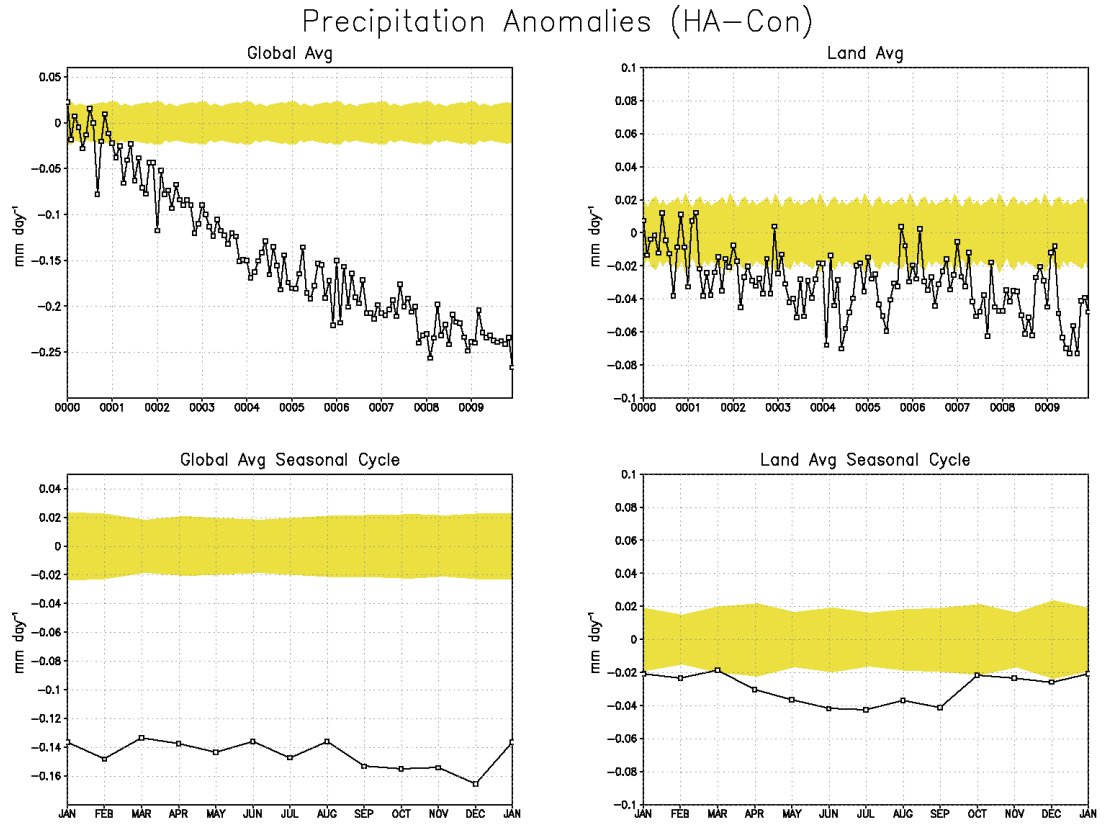
FIGURE 4.33. Average precipitation anomalies for middle stratospheric geoengineering (ensemble HA as described in Table 3.1). The left column of panels shows globally averaged anomalies, and the right column shows averages for land only. The top row of panels shows anomalies as a function of time, and the bottom row shows the ten year average seasonal cycle. Yellow shading denotes ±1.96σ of the average variability of the ten year average seasonal cycle of the control ensemble.
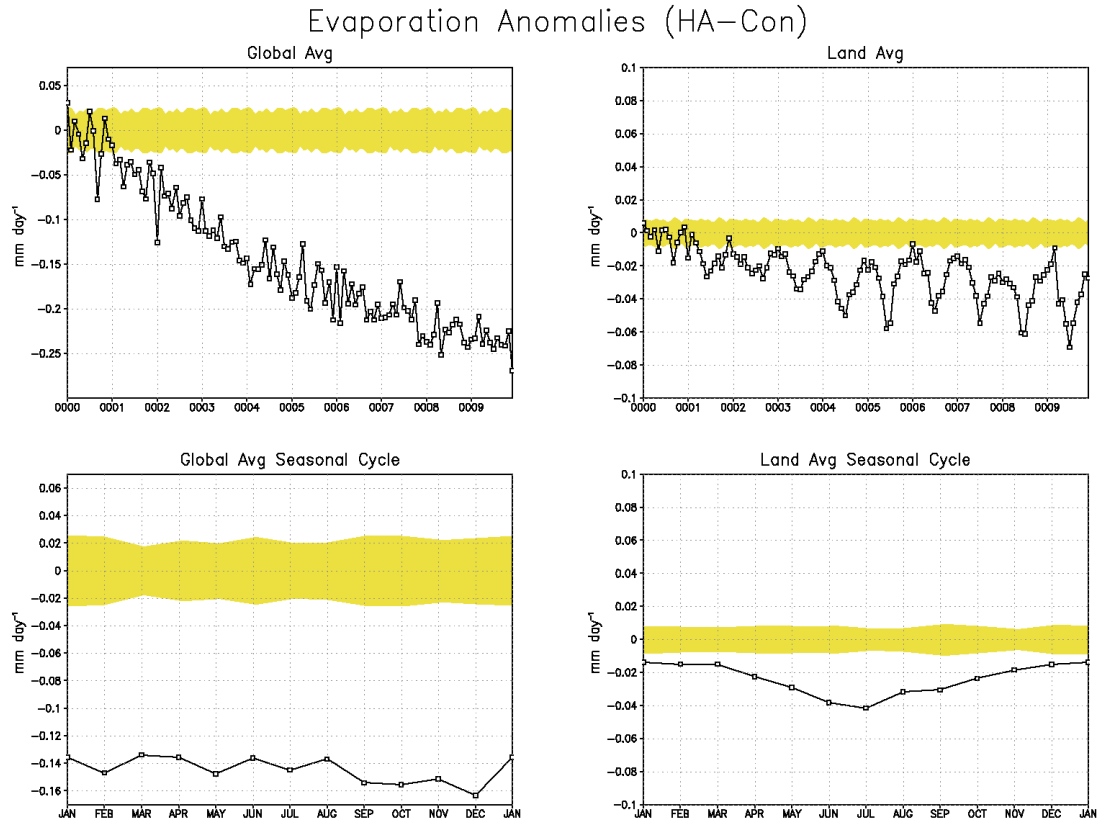
FIGURE 4.34. Average evaporation anomalies for middle stratospheric geoengineering (ensemble HA as described in Table 3.1). The left column of panels shows globally averaged anomalies, and the right column shows averages for land only. The top row of panels shows anomalies as a function of time, and the bottom row shows the ten year average seasonal cycle. Yellow shading denotes ±1.96σ of the average variability of the ten year average seasonal cycle of the control ensemble.

temperature. This also makes sense in the context of moist static energy, which is reduced due to thermal stabilization of the lower atmosphere. Figure 4.35 shows the latent heat anomalies due to geoengineering under this scenario. Toward the end of the simulation period, there is a precipitous decline in latent heat by approximately 7 W m^{-2}, which is nearly identical to the amount of TOA radiation anomaly as seen in Figure 4.7. In the global average, there is no particular season in which latent heat shows a large deficit. However, the land average shows a large seasonal cycle, with a significant negative anomaly in the boreal summer months and statistically significant, but not quite as large, anomalies in the other seasons. The largest global average latent heat anomaly over land is approximately 2 W m^{-2}, which suggests the vast majority of latent heat deficit is over the ocean, which could explain the large reductions in evaporation seen in Figure 4.34.

Figure 4.36 shows perturbations to soil moisture (top 1 m) and runoff. The globally averaged results show a gradual increase in soil moisture over the simulation period, exceeding natural variability. Total runoff (the sum of soil runoff and underground runoff) does show an overall average reduction when compared to the control case, most prominently in late spring. This reduction of up to 0.18 mm day^{-1} is statistically significant in some of the years of simulation but not in the average seasonal cycle.

To better analyze where these perturbations occur, Figure 4.37 shows spatial maps, averaged over the last three years of simulation, for these four hydrological variables. The precipitation field shows a strong reduction over
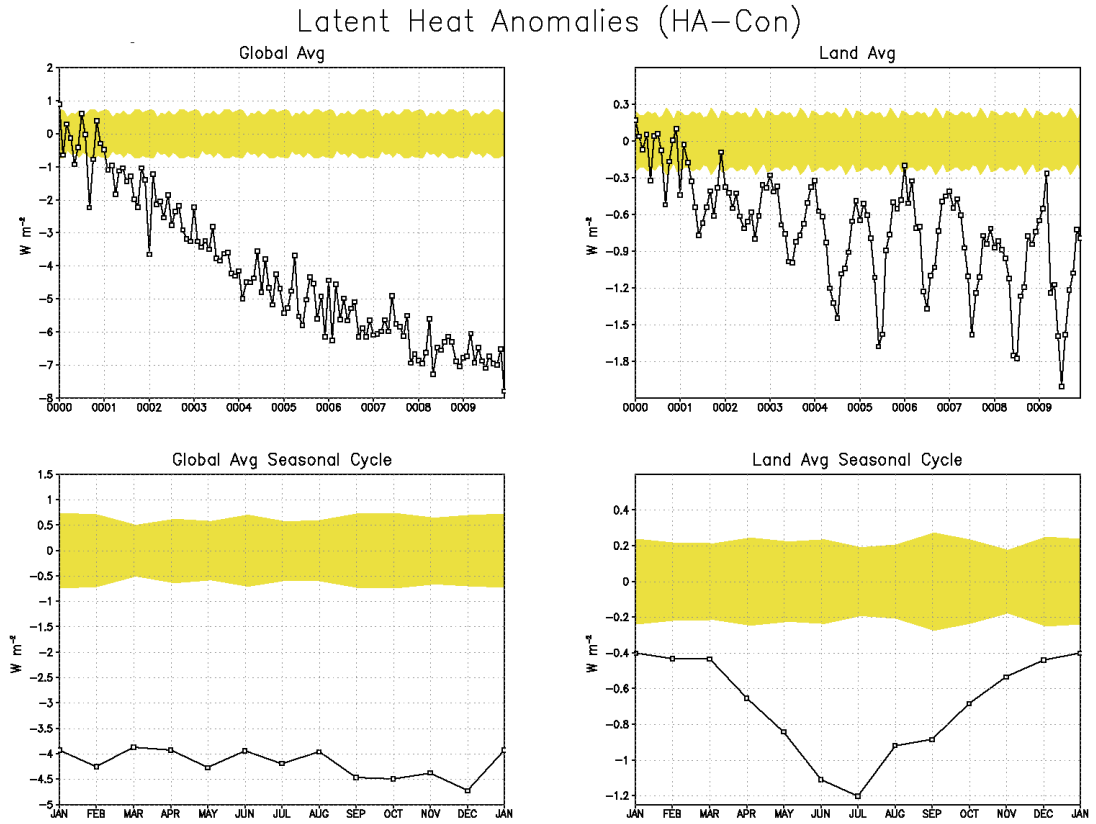
FIGURE 4.35. Latent heat anomalies for middle stratospheric geoengineering (ensemble HA as described in Table 3.1). The left column of panels shows globally averaged anomalies, and the right column shows averages for land only. The top row of panels shows anomalies as a function of time, and the bottom row shows the ten year average seasonal cycle. Yellow shading denotes ±1.96σ of the average variability of the ten year average seasonal cycle of the control ensemble.
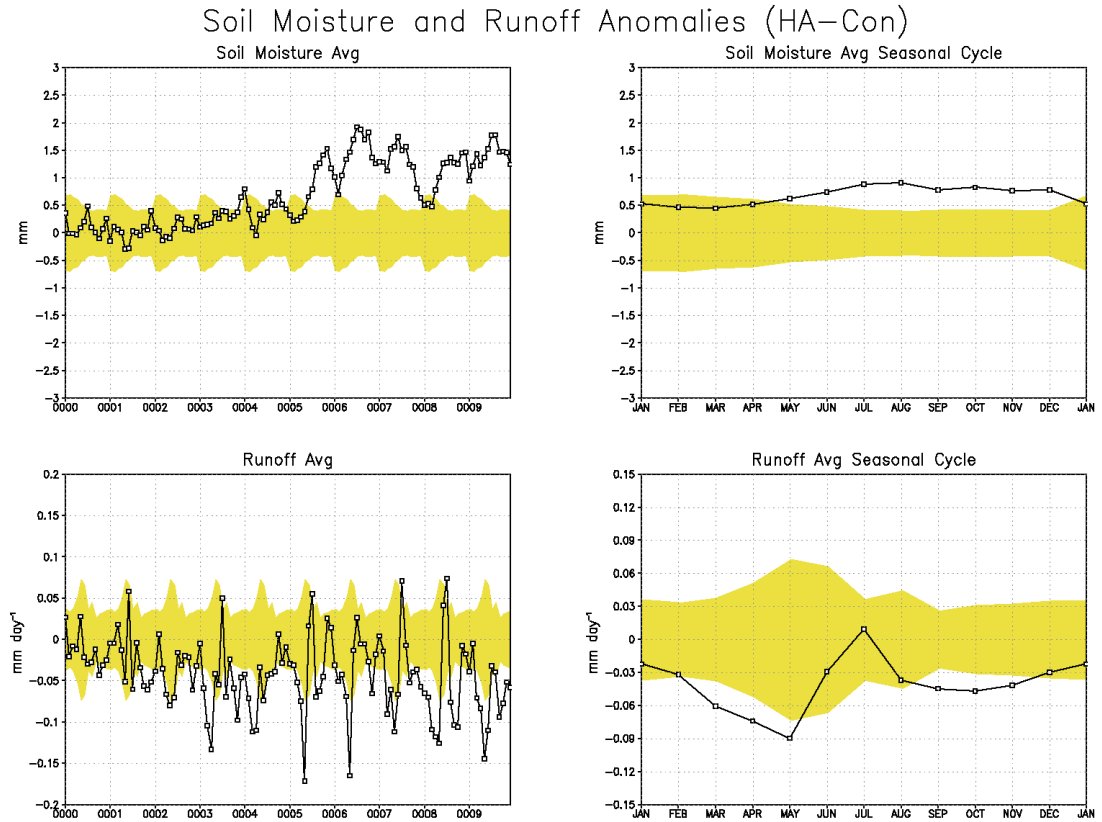
FIGURE 4.36. Average soil moisture (top 1 m, or model layers 1-4) and runoff anomalies for middle stratospheric geoengineering (ensemble HA as described in Table 3.1). The left column of panels shows anomalies as a function of time, and the right column shows the ten year average seasonal cycle. Yellow shading denotes ±1.96σ of the average variability of the ten year average seasonal cycle of the control ensemble. No distinction is made between global average and land average because these are land-only variables.
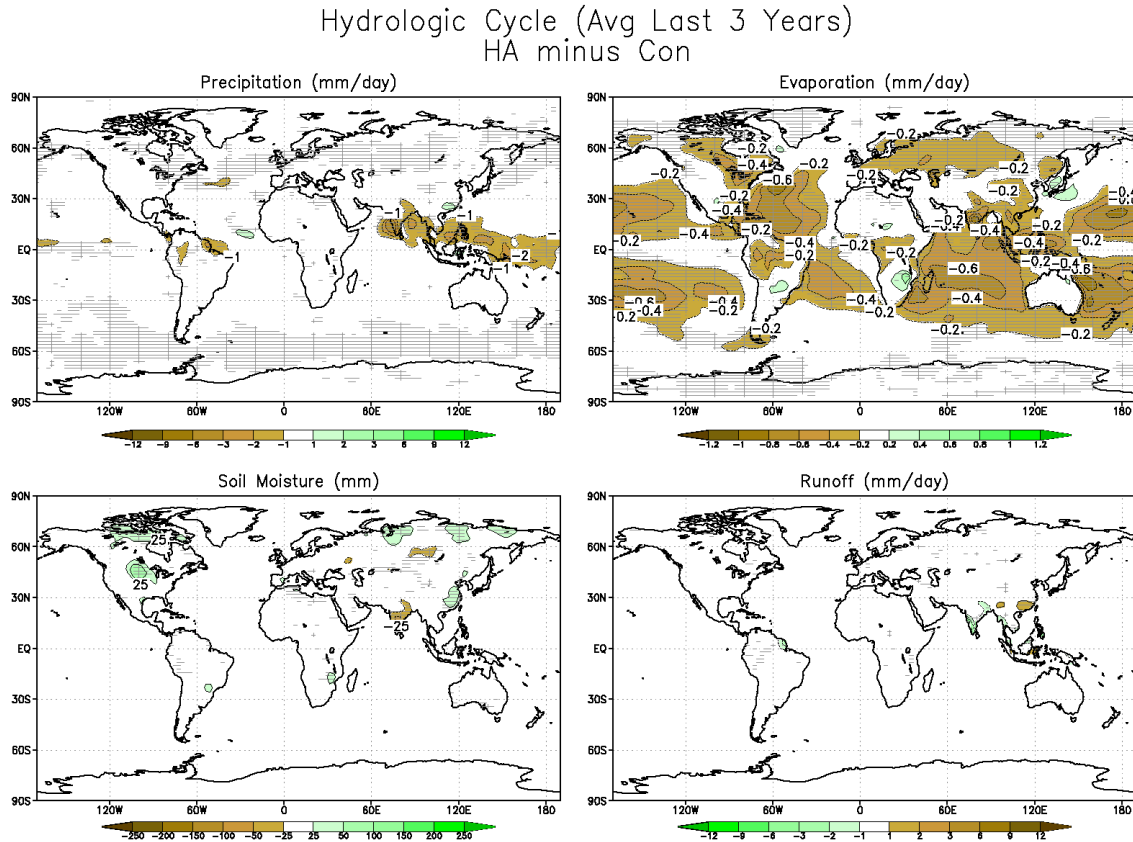
FIGURE 4.37. Hydrologic cycle anomalies that would result from middle stratospheric geoengineering (ensemble HA as described in Table 3.1). Spatial maps shown are averages over the last three years of simulation. Grey hatching denotes values that are statistically significant at the 95% confidence level as calculated by an unpaired two sample Student's *t* test.

India, East Asia, and the Western Pacific basin by up to 2 mm day^{-1}, with some of these values being statistically significant at the 95% confidence level. Evaporation shows a large amount of statistically significant values over most of the tropical and midlatitude oceans. Soil moisture and runoff show some local regions of increase and decrease, but nothing that resembles large scale patterns. However, this is likely due to contouring, as the smallest soil moisture contour in Figure 4.37 is 25 mm, but Figure 4.36 shows a globally averaged increase in soil moisture of up to 2 mm.

From Figures 4.33-36, we suspect a large amount of the hydrologic cycle perturbation is a disruption of the summer monsoon. Figure 4.38 shows the same fields as Figure 4.37, but averaging is only done over June, July, August, and September, which are the peak months of the summer monsoon. The precipitation field shows a vast reduction over India, East Asia, and the Western Pacific basin, much of which is statistically significant. Some of the anomalies calculated by the model exceed 6 mm day^{-1}, which indicates a large reduction of monsoonal precipitation. Evaporation patterns are similar to the annual average but with larger anomalies and many more statistically significant results. The soil moisture and runoff panels are quite similar to the results shown in the annual average, with the notable exception of India and Southeast Asia, which show reductions in soil moisture by over 5 cm. However, in light of the large natural variability of the soil moisture field as represented in the model, as well as in data [e.g., *Vinnikov et al.*, 1996], we do not believe that soil moisture will be significantly negatively affected by black carbon aerosol geoengineering, and in
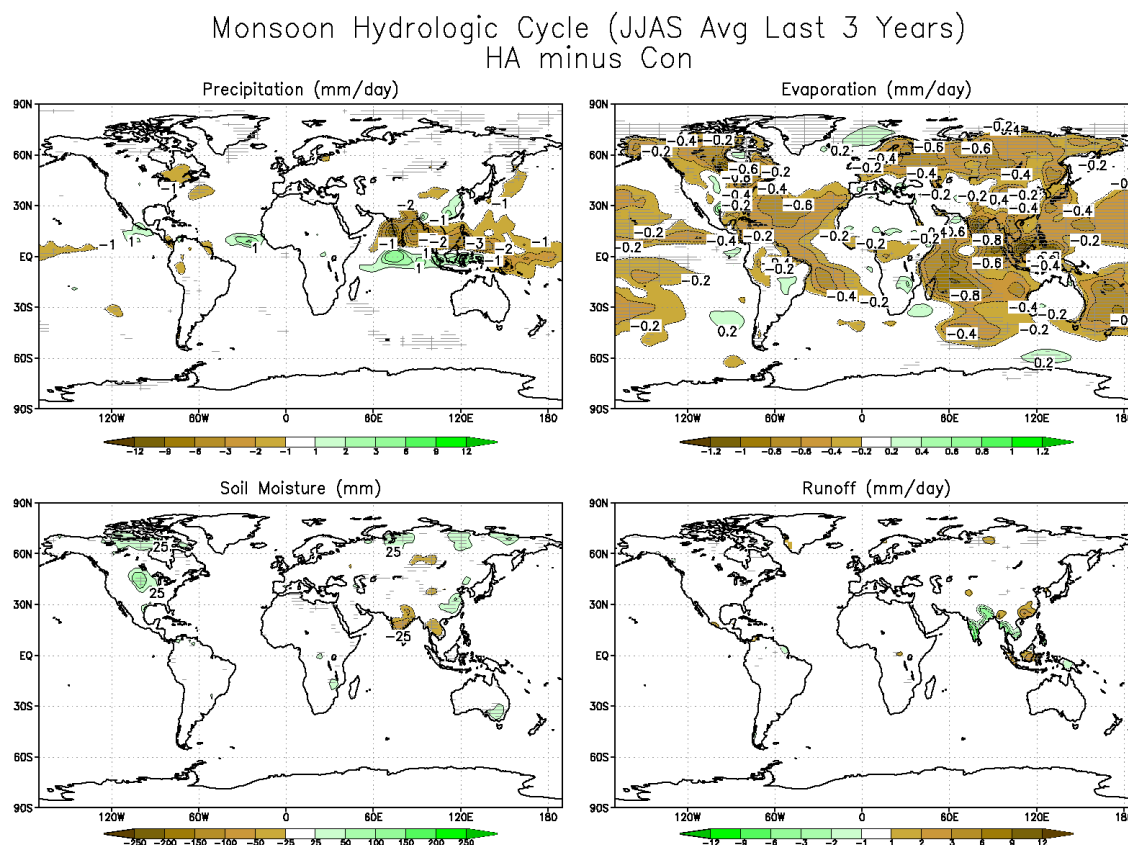
FIGURE 4.38. Hydrologic cycle anomalies that would result from middle

stratospheric geoengineering (ensemble HA as described in Table 3.1).

Anomalies pictured are averaged only averaged over June, July, August, and

September to highlight changes in the summer monsoon hydrologic cycle.

Spatial maps shown are averages over the last three years of simulation. Grey

hatching denotes values that are statistically significant at the 95% confidence

level as calculated by an unpaired two sample Student's *t* test.

many cases, the effect will be positive. Since this is the variable most important for vegetation, in this context, we conclude the effects of these perturbations to the hydrologic cycle are small and, with a few exceptions, mildly beneficial.

These results regarding the hydrologic cycle are strongly affected by the use of fixed sea surface temperatures in conducting our simulations. Allowing both the ocean and land to cool will strengthen the land-ocean temperature gradient from the results we have shown, which will temper the reductions in precipitation shown previously. However, this reduction in sea surface temperature will decrease evaporation over the Indian Ocean, as well as reducing the moist static energy available, which will exacerbate the disruption to the hydrologic cycle. However, the resulting impacts on soil moisture and runoff are unclear without further simulation.

4.5 EFFECTS ON THE CRYOSPHERE

The surface cooling and circulation changes described in Section 4.3 could potentially cause a regrowth of Arctic sea ice. Figure 4.39 shows polar stereographic projections of snow and ice fraction anomaly due to geoengineering. Much of the Arctic North of Canada shows statistically significant increases in snow and ice coverage, sometimes exceeding 15%. Nearly all of the Eurasian land mass also shows a statistically significant increase of 3-9%, as does Eastern Canada. The South polar projection shows no anomalies in ice and snow.

Snow and Ice Fraction Anom (%)
HA minus Con (Avg Last 3 Yrs)

North Polar Projection

South Polar Projection

−21 −18 −15 −12 −9 −6 −3 3 6 9 12 15 18 21
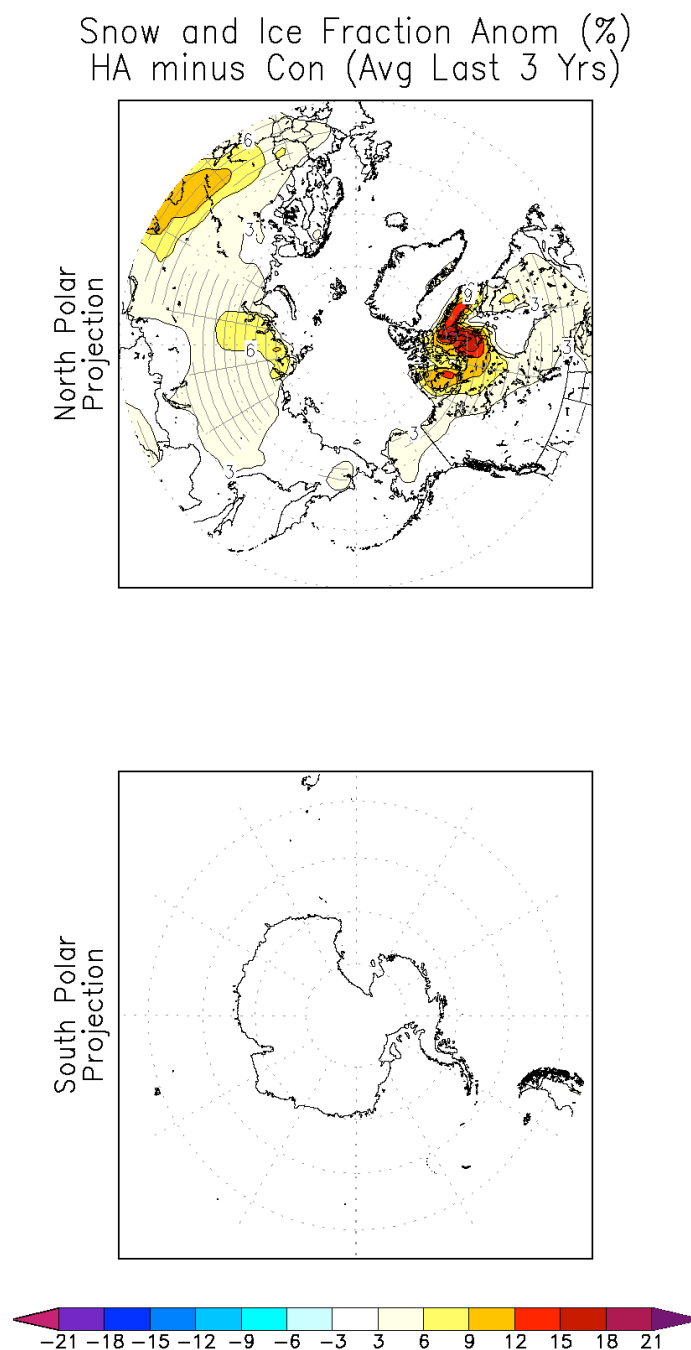
FIGURE 4.39. Polar stereographic projections of snow and ice fraction anomaly for middle stratospheric geoengineering (ensemble HA as described in Table 3.1), averaged over the last three years of simulation. Grey hatching denotes values that are statistically significant at the 95% confidence level as calculated by an unpaired two sample Student's *t* test.

Despite these results, the large anomalies are highly localized and do not show a large impact in terms of Northern Hemisphere average. Figure 4.40 shows the average snow and ice coverage anomaly across the Northern Hemisphere. This figure does not show any large changes, with no anomalies exceeding 1-2%, which is much smaller than the natural variability of the climate system. In the September only averages, which is the minimum period of Arctic sea ice, although the average anomaly is above 0.5%, indicating some regrowth of Arctic sea ice, but none of these anomalies, including the maximum of almost 1%, is statistically significant. We therefore conclude that, although there is some evidence of sea ice recovery as a result of geoengineering, this finding is not statistically robust for the simulations we have conducted. If we had allowed sea ice coverage to vary, any anomalies would likely be more prominent and more statistically significant.

Snow and Ice Fraction Anomaly
NH Avg (HA−Con)

September Only
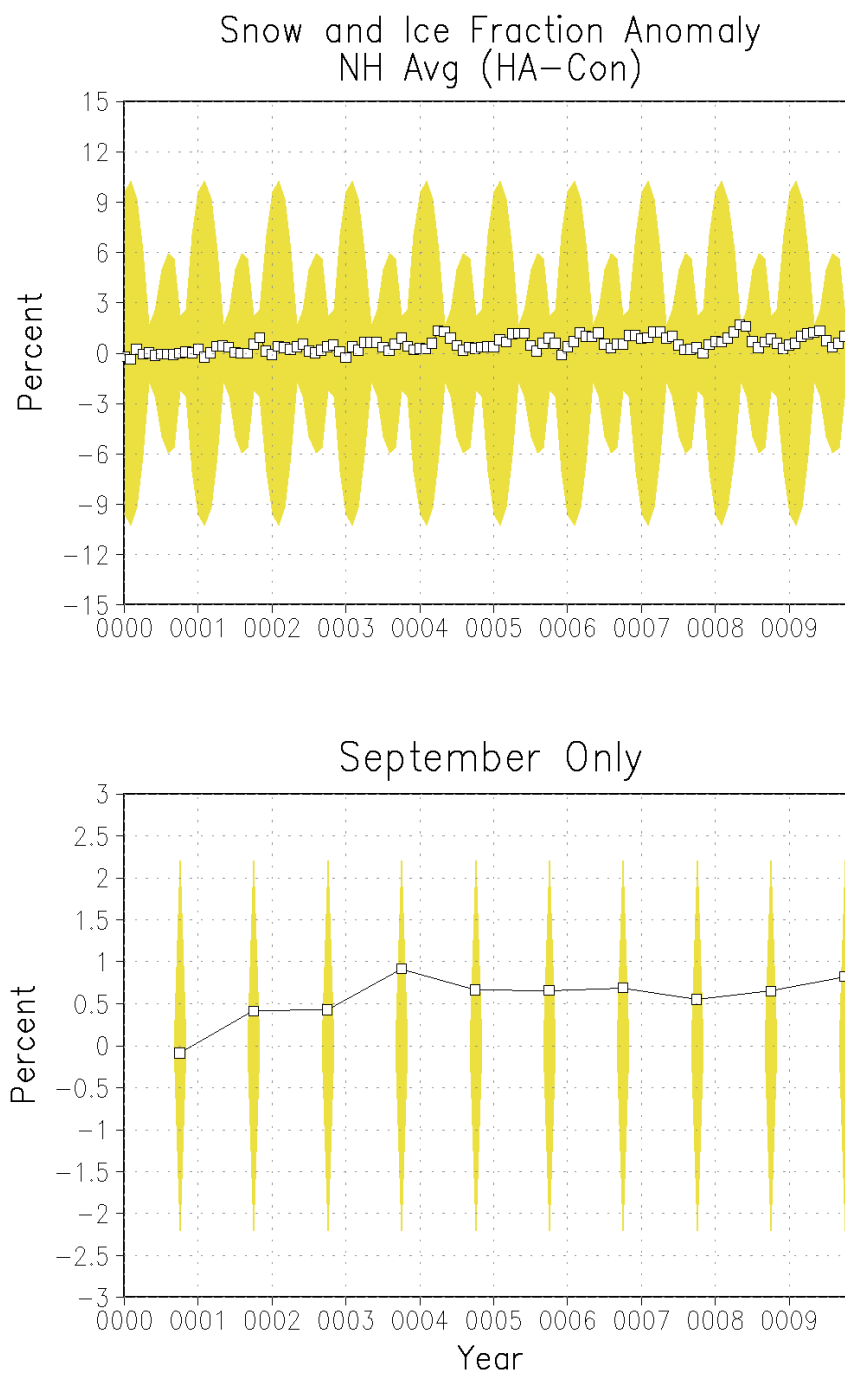
FIGURE 4.40. Northern Hemisphere average snow and ice fraction anomalies for middle stratospheric geoengineering (ensemble HA as described in Table 3.1). Yellow shading denotes ±1.96σ of the average variability of the ten year average seasonal cycle of the control ensemble.

CHAPTER 5: SENSITIVITY TO MODEL PARAMETERS

In the previous chapter, we established the climate impacts of

geoengineering under ensemble HA, which we considered to be the scenario that

would cause the most reasonable amount of cooling. However, the amount of

cooling, as well as the additional climate modifications and untoward side

effects, can be adjusted by the choice of specific aerosol parameters instead of

varying the amount of aerosols injected into the stratosphere. In this chapter, we

compare the different ensembles with a focus on the sensitivity of the climate

impacts to the altitude of injection, aerosol particle size, and the dirty snow

effect, or modification of ground albedo by deposited soot.

5.1 SURFACE AIR TEMPERATURE

Figure 5.1 is a repeat of Figure 4.1, showing globally averaged surface air

temperatures for each ensemble. In addition to the discussion provided in

Section 4.1, we compare the different ensembles.

The differences between ensembles LgR and HALgR are rather small.

Both of these ensembles involved injections of large particles (r=0.15 μm) into the

stratosphere, so the small temperature difference between these two ensembles is

due to altitude. For the default aerosol size (r=0.08 μm), the difference between

the ensembles is much more pronounced, as can be seen by comparing

ensembles Def and HA. We do not have a comparison for the small radius case

(r=0.03 μm), as ensemble HASmR caused model blowup. However, we can
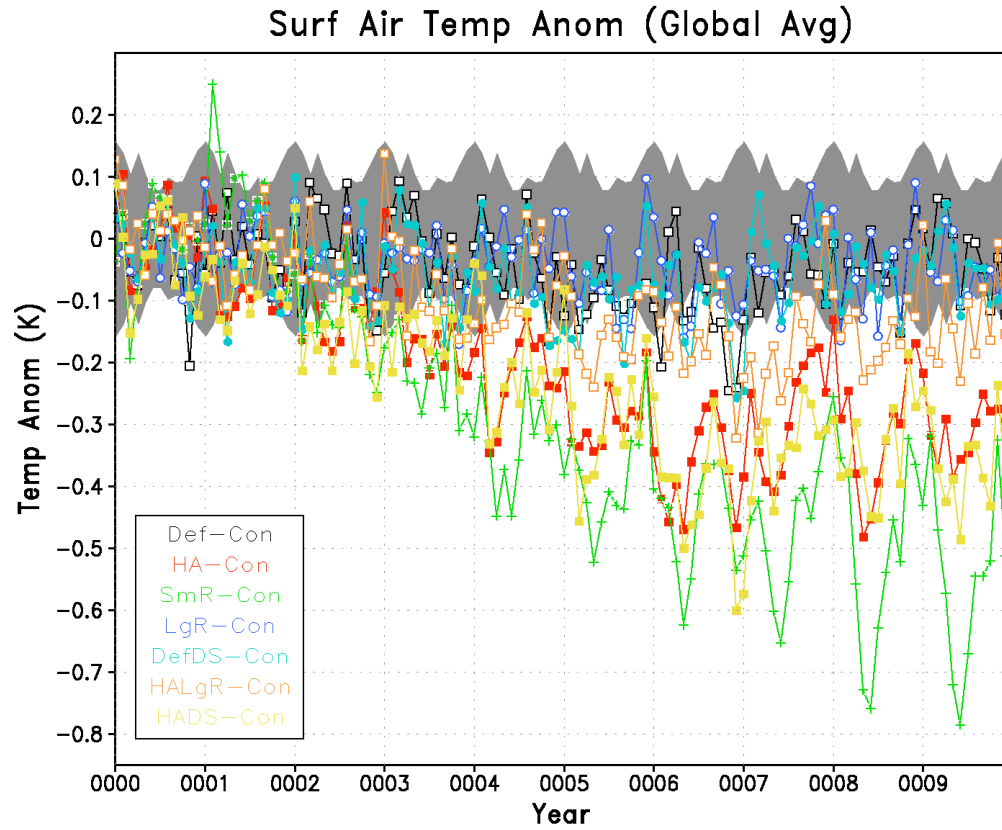
FIGURE 5.1. Globally averaged surface air temperature anomalies for each of the geoengineering ensembles. Ensemble descriptions are given in Table 3.1. Grey shading denotes ±1.96σ of the variability of the seasonal cycle of the control ensemble, averaged over the entire 10 year simulation.

conclude the relative effects of particle radius and altitude of injection have some nonlinear interaction, so neither parameter can be deemed more important than the other.

Comparing ensembles Def and DefDS or ensembles HA and HADS shows the differences introduced into the results by turning on the dirty snow effect. The very minor differences between these ensembles, none of which is statistically significant, suggests the dirty snow effect as represented by ModelE is quite small. We provide a deeper analysis of this effect in Section 5.7.

Furthering this comparison, Figure 5.2 shows spatial maps of surface air temperature differences, averaged over the last 3 years of simulation. For experiment LgR, although there are small areas of cooling, we see no discernible cooling pattern that would be expected from geoengineering. In contrast, experiment SmR shows large areas of cooling over all of the continents, with many of the anomalies being statistically significant at the 95% confidence level. These cooling patterns look like typical volcanic and geoengineering cooling patterns [*Robock*, 2000; *Robock et al.*, 2008]. However, the magnitude of cooling often exceeds 2°C and at some points exceeds 7°C. This is similar to the nuclear winter results of *Robock et al.* [2007b], who concluded this cooling would be catastrophic to agriculture [*Toon et al.*, 2007], leading us to assert this scenario represents too much cooling from geoengineering. Should geoengineering with small radius particles be undertaken, the annual amount injected should be much less than 1 Tg. Of particular interest is the warming by 2-3°C of the Tibetan Plateau. As we will discuss in Section 5.4, this is the result of longwave
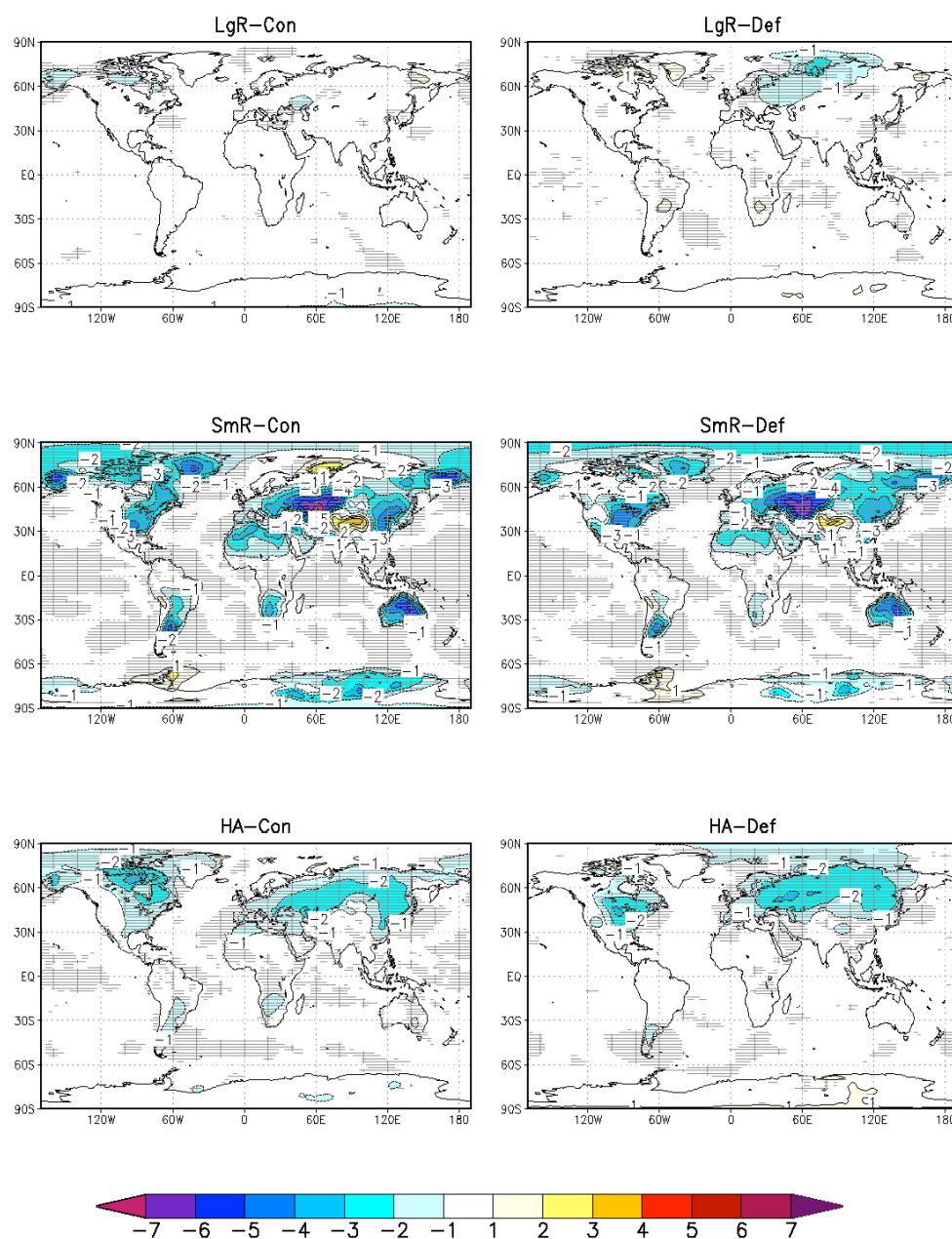
FIGURE 5.2. Surface air temperature anomalies for black carbon geoengineering, averaged over the last three years of simulation. Grey hatching denotes values that are statistically significant at the 95% confidence level as calculated by an unpaired two sample Student's *t* test.

emission from the aerosol layer that extends into the troposphere. Ensemble HA was discussed in Section 4.1, but in comparing with the other ensembles in Figure 5.2, we clearly see the typical volcanic cooling pattern, although the cooling is much more reasonable than in the small radius case.

5.2 RADIATION

Since these cooling patterns are primarily caused by radiative effects, we continue the analysis of the radiation budget as in Section 4.1, but now comparing each of the ensembles. Figures 5.3-5.11 show globally averaged solar, thermal, and total net radiation calculated by the model at the top of atmosphere (TOA), the tropopause, and the surface. As expected, ensemble LgR shows the smallest perturbation to the radiation budget, with equilibrium anomaly values less than 5 W m^{-2} in magnitude in all plots.

Ensemble HALgR shows equal or smaller in magnitude solar radiation perturbations than ensemble Def, yet the amount of cooling from ensemble HALgR was slightly larger and more statistically significant than ensemble Def, suggesting the configuration for HALgR increased the radiative efficiency of this particular experiment. This suggests the altitude of injection appears to have a more dominant effect on radiation than the particle radius, at least for the radii of the sizes considered. However, the difference between these two ensembles is approximately 5 W m^{-2}, which is a 1.5% difference in total insolation, using an average value of 342 W m^{-2}. In contrast, a radiation anomaly of 55 W m^{-2} in SmR reflects a 16.1% reduction in insolation. HALgR shows a low contribution to
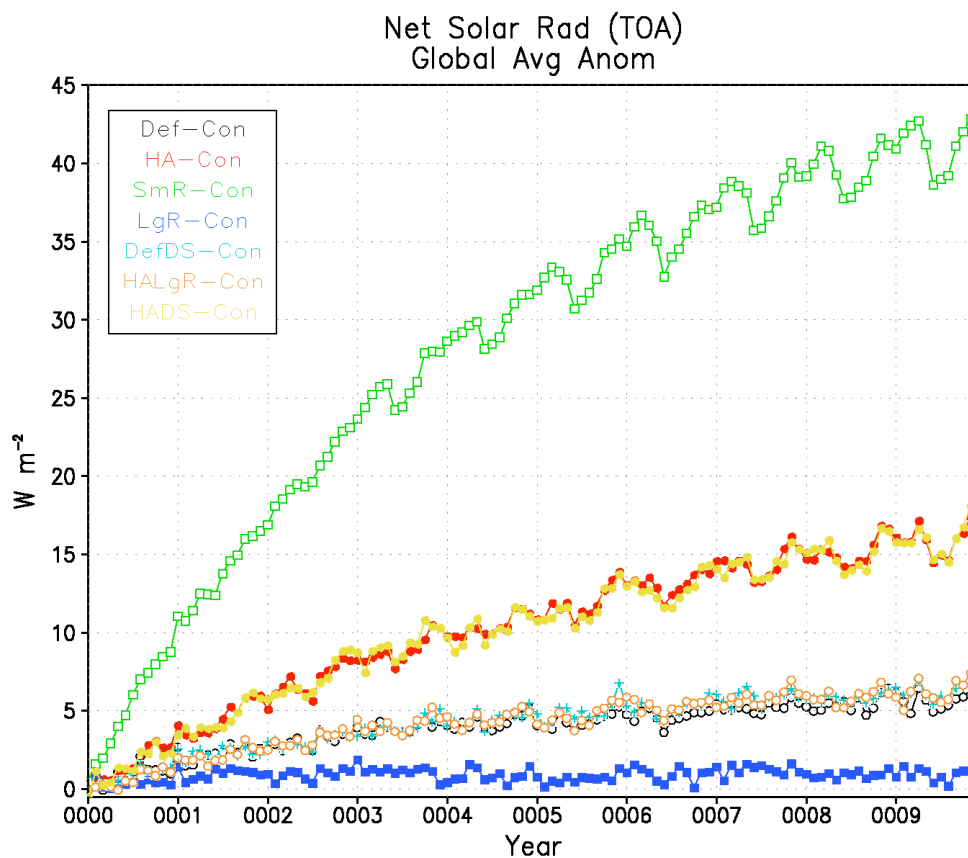
FIGURE 5.3. Globally averaged net solar radiation (down minus up) anomaly at the top of the atmosphere for each of the geoengineering ensembles. Ensemble descriptions are given in Table 3.1.
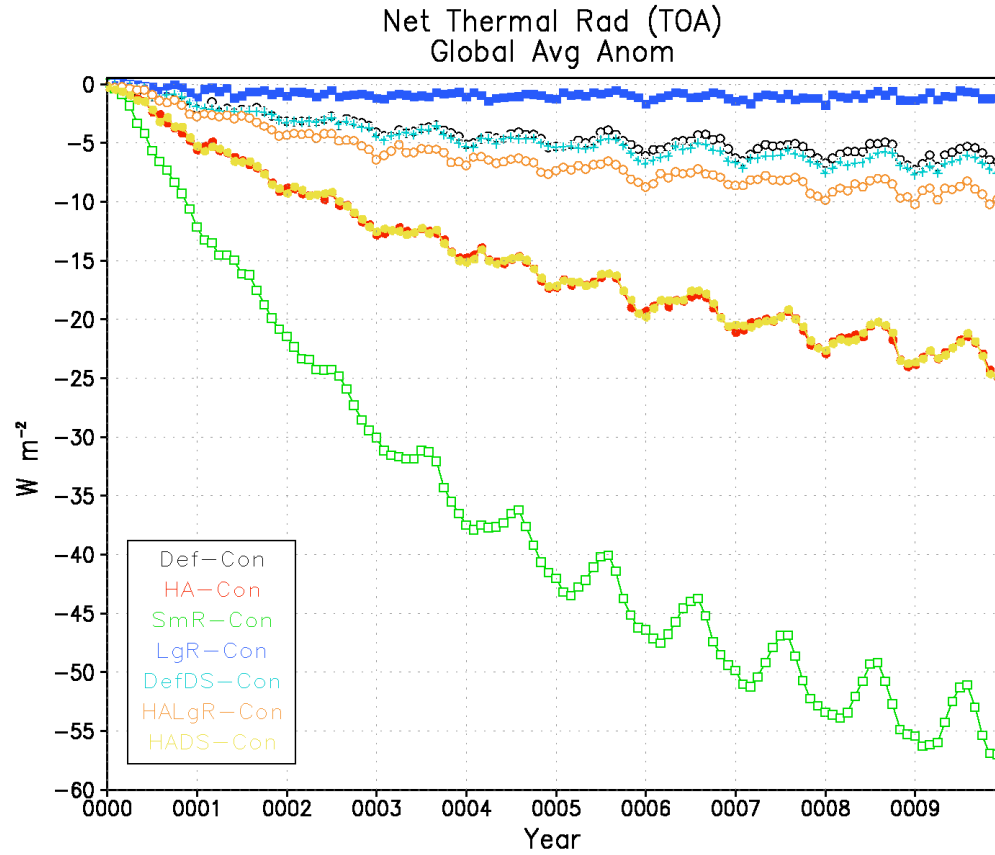
FIGURE 5.4. Globally averaged net thermal radiation (down minus up) anomaly at the top of the atmosphere for each of the geoengineering ensembles. Ensemble descriptions are given in Table 3.1.
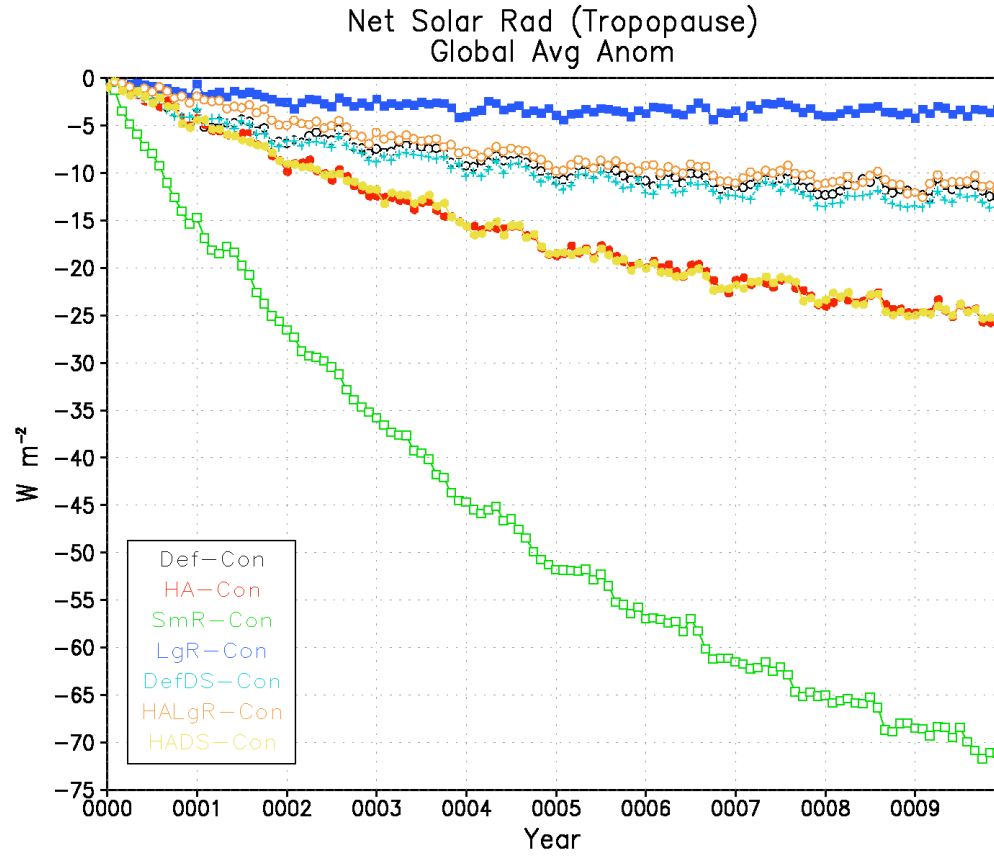
FIGURE 5.5. Globally averaged net solar radiation (down minus up) anomaly at the tropopause for each of the geoengineering ensembles. Ensemble descriptions are given in Table 3.1.
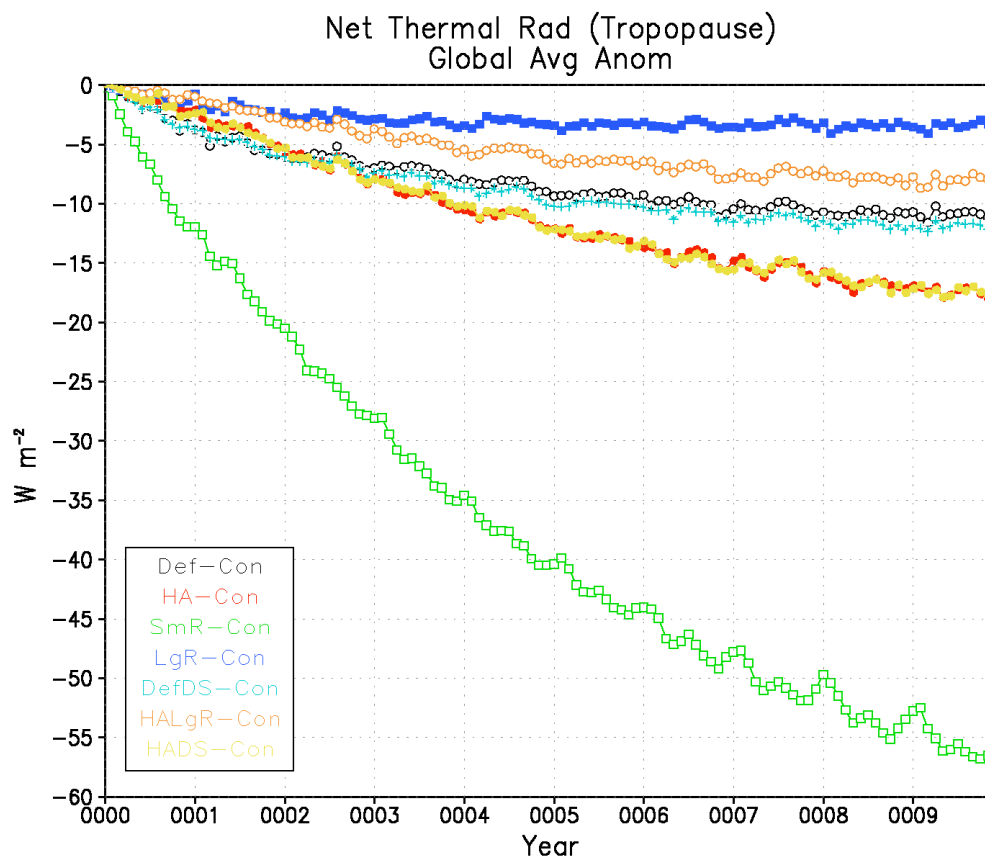
FIGURE 5.6. Globally averaged net thermal radiation (down minus up) anomaly at the tropopause for each of the geoengineering ensembles. Ensemble descriptions are given in Table 3.1.
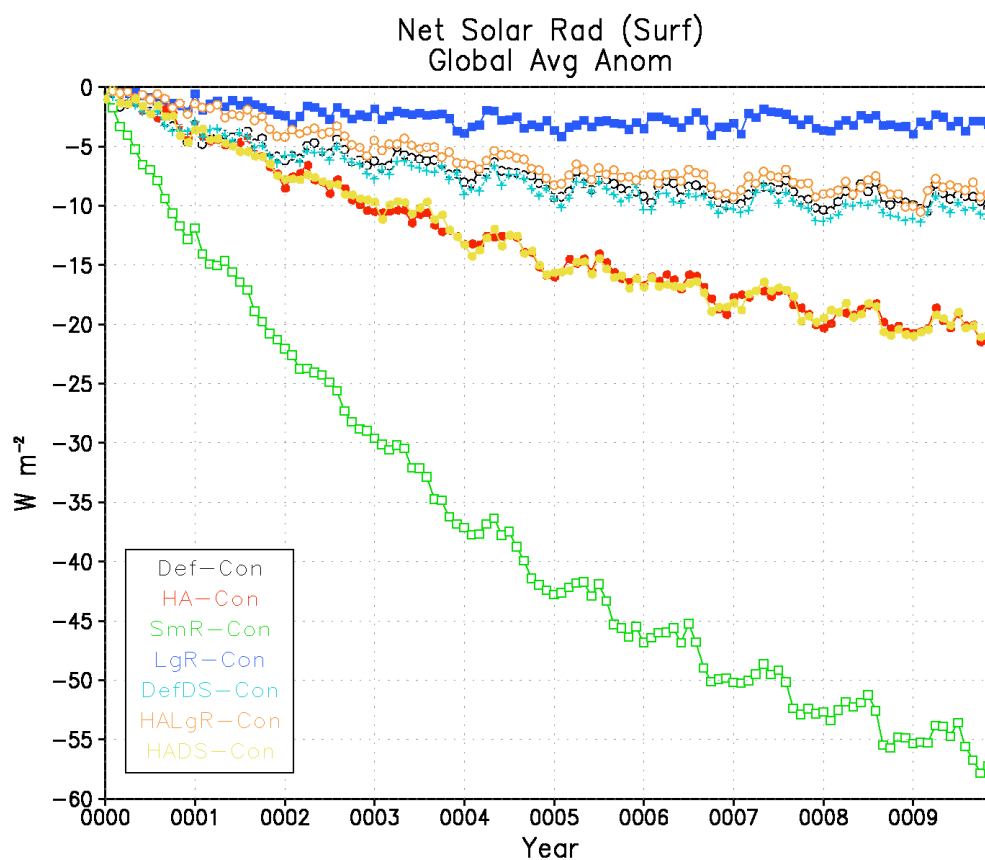
FIGURE 5.7. Globally averaged net solar radiation (down minus up) anomaly at the surface for each of the geoengineering ensembles. Ensemble descriptions are given in Table 3.1.
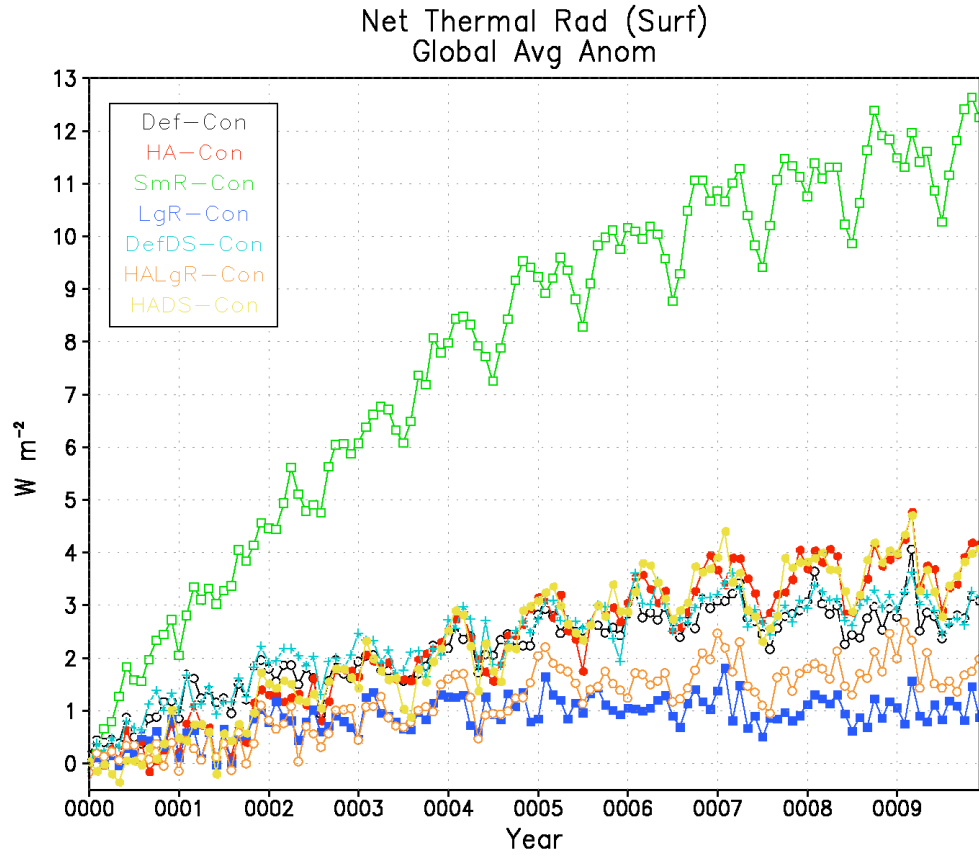
FIGURE 5.8. Globally averaged net thermal radiation (down minus up) anomaly at the surface for each of the geoengineering ensembles. Ensemble descriptions are given in Table 3.1.
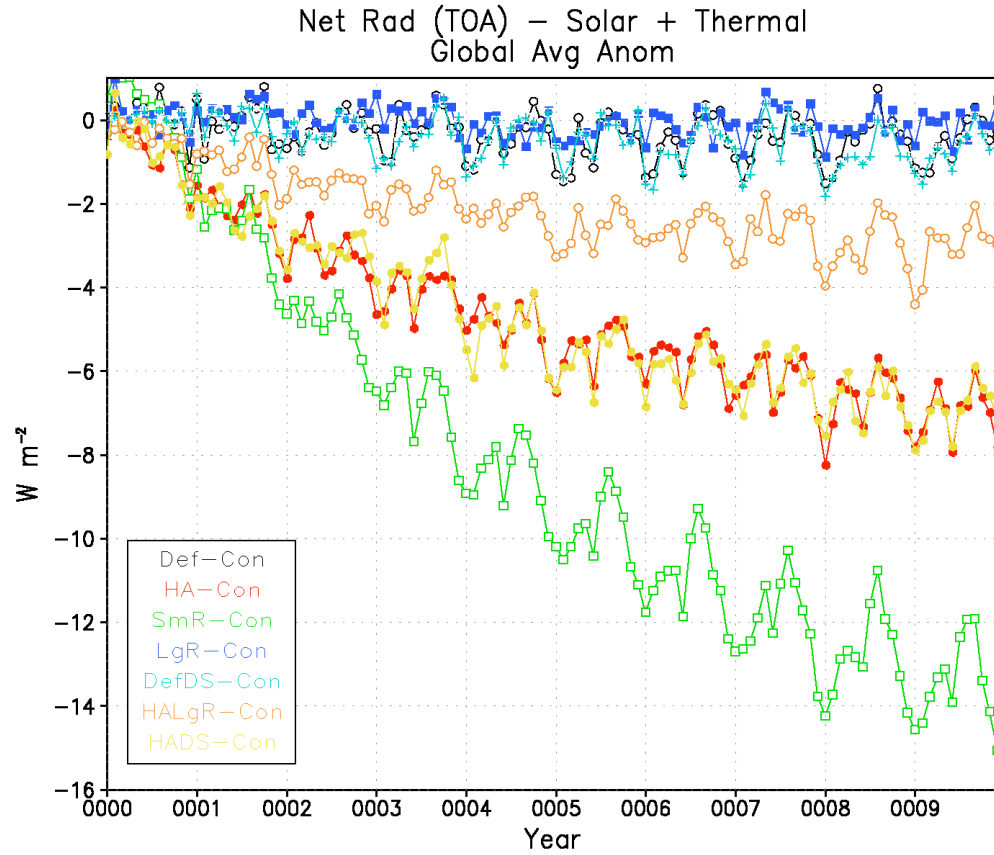
FIGURE 5.9. Globally averaged net total (solar plus thermal) radiation (down minus up) anomaly at the top of the atmosphere for each of the geoengineering ensembles. Ensemble descriptions are given in Table 3.1.
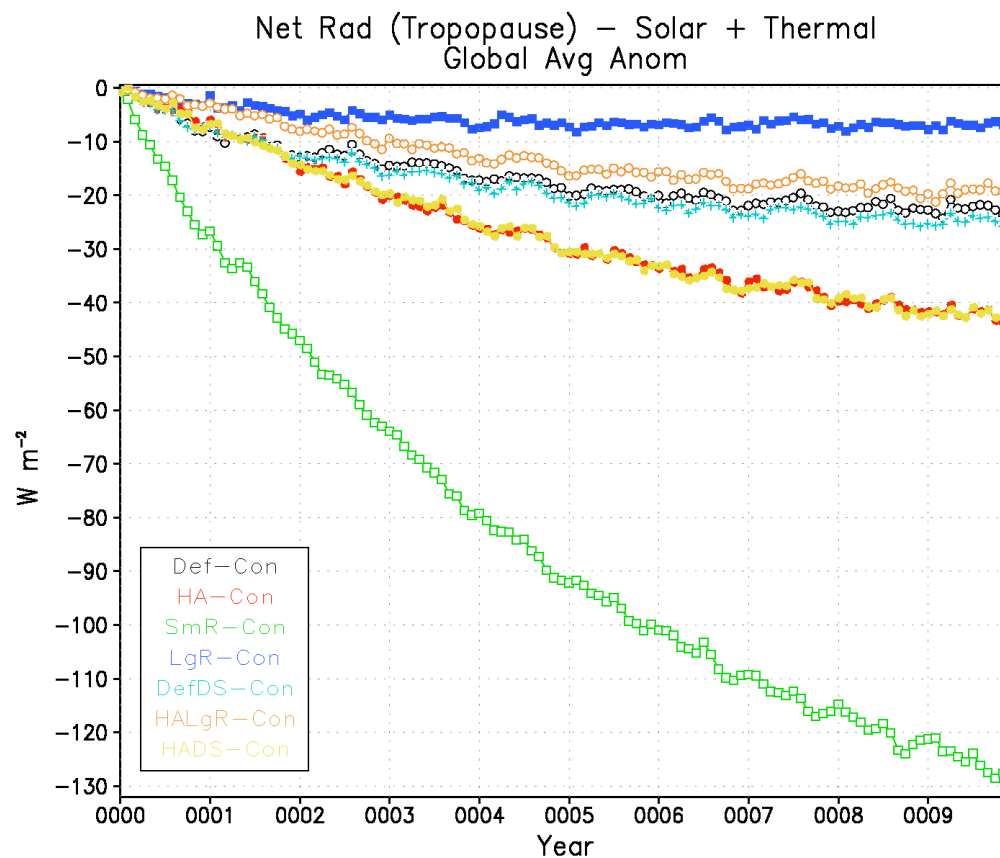
FIGURE 5.10. Globally averaged net total (solar plus thermal) radiation (down minus up) anomaly at the tropopause for each of the geoengineering ensembles. Ensemble descriptions are given in Table 3.1.
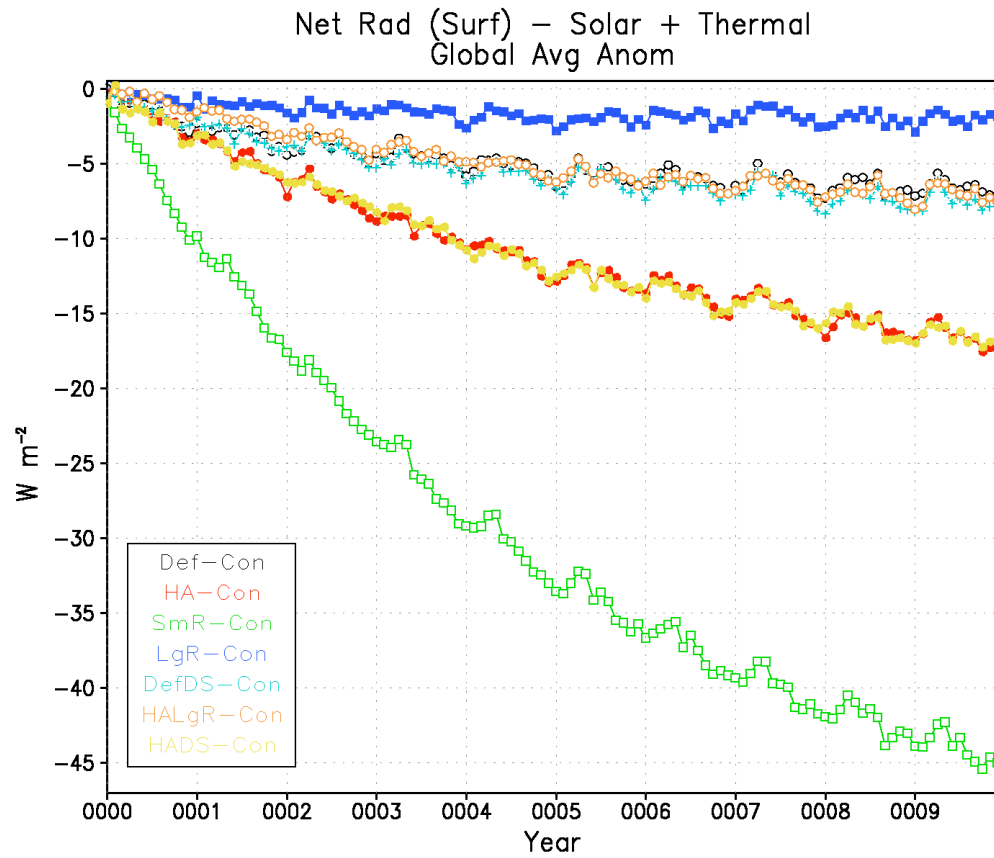
FIGURE 5.11. Globally averaged net total (solar plus thermal) radiation (down minus up) anomaly at the surface for each of the geoengineering ensembles. Ensemble descriptions are given in Table 3.1.

thermal radiation anomalies, regardless of the location at which the anomaly is calculated, because the large particles are less radiatively efficient than the smaller particles. However, in Figure 5.4 (thermal radiation anomaly at TOA), the altitude of the particles again appears to dominate the radiative effects, as ensemble HALgR shows more of a radiation anomaly in this figure than Def or DefDS.

HA and HADS, of which HA was the case used in Chapter 4, show more perturbation to the radiation fields than all other ensembles except SmR. Ensemble SmR shows more than twice the perturbation to any radiation field for ensembles HA and HADS, and often more than ten times the perturbation due to ensembles Def, LgR, DefDS, and HALgR. The smaller particles are quite radiatively efficient at absorbing sunlight, as is evidenced in Figure 5.3, which shows an extra 42 W m^{-2} of solar radiation being retained in the atmosphere by year ten of the simulations. Figures 5.6 and 5.8 again show the efficiency of this absorbing aerosol at such a small radius: an additional 12 W m^{-2} of thermal radiation is absorbed by the surface in year ten due to the aerosol layer. Figure 5.9 shows that the total TOA radiation imbalance due to this ensemble is approximately twice the amount due to ensemble HA. The total tropopause anomaly (Figure 5.10) is enormous, reaching -130 W m^{-2} by year ten, which is more than three times the next nearest ensemble. Part of this large anomaly is from the shortwave component and is due to blocked insolation by the aerosol layer above. Another large part is warming from the absorbing aerosol layer and subsequent radiation back to space. Since the injection altitude is near the

tropopause, the bulk of the aerosol layer remains there (as will be shown in the next section), which effectively adds to the upward thermal radiation component of the tropopause. Similarly, at the surface, the radiation imbalance approaches -45 W m^{-2} by year ten, although the thermal contribution to this is much less than for the tropopause, as the surface is somewhat removed from the aerosol layer.

In all of these figures, the lines for Def and DefDS nearly perfectly overlap, as do the lines for HA and HADS. This suggests there is little to no difference in radiation introduced into the experiment suite by the dirty snow effect. Again, this will be analyzed more thoroughly in Section 5.7.

Figures 5.12-5.17 show globally averaged solar, thermal, and total net radiative forcing from the black carbon aerosols, calculated at the tropopause and the surface. The results are very similar to the radiation anomalies described previously. The solar radiative forcing pictures are similar in magnitude to the solar radiation pictures, although we again note that, like in Section 4.1, these are calculations of instantaneous radiative forcing, not adjusted radiative forcing. However, the thermal radiation pictures have a much smaller magnitude, with the large radius ensembles showing tropopause thermal radiative forcing of less than 0.25 W m^{-2} (Figure 5.13) and surface radiative forcing of less than 0.03 W m^{-2} (Figure 5.15). Even the largest contribution to thermal radiative forcing, which is the contribution of ensemble SmR at the tropopause, is smaller in magnitude than 2 W m^{-2}. Although this large difference between the small and large particles is due to the increased radiative efficiency of smaller particles, this amount of radiative forcing is so small that it hardly contributes to the total.
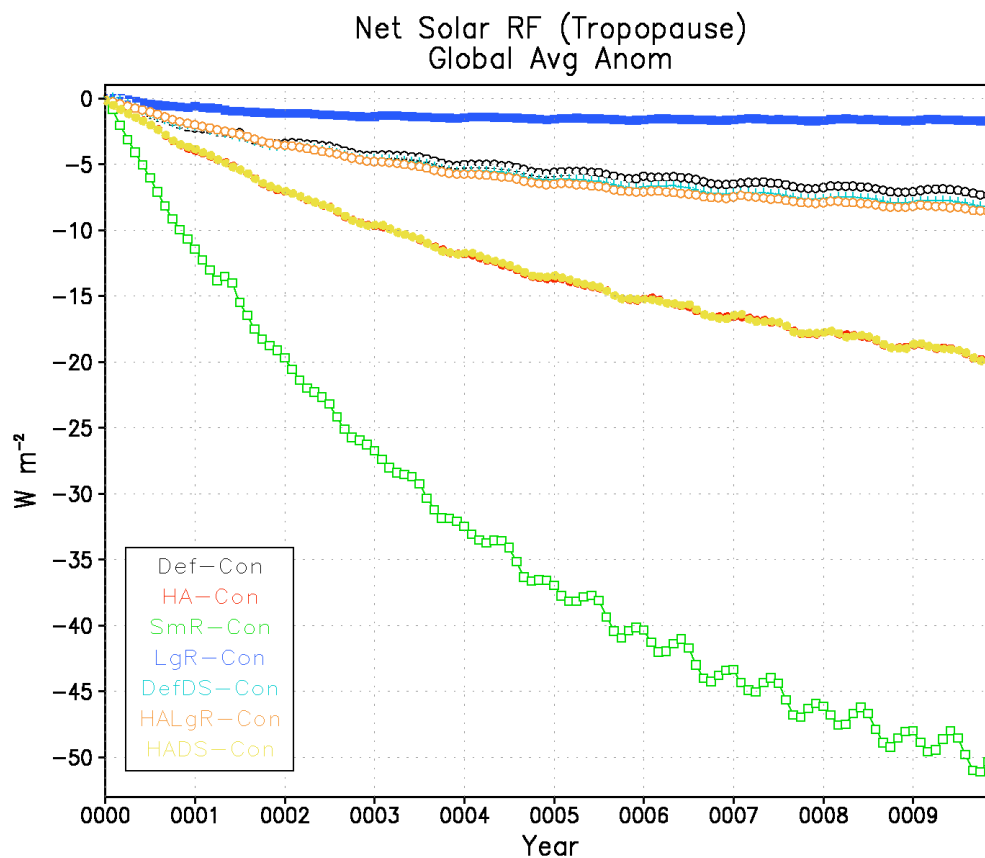
FIGURE 5.12. Globally averaged net solar radiative forcing anomaly at the tropopause for each of the geoengineering ensembles. Ensemble descriptions are given in Table 3.1.
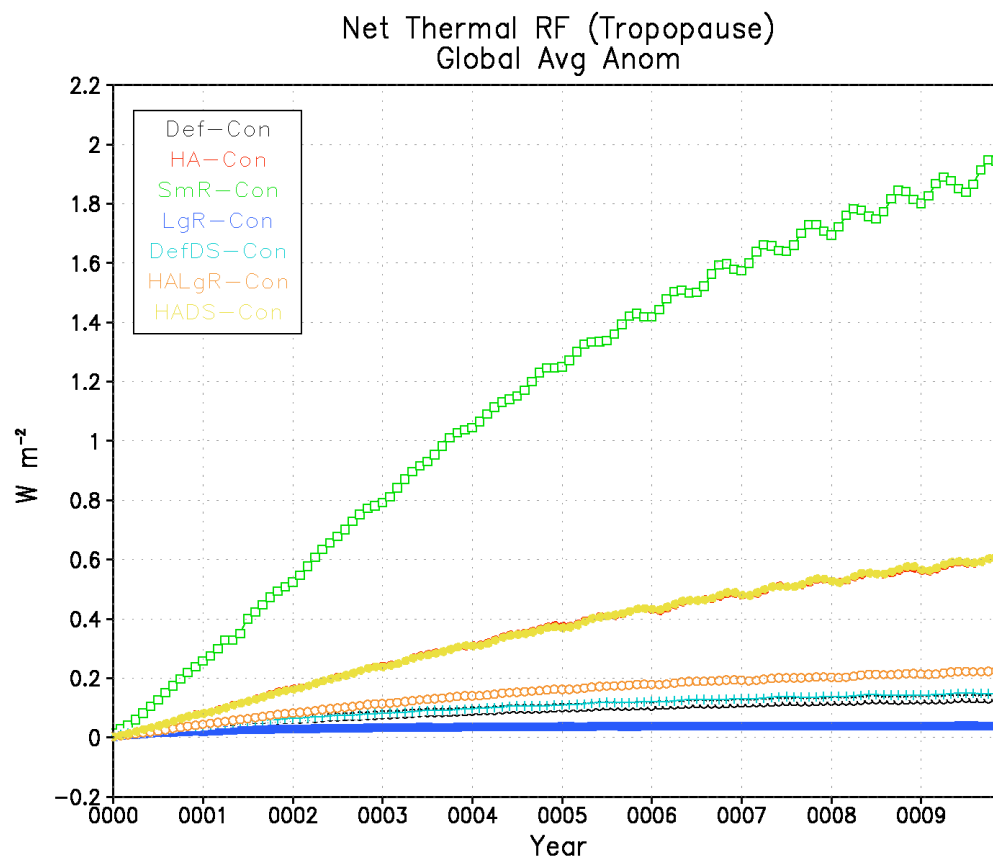
FIGURE 5.13. Globally averaged net thermal radiative forcing anomaly at the tropopause for each of the geoengineering ensembles. Ensemble descriptions are given in Table 3.1.
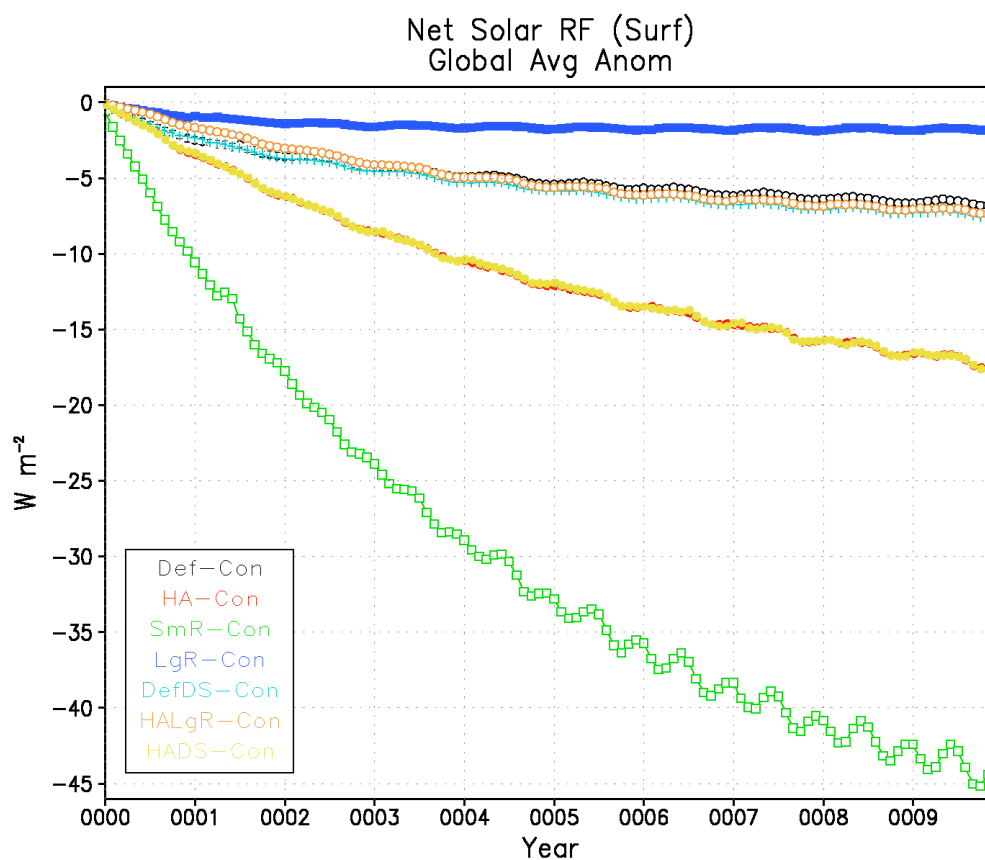
FIGURE 5.14. Globally averaged net solar radiative forcing anomaly at the surface for each of the geoengineering ensembles. Ensemble descriptions are given in Table 3.1.
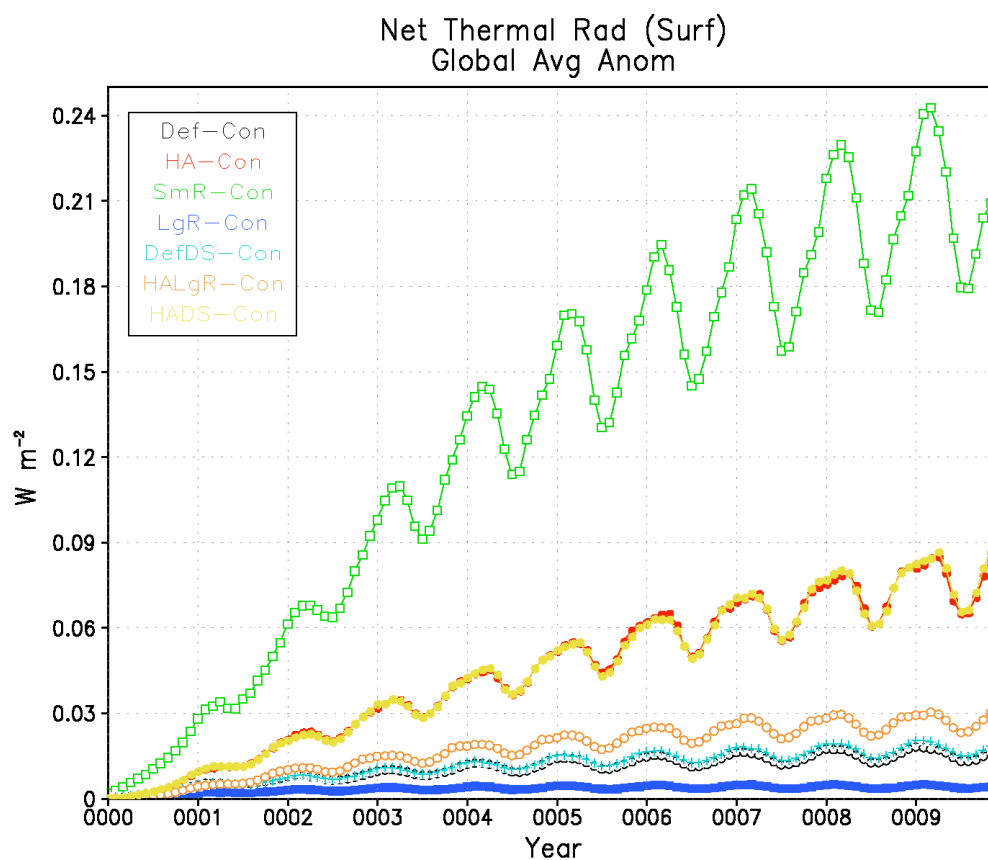
FIGURE 5.15. Globally averaged net thermal radiative forcing anomaly at the surface for each of the geoengineering ensembles. Ensemble descriptions are given in Table 3.1.
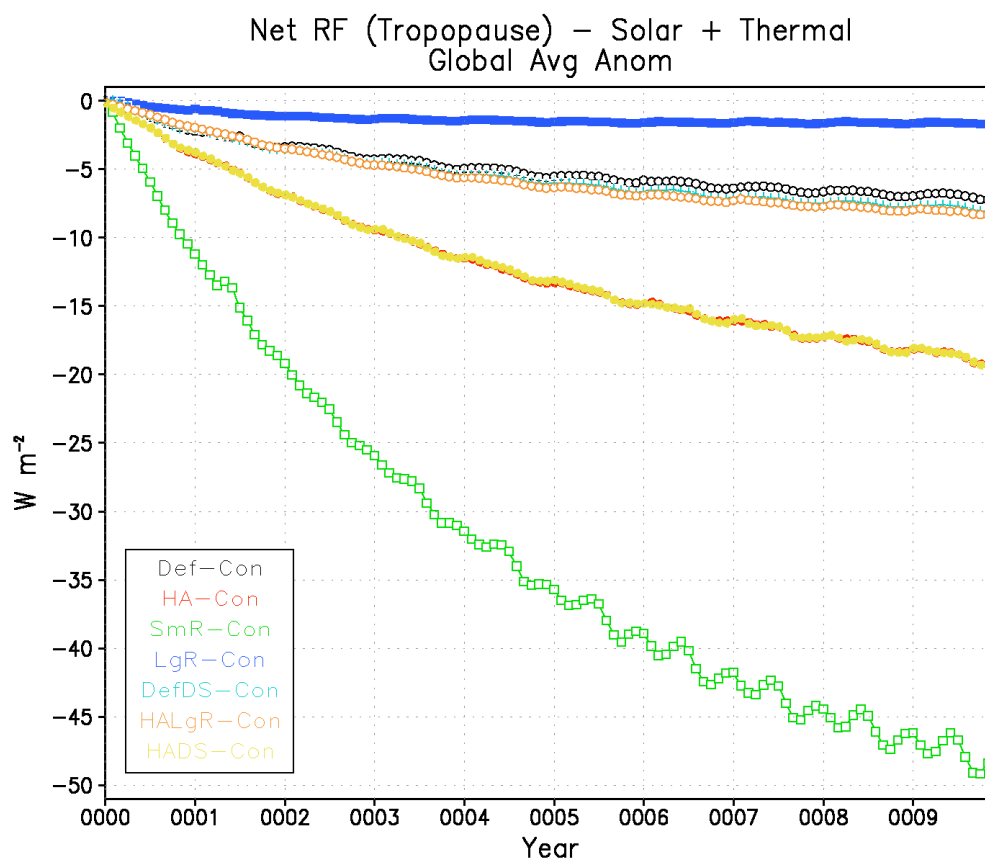
FIGURE 5.16. Globally averaged net total (solar plus thermal) radiative forcing anomaly at the tropopause for each of the geoengineering ensembles. Ensemble descriptions are given in Table 3.1.
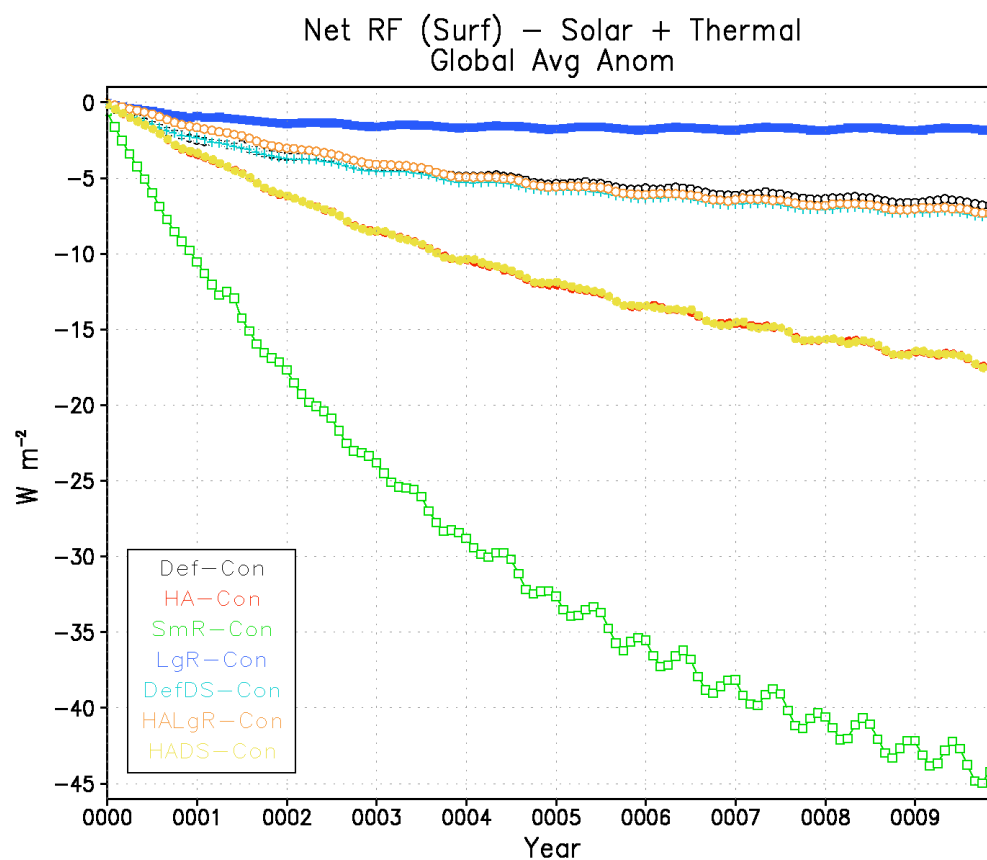
FIGURE 5.17. Globally averaged net total (solar plus thermal) radiative forcing anomaly at the surface for each of the geoengineering ensembles. Ensemble descriptions are given in Table 3.1.

Figure 5.18 shows black carbon aerosol optical depth anomalies in the visible spectrum due to geoengineering. These results look similar to the radiation and radiative forcing plots. The largest optical depth anomaly is 0.27, which is for ensemble SmR in the tenth year of simulations. This is nearly three times larger than the next nearest ensemble, which shows that smaller particles are much more radiatively efficient. The difference between an optical depth of 0.27 and the next nearest value of 0.1 is an additional attenuation of approximately 14.2% of incoming radiation, or ~48.5 W m^{-2} using an average value of 342 W m^{-2}. This is approximately the difference between the SmR and HA curves in Figure 5.5, which shows solar radiation anomalies at the tropopause.

Figure 5.19 shows the same but in a zonal average. LgR shows no optical depth values above 0.025, whereas SmR shows point values exceeding 0.25, mostly in the mid-latitudes, with some peaks in the polar summers.

5.3 MASS BURDEN AND DEPOSITION

Figure 5.20 shows black carbon mass burden for each of the ensembles. Of all the ensembles, only LgR has reached equilibrium by the end of the ten years of simulation. The high altitude injection cases (HA, HALgR, and HADS) have the greatest atmospheric burdens, which shows the altitude of injection has a strong impact on atmospheric lifetime. However, the particle radius does influence the mass burden, as smaller particles will have lower fall speeds,
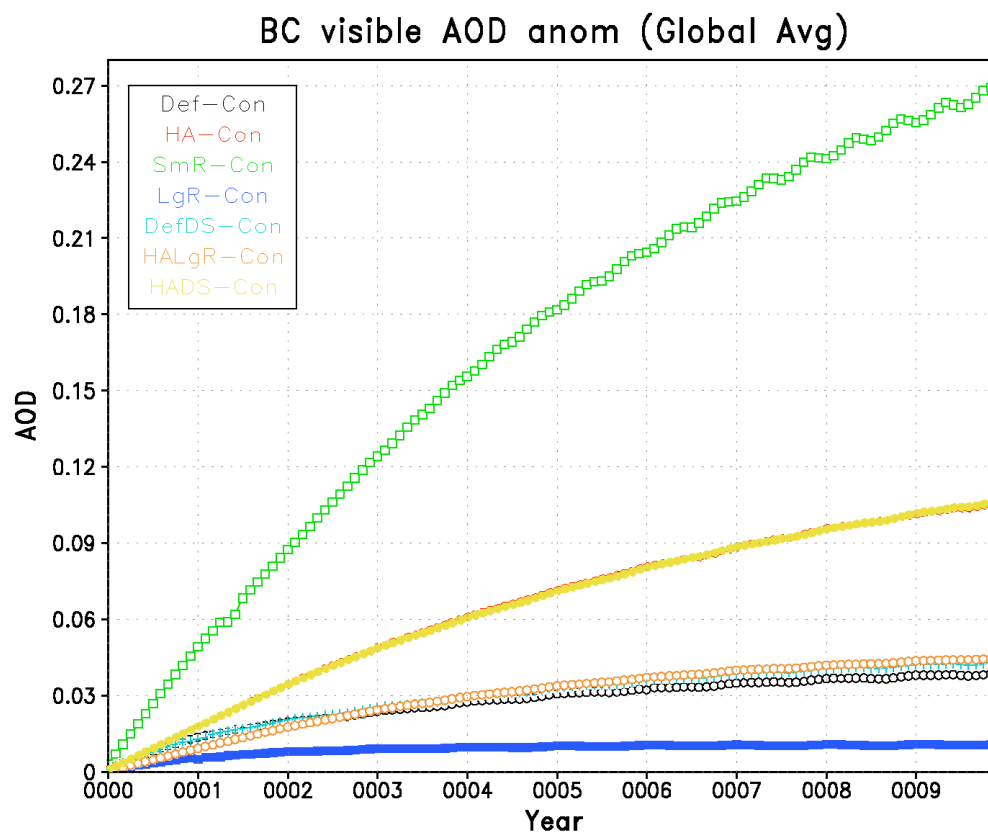
FIGURE 5.18. Globally averaged visible aerosol optical depth anomaly for each of the geoengineering ensembles. Ensemble descriptions are given in Table 3.1.

BC visible AOD anomaly comparison
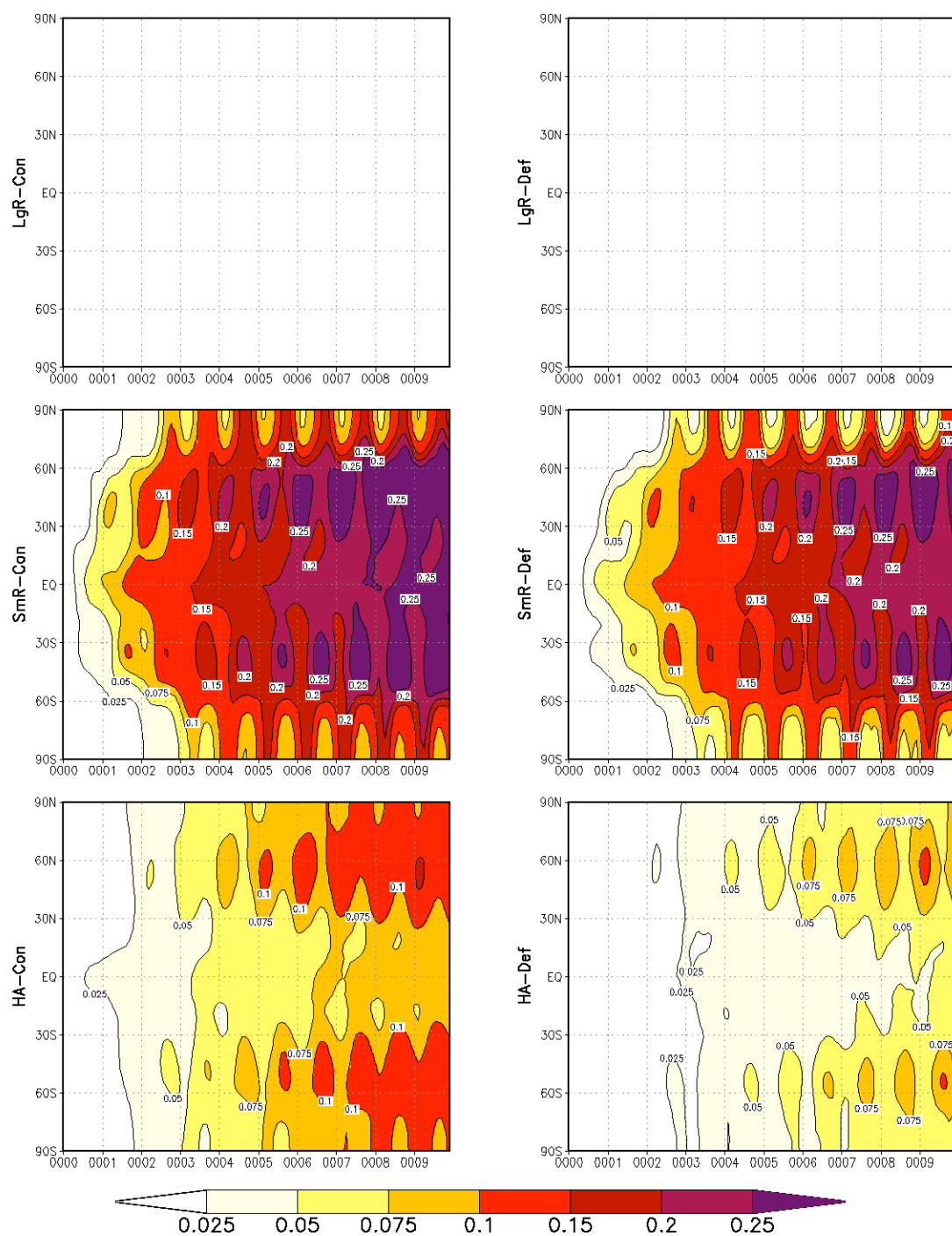
FIGURE 5.19. Zonally averaged aerosol optical depth anomalies for black carbon geoengineering.
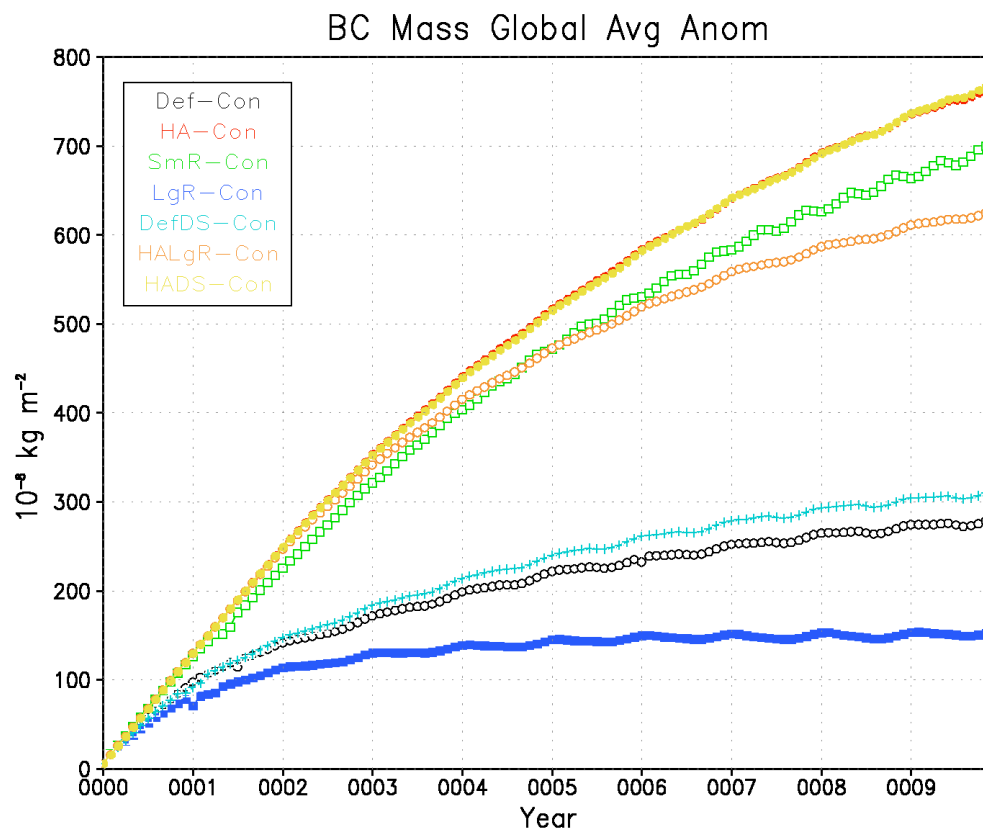
FIGURE 5.20. Globally averaged black carbon mass anomalies for each of the geoengineering ensembles. Ensemble descriptions are given in Table 3.1. Equilibrium mass burden and atmospheric lifetimes are given in Table 5.1.

allowing the aerosol layer to accumulate mass, as is seen for SmR. Comparing

ensembles HA and HALgR, which only differ by particle radius, the larger

particles have a higher fall speed, so their mass burden is less than for the smaller

particles.

Using the formula in Section A.1, we extrapolate the lines in Figure 5.20 to

calculate equilibrium atmospheric mass burden and lifetime, the results of which

are in Table 5.1. Ensemble LgR has an *e*-folding lifetime of 0.75 years, which is

less than the lifetime for large volcanic eruptions [e.g., *Robock*, 2000] and for the

Robock et al. [2008] simulations of tropical stratospheric sulfate aerosol

geoengineering. The largest atmospheric *e*-folding lifetime of 4.26 years is seen

in ensembles HA and HADS. With the exception of SmR, none of the low

altitude injections has an atmospheric mass burden of greater than 1.55 Tg, and

none of the high altitude injections has a mass burden of less than 3.31 Tg, which

is over twice the value for the low altitude cases. Therefore, we conclude that

with the exception of small particles, the altitude of injection is the most

important factor we tested that will determine atmospheric mass burden and

atmospheric lifetime of the aerosol particles.

Figure 5.21 shows the globally averaged mass burden as a function of

height. LgR shows little mass burden and very little self lofting, with most of the

aerosols confined to the altitudes of injection. SmR shows a greater degree of

self-lofting than HA, but the total mass burden is lower. This is likely due to the

greater radiative efficiency of the small particles, allowing for more heating by

the sun. Also, it appears a large portion of the aerosols stay near the altitude of

TABLE 5.1. Black carbon mass and atmospheric lifetime for each geoengineering ensemble. Values in column two are obtained from Figure 5.20. Values in column three are obtained by multiplying the values in column two by the surface area of Earth (5×10^{14} m^2) and using the mass balance equation in Section A.1.

Ensemble	Year 10: 10^{-8} kg m^{-2} (from Figure 5.20)	Equilibrium mass burden (Tg) and *e*-folding atmospheric lifetime (years)
Def	280	1.40
HA	770	4.26
SmR	700	3.77
LgR	150	0.75
DefDS	310	1.55
HALgR	630	3.31
HADS	770	4.26

$$10^{-11} \text{ kg BC / kg air}$$
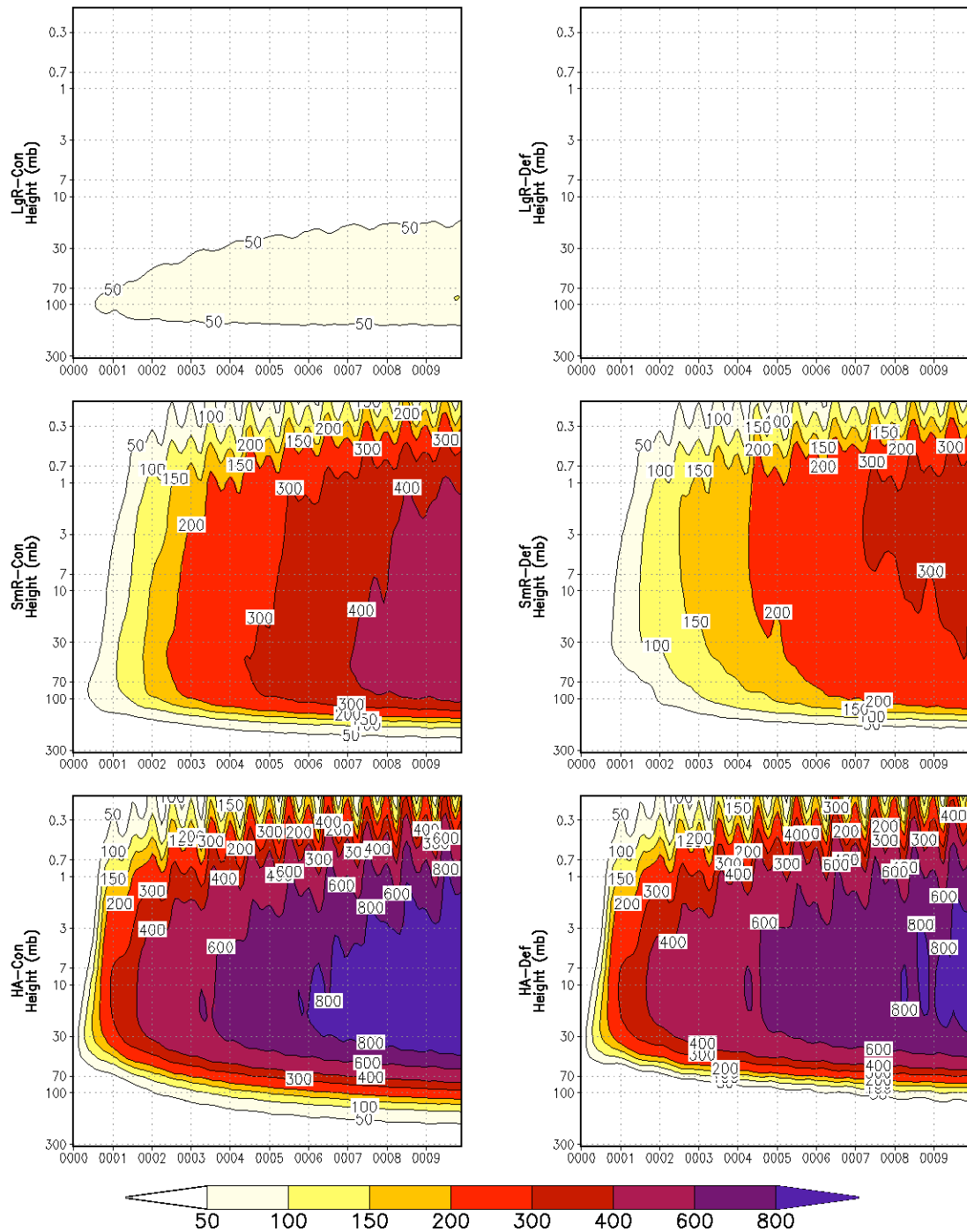
FIGURE 5.21. Globally averaged black carbon mass anomalies as a function of height for black carbon geoengineering.

injection, so the small radius particles, which were injected at a lower altitude, have a better chance of passing into the troposphere. Indeed, Figure 5.22 shows that SmR has higher deposition rates in winter for each hemisphere than HA, at times showing one of the highest deposition rates of all ensembles and certainly the largest seasonal variability of all ensembles. LgR still shows the largest average deposition, as the combination of large particles and a low altitude of injection will promote a low atmospheric lifetime. With the exception of SmR, which shows a high seasonal variability, the deposition curves can be divided into two distinct groups, with the low altitude injection scenarios having a higher deposition rate than the high altitude injection experiments.

Figures 5.23-5.25 show spatial maps of annual deposition rates for LgR, SmR, and HA, respectively. Figure 5.23 shows that the large aerosols are mostly deposited in the mid-latitude storm tracks. However, unusually, the small aerosols (Figure 5.24) are removed during the winter over the poles as wet deposition. This phenomenon is also seen, albeit to a lesser degree, in the high altitude case (Figure 5.25), which was discussed in Section 4.2. Again, we believe this is due to the introduction of a strong Arctic polar vortex, as was described in Section 4.3.

5.4 STRATOSPHERIC HEATING

As we discussed in Section 4.3, geoengineering with black carbon aerosols will cause stratospheric heating. However, the degree of heating, as well as the
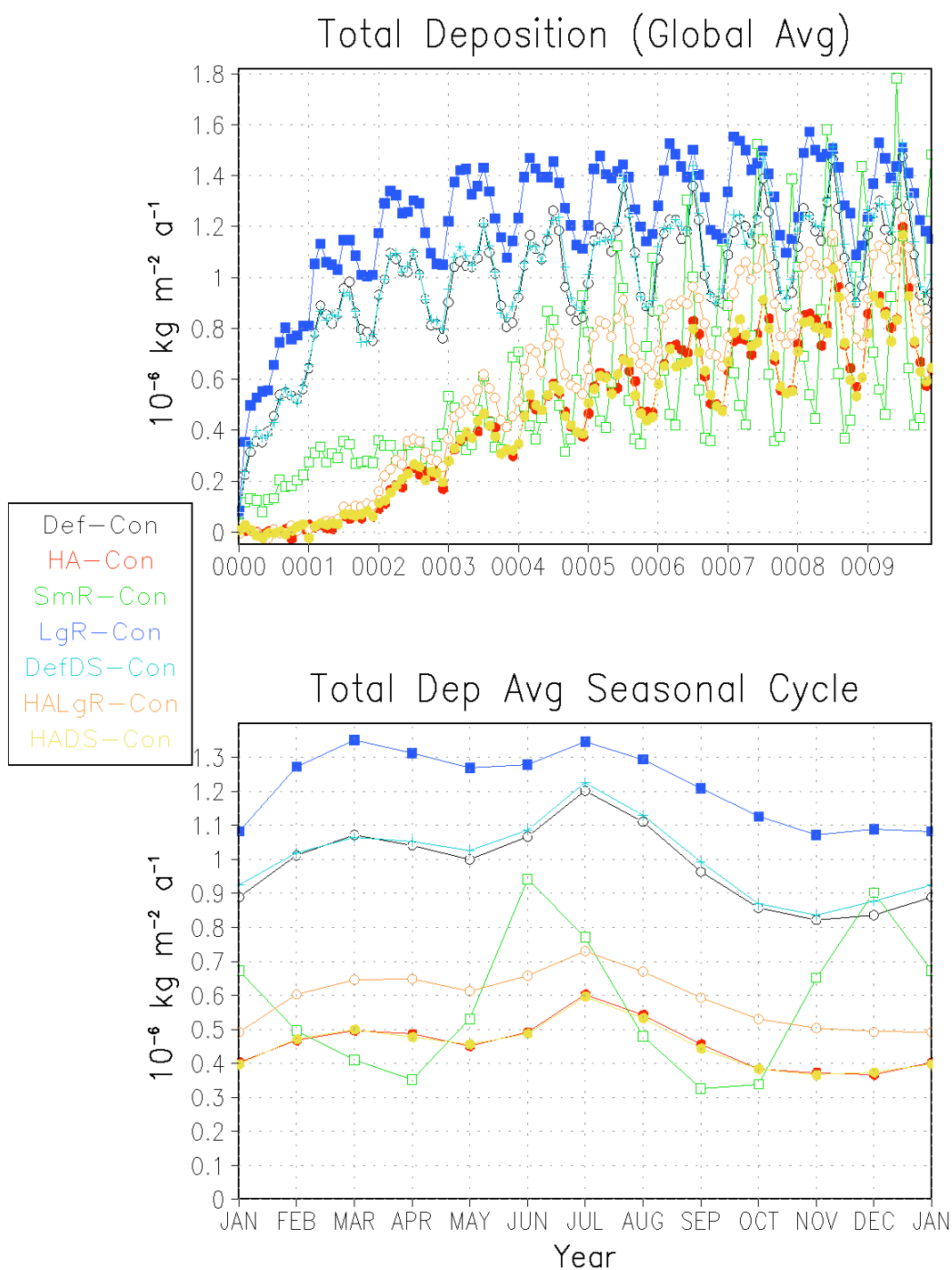
FIGURE 5.22. Globally averaged annual deposition rate and ten year average seasonal cycle anomalies for each of the geoengineering ensembles. Ensemble descriptions are given in Table 3.1.

Deposition Anom (10⁻⁸ kg m⁻² a⁻¹)
Increased Radius (avg last 3 years)
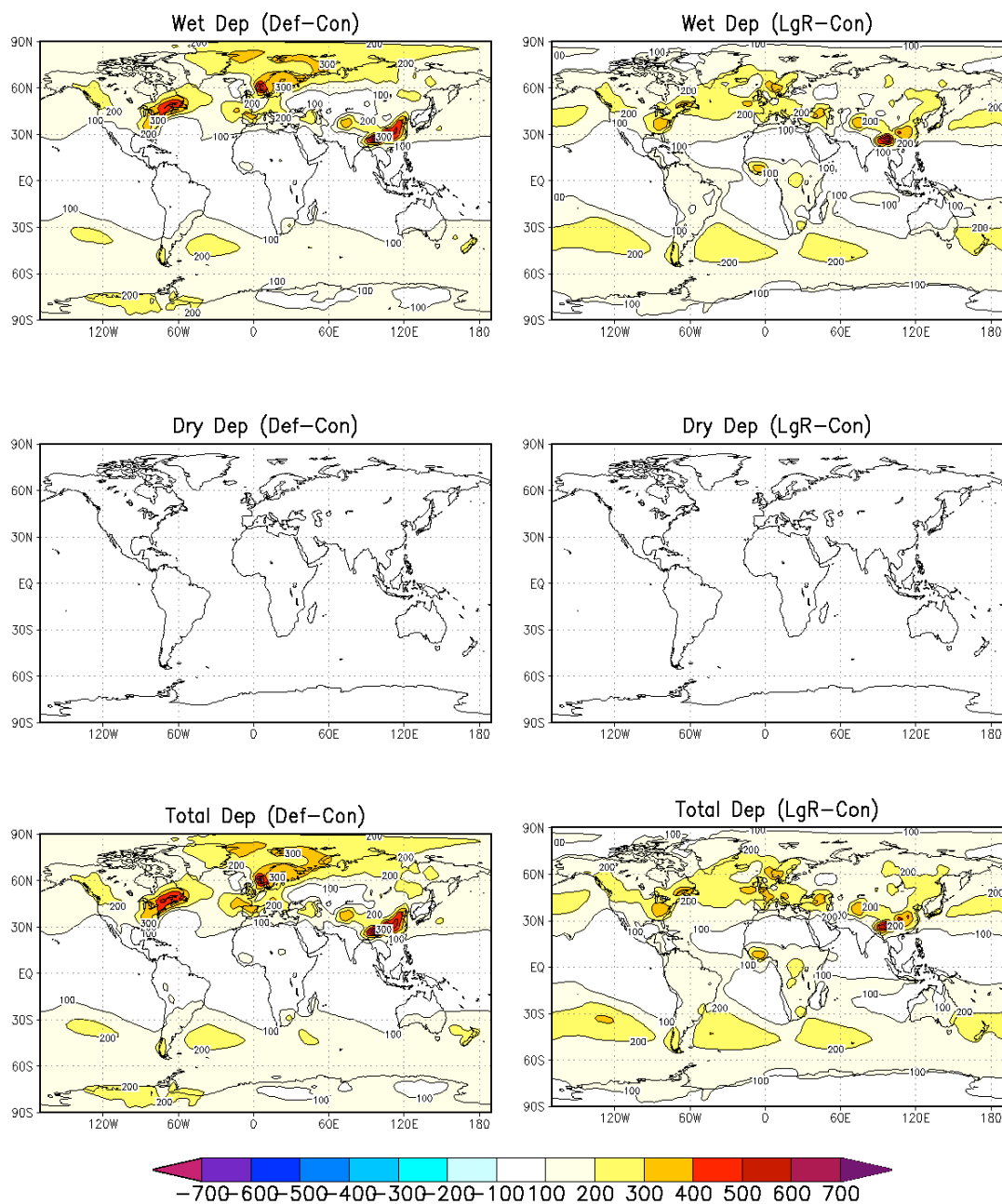
FIGURE 5.23. Wet, dry, and total deposition comparisons for Def and LgR, averaged over the last three years of simulation. Ensemble descriptions are given in Table 3.1. Total deposition is the sum of wet and dry deposition.
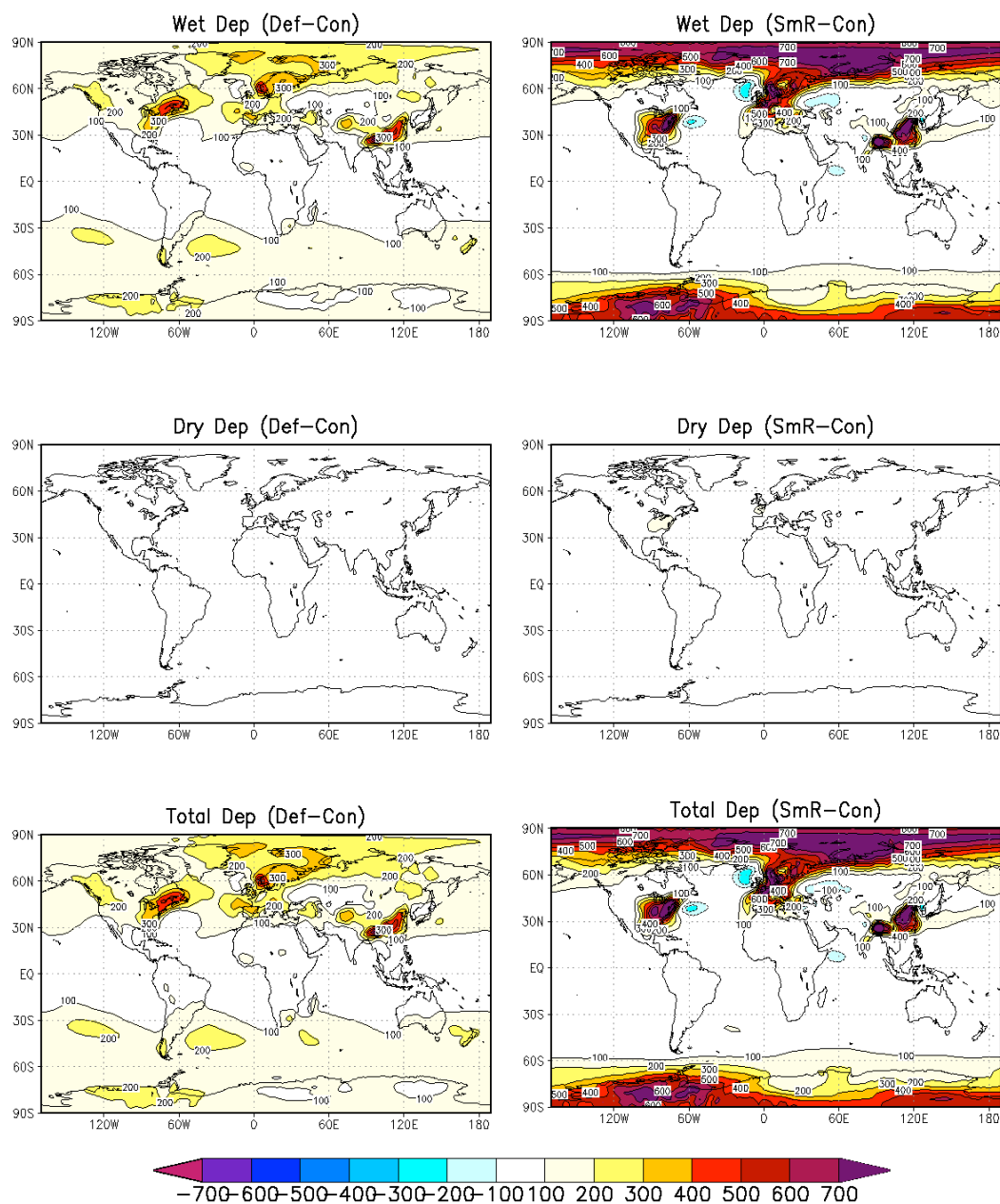
FIGURE 5.24. Wet, dry, and total deposition comparisons for Def and SmR, averaged over the last three years of simulation. Ensemble descriptions are given in Table 3.1. Total deposition is the sum of wet and dry deposition.

FIGURE 5.25. Wet, dry, and total deposition comparisons for Def and HA, averaged over the last three years of simulation. Ensemble descriptions are given in Table 3.1. Total deposition is the sum of wet and dry deposition.

resulting consequences we detailed in that section, depend upon the geoengineering parameters. Figure 5.26 shows a vertical profile of stratospheric heating that would result from geoengineering. In LgR, the stratospheric heating is comparatively modest, rarely exceeding 5°C and even then only in the immediate vicinity of the injection altitudes. LgR actually causes less warming than Def (top right panel), and certainly much less than HA, as is seen in the bottom panels and in Section 4.3. SmR shows a large degree of stratospheric heating, with point values in this figure of up to 80°C. Although the heating is concentrated around the altitude of injection, positive temperature anomalies of at least 5°C extend up to the stratopause (~1 mb). This is in contrast to the high altitude injections, in which positive temperature anomalies extended through the mesosphere up to the model top. Also, the seasonal cycle of mesospheric temperature anomalies is dampened in the small radius case compared to the high altitude case. In fact, the mesospheric temperature anomalies SmR are negative, sometimes exceeding -20°C.

To further assess the mechanisms at play, Figure 5.27 shows plots of the vertical profile of temperature, averaged over the last three years of simulation. All of the ensembles show a warming of the stratosphere and a lowering of the tropopause, reversing recent trends which have been attributed to anthropogenic warming [*Santer et al.*, 2003]. In all cases, the lower and middle stratosphere become less stable, and for the high altitude and small radius cases, the middle and upper stratosphere also become less stable. In SmR, the stratospheric lapse rate is reduced so much that the middle stratosphere becomes unstable, which

Temperature Comparison (°C)
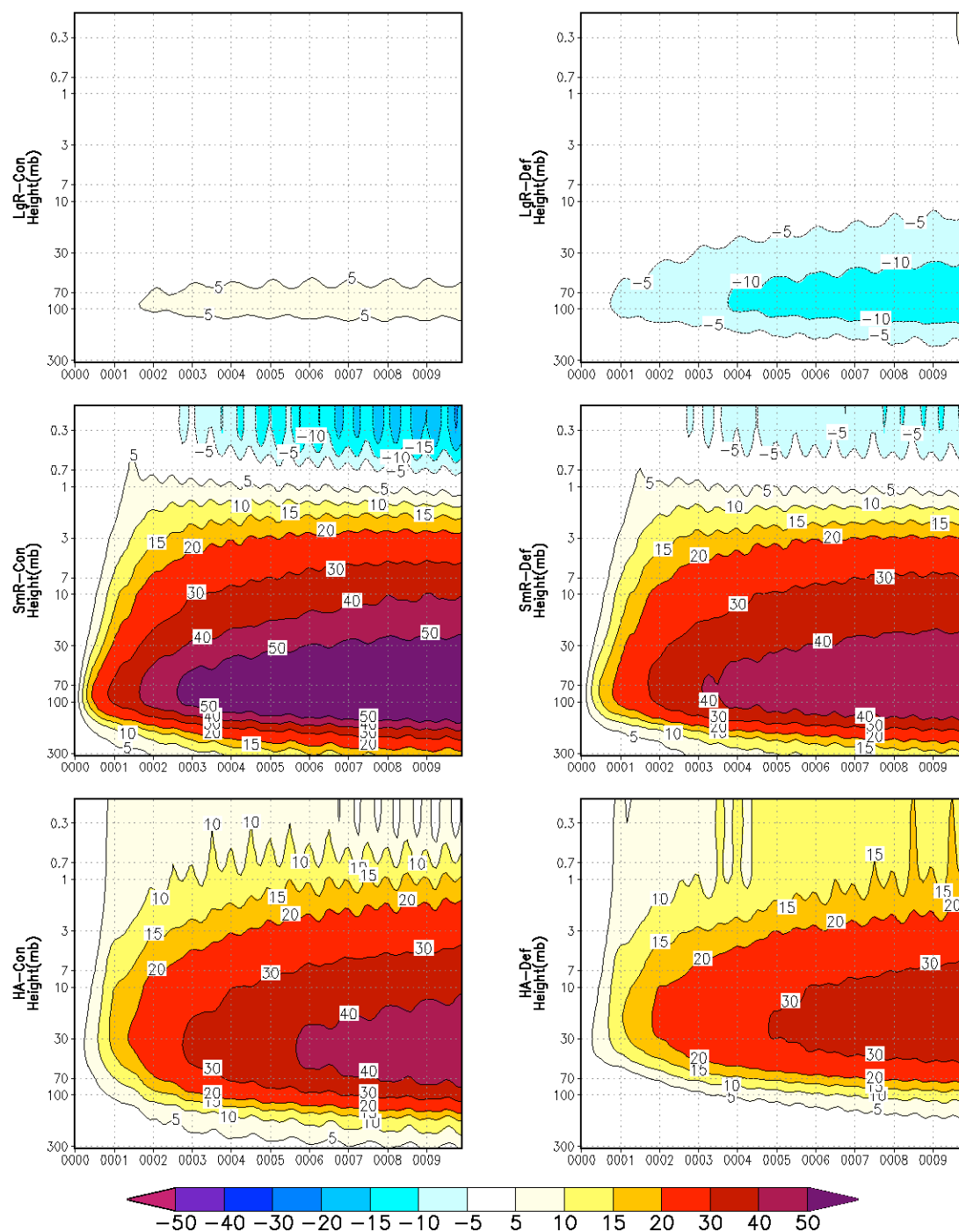
FIGURE 5.26. Stratospheric heating anomalies for black carbon geoengineering. Temperature anomalies are global averages as a function of height.
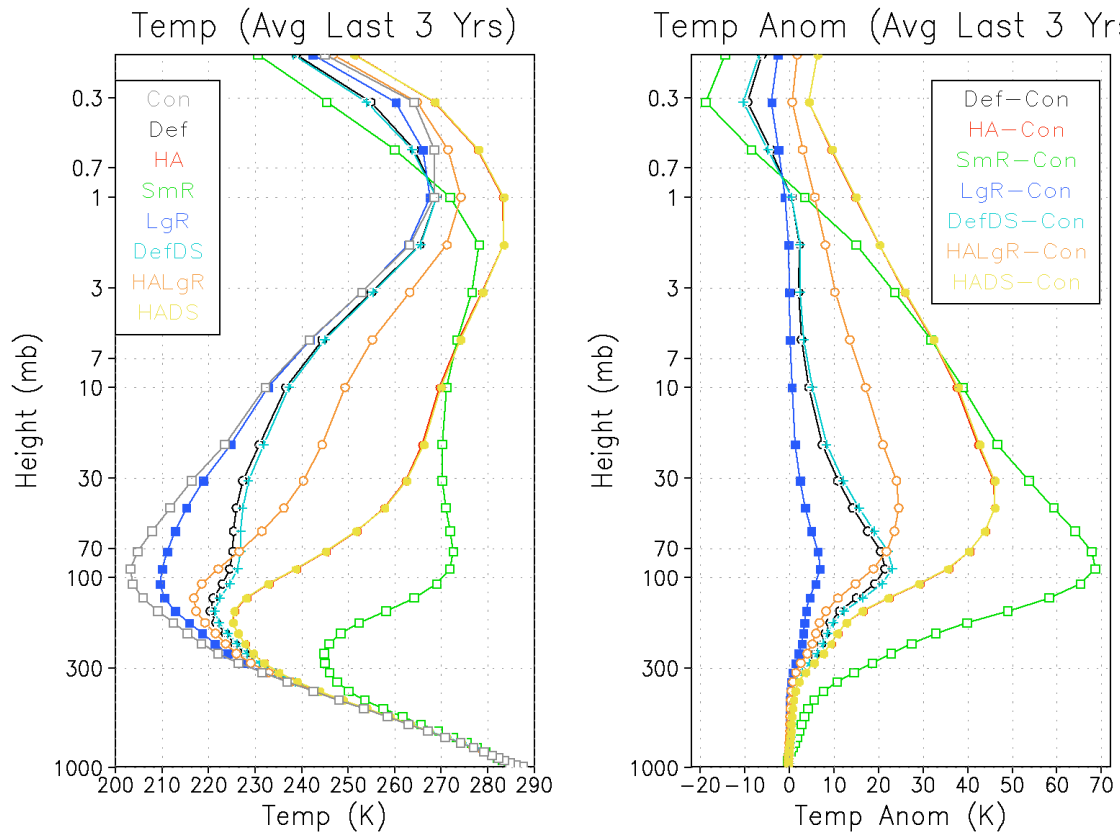
FIGURE 5.27. Vertical temperature profiles for all geoengineering ensembles. The left panel shows actual temperatures, and the right panel shows temperature anomalies. Ensemble descriptions are given in Table 3.1.

could further promote lofting of the black carbon aerosols. The mesospheric cooling seen in the middle panels of Figure 5.26 is due to a lowering of the stratopause in SmR, the only ensemble in which this occurs. With the exception of SmR, all of the ensembles show some degree of mesospheric warming, which appears to be due to stratospheric warming due to the aerosols but little to no change in the stratopause height.

The height of the stratopause is determined by an equilibrium balance between cooling due to thermal radiation of the planet to space and warming due to ultraviolet absorption by the ozone layer. As we saw in Section 4.3, black carbon geoengineering causes large amounts of ozone destruction, which should lower the stratopause. However, the introduction of absorbing aerosols into the stratosphere cause heating, as we saw in Figure 5.26, which could raise the stratopause in compensation, resulting in no net change in stratopause height. Additionally, we could expect that ozone destruction in SmR is so severe that this compensation is uneven, resulting in a lower stratopause. It is difficult to diagnose the exact mechanisms without knowledge of the local heating rates, which are not provided as output from this version of ModelE. We further address these ideas in Section 7.6. However, we can analyze the degree of ozone destruction caused by black carbon geoengineering.

Figure 5.28 shows globally averaged total column ozone anomalies for each ensemble. As predicted, ozone loss is significant for SmR, reaching nearly 50%. Def and DefDS actually show a slight increase in total column ozone, although the increase is modest, being less than 5% and only in the austral
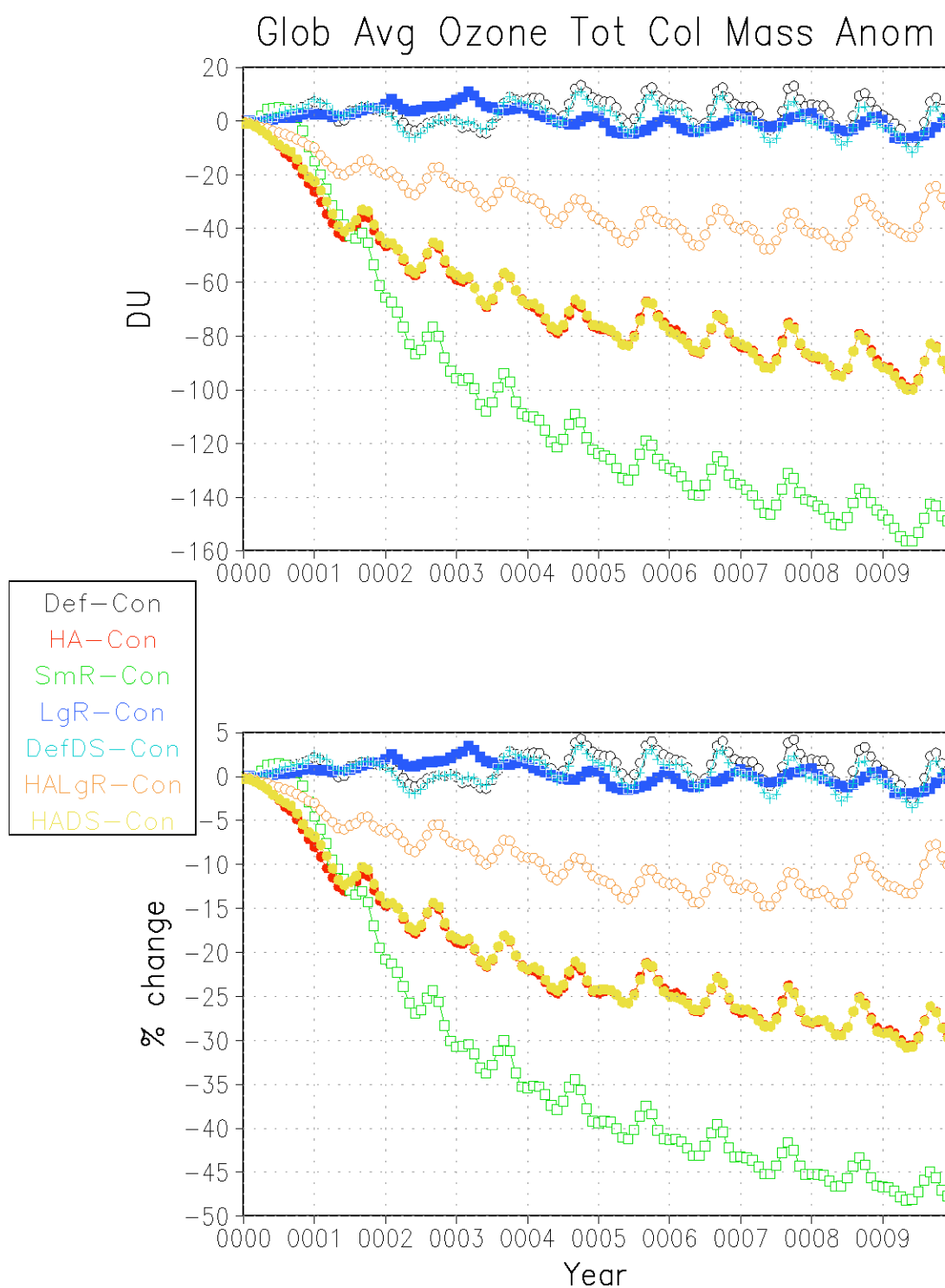
FIGURE 5.28. Globally averaged ozone total column mass for each of the geoengineering ensembles. Ensemble descriptions are given in Table 3.1.

spring. Figure 5.29 shows the same for three of the ensembles but with vertical resolution. LgR shows very small reductions in ozone in the upper troposphere with compensation below (as discussed in Section 4.3), resulting in little to no net ozone change. SmR shows a catastrophic reduction of the ozone layer, far greater than for HA, which we addressed in Section 4.3. The lower altitude compensation mechanisms are also in play, although they occur in the upper troposphere, unlike HA in which the compensation occurs in the lower stratosphere. The greatest percentage loss of ozone in SmR is in the mesosphere, but absolute amounts of ozone at this height are so small that this loss is practically negligible. However, there is still over 50% loss in the stratospheric ozone layer for this experiment.

Evaluating the same field but spatially, Figure 5.30 shows zonally averaged ozone anomalies as a function of height, averaged over the last three years of simulation. All three ensembles shown have a large percentage increase in ozone in the tropical lower stratosphere. HA and SmR show relatively uniform reductions in ozone throughout the middle stratosphere. Ozone loss is greatly enhanced over Antarctica, which is likely mostly due to temperature catalyzed ozone destruction, although other factors may play a potentially significant role. The impacts could potentially be different if we had chosen a later year, which would result in a large reduction in CFC concentrations, but this will require further investigation. Also, as in Section 4.3, SmR causes the introduction of an Arctic ozone hole, showing an even greater ozone loss than for HA.

Ozone Comparison (% change)
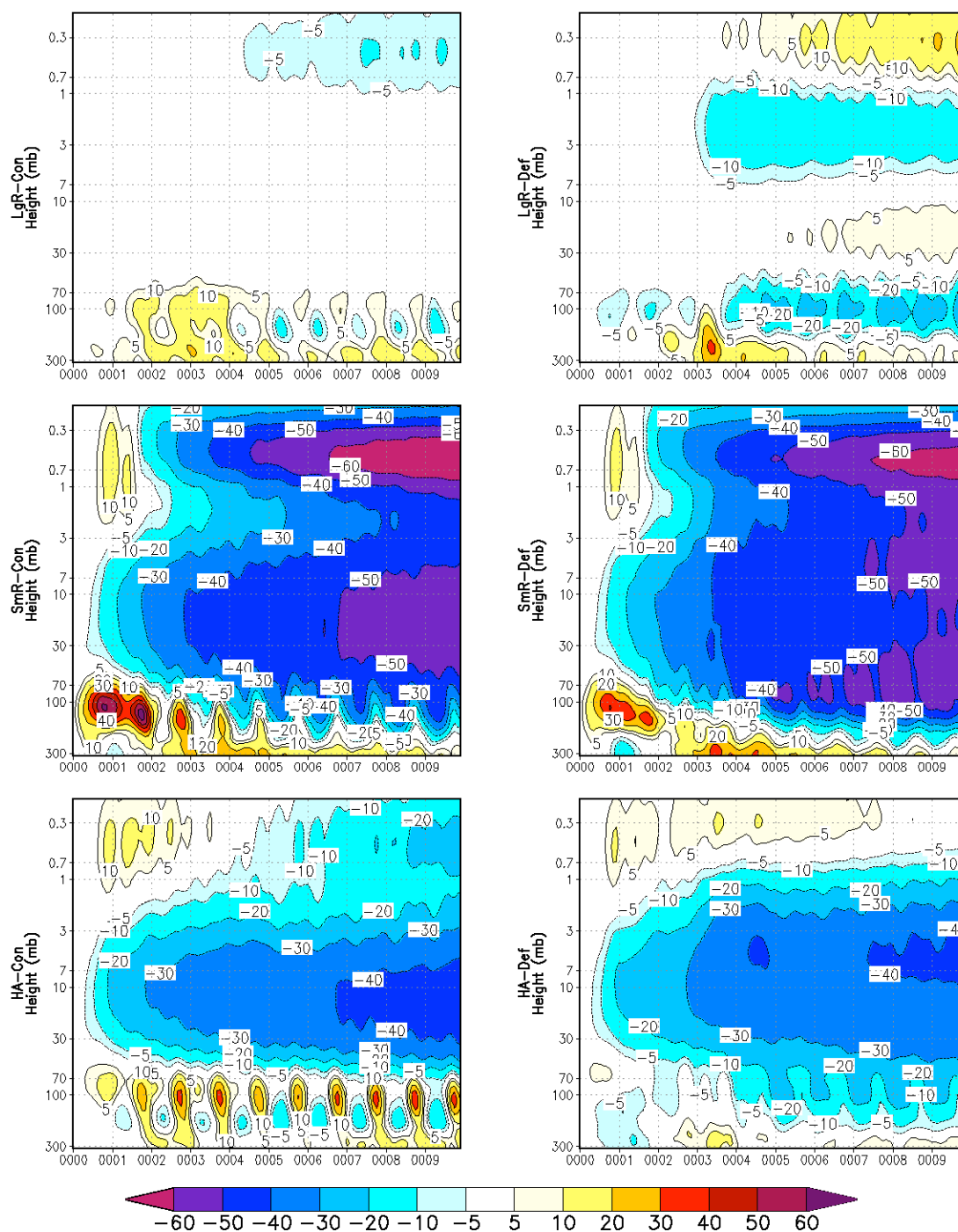
FIGURE 5.29. Stratospheric ozone anomalies for black carbon geoengineering.

Anomalies are global averages as a function of height.
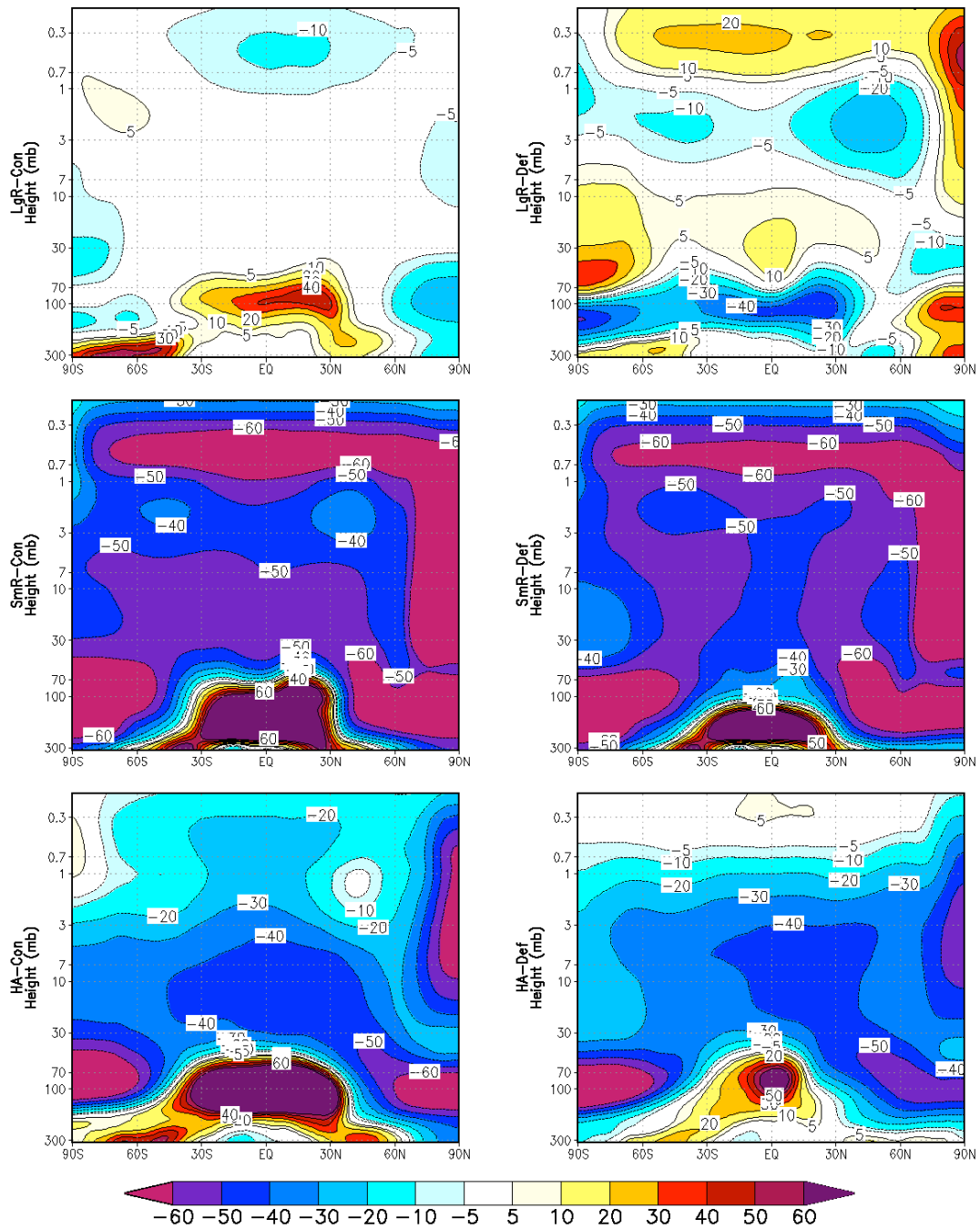
FIGURE 5.30. Stratospheric ozone anomalies for black carbon geoengineering. Anomalies are zonal averages as a function of height, averaged over the last three years of simulation.

We expect the same mechanisms that cause the Arctic ozone hole, as discussed in Section 4.3, to occur in SmR, but magnified. Therefore, we expect to see strengthening of the zonal wind anomalies for this ensemble, which does occur (Figures 5.31-5.32). Additionally, we also expect to see a strong positive mode of the Arctic Oscillation, as in Figure 5.33. In both of these figures, the anomalies shown are statistically significant at the 95% confidence level. LgR does not show the formation of an Arctic ozone hole, so we would not expect a large positive anomaly in the zonal wind, nor would we expect sea level pressure patterns that show a positive mode of the Arctic Oscillation for this ensemble, and indeed, the results support our suspicions.

One additional consequence of large stratospheric heating is the resulting warming of the troposphere due to longwave emission from the aerosol layer. Figure 5.34 shows the same field as Figure 5.26, but with the vertical extent of the plots changed to emphasize tropospheric warming. Even LgR, which shows very few climate effects, has some degree of tropospheric warming, reaching above 0.25°C below the 300 mb isobar. Ensemble SmR shows large amounts of warming, often extending into the planetary boundary layer. This also explains the localized warm spot in Figure 5.2 over the Tibetan Plateau that resulted from this experiment. The Tibetan Plateau has elevations reaching 5.7 km [*Zhisheng et al.*, 2001], which is roughly 500 mb, assuming an atmospheric scale height of 8 km. According to Figure 5.33, land masses at this height will show at least 1°C of warming by year ten from the aerosols, and likely more due to the low heat
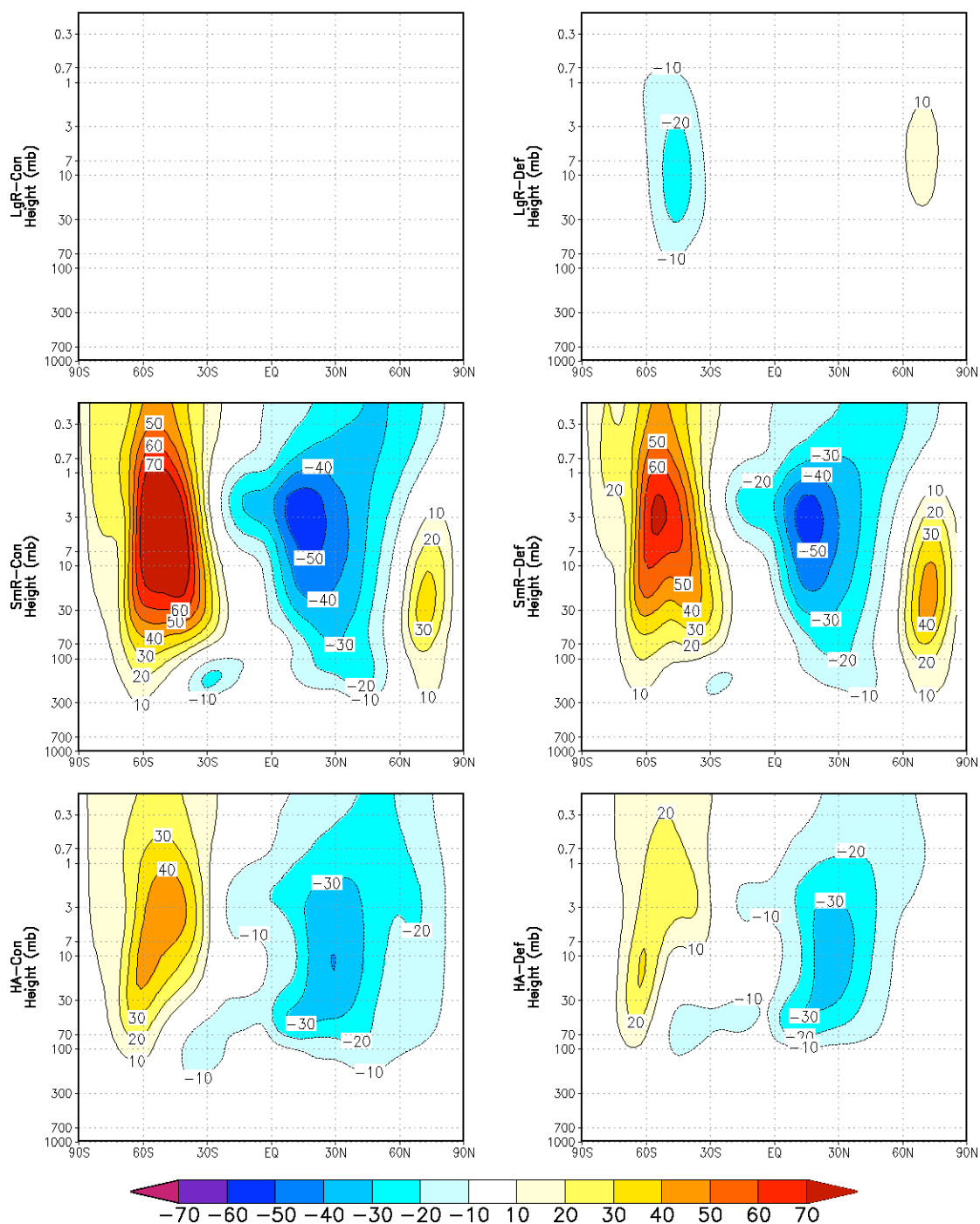
FIGURE 5.31. JJA zonal wind anomalies for black carbon geoengineering.

Values shown are averaged over the last three years of simulation.
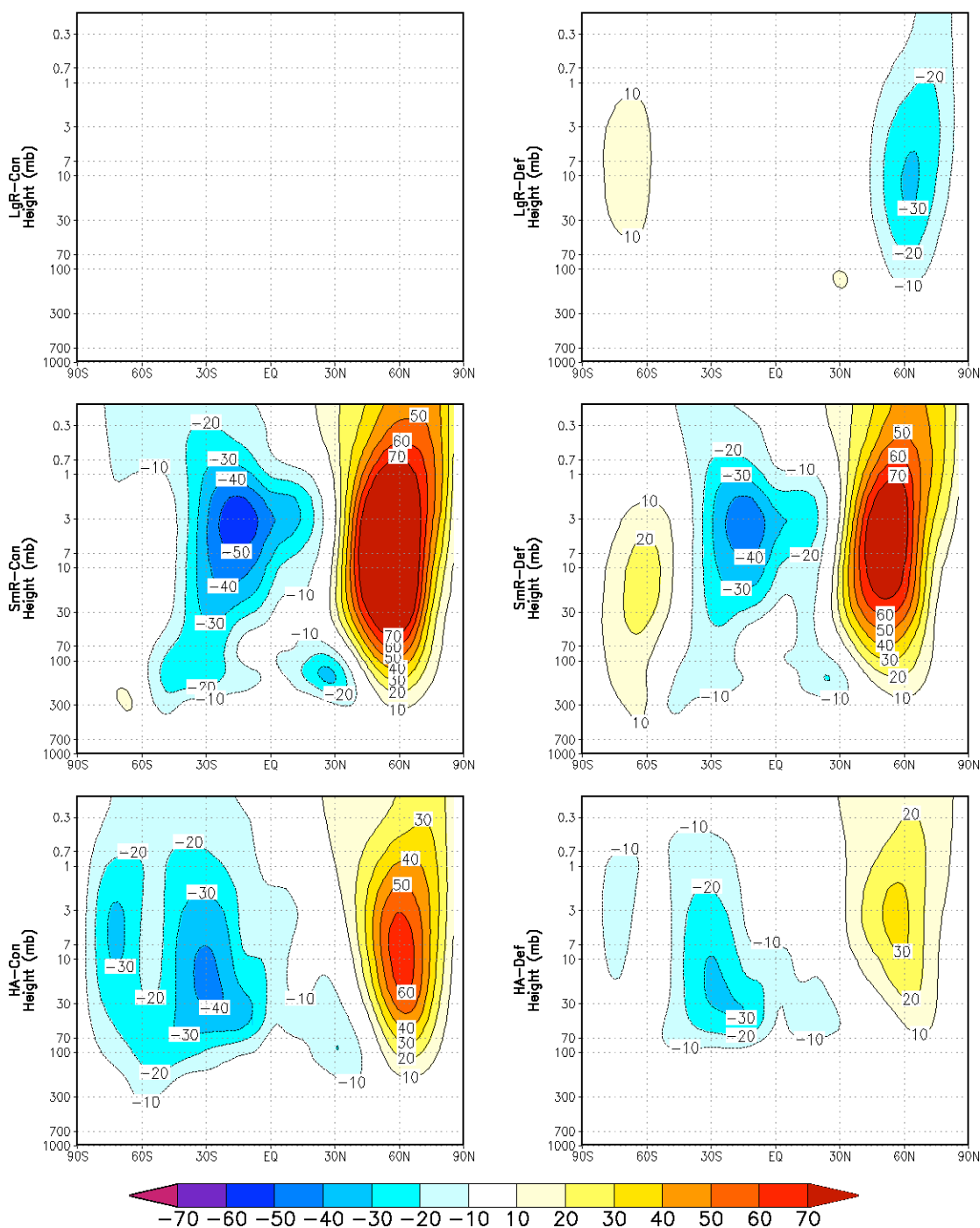
FIGURE 5.32. DJF zonal wind anomalies for black carbon geoengineering.

Values shown are averaged over the last three years of simulation.

SLP Anom (mb) — Avg Last 3 Yrs
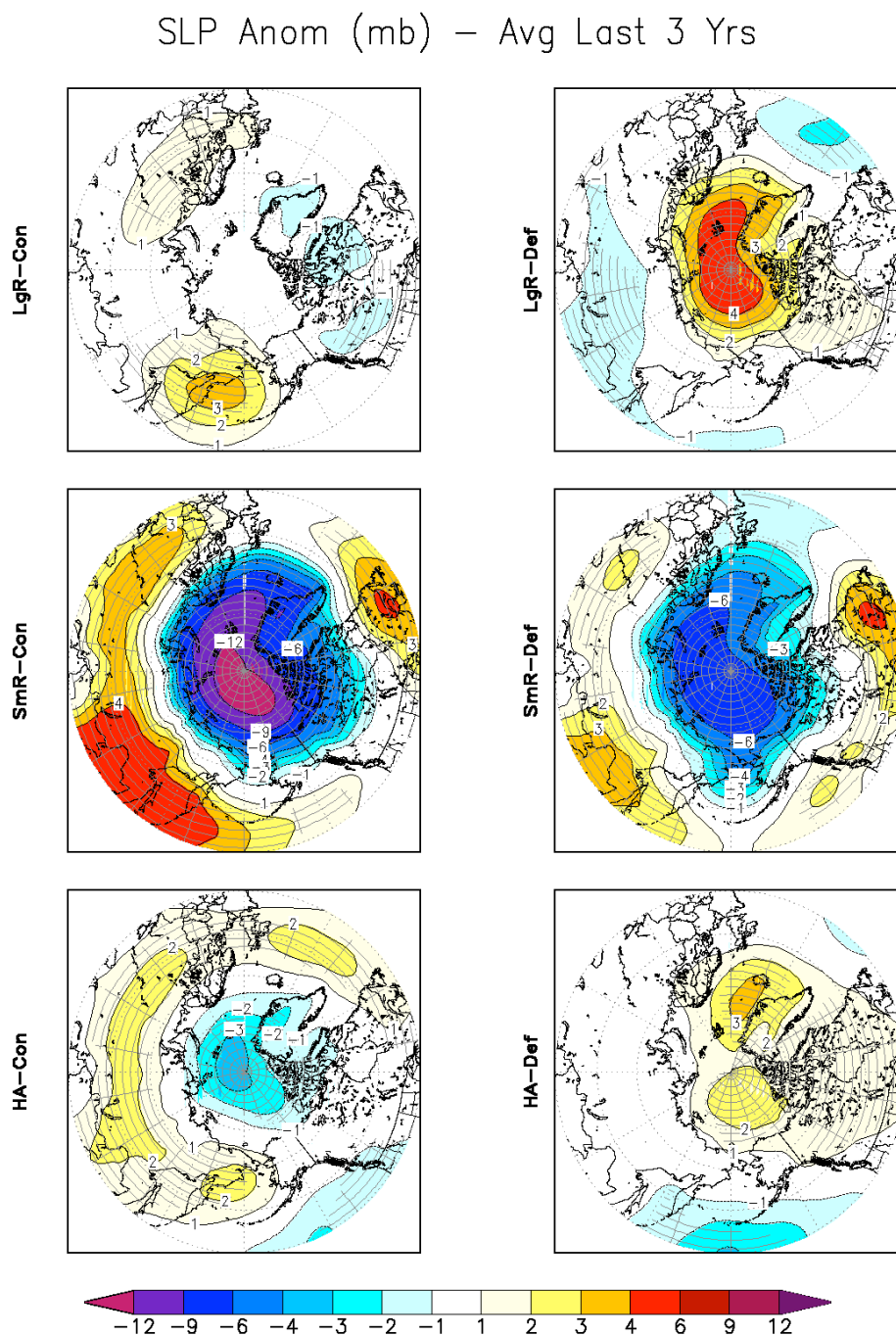
FIGURE 5.33. Sea level pressure anomalies for black carbon geoengineering, averaged over the last three years of simulation. Grey hatching denotes values that are statistically significant at the 95% confidence level as calculated by an unpaired two sample Student's *t* test.
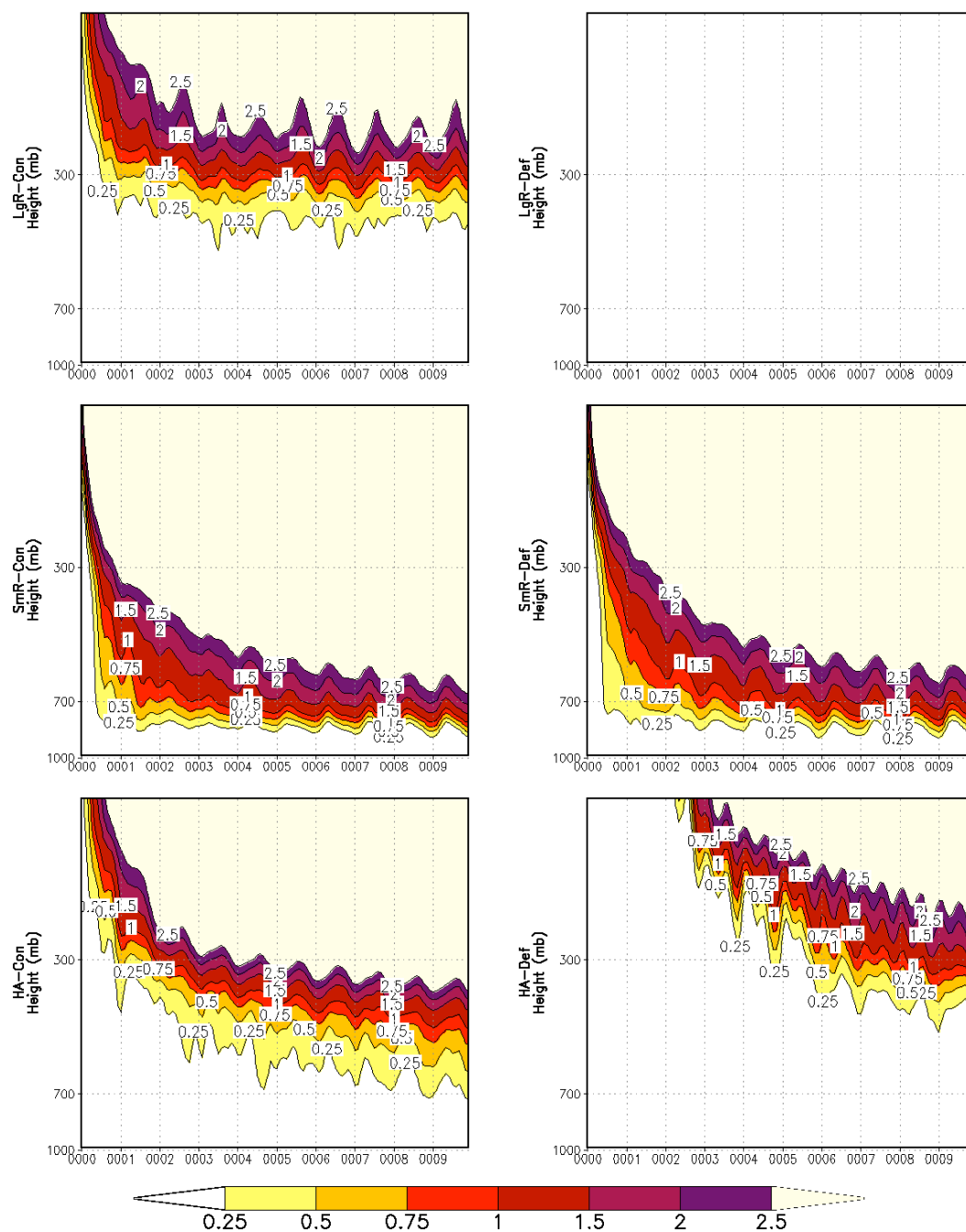
FIGURE 5.34. Tropospheric warming due to longwave emission from the aerosol layer for black carbon geoengineering. Temperature anomalies are global averages as a function of height.

capacity of land. Indeed, Figure 5.2 showed a small area of warming that
exceeded 2°C.

The Tibetan Plateau holds a large portion of the planet's glaciers, which
would certainly undergo catastrophic melting under such large warming
anomalies. Not only would this create a positive feedback causing further
warming, as melting of the glaciers will reduce the albedo of the Tibetan Plateau,
but it would also reduce the available fresh water to all of the population centers
downriver of the plateau, including China and India. In this sense, stratospheric
geoengineering with black carbon would be catastrophic, although much more
analysis is needed to exactly determine the degree of deglaciation and the
resulting impacts.

5.5 HYDROLOGIC CYCLE

As was discussed in Section 4.4, black carbon geoengineering is expected
to cause disturbances to the hydrologic cycle, specifically the summer monsoon
system in India, Africa, and East Asia. However, since this is primarily a
radiative effect, and the radiation plots shown in Section 5.2 were quite variable
between ensembles, we expect the degree of hydrologic cycle disruption to also
strongly depend upon the aerosol parameters chosen. We again note that using
fixed sea surface temperatures likely affected the results we present in this
section, although further investigation is needed to determine the total effects.

Figure 5.35 shows global and land averaged precipitation anomalies for
each ensemble. In the global average, all ensembles show statistically significant
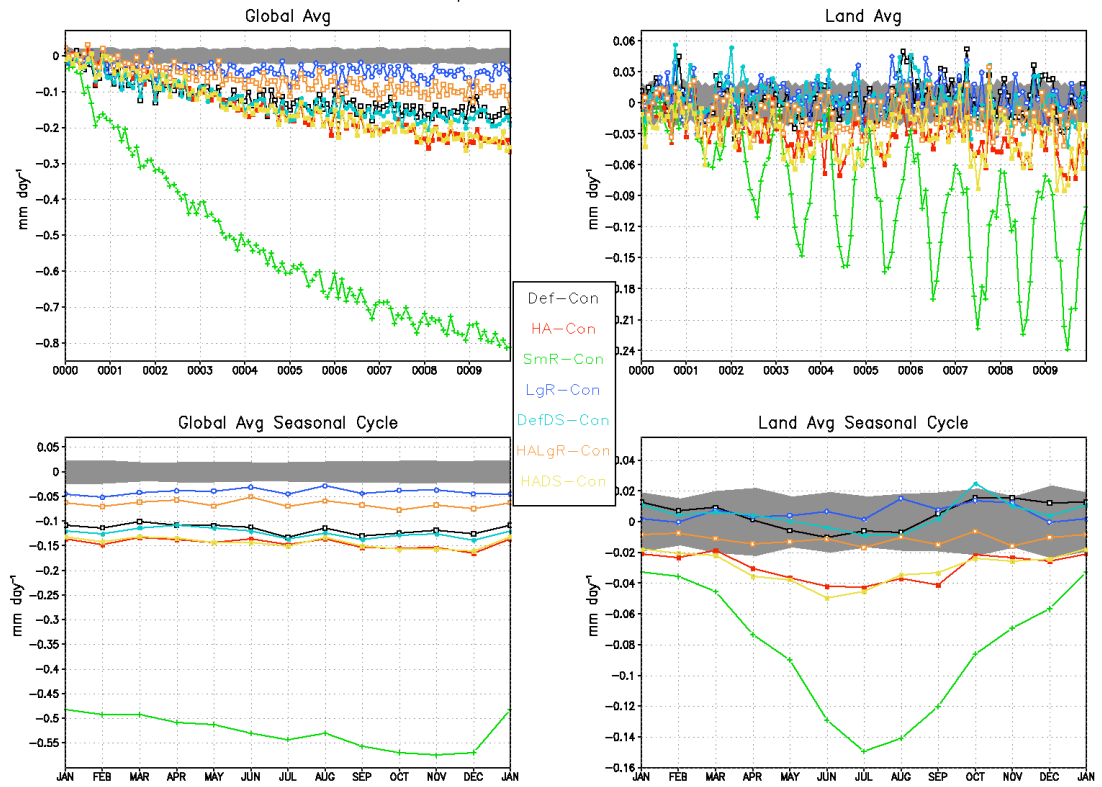
FIGURE 5.35. Average precipitation anomalies for all geoengineering ensembles. Ensemble descriptions are given in Table 3.1. The left column of panels shows globally averaged anomalies, and the right column shows averages for land only. The top row of panels shows anomalies as a function of time, and the bottom row shows the ten year average seasonal cycle. Grey shading denotes ±1.96σ of the average variability of the ten year average seasonal cycle of the control ensemble.

negative anomalies. With the exception of SmR, these anomalies are as much as

-0.25 mm day^{-1} of precipitation by year ten due to geoengineering. SmR vastly

outpaces the other ensembles, showing a precipitation anomaly of -0.8 mm day^{-1}

by year ten, and still with a decreasing trend. No particular month shows any

greater anomaly in the global average. In the land average, most of the

ensembles show no statistically significant anomalies. HA and HADS show

slight reductions in precipitation in some years but nothing exceeding 0.09 mm

day^{-1}. SmR is the only ensemble with a clear, large departure from natural

variability, showing statistically significant reductions in land precipitation of up

to -0.24 mm day^{-1} in the boreal summer of year ten. The seasonal cycle of the

land precipitation anomaly for this ensemble is quite large, ranging from -0.03

mm day^{-1} in the boreal winter to -0.15 mm day^{-1} in the summer, all of which is

significant at the 95% confidence level. These results suggest that HA and HADS

show a perturbation to summer monsoon precipitation, as we saw in Section 4.4,

and that SmR will show a large disruption of the summer monsoon.

The evaporation results (Figure 5.36) are very similar to the precipitation

results, but with more statistically significant anomalies over land and a much

larger summer disruption of land evaporation. Only Ensemble LgR does not

show a statistically significant reduction of land averaged summer evaporation.

As discussed in Section 4.4, since sea surface temperatures are fixed, the best

explanation for reductions in evaporation is a reduction in latent heat. Indeed,

Figures 5.36 and 5.37 are identical except for a scaling factor, and in
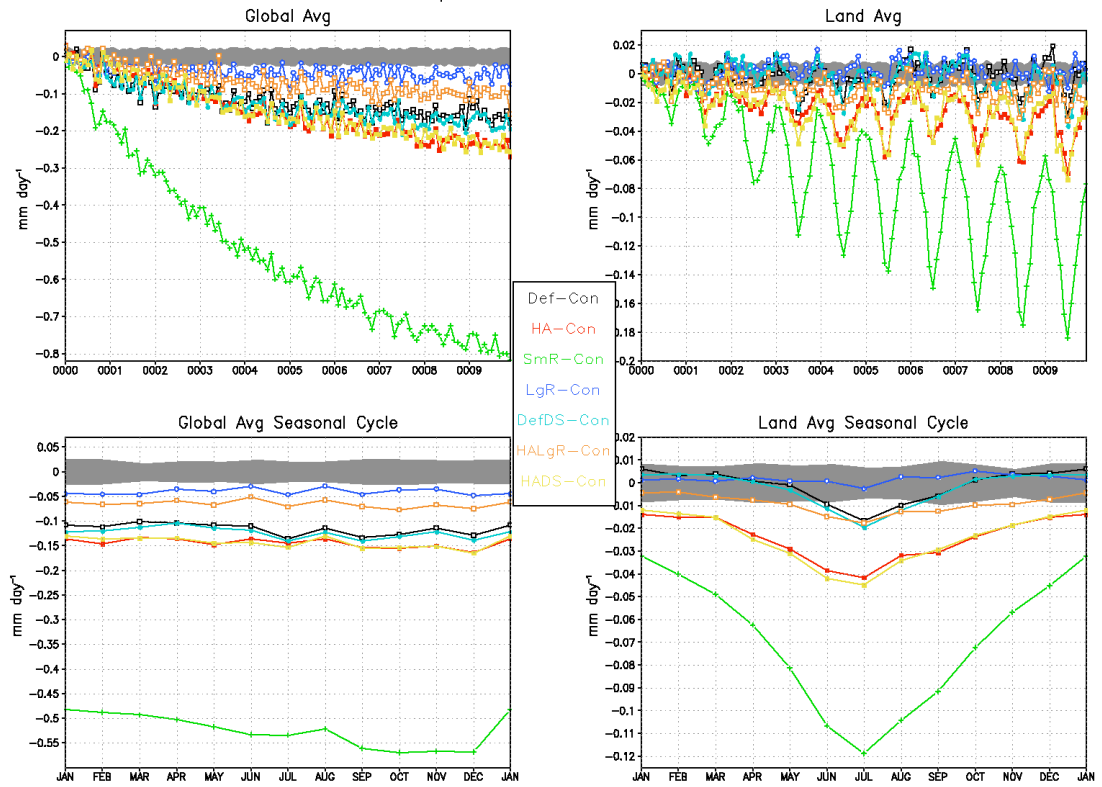
FIGURE 5.36. Average evaporation anomalies for all geoengineering ensembles. Ensemble descriptions are given in Table 3.1. The left column of panels shows globally averaged anomalies, and the right column shows averages for land only. The top row of panels shows anomalies as a function of time, and the bottom row shows the ten year average seasonal cycle. Grey shading denotes ±1.96σ of the average variability of the ten year average seasonal cycle of the control ensemble.
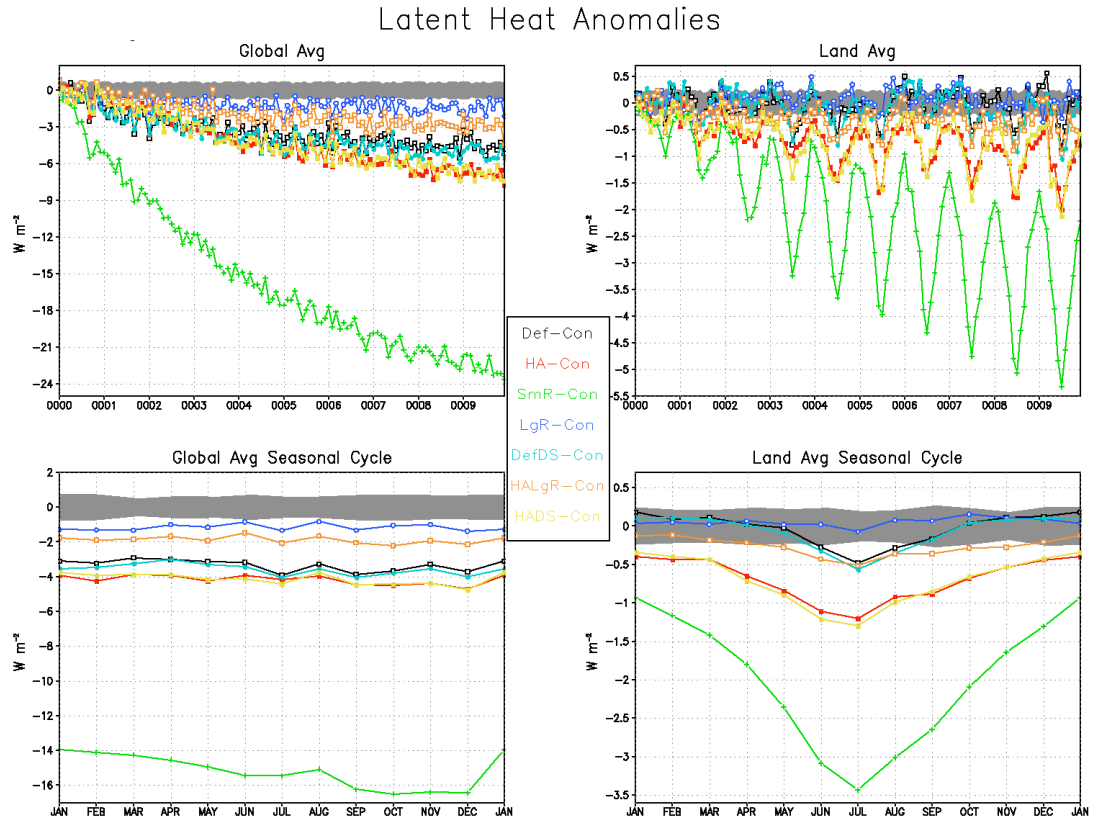
FIGURE 5.37. Average latent heat anomalies for all geoengineering ensembles. Ensemble descriptions are given in Table 3.1. The left column of panels shows globally averaged anomalies, and the right column shows averages for land only. The top row of panels shows anomalies as a function of time, and the bottom row shows the ten year average seasonal cycle. Grey shading denotes ±1.96σ of the average variability of the ten year average seasonal cycle of the control ensemble.

calculating ratios between these two fields, we find that the model prescribes evaporation in our experiments by the formula $E=0.03456L$, or $L=28.9352E$, where E is evaporation (mm day^{-1}) and L is latent heat (W m^{-2}).

Figure 5.38 shows global averages for soil moisture (top 1 m) and runoff. The results are similar to those shown in Section 4.4, i.e., globally averaged soil moisture increases over the course of the simulation, showing many statistically significant anomalies. Although HA and HADS have some years with statistically significant negative anomalies in runoff, the only ensemble that is consistently outside of the natural variability is SmR. Also, unlike the other ensembles, this one shows a double peak in runoff in summer for each hemisphere in which the negative anomalies are less negative.

Thus far, we can conclude that HA shows some disruption to the summer monsoon, as was discussed in Section 4.4, but the anomalies for this ensemble are not always statistically significant. SmR shows the largest anomalies, nearly all of which are statistically significant. We do not see many significant disruptions to the summer monsoon from the other ensembles, although all ensembles show a general increase in soil moisture.

To further determine the effects on the hydrologic cycle, we analyze spatial maps, in both the annual average (average of the last three years of simulation) and June, July, August, and September averages to highlight the effects on the summer monsoon of India, Africa, and East Asia. These results are presented in Figures 5.39-5.52.
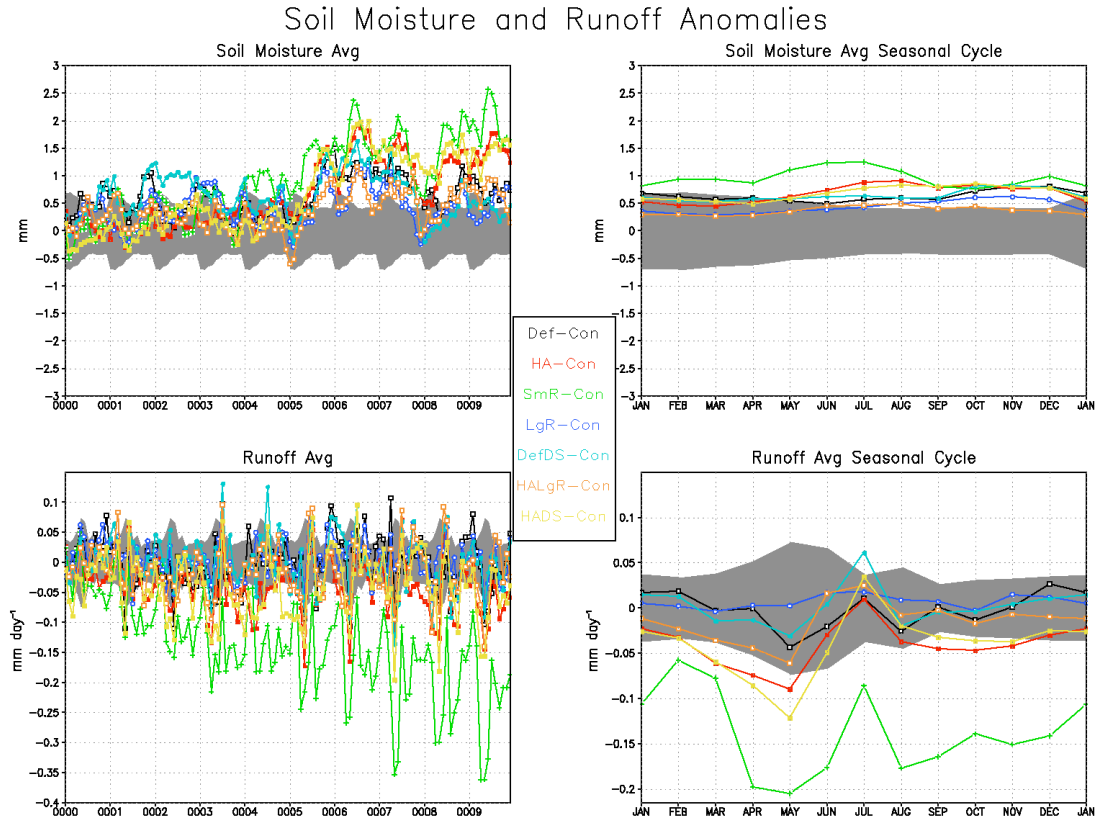
FIGURE 5.38. Average soil moisture (top 1 m, or model layers 1-4) and runoff anomalies for all geoengineering ensembles. Ensemble descriptions are given in Table 3.1. The left column of panels shows anomalies as a function of time, and the right column shows the ten year average seasonal cycle. Grey shading denotes ±1.96σ of the average variability of the ten year average seasonal cycle of the control ensemble. No distinction is made between global average and land average because these are land-only variables.
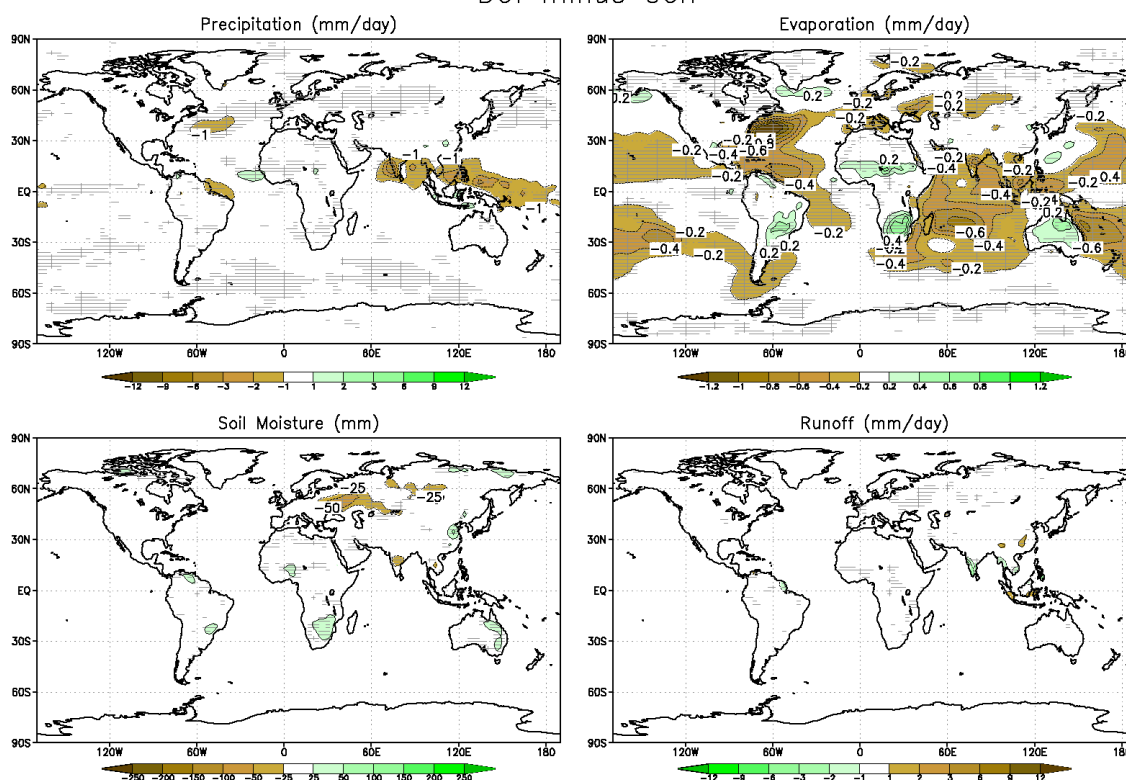
FIGURE 5.39. Hydrologic cycle anomalies for Def minus Con. Ensemble description is given in Table 3.1. Spatial maps shown are averages over the last three years of simulation. Grey hatching denotes values that are statistically significant at the 95% confidence level as calculated by an unpaired two sample Student's *t* test.
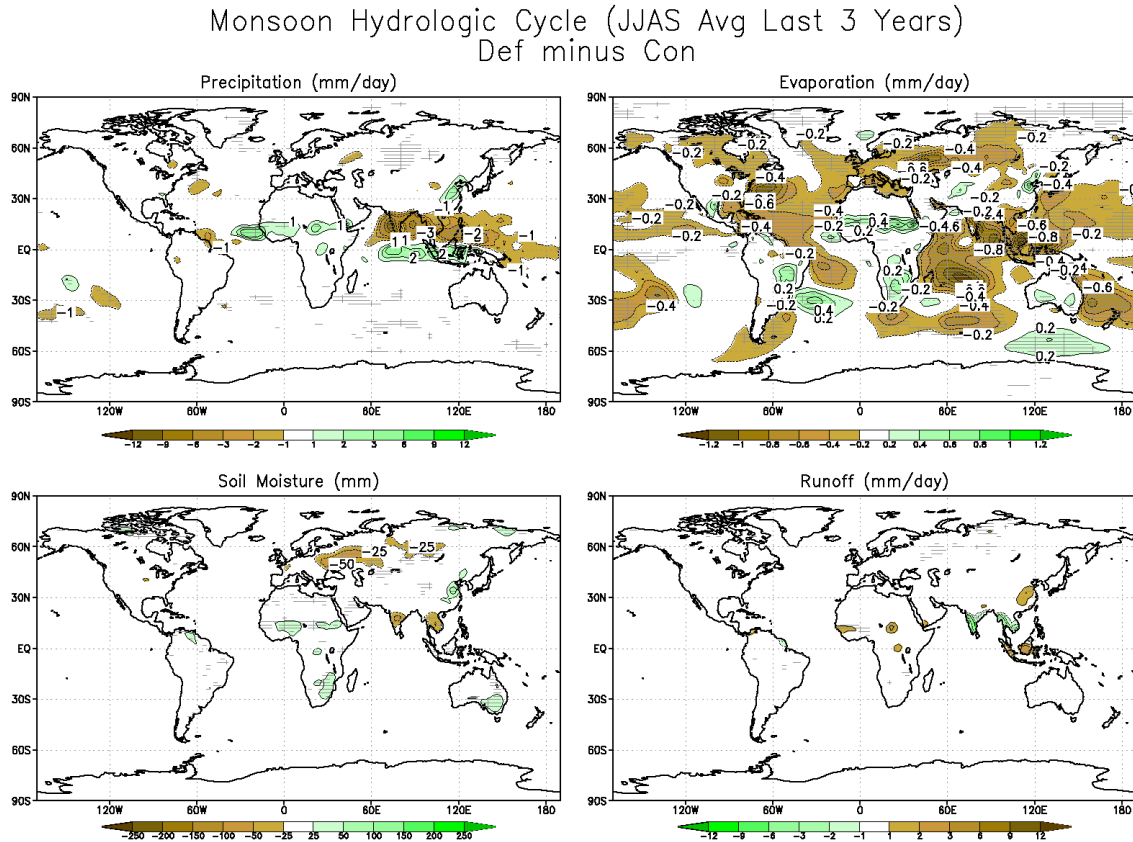
FIGURE 5.40. Hydrologic cycle anomalies for Def minus Con, averaged over June, July, August, and September to highlight changes in the summer monsoon hydrologic cycle. Ensemble description is given in Table 3.1. Spatial maps shown are averages over the last three years of simulation. Grey hatching denotes values that are statistically significant at the 95% confidence level as calculated by an unpaired two sample Student's *t* test.

FIGURE 5.41. Hydrologic cycle anomalies for LgR minus Con. Ensemble description is given in Table 3.1. Spatial maps shown are averages over the last three years of simulation. Grey hatching denotes values that are statistically significant at the 95% confidence level as calculated by an unpaired two sample Student's *t* test.

Monsoon Hydrologic Cycle (JJAS Avg Last 3 Years)
LgR minus Con
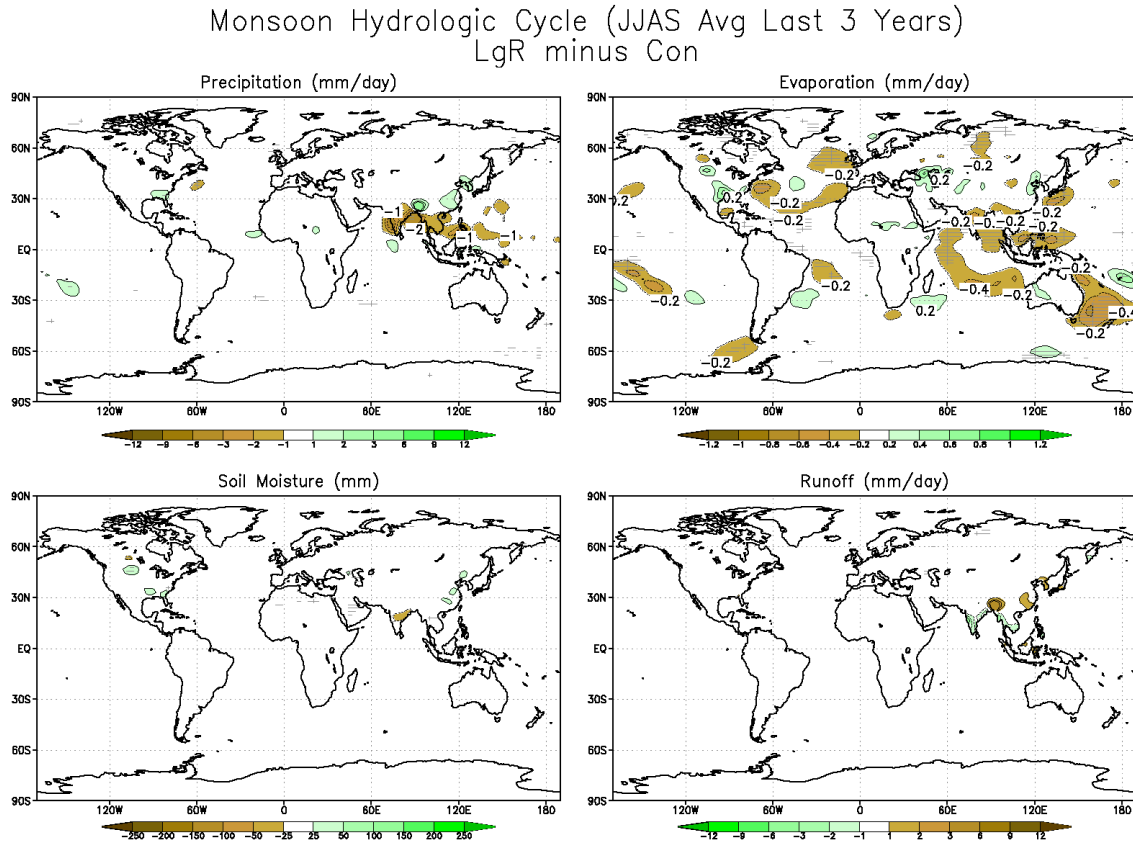
FIGURE 5.42. Hydrologic cycle anomalies for LgR minus Con, averaged over June, July, August, and September to highlight changes in the summer monsoon hydrologic cycle. Ensemble description is given in Table 3.1. Spatial maps shown are averages over the last three years of simulation. Grey hatching denotes values that are statistically significant at the 95% confidence level as calculated by an unpaired two sample Student's *t* test.

FIGURE 5.43. Hydrologic cycle anomalies for LgR minus Def. Ensemble description is given in Table 3.1. Spatial maps shown are averages over the last three years of simulation. Grey hatching denotes values that are statistically significant at the 95% confidence level as calculated by an unpaired two sample Student's *t* test.
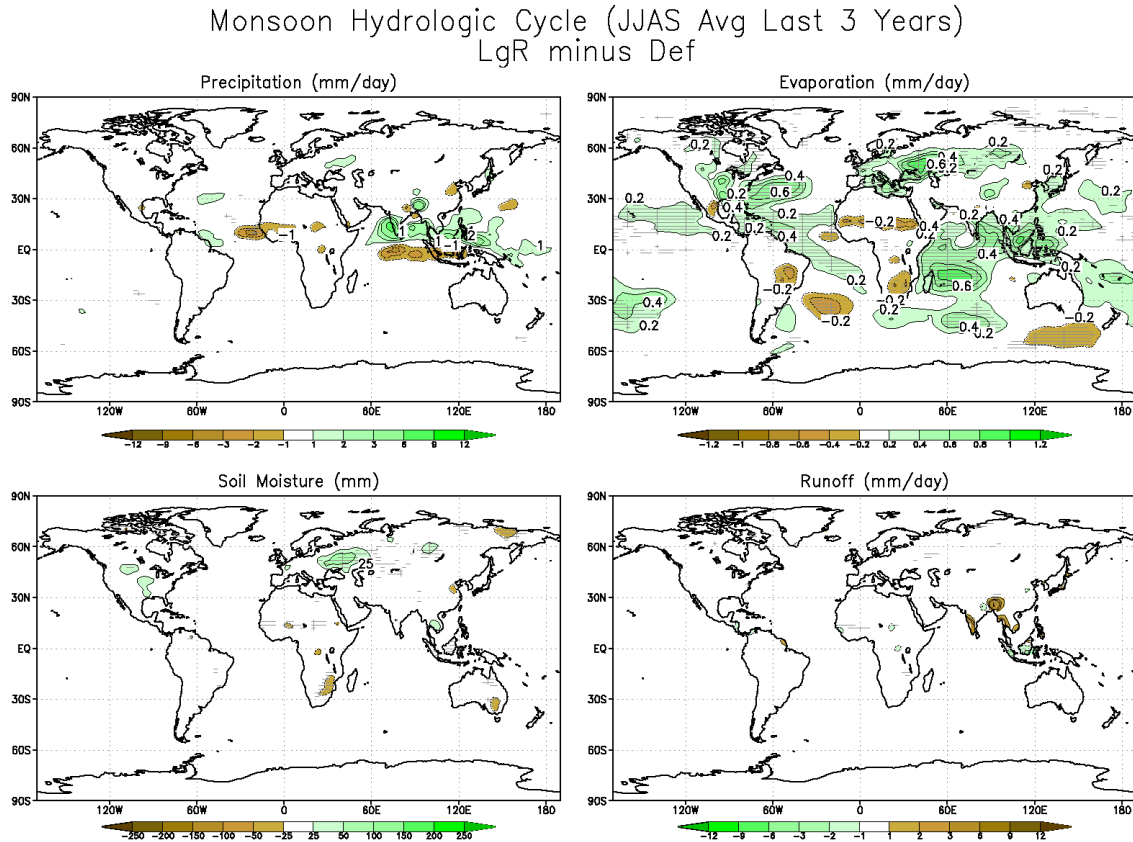
FIGURE 5.44. Hydrologic cycle anomalies for LgR minus Def, averaged over June, July, August, and September to highlight changes in the summer monsoon hydrologic cycle. Ensemble description is given in Table 3.1. Spatial maps shown are averages over the last three years of simulation. Grey hatching denotes values that are statistically significant at the 95% confidence level as calculated by an unpaired two sample Student's *t* test.

FIGURE 5.45. Hydrologic cycle anomalies for SmR minus Con. Ensemble description is given in Table 3.1. Spatial maps shown are averages over the last three years of simulation. Grey hatching denotes values that are statistically significant at the 95% confidence level as calculated by an unpaired two sample Student's *t* test.
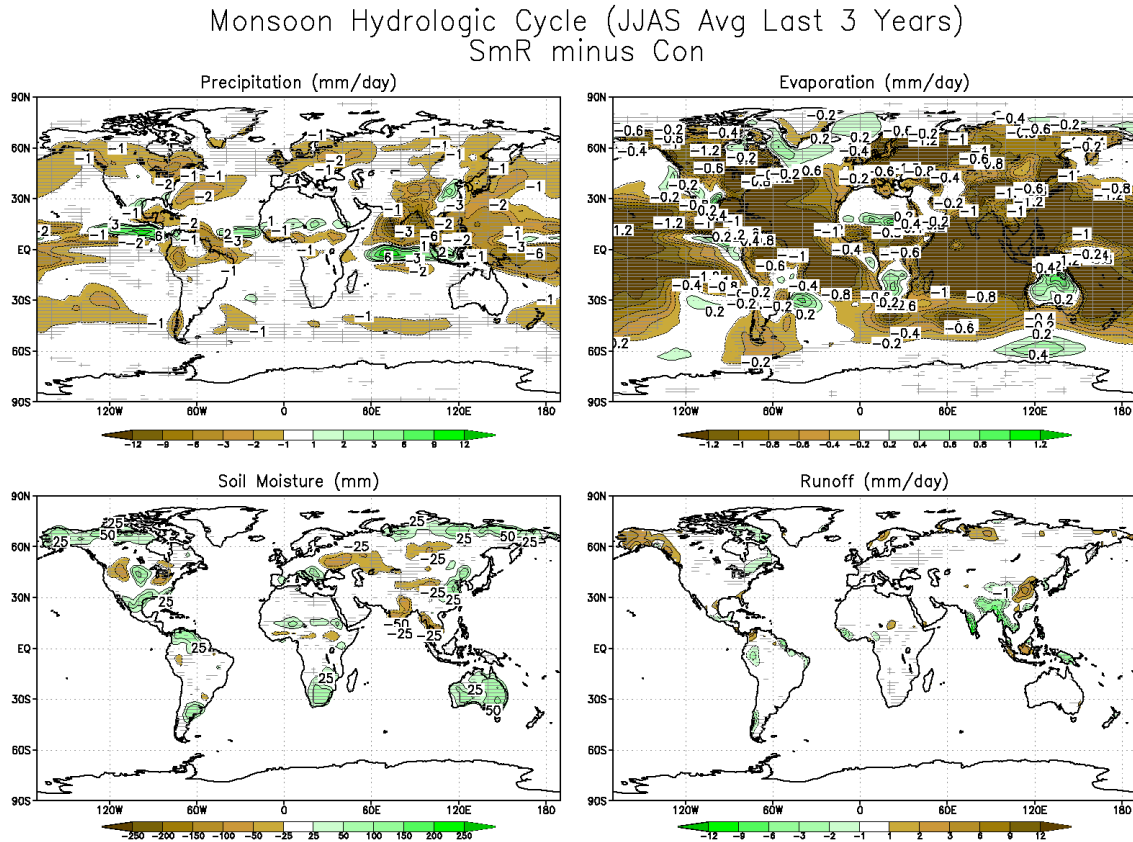
FIGURE 5.46. Hydrologic cycle anomalies for SmR minus Con, averaged over June, July, August, and September to highlight changes in the summer monsoon hydrologic cycle. Ensemble description is given in Table 3.1. Spatial maps shown are averages over the last three years of simulation. Grey hatching denotes values that are statistically significant at the 95% confidence level as calculated by an unpaired two sample Student's *t* test.

FIGURE 5.47. Hydrologic cycle anomalies for SmR minus Def. Ensemble description is given in Table 3.1. Spatial maps shown are averages over the last three years of simulation. Grey hatching denotes values that are statistically significant at the 95% confidence level as calculated by an unpaired two sample Student's *t* test.

Monsoon Hydrologic Cycle (JJAS Avg Last 3 Years)
SmR minus Def
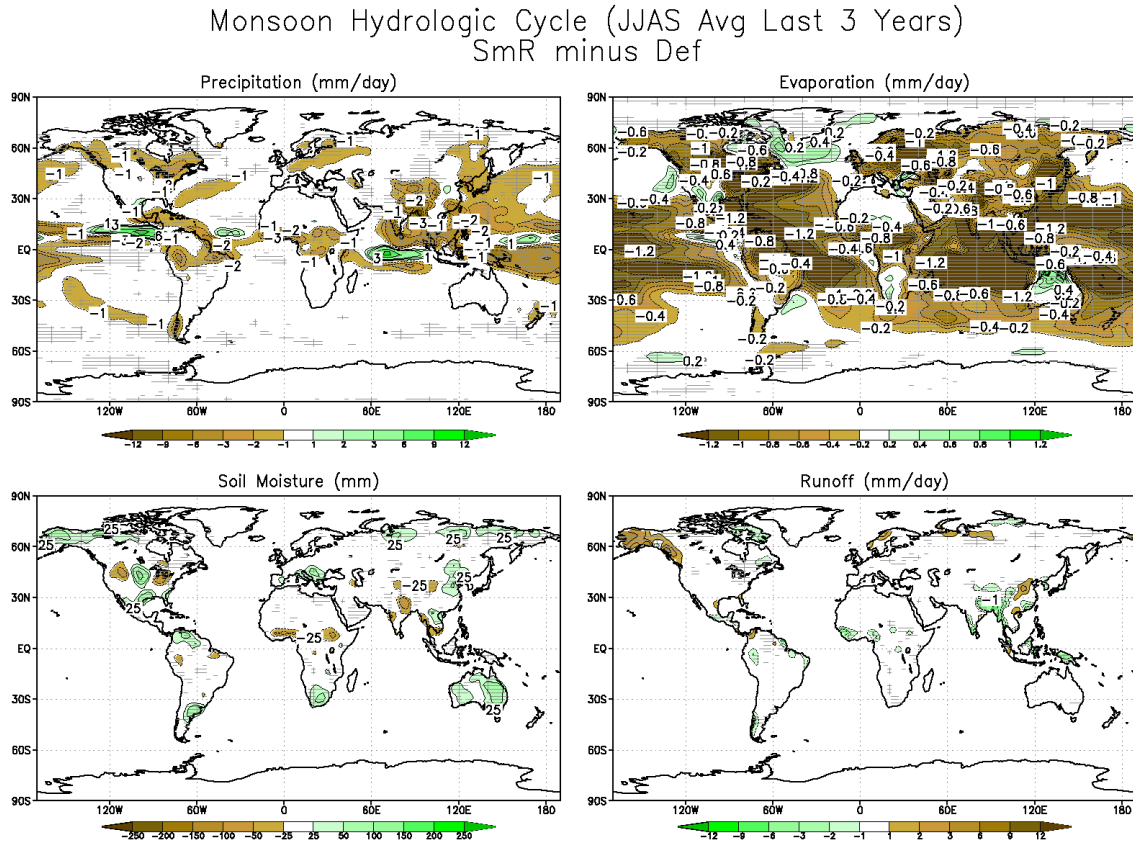
FIGURE 5.48. Hydrologic cycle anomalies for SmR minus Def, averaged over June, July, August, and September to highlight changes in the summer monsoon hydrologic cycle. Ensemble description is given in Table 3.1. Spatial maps shown are averages over the last three years of simulation. Grey hatching denotes values that are statistically significant at the 95% confidence level as calculated by an unpaired two sample Student's *t* test.
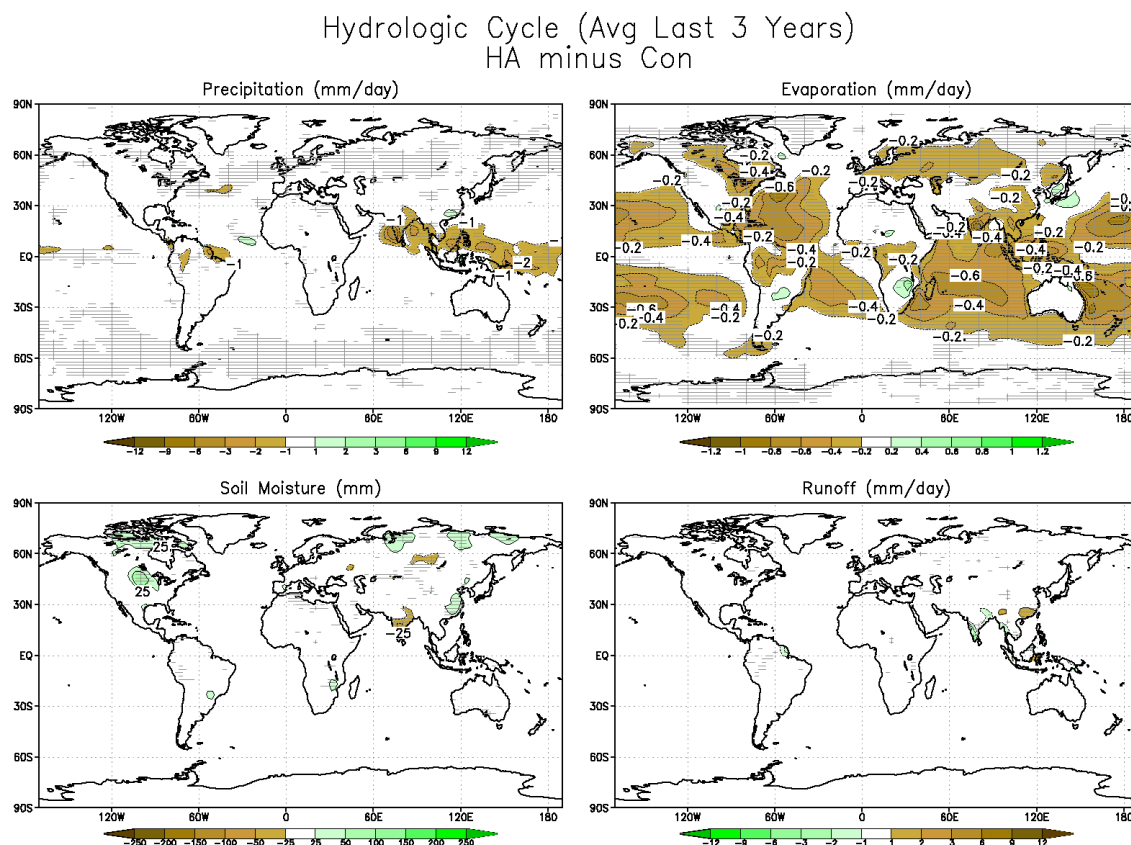
FIGURE 5.49. Hydrologic cycle anomalies for HA minus Con. Ensemble description is given in Table 3.1. Spatial maps shown are averages over the last three years of simulation. Grey hatching denotes values that are statistically significant at the 95% confidence level as calculated by an unpaired two sample Student's *t* test.
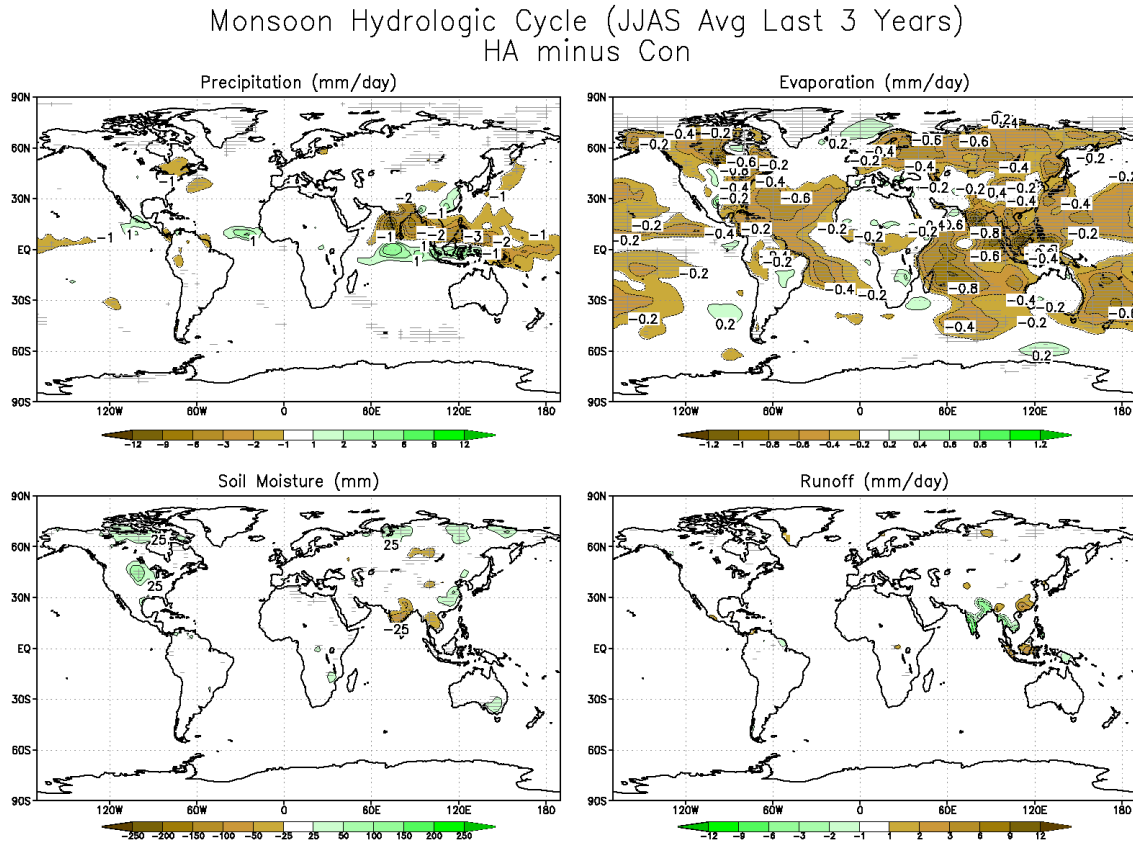
FIGURE 5.50. Hydrologic cycle anomalies for HA minus Con, averaged over June, July, August, and September to highlight changes in the summer monsoon hydrologic cycle. Ensemble description is given in Table 3.1. Spatial maps shown are averages over the last three years of simulation. Grey hatching denotes values that are statistically significant at the 95% confidence level as calculated by an unpaired two sample Student's *t* test.
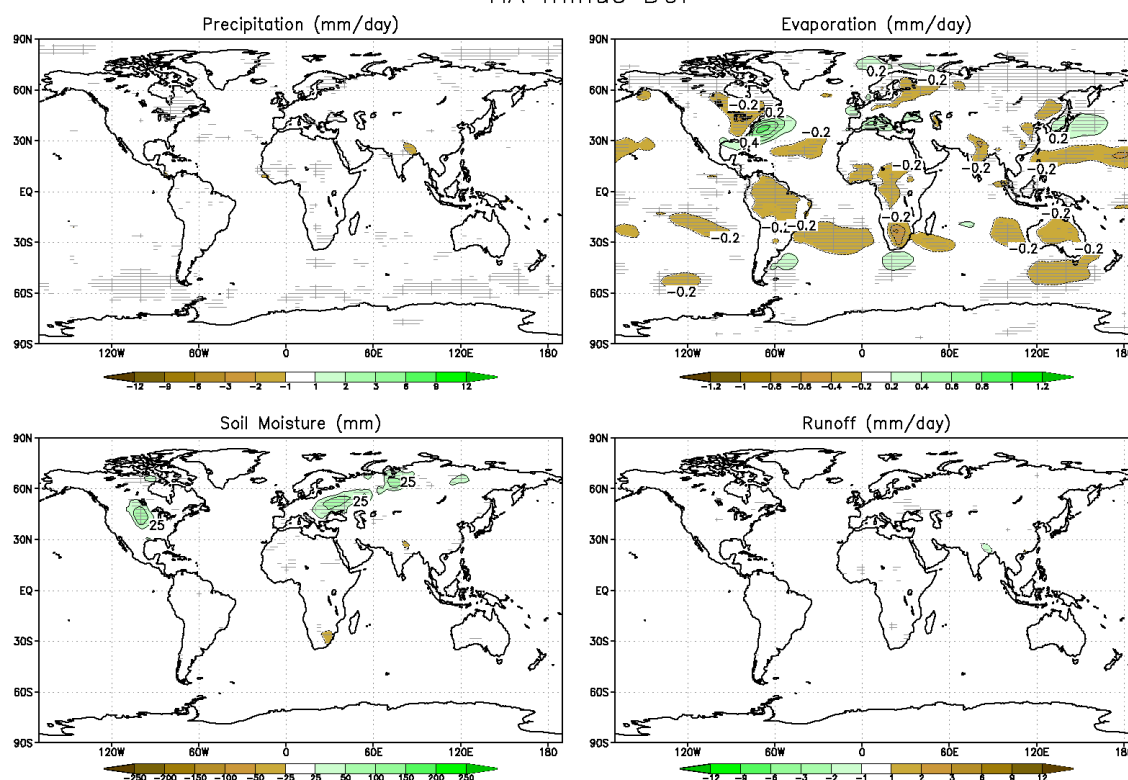
FIGURE 5.51. Hydrologic cycle anomalies for HA minus Def. Ensemble description is given in Table 3.1. Spatial maps shown are averages over the last three years of simulation. Grey hatching denotes values that are statistically significant at the 95% confidence level as calculated by an unpaired two sample Student's *t* test.
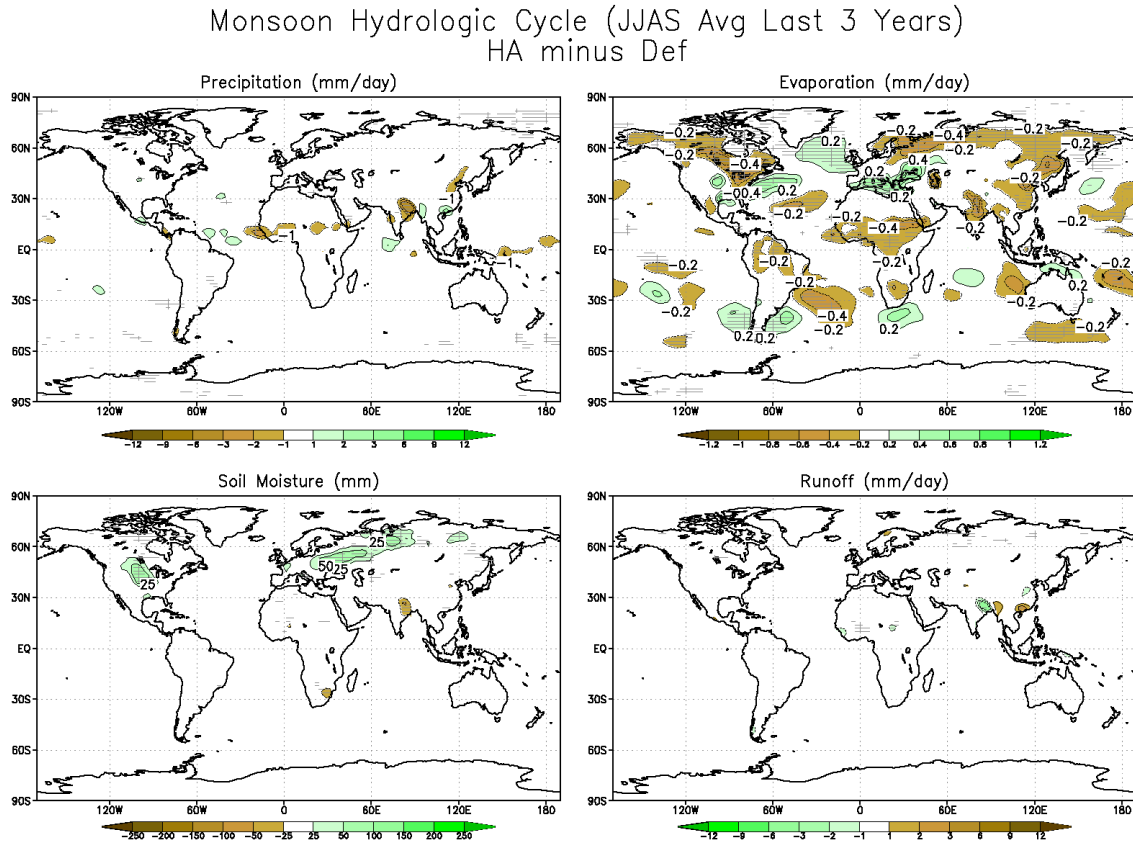
FIGURE 5.52. Hydrologic cycle anomalies for HA minus Def, averaged over June, July, August, and September to highlight changes in the summer monsoon hydrologic cycle. Ensemble description is given in Table 3.1. Spatial maps shown are averages over the last three years of simulation. Grey hatching denotes values that are statistically significant at the 95% confidence level as calculated by an unpaired two sample Student's *t* test.

Nearly all of the ensembles (except LgR) show large areas of negative precipitation anomaly over India and East Asia which are enhanced for JJAS averages. As expected, the largest anomalies are for SmR, which shows summer precipitation anomalies over India reaching -12 mm day^{-1}, indicating a collapse of the summer monsoon. HA also shows large reductions in monsoon precipitation. Of all the ensembles, only SmR shows a summer reduction in precipitation over the Sahel that has any statistically significance, sometimes exceeding 2 mm day^{-1}, although HA shows some patches of reduction in this area by over 1 mm day^{-1}.

All of the ensembles show reductions in evaporation over the oceans, with the largest anomalies occurring for SmR. With the exception of SmR, evaporation anomalies over land are modest, and the strongest anomalies are over India and East Asia during the summer. SmR shows negative anomalies in evaporation over most of the land masses, which are amplified in the JJAS averages, with the exception of Australia, which shows large positive anomalies.

For SmR, the Australian anomalies in evaporation are reflected in a large increase in soil moisture and no change in runoff, indicating Australia could potentially become more fertile for agriculture under black carbon geoengineering. In fact, many regions of the world show a large increase in soil moisture, with notable exceptions being the Sahara desert and the Middle East showing no soil moisture anomalies, and parts of Northern Canada, Eastern Europe, India, and Southeast Asia showing decreases in soil moisture. India and Southeast Asia also show an increase in runoff, indicating these areas will likely

become less suitable for agriculture under black carbon geoengineering. The anomalies in soil moisture and runoff are much less pronounced for the other ensembles, although the patterns are similar. Therefore, in the context of vegetation, the perturbations to the hydrologic cycle would likely be a slight improvement in agricultural conditions on a global scale, although particular regions may be strongly affected.

ModelE has a less sophisticated land surface module than many stand-alone models dedicated to diagnosing land surface and crop variables, so we are hesitant to assert robust conclusions regarding the effects of geoengineering on agriculture. However, the model does include some variables in its standard output which are useful for assessing these changes on an aggregate basis. Figure 5.53 shows gross primary productivity for each of the ensembles, again globally averaged. Most of the ensembles show no statistically significant anomalies in productivity, some exceptions being decreases in the summers of some years for HA and HADS by nearly 0.3 g[C] m^{-2} day^{-1}, or up to a 6% change. However, SmR shows a large decrease in productivity of between 0.2 and 0.9 g[C] m^{-2} day-1, depending upon the time of year, which is a 6-14% decrease. In this sense, geoengineering with small particles could actually exacerbate the underlying cause of anthropogenic warming by reducing the planetary carbon uptake. Putting these values into context, *Field et al.* [1998] estimated the total annual primary production for Earth, in areal terms, is approximately 566 g[C] m^{-2} a^{-1}, or 1.55 g[C] m^{-2} day^{-1}. Therefore, black carbon geoengineering under the specifications of SmR would be a reduction in
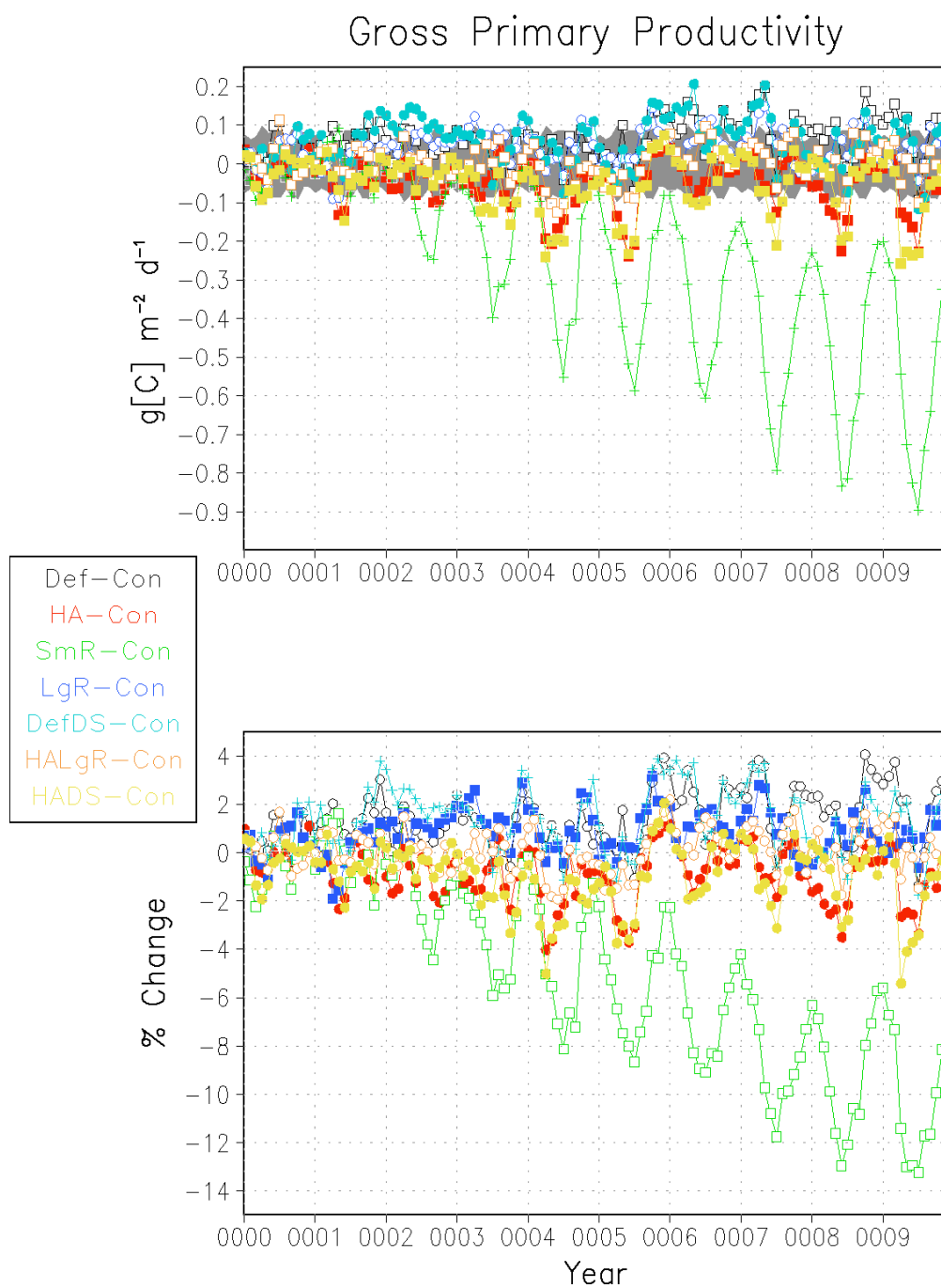
FIGURE 5.53. Globally averaged gross primary productivity anomalies for each of the geoengineering ensembles. Ensemble descriptions are given in Table 3.1. Grey shading denotes ±1.96σ of the variability of the average seasonal cycle of the control ensemble, averaged over the entire 10 year simulation.

planetary primary productivity by 35.5% on average. For HA, assuming an average decrease of 0.1 g[C] m^{-2} day^{-1}, the decrease in primary productivity would be 6.4%. Effects on gross primary productivity for the other ensembles are slightly positive, although rarely outside of the realm of natural variability.

5.6 CRYOSPHERE

Figure 5.54 shows North polar projections of snow and ice fraction anomalies for the geoengineering ensembles. South polar projections are not included, as the results of Section 4.5 showed these have no interesting anomalies. The bottom panels are the results shown in Section 4.5. The LgR panels show much fewer anomalies, although the small localized feature over Southern Europe is statistically significant at the 95% confidence level. The climate changes due to this ensemble were shown to be so minor in the previous sections that we would not expect this experiment to show large anomalies in snow and ice fraction. SmR shows very large anomalies in snow and ice fraction, sometimes exceeding 20% near the Arctic Ocean. Most of these values are statistically significant.

Figure 5.55 shows Northern Hemisphere averages and September averages of snow and ice coverage. Of all the ensembles, the only one that is statistically significant is SmR in late spring/early summer in the last few years of the simulation. The natural variability of this field is so large that statistical significance is very difficult to achieve. For the September averages, although the anomalies for SmR and HADS reach up to 1.5% by the tenth year, these

Snow and Ice Fraction Anom (%)
Avg Last 3 Years, North Polar Projection
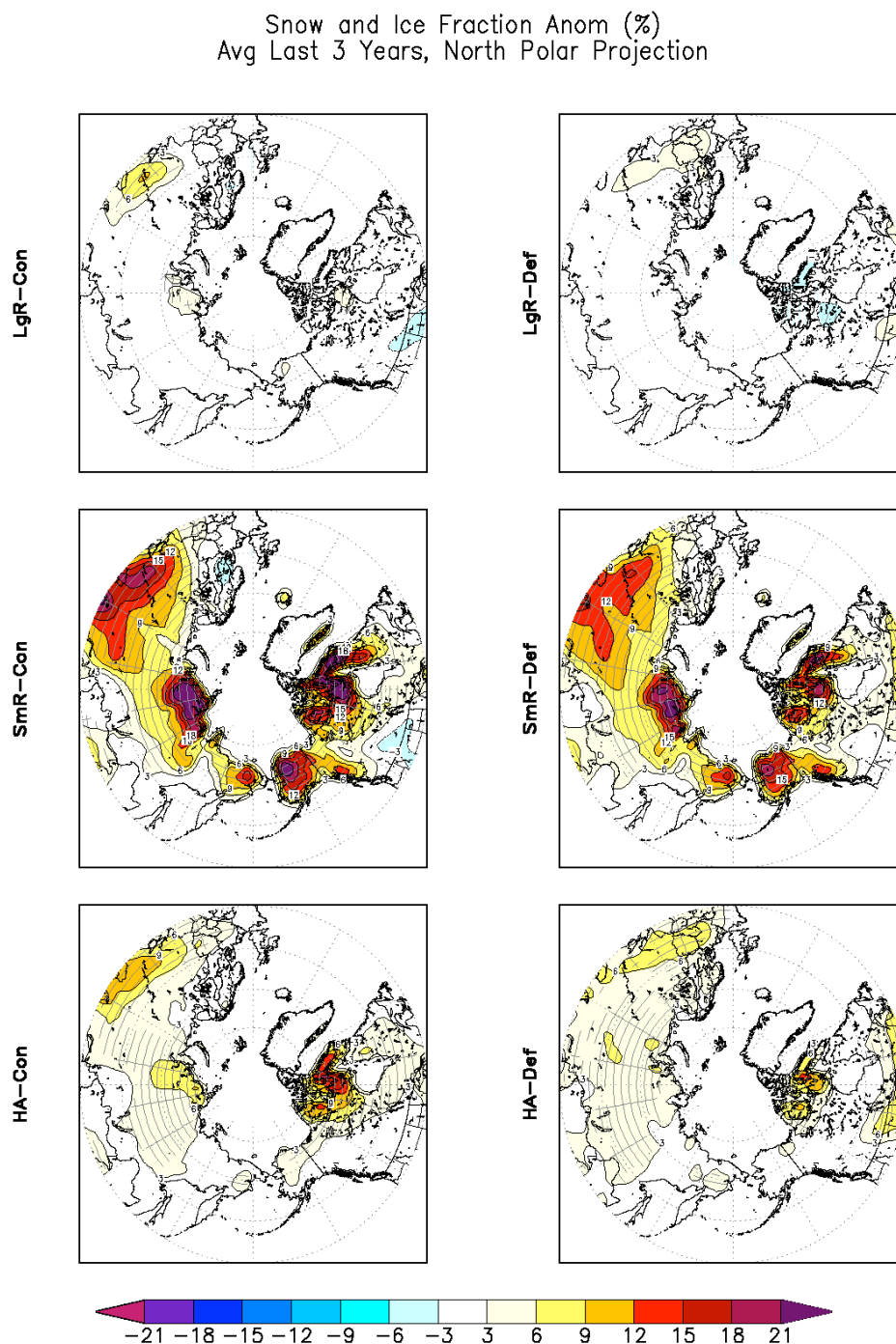
FIGURE 5.54. Snow and ice fraction anomalies for black carbon geoengineering, averaged over the last three years of simulation. Grey hatching denotes values that are statistically significant at the 95% confidence level as calculated by an unpaired two sample Student's *t* test.
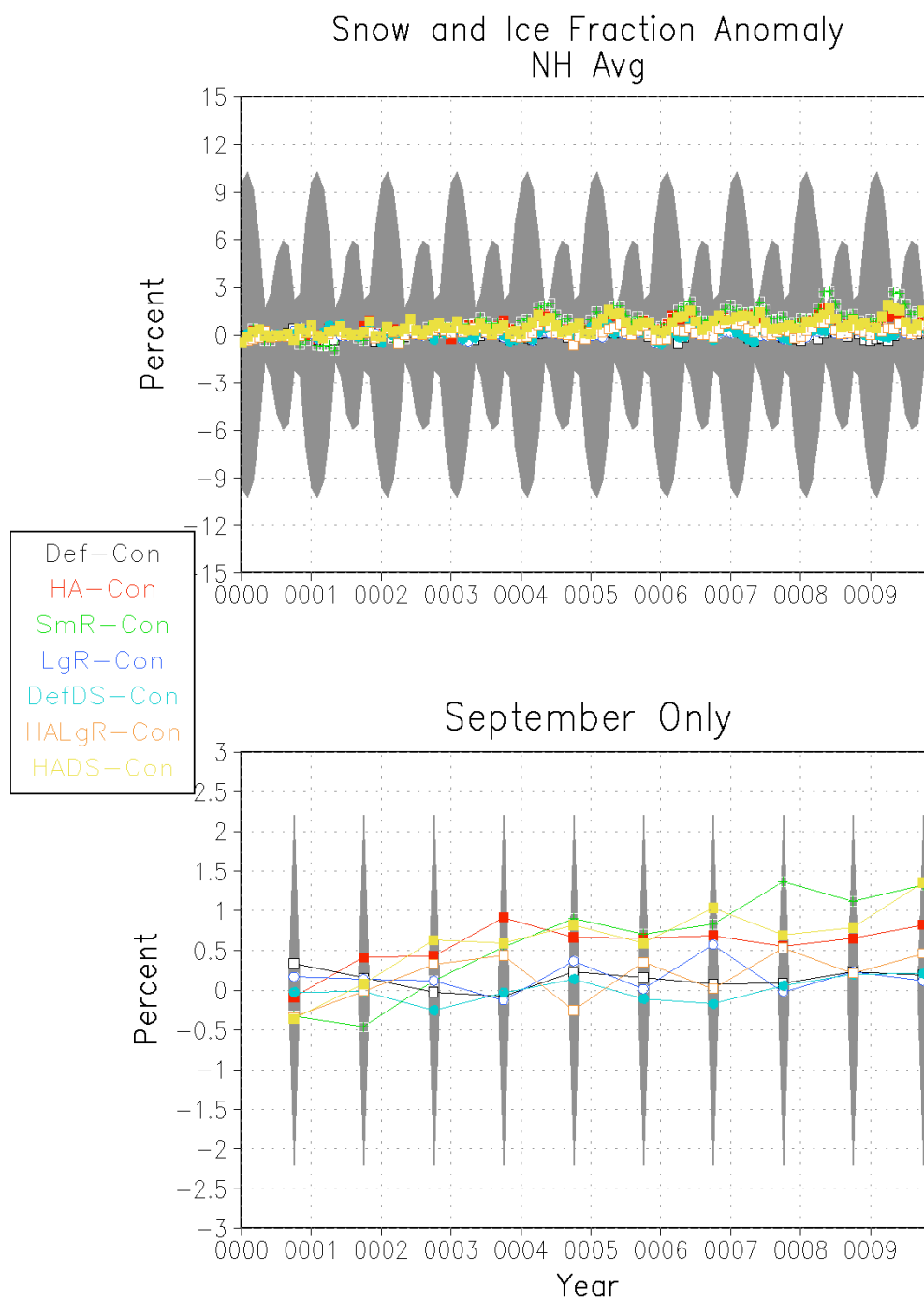
FIGURE 5.55. Northern Hemisphere average snow and ice fraction anomalies for all geoengineering ensembles. Ensemble descriptions are given in Table 3.1. Grey shading denotes ±1.96σ of the average variability of the ten year average seasonal cycle of the control ensemble.

anomalies are not statistically significant. We suspect that if the simulations were run longer, the snow and ice increase due to some of these ensembles would become more prominent, and the averaging would be sufficient to lower the variability of the control ensemble, making more of the increases in snow and ice coverage statistically significant. This field is also strongly affected by our simulation choice of using fixed sea surface temperatures and sea ice coverage, so the conclusions we can draw regarding impacts on the cryosphere from black carbon geoengineering are limited.

5.7 DIRTY SNOW EFFECT

One of the parameters our experiment is designed to evaluate is the model's treatment of the modification of the ground albedo by black carbon deposition, which is often called the "dirty snow effect." Our previous analysis of global averages suggests that in the manner in which we have conducted our experiments, the contribution of this effect is modest, if it contributes to climate effects at all, but we analyze these impacts in more detail.

As a first order analysis, Figure 5.56 shows how much ground albedo is modified by black carbon geoengineering. We have chosen polar projections, as these are the regions where snow is prominent, excluding high altitude regions. However, these high altitude regions are well below the grid box scale of 2° latitude by 2.5° longitude, so we would not expect the model to resolve these with enough confidence to make robust conclusions. Part of Europe shows an annual average increase in albedo of up to 5% in the lower altitude case (DefDS
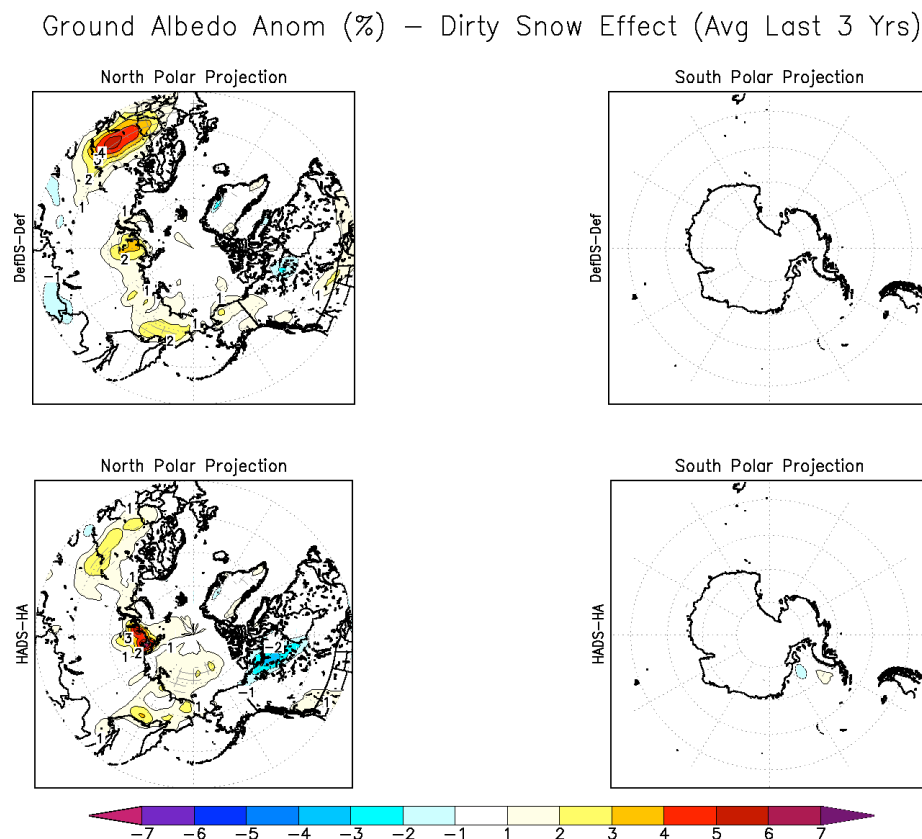
FIGURE 5.56. Polar stereographic projections of ground albedo anomalies from geoengineering, averaged over the last three years of simulation. Anomalies shown are the result of isolating the dirty snow effect in the model. Ensemble descriptions are given in Table 3.1. Grey hatching denotes values that are statistically significant at the 95% confidence level as calculated by an unpaired two sample Student's *t* test.
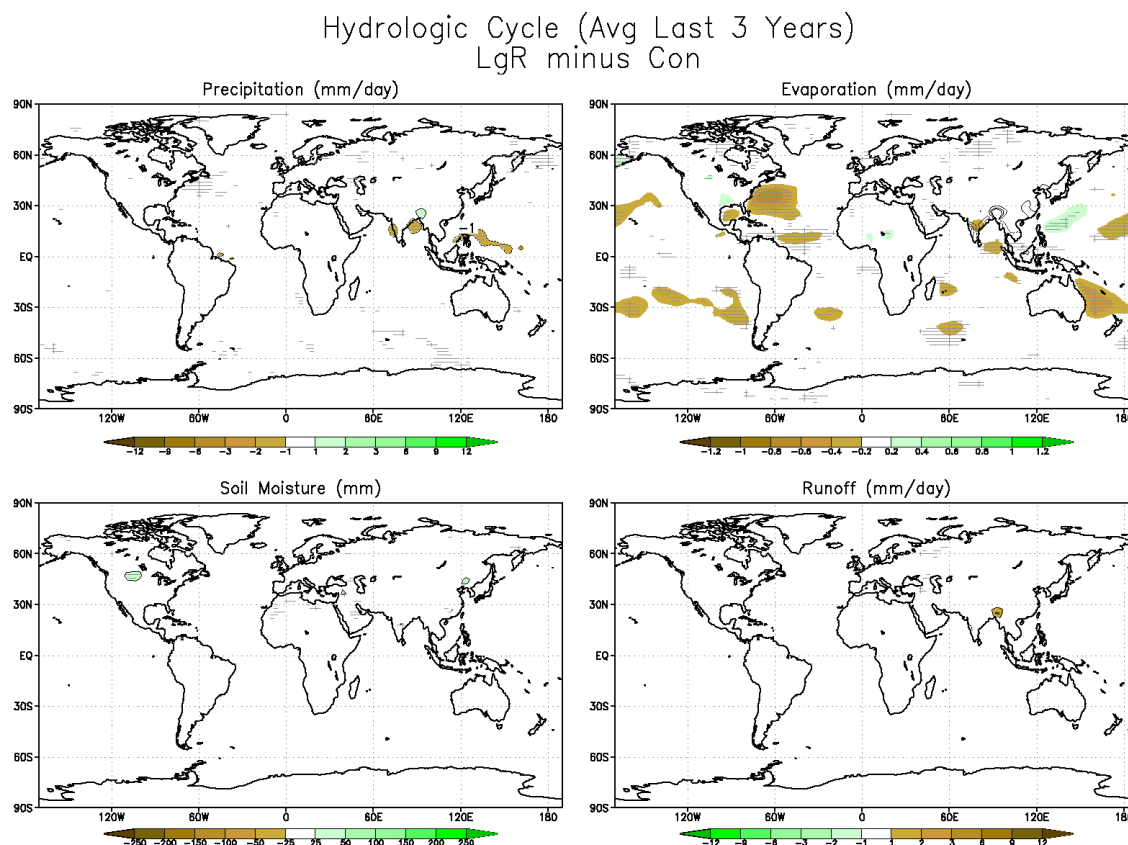
minus Def), which is statistically significant at the 95% confidence level. The higher altitude case (HADS minus HA) shows a smaller anomaly of up to 2%, which is still significant. Northern and Eastern Siberia show an increase in some places of up to 2% in the low altitude case and up to 5% in the high altitude case, which are also statistically significant. All other Northern Hemisphere anomalies are statistically insignificant, and the Southern Hemisphere shows very few point value anomalies at all. In the global average (not pictured), anomalies vary between -0.2 and 0.4% in both the low and high altitude cases. For comparison, the standard deviation of the control ensemble (Con) varies between 0.4 and 3.0%, so none of the albedo anomalies due to the dirty snow effect is statistically significant. Moreover, most of the albedo increases are positive, which suggests the dominant effect in this figure is more snow and ice coverage, which would cause an increase in albedo, rather than deposition of black carbon aerosols, which would decrease albedo. The effects on snow and ice are shown in Figure 5.63 and are discussed below. They are generally inconclusive regarding differences between the ensembles with the dirty snow effect and without, and there is no physical reason that DefDS and HADS should have higher ground albedos than Def and HA, so these statistically significant anomalies are most likely due to weather noise.

Figure 5.57 shows spatial maps of surface air temperature anomalies due to the dirty snow effect. Very few anomalies are over 1°C, and there are only small regions of statistical significance, particularly over Eastern Europe, Western Canada, and a small part of Antarctica. Moreover, all of these anomalies are
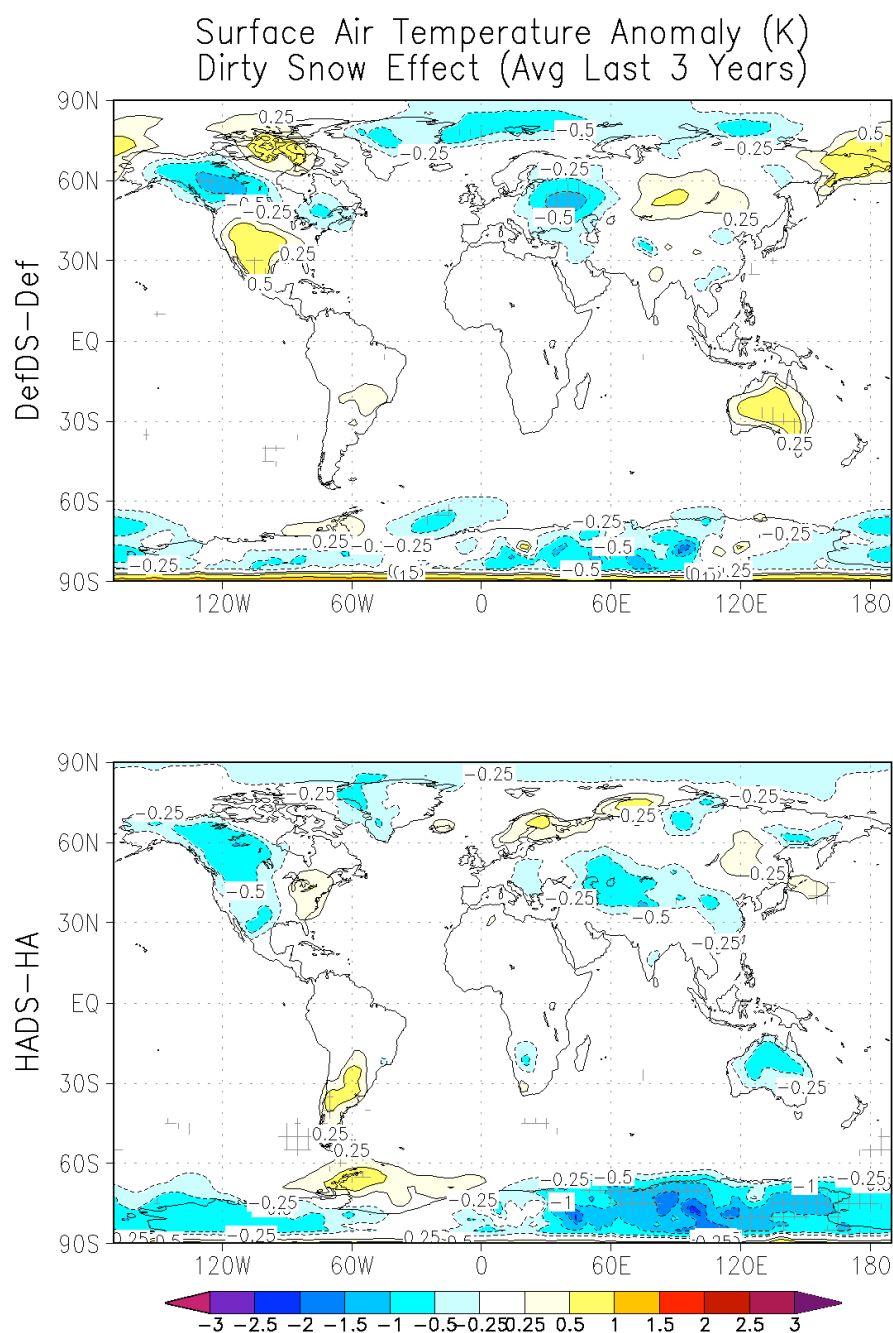
FIGURE 5.57. Surface air temperature anomalies from geoengineering, averaged over the last three years of simulation. Anomalies shown are the result of isolating the dirty snow effect in the model. Ensemble descriptions are given in Table 3.1. Grey hatching denotes values that are statistically significant at the 95% confidence level as calculated by an unpaired two sample Student's *t* test.

negative, whereas any reduction in ground albedo, which would be expected from black carbon deposition, should cause positive temperature anomalies. From this figure, we conclude that, according to the model results, any influence of the dirty snow effect on temperature would be minor and highly localized. Moreover, many areas of anomaly, such as Central America and Australia, do not receive much snowfall and likely would not under geoengineering, even with the large cooling values showed in Figure 5.2, so these anomalies must be due to noise. All of the modifications that would be reflected in the dirty snow effect would take place primarily in high latitudes, so we would not expect this parameter to alter monsoon precipitation. Indeed, Figure 5.58 shows very few anomalies at all, none being statistically significant.

In the plots of radiation (Figure 5.59-5.60) and instantaneous radiative forcing (Figures 5.61-5.62), the anomalies are very small compared to anomalies from the other ensembles shown in Section 5.2. Indeed, the line graphs in that section often show that ensembles Def and DefDS are indistinguishable in the global average from a radiation standpoint, as are HA and HADS. The radiation figures here show small areas of anomaly, but nothing resembling patterns that parallel snow and ice coverage, which we would expect to see if there were any modification due to the dirty snow effect. In the radiative forcing plots, there are positive anomalies in the Arctic for the HADS minus HA anomaly, which indicate an increase in downward shortwave radiative forcing due to black carbon geoengineering, both at the tropopause and surface. Although the anomalies are less than 2 W m^{-2}, compared to the globally averaged shortwave
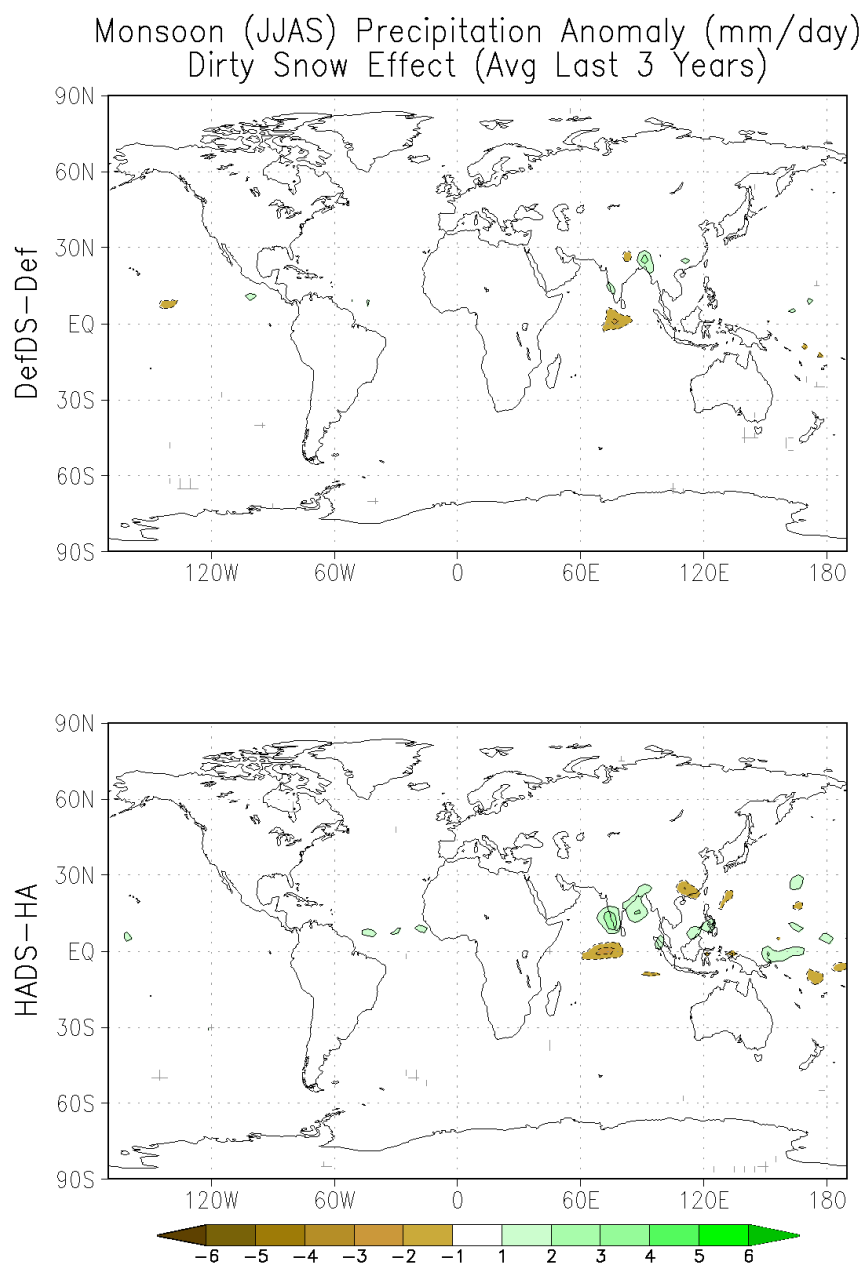
FIGURE 5.58. Summer monsoon (June, July, August, and September average) precipitation anomalies from geoengineering, averaged over the last three years of simulation. Anomalies shown are the result of isolating the dirty snow effect in the model. Ensemble descriptions are given in Table 3.1. Grey hatching denotes values that are statistically significant at the 95% confidence level as calculated by an unpaired two sample Student's *t* test.

Tropopause Rad Anom (W m⁻²)
Dirty Snow Effect (avg last 3 years)
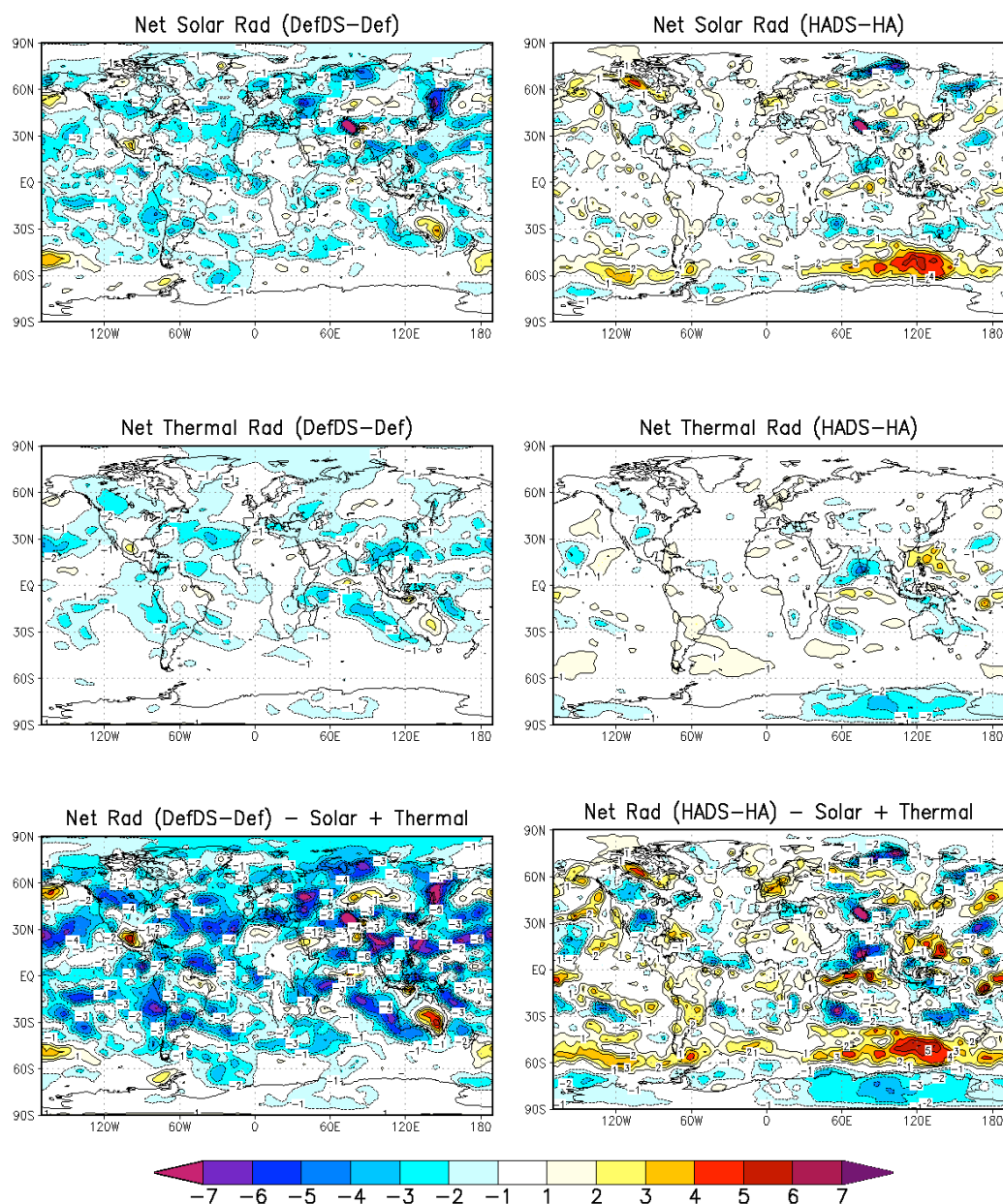
FIGURE 5.59. Tropopause radiation anomalies from geoengineering, averaged over the last three years of simulation. Anomalies shown are the result of isolating the dirty snow effect in the model. Ensemble descriptions are given in Table 3.1.

Surface Rad Anom (W m⁻²)
Dirty Snow Effect (avg last 3 years)
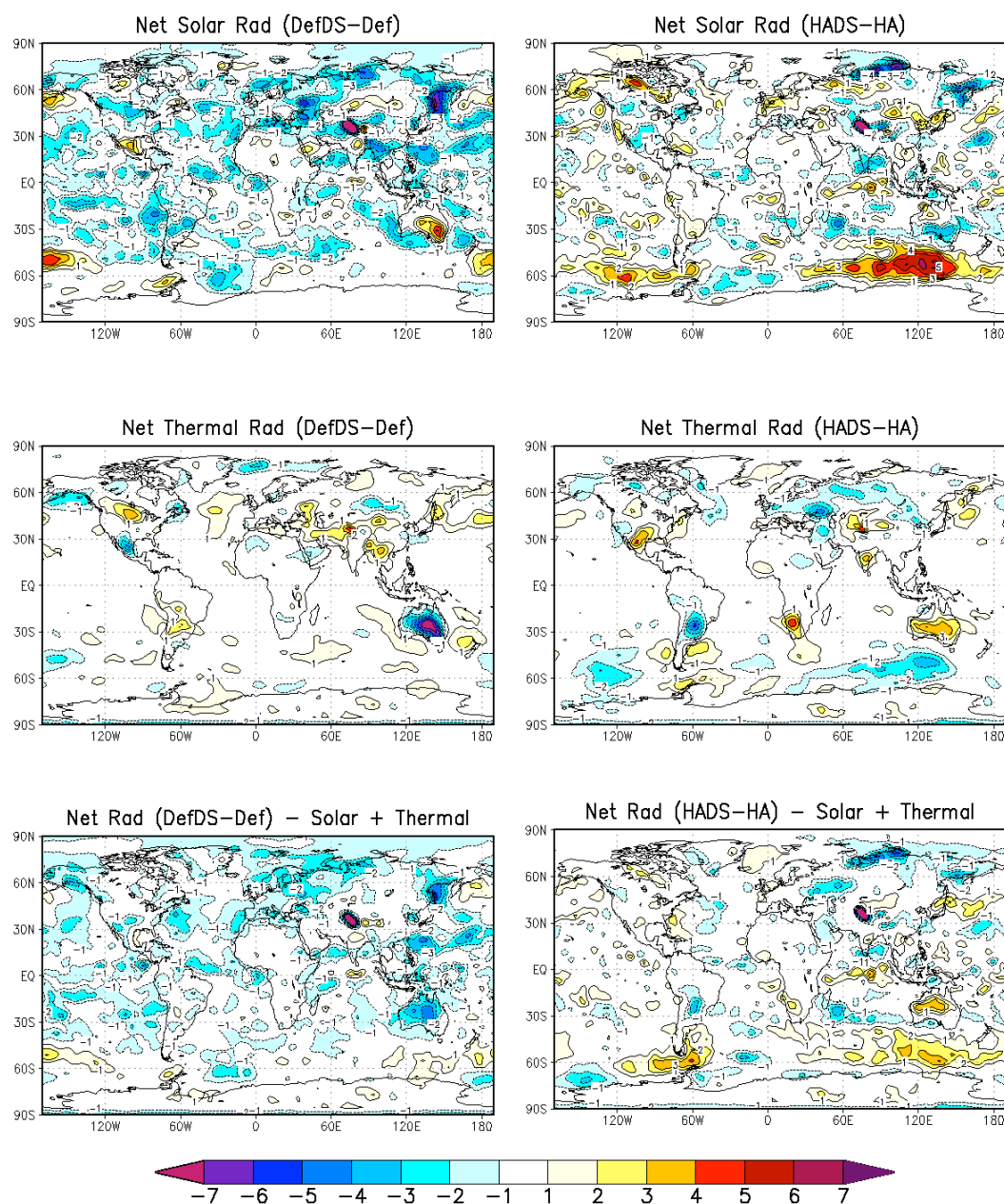
FIGURE 5.60. Surface radiation anomalies from geoengineering, averaged over the last three years of simulation. Anomalies shown are the result of isolating the dirty snow effect in the model. Ensemble descriptions are given in Table 3.1.

FIGURE 5.61. Tropopause radiative forcing anomalies from geoengineering, averaged over the last three years of simulation. Anomalies shown are the result of isolating the dirty snow effect in the model. Ensemble descriptions are given in Table 3.1.

FIGURE 5.62. Surface radiative forcing anomalies from geoengineering, averaged over the last three years of simulation. Anomalies shown are the result of isolating the dirty snow effect in the model. Ensemble descriptions are given in Table 3.1.

tropopause radiative forcing anomaly of 18 W m^{-2} (Figure 5.12), this pattern still suggests a small effect due to the dirty snow parameter in the model, regardless of whether this causes broader climate impacts. Qualitatively, the fields in the left columns of Figures 5.61-5.62 look suspicious, and the fields in the right columns look more like what would be expected from an analysis of the dirty snow effect. However, in comparison with the base fields (each ensemble separately, without anomalies), the anomalies shown in these figures are at least one order of magnitude smaller than the values in the actual radiative forcing fields for both columns. The apparent shift in contours between Def and DefDS is simply due to noise and having an insufficient number of ensemble members for averaging. We also note that as we saw in Sections 4.1 and 5.2, a large instantaneous radiative forcing for stratospheric injections of black carbon aerosols results in modest impacts on climate, so even large anomalies in this field are not particularly indicative of any significant impacts. Therefore, we conclude that all anomalies shown in the radiation and radiative forcing figures are due to noise and cannot be explained by any physical processes specifically related to the dirty snow effect.

Figure 5.63 shows a North polar projection of sea level pressure anomaly to determine whether the dirty snow effect influences circulation patterns by forcing a positive mode of the Arctic Oscillation, as was seen in Section 5.4. The bottom panel (HADS minus HA) shows a pattern that looks like a positive mode of the Arctic Oscillation, but very few of these anomalies are statistically significant, so we cannot make any robust conclusions.
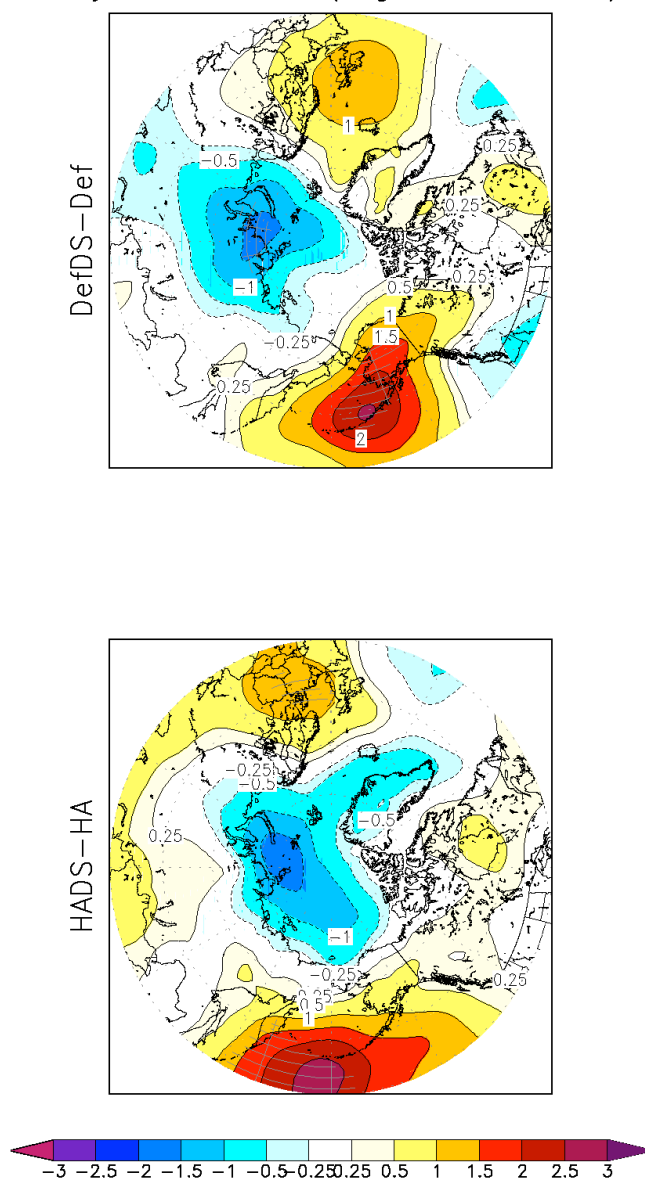
FIGURE 5.63. North polar stereographic projections of sea level pressure anomalies from geoengineering, averaged over the last three years of simulation. Anomalies shown are the result of isolating the dirty snow effect in the model. Ensemble descriptions are given in Table 3.1. Grey hatching denotes values that are statistically significant at the 95% confidence level as calculated by an unpaired two sample Student's *t* test.

Figure 5.64 shows anomalies in snow and ice coverage due to the dirty snow effect. Should the dirty snow effect have a significant climate impact, we would expect to see more heating at the ground due to modification of the ground albedo by the deposited absorbing aerosols, which would result in negative anomalies in snow and ice coverage. However, the anomalies in this figure in the Northern Hemisphere are nearly all positive. A physical mechanism that could explain these anomalies is additional cooling which would cause increased accumulation of snow and ice. However, this mechanism is inapplicable to the dirty snow effect, which should decrease snow and ice coverage, so as in the discussion for Figure 5.56, these anomalies are likely due to noise. The South polar projections show no anomalies.

Although the dirty snow effect appears to have little to no effect in the model under the simulation specifications we have chosen, the effects would likely be more prominent if sea surface temperatures and sea ice coverage were allowed to vary. Black carbon that deposits onto sea ice would cause local heating, melting the ice and amplifying the dirty snow effect seen in our results, as well as creating a positive feedback that reduces planetary albedo. These processes cannot occur under conditions of fixed sea ice coverage, so the dirty snow effect is likely suppressed under our experiments.

Snow and Ice Fraction Anom (%)
Dirty Snow Effect (Avg Last 3 Yrs)
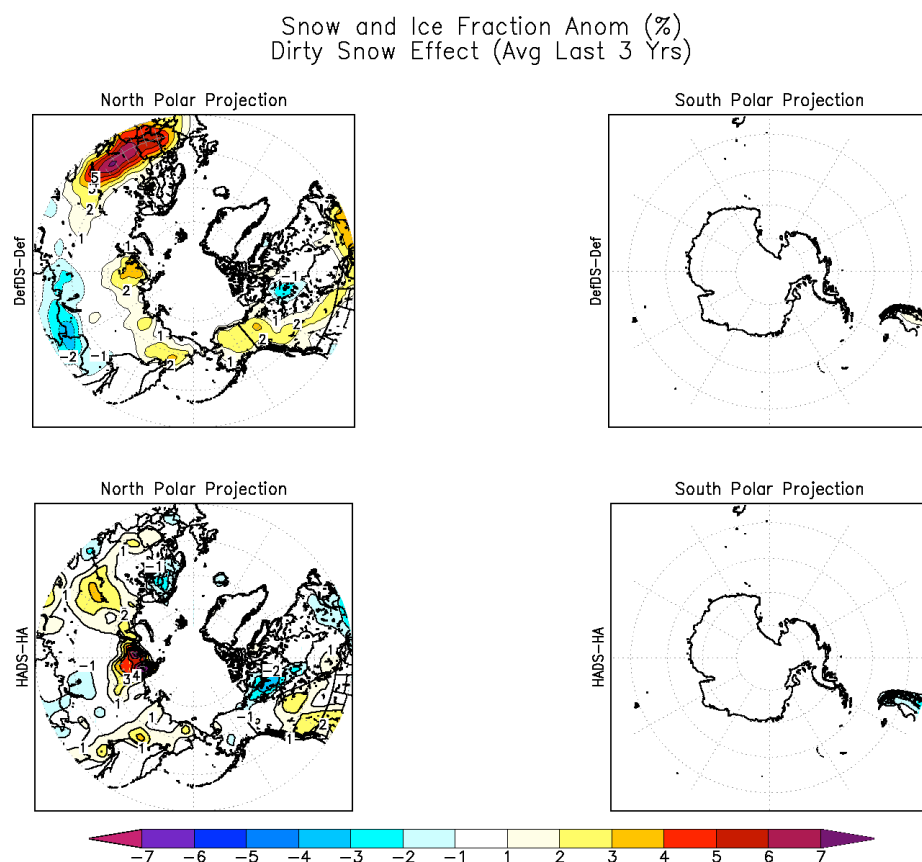
FIGURE 5.64. Polar stereographic projections of snow and ice fraction anomalies from geoengineering, averaged over the last three years of simulation. Anomalies shown are the result of isolating the dirty snow effect in the model. Ensemble descriptions are given in Table 3.1. Grey hatching denotes values that are statistically significant at the 95% confidence level as calculated by an unpaired two sample Student's *t* test.

CHAPTER 6: PRACTICALITY

In Chapter 4, we established some of the climate effects of stratospheric

geoengineering with black carbon aerosols, but we have not yet discussed some

of the residual effects and the practicality of doing so. *Robock et al.* [2009]

addressed some of these issues with regard to sulfur geoengineering, largely

concentrating on the logistics and cost of various delivery mechanisms. We

similarly include such a discussion in this chapter. However, geoengineering

with black carbon introduces several unique concerns, largely stemming from the

method of production of the aerosols, which we discuss in the following sections.

The first ready question is how one can produce 1 Tg of black carbon per

year in the stratosphere. Black carbon is formed from the incomplete combustion

of hydrocarbons, with most anthropogenic sources being the combustion of fossil

fuels. A significant portion of soot created worldwide is due to diesel engines,

both in commercial trucking and the industrial sector [*Ramanathan and*

Carmichael, 2008]. This large share of responsibility for soot production can

potentially be explained by sheer numbers, as diesel engines are in employ

throughout the world. Indeed, in 2002, there were approximately 686,000 diesel

engines operating in the state of Massachusetts alone [*Lyon et al.*, 2007]. Even if

this were not the case, soot production is a particularly sensitive marker of diesel

exhaust [*Fruin et al.*, 2004]. Additionally, diesel combustion has the significant

advantage of a vast infrastructure currently in place, including transportation

and regulation, which would lend this technology particularly well to geoengineering purposes.

However, the primary purpose of combustion of diesel fuel is not to produce black carbon, although it is an abundant product. Elemental carbon has industrial uses, and a manufacturing infrastructure exists to produce it. Carbon black is a compound resulting from furnace combustion of heavy fuel oil in low oxygen [*Crump*, 2000]. Carbon black is generally an agglomeration containing at least 97% elemental carbon particles, whereas black carbon aerosols often contain much less, depending upon the source of the emission [*Watson and Valberg*, 2001]. Carbon black is somewhat different from black carbon aerosols, but for the purposes of calculating logistics, we assume the two are interchangeable on a mass basis. We evaluate the applicability of this assumption in Section 6.5.

Many of the values we use in this chapter involve non-SI units, as the standard units of measurement in the oil and transportation industry in the United States do not follow the SI convention. Where appropriate, we have also included a conversion to SI units.

6.1 LOGISTICS AND COSTS OF USING DIESEL FUEL

Kirchstetter et al. [1999] and *Miguel et al.* [1998] calculate the black carbon emissions for heavy duty diesel vehicles are 1.3±0.3 and 1.4±0.16 g black carbon emitted per kg of fuel used, respectively. Taking the range of 1.0-1.6 g BC per kg diesel fuel, producing 1 Tg = 10^{12} g of black carbon would require 6.25×10^{11} - 10^{12} kg of diesel fuel. Diesel fuel is a mixture of hydrocarbons, and the precise

mixture depends on the refining process, so the density generally varies between 6.8-7.2 lbs gal^{-1}, or 3.08-3.27 kg gal^{-1} (0.81-0.86 kg L^{-1}) [*T. W. Brown Oil Co.*, 1999]. As an average value, we take the density to be 3.18 kg gal^{-1} (0.84 kg L^{-1}). Converting, we have a total requirement of 1.96-3.14×10^{11} gallons (7.41-11.88×10^{11} L) of diesel fuel.

Ban-Weiss et al. [2009] performed similar measurements to those described above and found an average emission of 1.7 g BC emitted per kg of diesel fuel burned, which is similar to the range previously reported. However, they found these results were skewed, in that the highest emitting 10% of all heavy duty diesel trucks were responsible for 42% of all black carbon emissions. The maximum value of this particular emission factor in their study was approximately 10 g BC per kg diesel fuel. Although undesirable near the surface, this particular engine is well suited to geoengineering. We assume diesel engines that produce such large amounts of black carbon are either available or can be readily manufactured. Recalculating with this new emissions factor, producing 10^{12} g of black carbon would require combustion of 3.14×10^{10} gallons (1.19×10^{11} L) of diesel fuel.

Lyon et al. [2007] report the highest emitter of PM2.5 is locomotive engines, which emit approximately 1-2 orders of magnitude more particulate matter per engine than more common engines, such as industrial or road engines. However, due to the relative rarity of these engines, as well as their prohibitive size for the means we discuss later, we exclude them from consideration in this study.

Putting these values into context, in 2003, worldwide consumption of oil was approximately 79 million barrels (1.26×10^{10} L) per day, where each barrel is 42 gallons (159 L) [*EIA*, 2010a]. For each barrel of oil, the petroleum refining process produces 10.04 gallons (38 L) of middle distillates, which consists of diesel fuel and heating oil [*EIA*, 2009]. Since the diesel fuel that would be produced for geoengineering is in addition to current consumption of petroleum products, we assume any additional refining of middle distillates can be tailored to produce only diesel fuel, i.e., for the purposes of calculation, all 10.04 gallons (38 L) of middle distillates are assumed to be diesel fuel. Multiplying, current worldwide diesel fuel production is

$$\frac{79\times10^6 \text{ barrels oil}}{1 \text{ day}} \cdot \frac{365 \text{ days}}{1 \text{ year}} \cdot \frac{10.04 \text{ gallons diesel}}{1 \text{ barrel oil}}$$

or 2.90×10^{11} gallons (1.10×10^{12} L) of diesel. Thus, the additional amount of diesel required for geoengineering would be approximately 10.8% of current production. Refineries in the United States are operating at approximately 90% capacity [*EIA*, 2010b]. Extrapolating this value worldwide, geoengineering by combustion of diesel would likely require additional expansion of the current refining capacity. However, we do not have estimates of cost for this expansion.

Refining 3.14×10^{10} gallons (1.19×10^{11} L) of diesel fuel per year would require consumption of an additional 8.6 million barrels (1.37×10^9 L) of oil per day. In 2009, worldwide oil production was 72.26 million barrels of oil per day [*EIA*, 2010c]. Thus geoengineering would necessitate an increase in production by 11.9%.

We assume the cost of obtaining the oil, refining it into diesel, and transporting it to its desired destination, which would be the geoengineering deployment site, is included in the at-the-pump fuel cost. If the price of diesel fuel is $3.00 per gallon, the cost of the diesel fuel itself is $94.3 billion. For each $0.01 increase in the market price of diesel fuel, the annual cost of geoengineering increases by $314 million.

The next question we address is how to combust this large amount of diesel fuel. Due to the vast prevalence of diesel engines, both new and used, as well as a large amount of experience with manufacturing and testing them, we assume availability of diesel engines is not a limiting factor in our calculations, i.e., the amount of diesel engines that can be manufactured with the proper emission factor is assumed to be unlimited. Instead, a limiting factor is the amount of time a diesel engine requires to combust this amount of fuel. An ideal type of diesel engine for geoengineering is an industrial engine. Many models are designed to run continuously at 100% capacity and need to be maintained relatively infrequently, generally requiring major maintenance after 12,000-30,000 hours of operation [*USP&E*, 2010].

Contrary to advances in technology, our purposes require the least fuel efficient engines available, in that we desire the diesel fuel to be exhausted as quickly as possible so as to produce black carbon aerosols quickly. We recognize that poor fuel economy and large emissions of black carbon possibly may not coincide in diesel engines, but we assume an engine with the desired characteristics can be engineered and manufactured with little effort.

As one of our models for calculation, we use specifications of the Caterpillar 3516B industrial engine [*Caterpillar*, 2010a]. It has an average size of 3221x2091x2053 mm, has a dry weight of 7795-8028 kg, and at maximum capacity consumes fuel on average at 100.4 gallons (380.01 L) per hour. However, the marine propulsion systems model of the same engine has a maximum fuel consumption of 143.4 gallons (542.77 L) per hour [*Caterpillar*, 2010b]. We assume that by various engineering means, the throughput of the engine can be modified to reach this maximum value of 143.4 gallons (542.77 L) per hour. Average costs for this particular engine are not available, but several auctions reported the sold price at $395,000 (used), which we adopt as our price estimate.

As a second model, we considered the Caterpillar 3406C industrial engine [*Caterpillar*, 2010a]. It is considerably smaller, with an average size of 1500x879x1295 mm, a dry weight of approximately 1481 kg, and at maximum capacity consumes 20.5 gallons (77.59 L) per hour. It is considerably cheaper, with searches revealing a price of approximately $18,000.

For the 3516B engine, combusting 3.14×10^{10} gallons (1.19×10^{11} L) of fuel at a rate of 143.4 gallons (542.77 L) per hour would require 2.19×10^8 hours. If we assume the engine will be in operation for 8 hours per day, 365 days per year, for a total of 2920 hours per year, this would require approximately 75,100 engines. If we assume the engine will be in operation continuously throughout the year, for a total of 8760 hours per year, this would require approximately 25,034 engines. At a unit cost of $395,000 each, the total cost for the engines would be $29.7 billion and $9.9 billion, respectively.

For the 3406C engine, combusting this same amount of fuel would require 1.53×10^9 hours. Assuming the same hours of operation as previously, this would require approximately 525,335 and 175,112 engines, respectively. At a unit cost of $18,000, the total cost for these engines would be $9.5 billion and $3.2 billion, respectively.

As with any machine, these engines will require periodic maintenance, which will incur both cost and downtime. According to the Caterpillar maintenance manual for the 3516B engine [*Caterpillar*, 2010c], light maintenance is required every 250 hours of operation, and a major overhaul is required every 18,000 hours. The 3406C engine requires light maintenance every 250 hours of operation or 2500 gallons (9462.5 L) of fuel consumed and an overhaul every 6000 hours of operation or 60,000 gallons (227,100 L) of fuel consumed [*Caterpillar*, 2010c]. We assume that for light maintenance, the engine will be unavailable for one 8 hour shift. For a major overhaul, we assume the engine will be unavailable for three consecutive shifts, or 24 hours total operation time.

Based on these scheduled downtimes, the 3516B engines will require light maintenance every 31 8-hour shifts, and the 3406C engines will require maintenance every 15 8-hour shifts. They will require major overhauls every 2322 and 389 shifts, respectively, which includes all shifts lost to light maintenance. Therefore, in an average year of one shift per day, the 3516B engine will lose 12 shifts to maintenance, and the 3406C will lose 26 shifts. In a year of three shifts per day, they will lose 36 and 79 shifts, respectively. Table 6.1 summarizes the calculations involved.

We were unable to find robust maintenance estimates for the engines we consider. However, we were able to find broad estimates for the Caterpillar G3520 industrial gas engine, widely in use by large utility companies. The estimates we found are a cost of approximately $0.007-0.008 per kilowatt-hour.[3] Since gas engines generally have more frequent and more expensive maintenance requirements [*USP&E*, 2010], we use $0.008 per kilowatt-hour as an upper limit for our calculations. We assume the cost of a mechanical crew to perform this maintenance is included in this cost estimate.

The 3516B engine runs at a maximum of 1492 kW of power generation, and the 3406C runs at a maximum of 313 kW [*Caterpillar*, 2010a]. In a year with 2920 hours of operation, based on a maintenance cost of $0.008 per kilowatt-hour, this amounts to annual costs of $34,853 and $7312, per engine, respectively. In a year with 8760 hours of operation, these increase to $104,559 and $21,935, per engine, respectively. *Caterpillar* [2010d] estimates a complete overhaul to be 40-70% of the cost of a new engine. At 8760 hours per year, the 3516B would require an overhaul approximately every 2 years, and the 3406C approximately every year, so these estimates of maintenance cost appear to be quite reasonable.

MacKay and Co. [2003] list average diesel engine lifespans to be in the range of 10-22 years [*Lyon et al.*, 2007]. We do not include the cost or logistics of

---

[3] Comment posted on message board "Caterpillar - Maintenance Costs" by Robert McConnell, SCS Energy National Caterpillar Maintenance Manager, on 24 December 2008. Available online at https://caterpillar.lithium.com/t5/Power-Generation-Site-Design/Maintenance-Costs/m-p/247.

TABLE 6.1. Calculations of maintenance requirements for the Caterpillar 3516B and 3406C engines. Estimates of maintenance frequency are taken from *Caterpillar* [2010c]. Details of the calculations are given in Section 6.1. One 8-hour shift per day is equivalent to 2920 hours per year, and three shifts per day is equivalent to 8760 hours per year.

	2920 hours per year		8760 hours per year	
	3516B	**3406C**	**3516B**	**3406C**
Lost shifts per year	12	26	36	79
Percentage down time	3.2%	7.1%	3.2%	7.1%
Engines required, assuming no downtime	75,100	525,335	25,034	175,112
Additional engines required to compensate for downtime	2553	40,291	851	13,616
Additional capital cost	$1 billion	$725 million	$336 million	$245 million
Total engines needed	74,053	565,626	25,885	188,728
Annual maintenance cost per engine	$34,853	$7312	$104,559	$21,935
Total annual maintenance cost	$2.6 billion	$4.1 billion	$2.7 billion	$4.1 billion

periodic replacement of the engines in this study, as we do not wish to make assumptions about how long geoengineering must be done.

Since we want the black carbon aerosols to be in the stratosphere, the most sensible idea would be to produce them directly in the stratosphere. A natural solution is to place these engines and diesel fuel in the cargo hold of airplanes and fly them to the stratosphere, as was done for the calculations of *Robock et al.* [2009]. *Robock et al.* assumed flights of 2 hours in length, 3 times per day, for 250 days per year. However, since the diesel engines we consider are designed to run continuously, we consider a longer flight of 8 hours, which motivates our choice above for the period of operation.

Robock et al. [2009] evaluated several choices of aircraft that would be suitable for geoengineering. Two of their choices for calculations are repeated in Table 6.2 and are the basis for our calculations here. They analyzed the F-15C Eagle, a fighter plane, and two refueling tankers: the KC-135 Stratotanker and the KC-10 Extender [*USAF*, 2010a, 2010b]. The F-15C can fly the highest of the three, easily reaching the stratosphere throughout the world, but its payload is by far the smallest and is prohibitively small for geoengineering using diesel fuel combustion with the engines we have described, so we do not include it in our calculations. The KC-10 has the largest payload but the lowest maximum altitude and is thus only capable of reaching the stratosphere at high latitudes. It is also the more expensive of the two airplanes. The KC-135 has a higher ceiling but a smaller payload.

TABLE 6.2. Two choices of airplanes that can be used for stratospheric geoengineering, after *Robock et al.* [2009]. All values for the KC-135 Stratotanker are from *USAF* [2010b], and the KC-10 Extender from *USAF* [2010a]. Prices were converted to 2010 dollars by *Williamson* [2010].

Airplane	Payload (kg)	Ceiling (km)	Unit Purchase Price (2010 dollars)
KC-135 Stratotanker	37,648	15.2	$52.1 million
KC-10 Extender	76,560	12.7	$116.0 million

Each airplane is capable of carrying more than one engine, so we decompose our calculations into units, which consists of an engine and 8 hours of diesel fuel. The 3516B engine weighs up to 8028 kg and can consume 1146.4 gallons (4339.12 L) of fuel in 8 hours, for a total unit weight of 11,977.0 kg. The 3406C engine weighs 1481 kg and can consume 164 gallons (620.74 L) of fuel in 8 hours, for a total unit weight of 2045.9 kg. Table 6.3 summarizes the carrying capacity of each airplane, as well as the number of required airplanes of a given type. Costs are roughly the same order of magnitude for all four combinations of engine and airplane type.

Curtin [2003] gives an estimate of $3.7 million in annual cost, based on 300 flying hours per year, for personnel, fuel, maintenance, modifications, and spare parts for the KC-135 airplane. As *Robock et al.* [2009] state, the KC-10 is a newer airplane and would likely be cheaper, so we use this value as an upper limit for our estimations. Scaling these maintenance costs, for each 8-hour shift a plane flies each day, annual maintenance and personnel costs will be approximately $36 million per plane. These values are also reported in Table 6.3.

Table 6.4 shows the separated fixed and annual costs for the four combinations (two types of engine and two types of airplane). Table 6.5 shows the total cost, including all initial fixed costs and annual costs previously discussed, after 5 years of geoengineering. We do not include line graphs of the different geoengineering combinations, as the lines do not overlap after the first year, so a 5 year cumulative cost figure is sufficient for determining the most inexpensive option. Comparisons between the two engines (Caterpillar 3516B

TABLE 6.3. Calculation of the number of airplanes needed to hold each diesel engine unit (engine plus 8 hours of fuel). Engine unit weight is 11977 kg for the 3516B engine and 2045.9 kg for the 3406C engine, as calculated in Section 6.1. Annual operational costs are assumed to be $36 million per airplane per 8-hour shift after scaling values in *Curtin* [2003].

	Caterpillar 3516B Engine		Caterpillar 3406C Engine	
	KC-135 Tanker	KC-10 Extender	KC-135 Tanker	KC-10 Extender
Number of Engine Units per Plane	3	6	18	37
Number of planes needed (2920 hours per year)	24,684	12,342	31,424	15,287
Total purchase price for airplanes (2920 hours per year)	$1.3 trillion	$1.4 trillion	$1.6 trillion	$1.8 trillion
Number of planes needed (8760 hours per year)	8628	4314	10,485	5101
Total purchase price for airplanes (8760 hours per year)	$450 billion	$500 billion	$546 billion	$592 billion
Total annual cost of operation (per 8-hour shift)	$889 billion	$444 billion	$1.1 trillion	$550 billion

TABLE 6.4. Fixed (one-time) and annual costs for geoengineering by combustion of diesel fuel for each combination of engine and airplane under consideration. Included in the annual costs are an estimate of fuel consumption with an at-the-pump price of $3.00 per gallon, for a total of $94.3 billion.

Engine/Airplane	2920 hours per year		8760 hours per year	
	Fixed	Annual	Fixed	Annual
3516B, KC-135	$1.3 trillion	$986 billion	$460 billion	$2.8 trillion
3516B, KC-10	$1.4 trillion	$541 billion	$510 billion	$1.4 trillion
3406C, KC-135	$1.6 trillion	$1.2 trillion	$549 billion	$3.4 trillion
3406C, KC-10	$1.8 trillion	$648 billion	$595 billion	$1.7 trillion

TABLE 6.5. Fixed costs plus cumulative annual costs for 5 years of geoengineering using diesel fuel combustion.

Engine/Airplane	2920 hours per year	8760 hours per year
3516B, KC-135	$6.2 trillion	$14.5 trillion
3516B, KC-10	$4.1 trillion	$7.5 trillion
3406C, KC-135	$7.6 trillion	$17.5 trillion
3406C, KC-10	$5.0 trillion	$9.1 trillion

and 3406C) show that although the 3516B engine is much more expensive, fewer are needed, which makes using this engine the cheaper option by approximately $1 trillion after 5 years, in all cases. Although the equipment costs are reduced if geoengineering 3 shifts per day, the maintenance costs are much higher and rapidly overtake the fixed costs, meaning geoengineering with one shift per day and more physical equipment is the cheaper option. Using the KC-10 Extender is cheaper than using the KC-135, with the increased payload capacity being the determining cost factor. Thus, the cheapest option is using the Caterpillar 3516B engine in the KC-10 Extender for one 8-hour shift per day. This has a fixed cost of $1.4 trillion and an annual cost of $541 billion.

For comparison, the world gross domestic product (purchasing power parity) in 2009 was $69.98 trillion [*CIA*, 2010]. Using the cheapest option as described previously, the initial investment would be approximately 2.0% of worldwide GDP, with an additional 0.8% each year. The range of options we have calculated are an initial investment of 0.7-2.6% of GDP, with an additional 0.8-4.9% per year. According to the Stern Review [*Stern et al.*, 2006], the cost of climate change for 2-3°C of warming could be a permanent loss of 0-3% of GDP, and a warming of 5-6°C would result in a loss of 5-10% of global GDP, with poor countries suffering possibly even greater losses than 10%. In that context, geoengineering with black carbon aerosols is slightly cheaper than the damage that would be caused by climate change and is vastly more expensive than geoengineering with sulfate aerosols [*Robock et al.*, 2009]. However, as we saw in

Chapter 4, this method of geoengineering will have undesirable side effects for which we have not calculated the potential costs. In contrast, *IPCC* [2007] calculates that mitigation to reach a stabilization of 535-590 ppm CO_2-eq would result in a GDP reduction by 0.2-2.5%, with a median reduction of 0.6% and an annual reduction of GDP growth rate by less than 0.1%. Compared to the cost of black carbon geoengineering, mitigation is cheaper, possibly by as much as one order of magnitude.

6.2 DIESEL COMBUSTION EMISSIONS FACTORS

Although our primary desired product of combustion of diesel fuel is black carbon aerosols, there will be many other products released. Table 6.6 summarizes the various emission factors for the most abundant products of combustion of diesel fuel in industrial engines, some of which we now examine in more detail.

6.2.1 CARBON DIOXIDE

Anthropogenic carbon dioxide is the chief contributor to climate change [*Solomon et al.*, 2007]. Since it is an abundant product of combustion, we analyze the amount that would be produced by geoengineering methods using diesel fuel. The Environmental Protection Agency has calculated the amount of CO_2 emitted by combusting one gallon of diesel fuel [*EPA*, 2005]. Assuming a diesel carbon content of 2778 g per gallon of fuel and that 99% of the fuel is eventually oxidized, they calculate an emission of 10.084 kg CO_2 per gallon of diesel fuel

TABLE 6.6. The prominent products of diesel fuel combustion and their emission factors. Values for CO_2 are obtained from *EPA* [2005] and are based on the assumptions as given in Section 6.2.1. Values in the second column are repeated from *EPA* [1996]. Values in the third column are obtained from the second column via the following formula:

$$n\frac{\text{lb emission}}{\text{MMBtu}} \cdot \frac{1 \text{ MMBtu}}{10^6 \text{ Btu}} \cdot m\frac{\text{Btu}}{\text{lb fuel}} \cdot p\frac{\text{lb}}{\text{gal fuel}} \cdot \frac{0.45359237 \text{ kg emission}}{\text{lb}}$$

$$= nmp \cdot 0.45359237 \times 10^{-6} \cdot \frac{\text{kg emission}}{\text{gal fuel}}$$

where m=19300 Btu per lb for diesel fuel, n is the particular emissions factor given in lb fuel input per MMBtu, and p is the density of diesel fuel, which we take as an average value to be 3.18 kg gal^{-1} (0.84 kg L^{-1}) [*T. W. Brown Oil Co.*, 1999], or 7.01 lb gal^{-1}.

Compound	Emissions Factor (lb per MMBtu fuel input)	Emissions Factor (kg per gallon/Liter fuel)
CO_2	164	10.084/2.664
NO_x	4.41	0.271/0.072
CO	0.95	0.058/0.015
Organic Compounds (exhaust)	0.35	0.021/0.006
PM-10	0.31	0.019/0.005
SO_x	0.29	0.018/0.005
Aldehydes	0.07	0.004/0.001
Organic Compounds (crankcase)	0.01	0.001/<0.001

burned. Therefore, combusting 3.14×10^{10} gallons (1.19×10^{11} L) of diesel fuel would release approximately 3.2×10^{11} kg of additional CO_2 per year. The total worldwide emissions of CO_2 are approximately 29.3×10^{12} kg of CO_2 per year [*IEA*, 2010], so this would constitute an additional 1.1% of annual emissions.

We also consider the additional CO_2 that would be produced from the airplanes used to inject the black carbon into the stratosphere. Jet fuel produces a similar amount of CO_2 to diesel fuel, with an emissions factor of 9.507 kg CO_2 per gallon of fuel [*EIA*, 2005].

Assuming the payloads for each of the three aircraft considered, as reported in Table 6.2, we can calculate how much of its own fuel each airplane can hold, based on the airplanes' dry weights and maximum take-off weights. These values are reported in Table 6.7. We also assume that during each 8-hour shift, the airplanes exhaust this entire capacity. Multiplying by the emissions factor given above, and given an average jet fuel density of 3.03 kg gal^{-1} (0.80 kg L^{-1}) [*Sprague*, 2006], the KC-135 Stratotanker will produce 172,515 kg CO_2 per shift per airplane, and the KC-10 will produce 251,167 kg.

Table 6.8 summarizes the additional CO_2 that would be emitted for each of the four cases (airplane type and engine type). The largest value in Table 6.8 is 4.26×10^9 kg, which is two orders of magnitude lower than the additional CO_2 that would be emitted from combustion of the diesel fuel, so we conclude this source of CO_2 is negligible. Moreover, in 2008, the commercial aviation industry produced 6.77×10^{11} kg of CO_2, or approximately 2.3% of worldwide emissions

TABLE 6.7. Payload capacity, dry weight, calculated jet fuel weight, and maximum take-off weights for each type of airplane. All values are in kg. Payload and maximum take-off weights are from *USAF* [2010a, 2010b]. Dry weights are from *Global Aircraft* [2010a, 2010b]. Jet fuel weight is calculated from the difference.

	KC-135 Tanker	KC-10 Extender
Payload	37,648	76,560
Dry Weight	53,654	108,890
Jet Fuel	54,983	80,050
Maximum Take-off Weight	146,285	265,500

TABLE 6.8. Additional CO_2 emissions from jet fuel combustion. Values in the first column are taken from Table 6.3. Values in the second column are from Section 6.2.1 and are based on the assumption that the airplanes exhaust their jet fuel capacity (Table 6.7) each 8-hour shift.

Engine/Airplane	Total shifts per year	CO_2 emitted per shift (kg)	Total CO_2 emitted per year (10^9 kg)
3516B, KC-135	24,684	172,515	4.26
3516B, KC-10	12,342	251,167	3.10
3406C, KC-135	31,424	172,515	3.70
3406C, KC-10	15,287	251,167	3.84

[*Enviro Aero*, 2009]. This additional CO_2 would constitute less than 1% of current aviation emissions.

6.2.2 NO_x

One of the major byproducts of diesel combustion is NO_x, essentially all of which is the result of high temperature dissociation of nitrogen in the air [*EPA*, 1996]. The emissions factor for NO_x as given in Table 6.6 is approximately 0.271 kg per gallon of fuel burned. Therefore, producing 1 Tg of black carbon would also result in the production of 8.51×10^9 kg of NO_x in the stratosphere. The total atmospheric mass is approximately 5×10^{18} kg. Approximately 90% of the atmosphere's mass is contained in the troposphere, and layers above the stratosphere have very little mass, so we assume this new amount of created NO_x is distributed throughout the remaining 10% of the atmosphere's mass. This results in an increase in the NO_x concentration of the stratosphere by approximately 1.70 ppb. Total worldwide NO emissions in 1990 were 49.6 Tg, or 4.96×10^{10} kg [*Stevenson et al.*, 2004]. NO_x emissions from diesel combustion for geoengineering would be an additional 17% of this figure.

NO_x is is an effective catalyst for destruction of stratospheric ozone [*Crutzen*, 1970]. NO_x concentrations in the stratosphere peak at approximately 10 ppb near the 10 mb level [*SPARC CCMVal*, 2010]. Thus geoengineering would result in a 17% increase in stratospheric NO_x concentrations, which would result in a reduction of stratospheric ozone. This is in addition to the ozone destruction

caused by stratospheric heating directly due to the aerosols, which we discussed in Chapter 4.

Calculating the actual destruction of ozone that would result from this increase in NO_x is not straightforward. Above approximately 26 km in altitude, which accounts for less than half the total ozone column, the NO_x catalytic cycle is the primary source of ozone destruction [*Jucks et al.*, 1996]. Below this level, ozone destruction mechanisms are more complicated, involving reactions between the NO_x, ClO_x, HO_x, and BrO_x cycles. Indeed, a large increase in NO_x in the stratosphere would cause a reduction of ozone in the middle stratosphere but an increase by nearly twice that magnitude in the lower stratosphere due to interactions between these cycles, as NO_x reduces ozone destruction by these species [*Finlayson-Pitts and Pitts*, 2000]. Moreover, production of a large amount of SO_x and black carbon aerosols in the stratosphere would increase the available surface area for stratospheric chemistry, which may further increase ozone loss rates but decreasing the direct impact of NO_x on ozone [*Stolarski et al.*, 1995].

Combining the effects of these different mechanisms to determine the exact chemical impact of geoengineering on ozone is not feasible without a chemistry model. However, *Stolarski et al.* [1995] performed a multi-model experiment, based on an idea of *Johnston* [1971], simulating ozone destruction due to a fleet of high speed civil transport aircraft flying in the stratosphere. They calculated that for a fleet of 500 aircraft, burning a total of 8.2×10^{10} kg fuel per year, the total ozone column would change by -0.3 to +0.1% for an emissions factor of 5 g NO_2 per kg fuel and -1.0 to -0.02% for a factor of 15 g NO_2 per kg

fuel. These correspond to 4.1×10^8 kg and 1.23×10^9 kg NO_x produced,

respectively. They also performed the same calculations for 1000 aircraft, or

double the amount of fuel, which resulted in -0.7 to -0.03% and -2.7 to -0.6%

change in total ozone column, respectively. Table 6.9 shows these calculations

more clearly.

Burning 3.14×10^{10} gallons (1.19×10^{11} L) of diesel fuel will produce 8.51×10^9

kg of NO_x by our calculations, or approximately 3.5 times the amount that would

be produced by 1000 planes at 15 g NO_2 per kg fuel burned. Based on the values

given by *Stolarski et al.* [1995], as well as our understanding of the mechanisms

and complex interactions involved, the total ozone column response to NO_x

appears to be nonlinear. However, applying a basic linear fit[4] to the points given

and extrapolating, we obtain the rough estimate that combustion of diesel fuel

for geoengineering could cause a -9.8 to -2.6% change in total ozone column due

to NO_x alone.

6.2.3 SO_x

Sulfur compounds resulting from diesel fuel combustion are due to sulfur

content of the fuel. During the combustion process, nearly all of the sulfur is

oxidized to SO_2, which is a precursor to sulfate aerosols [*EPA*, 1996].

Performing similar calculations using the emissions factor given in Table

6.6, creating 1 Tg of black carbon aerosols would result in the production

---

[4] The linear fit for the low end of the range (most negative) is described by $y=-0.1185x+0.2821$, where x is NO_x produced (10^8 kg) and y is the % change in total ozone column. The high end of the range (most positive) is described by $y=-0.0343x+0.2846$. The R^2 values for the fits are 0.9867 and 0.9375, respectively.

TABLE 6.9. NO_x production and subsequent catalytic ozone destruction from the ensembles presented in *Stolarski et al.* [1995]. The last line of the table contains our calculations. Our NO_x emissions factor is converted from Table 6.6. Our total column ozone change is constructed from the linear fit to the *Stolarski et al.* data, as described in Section 6.2.2.

Fuel Combusted (10^{10} kg)	NO_x emissions factor (g NO_2 per kg fuel)	Total NO_x Produced (10^8 kg)	Total Column Ozone Change (%)
8.2	5	4.1	-0.3 to +0.1
8.2	15	12.3	-1.0 to -0.02
16.4	5	8.2	-0.7 to -0.03
16.4	15	24.6	-2.7 to -0.6
9.98	85.2	85.1	-9.8 to -2.6

of 5.65×10^8 kg of SO_2, or approximately 0.57 Tg. In comparing this with the extensive literature on volcanic eruptions and geoengineering with sulfate aerosols, this amount of sulfur is likely insignificant from a climate perspective [*Robock et al.*, 2008; *Kravitz and Robock*, 2011]. It is also an insufficient amount to produce damaging acid rain [*Kravitz et al.*, 2009, 2010b].

Using the mass balance equation in Section A.1 and an *e*-folding lifetime of one year for sulfate aerosols [*Stenchikov et al.*, 1998], the peak atmospheric loading of sulfate would be 0.57 Tg. *Robock et al.* [2008] performed continuous tropical injections totaling 5 Tg SO_2 per year, which oxidizes into 7.5 Tg of sulfate aerosols per year. They reported a radiative forcing from this scenario of approximately 1.8 W m^{-2}, globally averaged. Since the amount of radiative forcing scales linearly with the atmospheric loading of sulfate aerosols [e.g., *Hansen et al.*, 2005; *Kravitz and Robock*, 2011], the sulfate from geoengineering with black carbon would result in a globally averaged radiative forcing of approximately 0.14 W m^{-2}. The temperature response also scales linearly with sulfate aerosol optical depth [e.g., *Ricke et al.*, 2010], so their reported cooling of approximately 0.4°C would scale in our case to a cooling by 0.03°C, which is undetectable against the background weather noise. We therefore conclude the climate effects due to the addition of sulfate would be negligible.

The chemistry effects of this increase in SO_x may not be trivial, especially when considering the effects on ozone. *Tilmes et al.* [2009] performed model simulations of stratospheric injections of 2 Tg S per year, which is approximately 7 times more sulfur than our current calculations. They discovered a much

higher polar ozone destruction rate, causing a delay in the recovery of the
Antarctic ozone hole by approximately 30 years. Interpolating these results to
our own is not straightforward, due to the nonlinearity of the ozone response,
interactions with other cycles, and increased stratospheric surface area that
would result, but the results of *Tilmes et al.* suggest the additional SO_x from our
diesel fuel combustion calculations would increase ozone destruction rates.

The SO_x emissions factors reported in Table 6.6 were calculated in 1996.
Since that time, ultra-low sulfur diesel has been introduced to the market, and in
recent years is the only diesel fuel readily available in the United States [*EPA*,
2009]. Therefore, the sulfur introduced into the stratosphere from
geoengineering by diesel combustion would likely be smaller than the values
above. However, we do not have sufficient data of new emissions factors to
calculate this difference.

6.3 LOGISTICS AND COSTS OF USING CARBON BLACK

Carbon black feedstock is produced from fractional distillation of
petroleum and is generally extracted as a heavy or residual fuel oil [*Dow*, 2010a,
2010b; *ICBA*, 2004]. We are unable to find an exact figure for what portion of
petroleum refining products are used by the carbon black industry, but residual
fuel oil comprises approximately 8% of U.S. refinery yields [*EIA*, 2010b], so we
assume the same 8% yield from each barrel of oil will be suitable for making
carbon black feedstock. Using this value, of the 44.08 gallons (166.84 L) of
products from each barrel of oil [*EIA*, 2009], each 42 gallon (159 L) barrel would

yield 3.53 gallons (13.36 L) of petroleum products that could serve as feedstock for the carbon black manufacturing process.

EPA [1995] reports that for the oil furnace process, carbon black yields are 35-65%, depending on the chosen feedstock and the desired particle size, with smaller particles resulting in lower yields. As we desire these smaller particles, we assume the lowest value in this range, in that 1 kg of fuel feedstock will result in 0.35 kg of carbon black. Given an average density of carbon black feedstock of 4.09 kg gal^{-1} (1.08 kg L^{-1}) [*Dow*, 2010b], each gallon of fuel combusted produces 1.43 kg of carbon black. This means producing 1 Tg of carbon black will require 7×10^8 gallons of fuel. Assuming each barrel of oil yields 3.53 gallons (13.36 L) of feedstock, this would require 2×10^8 barrels (3.18×10^{10} L) of oil per year.

As in Section 6.2.1, worldwide consumption of petroleum is 79 million barrels (1.26×10^{10} L) per day, or 2.88×10^{10} barrels (2.62×10^{12} L) per year [*EIA*, 2010a]. Thus, the additional oil required would be 0.7% of current consumption. Assuming refineries worldwide are operating at 90% capacity, producing this additional amount of petroleum products would not require an expansion of refining capacity.

The requirement of 2×10^8 barrels (3.18×10^{10} L) of oil per year is approximately 550,000 barrels (8.74×10^7 L) per day. As stated previously, in 2009, worldwide oil production was 72.26 million barrels (1.15×10^{10} L) of oil per day

[*EIA*, 2010c]. Therefore, this additional requirement would be approximately 0.8% of current production.

In 1998, the estimated total furnace black manufacturing capacity of carbon black in the United States was 1.9×10^9 kg [*Crump*, 2000]. Of the plants surveyed by *Crump*, their total output was 16% of capacity, meaning the additional availability of carbon black that could be produced by these plants alone was approximately 1.6×10^9 kg.

The annual production costs for all carbon black produced in 1998 in the United States was $625 million [*Crump*, 2000], which averages to approximately $0.33 per kg. The finest grade carbon black, which has the smallest particle diameter and would thus be the most useful for geoengineering, had a 1998 cost of approximately $1.03 per kg. If the party deciding to engage in geoengineering wishes to produce its own carbon black, it would cost them $330 million dollars per Tg per year. If they wish to buy at market rates, it would cost $1 billion per Tg per year. Since building a parallel refining and production infrastructure would likely cost significantly more than $670 million, and the current infrastructure has the capacity to produce enough carbon black to satisfy the requirements of geoengineering 1 Tg of carbon black per year, for the purpose of calculating costs, we assume carbon black used in geoengineering will be purchased at market rates.

The costs of ferrying 1 Tg of carbon black to the stratosphere are the same as reported in *Robock et al.* [2009], as their calculations were for 1 Tg of generic material. We repeat some of the relevant calculations here, as in Section 6.1. The

airplane unit costs will be the same as in Table 6.2. *Robock et al.* [2009] assumed the airplanes would be capable of dispersing their payload of material in 2-hour shifts, and the airplanes would fly three shifts per day. We similarly assume the payload can be dispersed in 2-hour shifts, but we choose to geoengineer in 4 shifts per day, allowing us to use our previous calculations for 8-hour intervals.

The calculations of cost for transporting 1 Tg of carbon black to the stratosphere via airplanes each year are given in Table 6.10. Again, the larger payload capacity of the KC-10 Extender is the determining factor in cost, as this is the cheapest option with fixed costs of $1 billion and annual costs of $324 million. The total per-teragram cost of geoengineering with carbon black is $1 billion fixed and $1.3 billion annually, which is approximately three orders of magnitude cheaper than using diesel combustion. We do not include the cost of transporting the carbon black to the geoengineering site in these estimates, as we do not wish to speculate on where the geoengineering site(s) would be.

6.4 CARBON BLACK EMISSIONS FACTORS

The most common method of manufacturing carbon black is the furnace black process, in which heavy crude distillates are combusted in low oxygen [*Crump*, 2000]. Since this accounts for over 95% of carbon black production, we use the emissions factors for this particular method. Table 6.11 gives the most prominent byproducts of the furnace black process. From a climate perspective, the byproducts of concern here are carbon monoxide and methane.

TABLE 6.10. Airplanes required to deliver 1 Tg of carbon black to the stratosphere. Calculations are based on each plane making four 2-hour trips to the stratosphere and dumping its payload during each shift. Purchase prices are as in Table 6.2. Annual operational costs are assumed to be $36 million per airplane per 8-hour shift after scaling values in *Curtin* [2003].

	KC-135 Stratotanker	**KC-10 Extender**
Delivery amount per plane per day	150,592 kg	306,240 kg
Delivery amount per plane per year	5.50×10^7 kg	1.12×10^8 kg
Number of planes needed	19	9
Total purchase price	$990 million	$1044 million
Annual operation costs	$684 million	$324 million

TABLE 6.11. Emissions factors for oil furnace carbon black manufacture. All values are from *EPA* [1995]. All unlisted products have an emissions factor at least one order of magnitude below all listed products.

Compound	Emissions Factor (kg emission per Mg carbon black produced)
Carbon monoxide	1400
Hydrogen sulfide	30
Carbon disulfide	30
Carbonyl sulfide	10
Methane	25
Acetylene	45

6.4.1 CARBON MONOXIDE

CO is by far the predominant product of carbon black manufacturing, although the concentrations can be reduced by up to 99.8 percent by controlling with CO boilers, incinerators, or flares [*EPA*, 1995]. Without these controls, producing 10^9 kg of carbon black would result in the emission of 1.4×10^9 kg of CO. Carbon monoxide is naturally produced at a rate of 5×10^{12} kg annually in the troposphere, which is approximately 25 times larger than combustion sources [*Weinstock and Niki*, 1972]. Therefore, from an aggregate standpoint, the additional CO from producing this large amount of carbon black would be negligible. The stratosphere is a natural sink for carbon monoxide, due to reaction with the hydroxyl radical [*Pressman and Warneck*, 1970], so we anticipate this emissions factor would not cause any noticeable adverse effects. With the reductions in CO concentrations at the source, this total annual emission can be reduced to as little as 2.8×10^6 kg.

6.4.2 METHANE

Methane is a powerful greenhouse gas, 23 times more effective than CO_2 [*Solomon et al.*, 2007]. From the emissions factor reported in Table 6.11, producing 10^9 kg of carbon black would result in the production of 2.5×10^7 kg of methane. Given that the total atmospheric mass is approximately 5×10^{18} kg, this is an increase in the atmospheric methane concentration by 4.9 parts per trillion. Current concentrations of methane are six orders of magnitude larger [*Solomon et al.*], so this is a negligible contribution to atmospheric methane.

6.5 ADDITIONAL ASSESSMENTS

Although calculating the logistics and costs of geoengineering is rather straightforward based on the assumptions we have made, there are several issues which we cannot so easily quantify. Possibly the most important problem we encounter is the health effects of geoengineering. Diesel fuel, black carbon aerosols, carbon black, and their respective byproducts of manufacture and combustion are hazardous to human health [e.g., *CDC*, 1999; *Baan et al.*, 2006]. This poses a risk to all those in the employ of the geoengineering program, as well as those affected by deposition of the particulate matter. Additionally, in combustion of diesel fuel, a small portion of the emissions (2-3%) are through the crankcase instead of the exhaust, which could pose a hazard to the airplane pilots and the maintenance crews [*EPA*, 1996].

One of the problems specific to carbon black regards its feasibility as a substitute for black carbon aerosols. Carbon black is almost purely elemental carbon, whereas black carbon aerosols have a larger portion of adsorbed organic carbons [*Watson and Valberg*, 2001]. However, the mechanisms of formation of the two compounds are quite similar [*Medalia et al.*, 1983], so we can assume the particle density and refractive indices are similar without introducing a large amount of error into our calculations [*Fuller et al.*, 1999].

Despite this similarity, carbon black particles are much larger than black carbon aerosols. A typical radius of black carbon aerosol is approximately 0.1 μm [*Rose et al.*, 2006]. However, a typical carbon black agglomerate can have a diameter on the order of millimeters [*Gandhi*, 2005]. A larger diameter means a

greatly increased fall speed, so the same mass of carbon black may be significantly less effective for geoengineering. We suggest the possibility that the carbon black agglomerates can be ground or dissociated into the smaller individual particles, similar in size to black carbon aerosols, but this idea requires further investigation.

One additional point regards aerosol production by the combustion of jet fuel in the process of transporting the soot or soot-making apparatus to the stratosphere. Jet fuel is similar to diesel fuel, except it is often much more carefully refined and is treated with additives to better help the combustion process tolerate the extreme temperatures and chemical conditions found in the middle atmosphere [*Chertkov*, 1971]. Extrapolating from the values in Table 6.7, the maximum amount of jet fuel combusted would be 5.7×10^8 gallons (9.06×10^{10} L), or two orders of magnitude less than the amount of diesel fuel combusted. Therefore, even if the black carbon emission factors were the same for diesel fuel, the amount of jet fuel combusted would be very small compared to the amount of diesel fuel combusted, so any potential contributions of jet fuel to the soot aerosol mass would be negligible.

CHAPTER 7: UNCERTAINTIES AND FUTURE WORK

As in any study, our experiment invites many more questions. Some of

these involve uncertainties and assumptions we made in our study, as the tools

we have available to us, namely a general circulation model, are not

all-encompassing and are not necessarily best suited to answer every question.

Some others involve further investigations we can pursue using different tools,

such as other more specialized models. In this chapter, we present our

uncertainties and assumptions, and we highlight future investigations we would

like to undertake to resolve some of these additional questions.

7.1 UNANSWERED QUESTIONS

In the course of our study, two questions arose which we could not

answer. The first is why the aerosol deposition in the ensembles appears to be

dominated by wet deposition over the poles during winter, despite no increase in

polar precipitation. We have postulated a reason which involves the aerosols

being trapped inside the polar vortex, so they are scavenged every time there is

an Arctic precipitation event, but this requires further investigation. Indeed, we

can further this question by asking how black carbon geoengineering has

modified deposition rates in the model such that all of the anomalies in Figures

4.6 and 5.23-35 are positive and increasing.

The second is why the mesospheric temperature anomalies due to black

carbon geoengineering lessen as the simulation progresses, as was seen in Section

4.3. One possible explanation is that the thick aerosol cloud is blocking

longwave radiation from the planet's surface. Another is due to expansion of the

stratosphere, which changes the dynamics. Investigation of both of these reasons

would benefit from knowledge of the local heating rates which are unavailable in

the standard model output. We refer to this again in Section 7.6 below.

7.2 SURFACE CHEMISTRY

The introduction of this large amount of aerosols into the stratosphere

dramatically increases the available surface area for chemical interactions.

Heterogeneous chemistry on the surface of these particles is a large source of

uncertainty, as many of the mechanisms involved are unknown.[5] For example,

Springmann et al. [2009] study the effects of chemistry on the aerosol surface

when it has a coating, which is not handled by the bulk aerosol treatment in the

model. Additionally, *Kuwata et al.* [2009] determined that in an urban plume,

there is a critical mass of aerosol, below which the plume is hydrophobic, but

above which the aerosols are hydrophilic. There are numerous sources of

uncertainty regarding particle chemistry that we are unable to assess in our

study.

Related to this is the interaction of the black carbon aerosols with ozone.

In addition to the temperature-catalyzed ozone destruction described in

Chapters 4 and 5, which is the dominant means of ozone destruction in these

experiments, ozone can be lost on the surfaces of the aerosols themselves. This

---

[5] D. Shindell and K. Tsigaridis, personal communications.

process is not included in the model and warrants investigation, even though the effects are likely small [*Jacob*, 2000]. Perhaps a more important effect is that ozone will oxidize the particle surfaces, consuming black carbon [e.g., *Smith and Chughtai*, 1997]. If the reaction time is sufficiently fast, combined with the long atmospheric lifetime of the aerosols in our experiments, this effect could have a profound impact on our results. It will decrease the aerosol size, increasing radiative efficiency and atmospheric lifetime. It will also expose new layers of the soot aerosols to heterogeneous chemistry, possibly enhancing any chemical effects we have discussed previously. Investigating these two ideas will require further investigation and simulation.

7.3 AEROSOL INDIRECT EFFECTS

As the black carbon aerosols settle through the troposphere, they would interact with clouds and could potentially enhance the cloud indirect effects [*Haywood and Boucher*, 2000]. We did not include cloud indirect effects in our simulations to avoid added complications, and the prominence of these effects is still a large source of uncertainty, but these effects are certainly of concern. Additionally, although technically not an aerosol indirect effect, *Liu et al.* [2002] state that the magnitude of the absorption of solar radiation by black carbon when it is mixed with cloud droplets depends strongly on the size, shape, and porosity of the aerosol particle. This serves as an additional source of uncertainty in our simulations, as these processes are likely not well parameterized in the model.

7.4 PRACTICALITY

Our study of the practicality of black carbon geoengineering, as discussed in Chapter 6, has several uncertainties. We had to make assumptions regarding how "dirty" diesel combustion could be. However, if the primary purpose of combusting diesel is to produce soot, perhaps a diesel engine is not the proper technology for geoengineering. This is a question that could be taken up by industrial or chemical engineers, should the need ever arise. Additionally, carbon black is a very large agglomeration of particles, and pulverizing or otherwise converting this agglomeration into small aerosol particles of a useful size for geoengineering may not be possible. This is also a question that could potentially be answered by engineers.

The emissions factors used in Chapter 6 may not necessarily be robust. Many of the reported values were based on only a few test cases. Should the means of geoengineering discussed here actually be implemented, much more testing of these factors will be necessary to determine the risks involved in black carbon geoengineering.

7.5 DYNAMIC OCEAN

Our simulations were the preliminary stages of a more thorough study of black carbon geoengineering. One shortcoming of our simulations was the use of fixed sea surface temperatures, which undoubtedly had an effect on temperature, hydrologic cycle, and cryosphere anomalies. Now that we know which aerosol parameters are important, such as using a high altitude of injection

or a small particle size, we can narrow our experiments to ones that are more realistic and re-simulate them using longer runs and a dynamic ocean.

We will likely conduct three experiments in this new suite. If we assume our goal is to offset the radiative forcing from a doubling of CO_2, which is 3.7 W m^{-2} [*Solomon et al.*, 2007], scaling the results in Figure 5.5 (net solar radiation at the tropopause for each ensemble) should give us an indication as to the amount of aerosol required. The first will involve middle stratospheric injection of particles of the default size (r=0.08 μm), as in experiment HA. Since Figure 5.5 shows the radiative forcing from this ensemble to be approximately -27 W m^{-2} by year ten, or approximately 7.3 times the amount necessary, this first experiment should involve stratospheric injections of approximately 0.15 Tg black carbon aerosols per year. The second experiment will involve injections of small particles (r=0.03 μm), as in experiment SmR. Scaling by the values in Figure 5.5, this experiment will have an injection of 0.05 Tg per year. The third experiment will be small particles injected into the middle stratosphere, as in the failed experiment HASmR. Since the effects of altitude and small radius will combine in this experiment, the amount needed will be much smaller, so as a first order estimate, we will plan on injecting 0.0075 Tg per year, or 7.5 million kg. Unlike in our HASmR experiment, we suspect this amount will be small enough not to cause model blowup.

7.6 ADDITIONAL MODELING STUDIES

Many of the results presented here would benefit from additional studies with more specialized models. For example, one topic of interest regards the cloud semi-direct effect, in which heating from the black carbon aerosols evaporates liquid water, affecting cloud cover [*Hansen et al.*, 1997]. Although cloud forcing represents the single greatest source of uncertainty [*Solomon et al.*, 2007], we could assess whether there are significant perturbations in cloud cover due to the semi-direct effect, independent of real world accuracy. We are unable to assess this with our simulations, as ModelE does not output heating rates. However, we could conduct simulations of black carbon geoengineering using the Rapid Radiative Transfer Model (RRTM) [*Mlawer et al.*, 1997], which is well suited to assessing this effect.

Another topic for which we could use RRTM regards our investigation in Section 5.4 of the stratopause height. We posited that changes in the stratopause height are due to the combination of stratospheric ozone destruction and stratospheric heating by the aerosol layer. A radiative transfer model is an ideal tool to pick apart the individual mechanisms involved and their interactions.

In Chapter 6, we mentioned the additional NO_x from stratospheric geoengineering could cause further ozone destruction [*Finlayson-Pitts and Pitts*, 2000], but interactions between the NO_x, ClO_x, HO_x, and BrO_x cycles complicate our determination of the degree of this effect. However, a coupled chemistry

climate model (CCM) would be ideal for analyzing these effects and determining the exact impact on ozone.

Moreover, sulfate geoengineering has been shown to have complex microphysics that are only properly resolved by detailed aerosol treatments that are generally not present in the bulk aerosol treatment of the general circulation models [*Heckendorn et al.*, 2009; *Pierce et al.*, 2010]. To determine whether black carbon has similar issues, simulations with CCMs or perhaps with ModelE in conjunction with the MATRIX model [*Bauer et al.*, 2008] would be necessary to resolve some of the unknowns regarding particle chemistry and interactions.

Although ModelE has a land surface component [*Aleinov and Schmidt*, 2006], it is not as sophisticated as many specialized agriculture models. To address the impacts of the monsoon perturbations as discussed in Section 5.5, we will need to use a more specialized model which has a focus on agriculture.

Finally, some of the discussions in Chapter 6 involve large portions of the supply of the oil industry, as well as a large portion of GDP. This will undoubtedly have economic impacts, so our study would benefit from an economic model. One of the points we think should have special focus in this economic modeling study is the concept of peak oil and allocation of oil resources to diesel combustion for geoengineering.

7.7 HEALTH IMPACTS

As we discussed previously, black carbon aerosols are known to have adverse impacts on human health [e.g., *CDC*, 1999; *Baan et al.*, 2006]. An

introduction of such a large amount of black carbon into the atmosphere, all of which will eventually deposit onto the surface, as well as a lowering of the tropopause, has the potential to dramatically increase the tropospheric concentration of black carbon aerosols. For urban areas that are already at or above a threshold for negative impacts on human health, introduction of this additional black carbon could have serious implications. This study would benefit from a detailed analysis of the increases in tropospheric black carbon aerosol concentrations, as well as the projected consequences.

CHAPTER 8: CONCLUSIONS

Based on our studies, geoengineering with black carbon aerosols would be effective in cooling the surface, which is the primary purpose of geoengineering. However, we have discovered several consequences of doing so, some of which could be catastrophic. Although geoengineering can be tailored to some degree by varying the particle radius, altitude of injection, and the amount of annual injection, any decision to geoengineer using this method will need to be carefully evaluated with a full assessment of the impacts and risks involved.

Moreover, the two methods we have discussed on how one might geoengineer with black carbon aerosols are rather impractical. Both have huge engineering obstacles, and using diesel fuel is prohibitively expensive, despite being slightly cheaper than the cost of doing nothing and suffering the consequences of climate change. If carbon black is used, assuming the engineering difficulties could be resolved, the costs would be quite negligible and could easily be absorbed by a single entity, in that geoengineering could be performed unilaterally. If diesel fuel is used, the likelihood of unilateral geoengineering is small, as the large costs and infrastructure required would necessitate cooperation among multiple wealthy nations. Moreover, the infrastructure to geoengineer with diesel fuel is currently insufficient. If this method were to be chosen, there would likely be significant additional costs to amplify the existing infrastructure, resulting in increased cost.

One significant advantage to this method of geoengineering is that it can be done with current technology. Assuming all of the equipment were manufactured and available on the market, the time to deployment would be very short. As we discussed previously, sulfur geoengineering has a number of difficulties, including untested technologies, which need to be addressed before that means of geoengineering could be considered deployment-ready.

We stress that, despite the potential feasibility of this method of geoengineering, the multiple, serious side effects cannot be ignored and must be weighed in the balance of determining whether geoengineering with black carbon, or geoengineering in general, should be undertaken. Moreover, it has often been argued [e.g., *Robock* 2008] that geoengineering will not prevent ocean acidification due to increasing amounts of dissolved carbon dioxide. *Matthews et al.* [2009] quantified and confirmed this suspicion, meaning ecological concerns for a very large portion of the biosphere will need to be addressed when considering the implementation of geoengineering.

This method of geoengineering, as well as most other methods, requires a great deal of further study before it can even enter the real-world testing phase, let alone implementation. Some have argued that the climate has already reached a tipping point, and soon it may be too late to geoengineer the climate. However, there is no disadvantage to delaying geoengineering until absolutely necessary, since geoengineering works quickly [*Matthews and Caldeira*, 2007].

This invites concern for another issue, in that once geoengineering is no longer necessary, stopping instantly would result in catastrophically rapid warming [*Wigley*, 2006]. Also, unless ambient carbon dioxide concentrations are actively reduced, geoengineering would have to be continued practically indefinitely due to the long atmospheric lifetime of carbon dioxide [*Brovkin et al.*, 2008].

We stress that geoengineering is not a substitute for mitigation of carbon dioxide emissions, nor is it a permanent solution to the problem of climate change. The only permanent solution is cessation of the emissions of anthropogenic greenhouse gases. Despite this, black carbon geoengineering, although some may consider it inferior to sulfate geoengineering, could be considered as a temporary, emergency measure to limit dangerous temperature rise until a proper solution to the problem of global warming is found.

APPENDIX A: FORMULAS

A.1 MASS BALANCE EQUATION

We consider a mass balance equation that has a constant source rate term S (mass per unit time). We assume the amount of material decays in proportion to the amount in the atmosphere. Then we have a differential equation

$$\frac{\mathrm{d}m(t)}{\mathrm{d}t} = S - km$$

where $m(t)$ is the mass as a function of time t, and k is the constant of proportionality. k also defines the e-folding lifetime τ of the material, where

$k = \dfrac{1}{\tau}$. Integrating this equation, we get

$$m = \frac{S}{k} + Ce^{-kt}$$

for some constant C. If we consider the initial conditions $(t,m)=(0,m_0)$ for some initial mass m_0, then we have $C = m_0 - \dfrac{S}{k}$, so

$$m = m_0 e^{-kt} + \frac{S}{k}\left(1 - e^{-kt}\right)$$

This equation cannot be solved for k empirically, so any solutions given are solved graphically.   Determining peak loading is an optimization problem, i.e., peak loading will occur when $m'(t)=0$, or when $m = \dfrac{S}{k}$. This is the same as the equilibrium value, i.e., $\lim\limits_{t \to \infty} m = \dfrac{S}{k}$.

APPENDIX B: MODEL DETAILS

TABLE B.1. Pressure levels at the bottom of each model layer. Blue shaded boxes denote tropospheric layers. The model top is at 0.1 mb.

Layer	Pressure (mb)	Layer	Pressure (mb)	Layer	Pressure (mb)
1	984	15	441	29	57
2	964	16	396	30	43
3	942	17	354	31	31
4	917	18	316	32	20
5	890	19	282	33	10
6	860	20	251	34	5.62
7	825	21	223	35	3.16
8	785	22	197	36	1.78
9	740	23	173	37	1
10	692	24	150	38	0.562
11	642	25	128	39	0.316
12	591	26	108	40	0.178
13	539	27	90		
14	489	28	73		

TABLE B.2. The six spectral intervals (nominal Mie scattering band subdivisions) as represented in the model (L=1 to 6). These overlap the 16 solar k-distribution intervals given in Table B.3.

L	Approximate Wavelength Range (nm)
1	2200-4000
2	1500-2200
3	1250-1500
4	860-1250
5	770-860
6	300-770

TABLE B.3. The 16 solar k-distribution intervals (K=1 to 16) represented in the model. The first 14 intervals (K=1 to 14) are overlapped by the 6 spectral intervals (L=1 to 6) given in Table B.2. K=15 represents ultraviolet radiation absorption by ozone. K=16 is reserved for strong absorbing spectral regions in the IR. The density column shows the fraction of solar energy represented by that particular interval.

K	L	Approximate Wavelength Range (nm)	Density
1	1	3000-3400	0.010
2	1	2200-3000	0.030
3	2	1740-2200	0.040
4	2	1500-1740	0.040
5	5	810-860	0.040
6	5	805-810	0.002
7	5	795-805	0.004
8	5	770-795	0.013
9	1	3800-4000	0.002
10	1	3500-3800	0.003
11	1	3400-3600	0.003
12	3	1250-1500	0.072
13	4	860-1250	0.200
14	6	360-770	0.480
15	6	200-360	0.050
16	1	4000-9999	0.011

REFERENCES

Ackerman, A. S., M. P. Kirkpatrick, D. E. Stevens, and O. B. Toon (2004), The impact of humidity above stratiform clouds on indirect aerosol climate forcing, *Nature*, *342*, 1014-1017, doi:10.1038/nature03174.

Akbari, H., S. Menon, and A. Rosenfeld (2009), Global cooling: Increasing world-wide urban albedos to offset CO_2, *Climatic Change*, *94*, 275-286, doi: 10.1007/s10584-008-9515-9.

Aleinov, I., and G. A. Schmidt (2006), Water isotopes in the GISS ModelE land surface scheme, *Global and Planetary Change, 51*, 108-120, doi:10.1016/j.gloplacha.2005.12.010.

Aleksandrov, V. V. and G. L. Stenchikov (1983), On the modeling of the climatic consequences of the nuclear war, *The Proceedings of Applied Mathematics*, The Computing Centre of the USSR Academy of Sciences, Moscow, 21 pp.

Angel, R. (2006), Feasibility of cooling the Earth with a cloud of small spacecraft near the inner Lagrange point (L1), *Proceedings of the National Academy of Sciences*, *103*, 17184-17189, doi:10.1073/pnas.0608163103.

Aumont, O. and L. Bopp (2006), Globalizing results from ocean in situ iron fertilization studies, *Global Biogeochemical Cycles*, *20*, GB2017, doi: 10.1029/2005GB002591.

Baan, R., K. Straif, Y. Grosse, B. Secretan, F. El Ghissassi, and V. Cogliano (2006), Carcinogenicity of carbon black, titanium dioxide, and talc, *The Lancet Oncology*, *7*(4), 295-296, doi:10.1016/S1470-2045(06)70651-9.

Bala, G., P. B. Duffy, and K. E. Taylor (2008), Impact of geoengineering schemes on the global hydrological cycle, *Proceedings of the National Academy of Sciences*, *105*(22), 7664-7669, doi:10.1073/pnas.0711648105.

Ban-Weiss, G. A., M. M. Lunden, T. W. Kirchstetter, and R. A. Harley (2009), Measurement of black carbon particle number emission factors from individual heavy-duty trucks, *Environmental Science and Technology*, *43*(5), 1419-1424, doi:10.1021/es8021039.

Ban-Weiss, G. A., K. Caldeira, L. Cao, and G. Bala (2011), Dependence of climate forcing and response on the altitude of black carbon aerosols, submitted.

Barrett, S. (2008), The incredible economics of geoengineering, *Environmental and Resource Economics*, *39*, 45-54, doi:10.1007/s10640-007-9174-8.

Bauer, S. E., D. L. Wright, D. Koch, E. R. Lewis, R. McGraw, L.-S. Chang, S. E. Schwartz, and R. Ruedy (2008), MATRIX (Multiconfiguration Aerosol TRacker of mIXing state): an aerosol microphysical model for global atmospheric models, *Atmospheric Chemistry and Physics*, *8*(20), 6003-6035, doi: 10.5194/acp-8-6003-2008.

Boos, W. R. and Z. Kuang (2010), Dominant control of the South Asian monsoon by orographic insulation versus plateau heating, *Nature*, *463*, 218-222, doi: 10.1038/nature08707.

Bower, K., T. Choularton, J. Latham, J. Sahraei, and S. Salter (2006), Computational assessment of a proposed technique for global warming mitigation via albedo-enhancement of marine stratocumulus clouds, *Atmospheric Research*, *82*, 328-336, doi:10.1016/j.atmosres.2005.11.013.

Boyd, P. W., R. Strzepek, S. Takeda, G. Jackson, C. S. Wong, R. M. McKay, C. Law, H. Kiyosawa, H. Saito, N. Sherry, K. Johnson, J. Gower, and N. Ramaiah (2005), The evolution and termination of an iron-induced mesoscale bloom in the northeast subarctic Pacific, *Limnology and Oceanography*, *50*(6), 1872-1886.

Brovkin, V., V. Petoukhov, M. Claussen, E. Bauer, D. Archer, and C. Jaeger (2008), Geoengineering climate by stratospheric sulfur injections: Earth system vulnerability to technological failure, *Climatic Change*, doi:10.1007/s10584-008-9490-1.

Budyko, M. I. (1974), Climate and life, Academic Press, New York, New York, 508 pp.

Budyko, M. I. (1977), Climatic Changes, American Geophysical Union, Washington, DC, 261 pp.

Bunzl, M. (2008), An ethical assessment of geoengineering, *Bulletin of the Atomic Scientists*, *64*(2), 18, doi:10.2968/064002006.

Bunzl, M. (2009), Researching geoengineering: Should not or could not?, *Environmental Research Letters*, *4*, 0451014, doi:10.1088/1748-9326/4/4/045104.

Caldeira, K. and L. Wood (2008), Global and Arctic climate engineering: Numerical model studies, *Philosophical Transactions of the Royal Society A*, *366*(1882), 4039-4056, doi:10.1098/rsta.2008.0132.

Caterpillar (2010a), Caterpillar industrial wizard, available online at http://
industrialwizard.catmms.com/catwizards/industrialWizard/jsp/
caterpillar.jsp.

Caterpillar (2010b), Caterpillar marine and power systems, available online at
http://marine.cat.com/cat-3516B.

Caterpillar (2010c), Caterpillar product operation and maintenance manuals
(OMMS), available online at http://safety.cat.com/cda/layout?
m=133362&x=7.

Caterpillar (2010d), Engine maintenance and repair options flowchart, available
online at http://www.cat.com/cda/components/fullArticle?
m=40302&x=7&id=87704.

CDC (1999), Elemental carbon (diesel particulate): Method 5040, Issue 3
(Interim), National Institute for Safety and Health, Centers for Disease
Control and Prevention, In *NIOSH Manual of Analytical Methods*, 4th rev. ed., 5
pp., available online at http://www.cdc.gov/niosh/docs/2003-154/pdfs/
5040f3.pdf.

Charlson, R. J., J. E. Lovelock, M. O. Andreae, and S. G. Warren (1987), Oceanic
phytoplankton, atmospheric sulphur, cloud albedo and climate, *Nature*, *326*,
655-661, doi:10.1038/326655a0.

Charlson, R. J., S. E. Schwartz, J. M. Hales, R. D. Cess, J. A. Coakley, Jr., J. E.
Hansen, and D. J. Hofmann (1992), Climate forcing by anthropogenic
aerosols, *Science*, *255*, 423-430, doi:10.1126/science.255.5043.423.

Chertkov, Ya. B. (1971), Jet aircraft fuel additives (a review), *Chemistry and
technology of fuels and oils*, *7*(8), 632-635, doi:10.1007/BF00714042, translated
from *Khimiya i Tekhnologiya Topliv i Masel*, 8, 59-61.

CIA (2010), The world factbook: World, Central Intelligence Agency, available
online at https://www.cia.gov/library/publications/the-world-factbook/
geos/xx.html.

Covey, C., S. H. Schneider, and S. L. Thompson (1984), Global atmospheric effects
of massive smoke injections from a nuclear war: Results from general
circulation model simulations, *Nature*, *308*, 21-25, doi:10.1038/308021a0.

Crump, E. L. (2000), Economic Impact Analysis For the Proposed Carbon Black
Manufacturing NESHAP, Environmental Protection Agency, EPA-452/

D-00-003, 16 pp., available online at http://www.epa.gov/ttnecas1/regdata/ EIAs/carbonblackeia.pdf.

Crutzen, P. J. (1970), The influence of nitrogen oxides on the atmospheric ozone content, *Quarterly Journal of the Royal Meteorological Society*, *96*(408), 320-325, doi:10.1002/qj.49709640815.

Crutzen, P. J. and J. W. Birks (1982), Atmosphere after a nuclear war: Twilight at noon, *Ambio*, *11*(2/3), 114-125.

Crutzen, P. J. (2006), Albedo enhancement by stratospheric sulfur injections: A contribution to resolve a policy dilemma? *Climatic Change*, *77*, 211-219, doi: 10.1007/s10584-006-9101-y.

Curtin, N. P. (2003), Information on Air Force serial refueling tankers, testimony before the Subcommittee on Projection Forces, Committee on Armed Services, House of Representatives, *Rep. GAO-03-938T*, 8 pp., Gov. Account. Off., Washington, D.C., available online at http://www.gao.gov/new.items/ d03938t.pdf.

Dickinson, R. E. (1996), Climate engineering: A review of aerosol approaches to changing the global energy balance, *Climatic Change*, *33*(3), 279-290, doi: 10.1007/BF00142576.

Dow (2010a), Carbon black feed safety data sheet, Dow Chemical Company, 8 pp., available online at http://www.dow.com/PublishedLiterature/ dh_03df/0901b803803df6d8.pdf.

Dow (2010b), Carbon black feedstock product safety assessment, Dow Chemical Company, 6 pp., available online at http://www.dow.com/ PublishedLiterature/dh_0538/0901b80380538c53.pdf.

Early, J. T. (1989), Space-based solar shield to offset greenhouse effect, *Journal of the British Interplanetary Society*, *42*, 567-569.

Ehlig-Economides, C. and M. J. Economides (2010), Sequestering carbon dioxide in a closed underground volume, *Journal of Petroleum Science and Engineering*, *70*, 123-130, doi:10.1016/j.petrol.2009.11.002.

EIA (2005), Documentation for Emissions of Greenhouse Gases in the U.S. 2005, DOE/EIA-0638, 240 pp., available online at http://www.eia.doe.gov/oiaf/ 1605/ggrpt/documentation/pdf/0638(2005).pdf.

EIA (2009), Refining crude oil, *Petroleum Supply Annual 2009,* U.S. Energy Information Administration, available online at http://www.eia.doe.gov/energyexplained/index.cfm?page=oil_refining.

EIA (2010a), Global oil consumption, U.S. Energy Information Administration, available online at http://www.eia.doe.gov/pub/oil_gas/petroleum/analysis_publications/oil_market_basics/demand_text.htm.

EIA (2010b), U.S. refining capacity, U.S. Energy Information Administration, available online at http://www.eia.doe.gov/pub/oil_gas/petroleum/analysis_publications/oil_market_basics/refining_text.htm#U.S.%20Refining%20Capacity.

EIA (2010c), World crude oil production, 1960-2009 (Million barrels per day), U.S. Energy Information Administration, available online at http://www.eia.doe.gov/aer/txt/ptb1105.html.

Enviro Aero (2009), Beginner's Guide to Aviation Biofuels, available online at http://www.enviro.aero/biofuels.

EPA (1995), Carbon black, Chapter 6: Organic Chemical Process Industry, Compilation of Air Pollutant Emission Factors, EPA AP 42, Fifth Edition, Volume I, 10 pp., available online at http://www.epa.gov/ttnchie1/ap42/ch06/final/c06s01.pdf.

EPA (1996), Emissions Factors & AP 42, Compilation of Air Pollutant Emission Factors, Environmental Protection Agency, EPA AP-42, 9 pp., available online at http://www.epa.gov/ttnchie1/ap42/ch03/final/c03s03.pdf.

EPA (2005), Average carbon dioxide emissions resulting from gasoline and diesel fuel, U.S. Environmental Protection Agency Office of Transportation and Air Quality, EPA 420-F-05-001, 3pp., available online at http://www.epa.gov/oms/climate/420f05001.pdf.

EPA (2009), Heavy-duty highway diesel program, Environmental Protection Agency, available online at http://www.epa.gov/otaq/highway-diesel/index.htm.

Falkowski, P. (1997), Evolution of the nitrogen cycle and its influence on the biological sequestration of CO_2 in the ocean, *Nature, 387,* 272-275, doi: 10.1038/387272a0.

Field, C. B., M. J. Behrenfeld, J. T. Randerson, and P. Falkowski (1998), Primary production of the biosphere: Integrating terrestrial and oceanic components, *Science, 281*(5374), 237-240, doi:10.1126/science.281.5374.237.

Finlayson-Pitts, B. J. and J. N. Pitts, Jr. (2000), Chemistry of the Upper and Lower Atmosphere: Theory, Experiments, and Applications, Academic Press, San Diego, California, 969 pp.

Flannery, B. P., G. Marland, W. Broecker, H. Ishatani, H. Keshgi, H. Komiyama, M. MacCracken, N. Rosenberg, M. Steinberg, and T. Wigley (1997), Geoengineering climate, in Robert G. Watts (ed.), Chapter 8, 379-427, Lewis Publishers, Boca Raton.

Fleming, J. R. (2006), Global climate change and human agency: Inadvertent influence and "Archimedean" interventions, *Intimate Universality*, 223-248.

Fleming, J. R. (2007), The climate engineers: Playing God to save the planet, *The Wilson Quarterly*, *31*(2), 46-60.

Fleming, J. R. (2010), Fixing the sky: The checkered history of weather and climate control, Columbia University Press, New York, New York, 344 pp.

Fruin, S. A., A. M. Winer, and C. E. Rodes (2004), Black carbon concentrations in California vehicles and estimation of in-vehicle diesel exhaust particulate matter exposures, *Atmospheric Environment*, *38*, 4123-4133, doi:10.1016/j.atmosenv.2004.04.026.

Fuller, K. A., W. C. Malm, and S. M. Kreidenweis (1999), Effects of mixing on extinction by carbonaceous particles, *Journal of Geophysical Research*, *104*(D13), 15941-15954, doi:10.1029/1998JD100069.

Gandhi, B. (2005), Reassessment of one Exemption from the Requirement of a Tolerance for Carbon Black, Environmental Protection Agency, Inert Ingredient Assessment Branch, 9 pp., available online at http://www.epa.gov/opprd001/inerts/carbonblack.pdf.

Global Aircraft (2010a), KC-10 Extender, The Global Aircraft Organization, available online at http://www.globalaircraft.org/planes/kc-10_extender.pl.

Global Aircraft (2010b), KC-135 Stratotanker, The Global Aircraft Organization, available online at http://www.globalaircraft.org/planes/kc-135_stratotanker.pl.

Govindasamy, B. and K. Caldeira (2000), Geoengineering Earth's radiation balance to mitigate CO_2-induced climate change, *Geophysical Research Letters*, *27*(14), 2141-2144, doi:10.1029/1999GL006086.

Govindasamy, B., S. Thompson, P. B. Duffy, K. Caldeira, and C. Delire (2002), Impact of geoengineering schemes on the terrestrial biosphere, *Geophysical Research Letters*, *29*(22), 2061-2064, doi:10.1029/2002GL015911.

Govindasamy, B., K. Caldeira, and P. B. Duffy (2003), Geoengineering Earth's radiation balance to mitigate climate change from a quadrupling of CO_2, *Global and Planetary Change*, *37*, 157-168, doi:10.1016/S0921-8181(02)00195-9.

Gu, L., D. D. Baldocchi, S. C. Wofsy, J. W. Munger, J. J. Michalsky, S. P. Urbanski, and T. A. Boden (2003), Response of a deciduous forest to the Mount Pinatubo eruption: Enhanced photosynthesis, *Science*, *299*(5615), 2035-2038, doi: 10.1126/science.1078366.

Hahn, D. G. and S. Manabe (1975), The role of mountains in the south Asian monsoon circulation, *Journal of Atmospheric Sciences*, *32*, 1515-1541, doi: 10.1175/1520-0469(1975)032<1515:TROMIT>2.0.CO;2.

Hamwey, R. (2007), Active amplification of the terrestrial albedo to mitigate climate change: An exploratory study, *Mitigation and Adaptation Strategies for Global Change*, *12*(4), 419-439, doi:10.1007/s11027-005-9024-3.

Hansen, J., D. Johnson, A. Lacis, S. Lebedeff, P. Lee, D. Rind, and G. Russell (1981), Climate impact of increasing atmospheric carbon dioxide, *Science*, *213*(4511), 957-966, doi:10.1126/science.213.4511.957.

Hansen, J. E., M. Sato, and R. Ruedy (1997), Radiative forcing and climate response, *Journal of Geophysical Research*, *102*, 6831–6864, doi: 10.1029/96JD03436.

Hansen, J., Mki. Sato, R. Ruedy, L. Nazarenko, A. Lacis, G.A. Schmidt, G. Russell, I. Aleinov, M. Bauer, S. Bauer, N. Bell, B. Cairns, V. Canuto, M. Chandler, Y. Cheng, A. Del Genio, G. Faluvegi, E. Fleming, A. Friend, T. Hall, C. Jackman, M. Kelley, N.Y. Kiang, D. Koch, J. Lean, J. Lerner, K. Lo, S. Menon, R. L. Miller, P. Minnis, T. Novakov, V. Oinas, Ja. Perlwitz, Ju. Perlwitz, D. Rind, A. Romanou, D. Shindell, P. Stone, S. Sun, N. Tausnev, D. Thresher, B. Wielicki, T. Wong, M. Yao, and S. Zhang (2005), Efficacy of climate forcings, *Journal of Geophysical Research, 110*, D18104, doi:10.1029/2005JD005776.

Hansen, J., R. Ruedy, M. Sato, and K. Lo (2010), Global surface temperature change, *Reviews of Geophysics*, *48*, RG4004, doi:10.1029/2010RG000345.

Haywood, J. and O. Boucher (2000), Estimates of the direct and indirect radiative forcing due to tropospheric aerosols: A review, *Reviews of Geophysics*, *38*, 513-543, doi:10.1029/1999RG000078.

Heckendorn, P., D. Weisenstein, S. Fueglistaler, B. P. Luo, E. Rozanov, M. Schraner, L. W. Thomason, and T. Peter (2009), The impact of geoengineering aerosols on stratospheric temperature and ozone, *Environmental Research Letters*, 4, 045108, doi:10.1088/1748-9326/4/4/045108.

Held, I. M. (1983), Stationary and quasi-stationary eddies in the extratropical troposphere: theory, In *Large-Scale Dynamical Processes in the Atmosphere*, B. Hoskins and R. Pearce, eds., Academic Press, San Diego, California, 127–168.

Hofmann, D. J. and S. Solomon (1989), Ozone destruction through heterogeneous chemistry following the eruption of El Chichón, *Journal of Geophysical Research*, *94*(D4), 5029-5041, doi:10.1029/JD094iD04p05029.

ICBA (2004), Carbon black user's guide: Safety, health, and environmental information, International Carbon Black Association, 11 pp., available online at http://www.carbon-black.org/carbonblackuserguide.pdf.

IEA (2010), CO_2 Emissions from Fuel Combustion, International Energy Agency, 130 pp., available online at http://www.iea.org/co2highlights/CO2highlights.pdf.

Intergovernmental Panel on Climate Change (IPCC) (2005), Carbon dioxide capture and storage, edited by B. Metz, O. Davidson, H. de Coninck, M. Loos, and L. Meyer, Cambridge University Press, UK, 431 pp.

Intergovernmental Panel on Climate Change (IPCC) (2007), Summary for Policymakers, in Climate Change 2007: Mitigation, Contribution of Working Group III to the Fourth Assessment Report of the Intergovernmental Panel on Climate Change (B. Metz, O. R. Davidson, P. R. Bosch, R. Dave, L. A. Meyer, eds.), Cambridge University Press, UK, 23 pp.

Izrael, Yu. A., V. M. Zakharov, N. N. Petrov, A. G. Ryaboshapko, V. N. Ivanov, A. V. Savchenko, Yu. V. Andreev, Yu. A. Puzov, B. G. Danelyan, and V. P. Kulyapin (2009), Field experiment on studying solar radiation passing through aerosol layers, *Russian Meteorology and Hydrology*, *34*(5), 265-273, doi: 10.3103/S106837390905001X.

Jacob, D. J. (2000), Heterogeneous chemistry and tropospheric ozone, *Atmospheric Environment*, *34*, 2131-2159, doi:10.1016/S1352-2310(99)00462-8.

Johnston, H. S. (1971), Reduction of stratospheric ozone by nitrogen oxide catalysts from supersonic transport exhaust, *Science*, *173*(3996), 517-522, doi: 10.1126/science.173.3996.517.

Jones, A., J. Haywood, and O. Boucher (2009), Climate impacts of geoengineering marine stratocumulus clouds, *Journal of Geophysical Research*, *114*, D10106, doi: 10.1029/2008JD011450.

Jones, A., J. Haywood, O. Boucher, B. Kravitz, and A. Robock (2010), Geoengineering by stratospheric SO_2 injection: Results from the Met Office HadGEM2 climate model and comparison with the Goddard Institute for Space Studies ModelE, *Atmospheric Chemistry and Physics*, *10*, 5999-6006, doi: 10.5194/acp-10-5999-2010.

Jucks, K. W., D. G. Johnson, K. V. Chance, W. A. Traub, R. J. Salawitch, and R. A. Stachnik (1996), Ozone production and loss rate measurements in the middle stratosphere, *Journal of Geophysical Research*, *101*(D22), 28785-28792, doi: 10.1029/96JD02739.

Keith, D. W. (2000), Geoengineering the climate: History and prospect, *Annual Review of Energy and the Environment*, *25*, 245-284, doi:10.1146/annurev.energy. 25.1.245.

Keith, D. W., M. Ha-Duong, and J. K. Stolaroff (2006), Climate strategy with CO_2 capture from the air, *Climatic Change*, *74*, 17-45, doi:10.1007/ s10584-005-9026-x.

Keith, D. W. (2010), Photophoretic levitation of engineered aerosols for geoengineering, *Proceedings of the National Academy of Sciences*, in press, doi: 10.1073/pnas.1009519107.

Kelemen, P. and J. Matter (2008), In situ mineral carbonation in peridotite for CO_2 capture and storage, *Proceedings of the National Academy of Sciences*, *105*(45), 17295-17300, doi:10.1073/pnas.0805794105.

Khan, E., W. Ferrell, M. C. MacCracken, S. E. Schwartz, P. B. Duffy, S. Thompson, and G. H. Marland (2001), Response options to limit rapid or severe climate change, U.S. Department of Energy, 37 pp.

Kiehl, J. T., J. J. Hack, G. B. Bonan, B. A. Boville, D. L. Williamson, and P. J. Rasch (1998), The National Center for Atmospheric Research Community Climate Model, CCM3, *Journal of Climate, 11*(6), 1131–1149, doi:10.1175/1520-0442 (1998)011<1131;TNCFAR>2.0.CO;2.

Kinnison, D. E., K. E. Grant, P. S. Connell, D. A. Rotman, and D. J. Wuebbles (1994), The chemical and radiative effects of the Mount Pinatubo eruption, *Journal of Geophysical Research, 99*, 25705–25731, doi:10.1029/94JD02318.

Kirchstetter, T. W., R. A. Harley, N. M. Kreisberg, M. R. Stolzenburg, and S. V. Hering (1999), On-road measurement of fine particle and nitrogen oxide emissions from light and heavy duty motor vehicles, *Atmospheric Environment*, *33*(18), 2955-2968, doi:10.1016/S1352-2310(99)00089-8.

Koch, D., G. A. Schmidt, and C. V. Field (2006), Sulfur, sea salt, and radionuclide aerosols in GISS ModelE, *Journal of Geophysical Research*, *111*, D06206, doi:10.1029/2004JD005550.

Kravitz, B., A. Robock, L. Oman, G. Stenchikov, and A. B. Marquardt (2009), Sulfuric acid deposition from stratospheric geoengineering with sulfate aerosols, *Journal of Geophysical Research*, *114*, D14109, doi:10.1029/2009JD011918.

Kravitz, B., A. Robock, A. Bourassa, and G. Stenchikov (2010a), Negligible climatic effects from the 2008 Okmok and Kasatochi volcanic eruptions, *Journal of Geophysical Research*, *115*, D00L05, doi:10.1029/2009JD013525.

Kravitz, B., A. Robock, L. Oman, G. Stenchikov, and A. B. Marquardt (2010b), Correction to "Sulfuric acid deposition from stratospheric geoengineering with sulfate aerosols", *Journal of Geophysical Research*, *115*, D16119, doi:10.1029/2010JD014579.

Kravitz, B. and A. Robock (2011), The climate effects of high latitude eruptions: The role of the time of year, *Journal of Geophysical Research*, *116*, D01105, doi:10.1029/2010JD014448.

Kravitz, B., A. Robock, A. Bourassa, T. Deshler, D. Wu, I. Mattis, F. Finger, A. Hoffmann, C. Ritter, L. Bitar, T. J. Duck, and J. E. Barnes (2011a), Simulation and observations of stratospheric aerosols from the 2009 Sarychev volcanic eruption, *Journal of Geophysical Research*, submitted.

Kravitz, B., A. Robock, O. Boucher, H. Schmidt, K. E. Taylor, G. Stenchikov, and M. Schulz (2011b), The geoengineering model intercomparison project (GeoMIP), *Atmospheric Science Letters*, in press.

Kuwata, M., Y. Kondo, and N. Takegawa (2009), Critical condensed mass for activation of black carbon as cloud condensation nuclei in Tokyo, *Journal of Geophysical Research*, *114*, D20202, doi:10.1029/2009JD012086.

Lacis, A. A., and M. I. Mishchenko (1995), Climate forcing, climate sensitivity, and climate response: A radiative modeling persepctive on atmospheric aerosols. In Aerosol Forcing of Climate: Report of the Dahlem Workshop on Aerosol Forcing of Climate, Berlin 1994, April 24-29. R.J. Charlson and J. Heintzenberg, Eds. John Wiley Sons.

Lacis, A. A., J. L. Alltop, S. M. Hsiang, K. D. Knobelspiesse, J. Li, and C. B. Pearl, A critique of proposed geoengineering countermeasures to global warming, unpublished.

Lackner, K. S., D. P. Butt, C. H. Wendt, and D. H. Sharp (1996), Carbon dioxide disposal in solid form, In Proceedings of the 21st International Conference on Coal Utilization and Fuel System, Coal Technology Association, Clearwater, FL.

Lackner, K. S. (2003), Climate change: A guide to CO_2 sequestration, *Science*, *300* (5626), 1677-1678, doi:10.1126/science.1079033.

Lackner, K. S. (2009), Capture of carbon dioxide from ambient air, *European Physics Journal Special Topics*, *176*, 93-106, doi:10.1140/epjst/e2009-01150-3.

Lampitt, R. S., E. P. Achterberg, T. R. Anderson, J. A. Hughes, M. D. Iglesias-Rodriguez, B. A. Kelly-Gerreyn, M. Lucas, E. E. Popova, R. Sanders, J. G. Shepherd, D. Smythe-Wright, and A. Yool (2008), Ocean fertilization: A potential means of geoengineering?, *Philosophical Transactions of the Royal Society A*, *366*(1882), 3919-3945, doi:10.1098/rsta.2008.0139.

Lane, L., K. Caldeira, R. Chatfield, and S. Langhoff (2007), Workshop report on managing solar radiation, National Aeronautics and Space Administration, NASA/CP-2007-214558, 31 pp.

Latham, J. (1990), Control of global warming?, *Nature*, *347*, 339-340, doi: 10.1038/347339b0.

Latham, J. (2002), Amelioration of global warming by controlled enhancement of the albedo and longevity of low-level maritime clouds, *Atmospheric Science Letters*, *3*(2-4), 59-70, doi:10.1006/asle.2002.0048.

Latham, J., P. Rasch, C.-C. Chen, L. Kettles, A. Gadian, A. Gettelman, H. Morrison, K. Bower, and T. Choularton (2008), Global temperature stabilization via controlled albedo enhancement of low-level maritime clouds, *Philosophical Transactions of the Royal Society A*, *366*, 3969-3987, doi:10.1098/ rsta.2008.0137.

Lawrence, M. G. (2006), The geoengineering dilemma: To speak or not to speak, *Climatic Change*, *77*, 245-248, doi:1007/s10584-006-9131-5.

Lehmann, J., J. Gaunt, and M. Rondon (2006), Bio-char sequestration in terrestrial ecosystems - A review, *Mitigation and Adaptation Strategies for Global Change*, *11*, 395-419, doi:10.1007/s11027-005-9006-5.

Lehmann, J. (2007), Bio-energy in the black, *Frontiers in Ecology and the Environment*, *5*(7), 381-387, doi:10.1890/1540-9295(2007)5[381:BITB]2.0.CO;2.

Leemans, R., S. Agrawala, J. A. Edmonds, M. C. MacCracken, R. Moss, and P. S. Ramakrishnan (1995), Mitigation: Cross-sectoral and other issues, In IPCC Working Group II Second Assessment Report, Cambridge University Press, Cambridge, Chapter 25, 799-819.

Lenton, T. M. and N. E. Vaughan (2009), The radiative forcing potential of different climate geoengineering options, *Atmospheric Chemistry and Physics*, *9*, 5539-5561, doi:10.5194/acp-9-5539-2009.

Liu, L., M. I. Mischenko, S. Menon, A. Macke, and A. A. Lacis (2002), The effect of black carbon on scattering and absorption of solar radiation by cloud droplets, *Journal of Quantitative Spectroscopy and Radiative Transfer*, *74*(2), 195-204, doi:10.1016/S0022-4073(01)00232-1.

Llewellyn, E. J., N. D. Lloyd, D. A. Degenstein, R. L. Gattinger, S. V. Petelina, A. E. Bourassa, J. T. Wiensz, E. V. Ivanov, I. C. McDade, B. H. Solheim, J. C. McConnell, C. S. Haley, C. von Savigny, C. E. Sioris, C. A. McLinden, E. Griffioen, J. Kaminski, W. F. J. Evans, E. Puckrin, K. Strong, V. Wehrle, R. H. Hum, D. J. W. Kendall, J. Matsushita, D. P. Murtagh, S. Brohede, J. Stegman, G. Witt, G. Barnes, W. F. Payne, L. Piché, K. Smith, G. Warshaw, D.-L. Deslauniers, P. Marchand, E. H. Richardson, R. A. King, I. Wevers, W. McCreath, E. Kyrölä, L. Oikarinen, G. W. Leppelmeier, H. Auvinen, G. Mégie, A. Hauchecorne, F. Lefèvre, J. de La Nöe, P. Ricaud, U. Frisk, F. Sjoberg, F. von Schéele, and L. Nordh (2004), The OSIRIS instrument on the Odin spacecraft, *Canadian Journal of Physics*, *82*(6), 411-422, doi:10.1139/p04-005.

Lyon, S. (2007), The Massachusetts 2002 diesel particulate matter inventory, Massachusetts Department of Environmental Protection, 123 pp., available online at http://www.mass.gov/dep/air/priorities/02dslinv.pdf.

MacKay & Co. (2003), America's fleet remains strong, *Construction Equipment*, August 2003.

Manabe, S. and T. B. Terpstra (1974), The effects of mountains on the general circulation of the atmosphere as identified by numerical experiments, *Journal of the Atmospheric Sciences*, *31*, 3-42, doi:10.1175/1520-0469(1974) 031<0003:TEOMOT>2.0.CO;2.

Marchetti, C. (1977), On geoengineering and the CO_2 problem, *Climatic Change, 1,* 59-68, doi:10.1007/BF00162777.

Matthews, H. D. and K. Caldeira (2007), Transient climate-carbon simulations of planetary geoengineering, *Proceedings of the National Academy of Sciences, 104* (24), 9949-9954, doi:10.1073/pnas.0700419104.

Matthews, H. D., L. Cao, and K. Caldeira (2009), Sensitivity of ocean acidification to geoengineered climate stabilization, *Geophysical Research Letters, 36,* L10706, doi:10.1029GL037488.

Medalia, A. I., D. Rivin, and D. R. Sanders (1983), A comparison of carbon black with soot, *Science of the Total Environment, 31*(1), 1-22, doi:10.1016/0048-9697 (83)90053-0.

Mercado, L. M., N. Bellouin, S. Sitch, O. Boucher, C. Huntingford, M. Wild, and P. M. Cox (2009), Impact of changes in diffuse radiation on the global land carbon sink, *Nature, 458,* 1014-1018, doi:10.1038/nature07949.

Miguel, A. H., T. W. Kirchstetter, and R. A. Harley (1998), On-road emissions of particulate polycyclic aromatic hydrocarbons and black carbon from gasoline and diesel vehicles, *Environmental Science and Technology, 32*(4), 450-455, doi: 10.1021/es970566w.

Mills, M. J., O. B. Toon, R. P. Turco, D. E. Kinnison, and R. R. Garcia (2008), Massive global ozone loss predicted following regional nuclear conflict, *Proceedings of the National Academy of Sciences, 105*(14), 5307-5312, doi:10.1073/ pnas.0710058105.

Mlawer, E. J., S. J. Taubman, P. D. Brown, M. J. Iacono, and S. A. Clough (1997), Radiative transfer for inhomogeneous atmospheres: RRTM, a validated correlated-k model for the longwave, *Journal of Geophysical Research, 102*(D14), 16663-16682, doi:10.1029/97JD00237.

Molnar, P., W. R. Boos, and D. S. Battisti (2010), Orographic controls on climate and paleoclimate of Asia: Thermal and Mechanical Roles for the Tibetan Plateau, *Annual Reviews of Earth and Planetary Science, 38,* 77-102, doi:10.1146/ annurev-earth-040809-152456.

Murphy, D. M. (2009), Effect of stratospheric aerosols on direct sunlight and implications for concentrating solar power, *Environmental Science and Technology, 43*(8), 2784-2786, doi:10.1021/es802206b.

National Academy of Sciences (NAS) (1992), Policy implications of greenhouse warming: Mitigation, adaptation, and the science base, National Academy Press, Washington, D.C., 433-464.

Niki, T., M. Kunugi, and A. Otsuki (2000), DMSP-lyase activity in five marine phytoplankton species: Its potential importance in DMS production, *Marine Biology*, *136*(5), 759-764, doi:10.1007/s002279900235.

Oman, L., A. Robock, G. L. Stenchikov, and T. Thordarson (2006), High-latitude eruptions cast shadow over the African monsoon and the flow of the Nile, *Geophysical Research Letters*, *33*, L18711, doi:10.1029/2006GL027665.

Ornstein, L., I. Aleinov, and D. Rind (2009), Irrigated afforestation of the Sahara and Australian outback to end global warming, *Climatic Change*, *97*(3-4), 409-437, doi:10.1007/s10584-009-9626-y.

Pearson, J., J. Oldson, and E. Levin (2006), Earth rings for planetary environment control, *Acta Astronautica*, *58*(1), 44-57, doi:10.1016/j.actaastro.2005.03.071.

Pierce, J. R., D. K. Weisenstein, P. Heckendorn, T. Peter, and D. W. Keith (2010), Efficient formulation of stratospheric aerosol for climate engineering by emission of condensible vapor from aircraft, *Geophysical Research Letters*, *37*, L18805, doi:10.1029/2010GL043975.

Pinto, J. P., R. P. Turco, and O. B. Toon (1989), Self-limiting physical and chemical effects in volcanic eruption clouds, *Journal of Geophysical Research*, *94*(D8), 11165-11174, doi:10.1029/JD094iD08p11165.

Pittock, A. B., T. P. Ackerman, P. J. Crutzen, M. C. MacCracken, C. S. Shapiro, and R. P. Turco (Eds.) (1986), *Environmental Consequences of Nuclear War*, SCOPE 28, vol. I, Physical and Atmospheric Effects, John Wiley, New York.

Pressman, J. and P. Warneck (1970), The stratosphere as a chemical sink for carbon monoxide, *Journal of the Atmospheric Sciences*, *27*(1), 155-163.

Pueschel, R. F., S. Verma, H. Rohatschek, G. V. Ferry, N. Boiadjieva, S. D. Howard, and A. W. Strawa (2000), Vertical transport of anthropogenic soot aerosol into the middle atmosphere, *Journal of Geophysical Research*, *105*(D3), 3727-3736, doi:10.1029/1999JD900505.

Ramanathan, V. and G. Carmichael (2008), Global and regional climate changes due to black carbon, *Nature Geoscience*, *1*, 221-227, doi:10.1038/ngeo156.

Rasch, P. J., P. J. Crutzen, and D. B. Coleman (2008a), Exploring the geoengineering of climate using stratospheric sulfate aerosols: The role of particle size, *Geophysical Research Letters*, *35*, L02809, doi: 10.1029/2007GL032179.

Rasch, P. J., S. Tilmes, R. P. Turco, A. Robock, L. Oman, C.-C. Chen, G. L. Stenchikov, and R. R. Garcia (2008b), An overview of geoengineering of climate using stratospheric sulfate aerosols, *Philosophical Transactions of the Royal Society A*, *366*, 4007-4037, doi:10.1098/rsta.2008.0131.

Raven, J., K. Caldeira, H. Elderfield, O. Hoegh-Guldberg, P. Liss, U. Riebesell, J. Shepherd, C. Turley, A. Watson (2005), Ocean acidification due to increasing atmospheric carbon dioxide, Policy document 12/05, The Royal Society, London, UK, 68 pp.

Rayner, N. A., D. E. Parker, E. B. Horton, C. K. Folland, L. V. Alexander, D. P. Rowell, E. C. Kent, and A. Kaplan (2003), Global analyses of sea surface temperature, sea ice, and night marine air temperature since the late nineteenth century, *Journal of Geophysical Research*, *108*(D14), 4407, 10.1029/2002JD002670.

Ricke, K. L., M. G. Morgan, and M. R. Allen (2010), Regional climate response to solar-radiation management, *Nature Geoscience*, *3*, 537-541, doi:10.1038/ngeo915.

Ridgwell, A., J. S. Singarayer, A. M. Hetherington, and P. A. Valdes (2009), Tackling regional climate change by leaf albedo biogeoengineering, *Current Biology*, *19*, 146-150, doi:10.1016/j.cub.2008.12.025.

Robock, A. (1988), Enhancement of surface cooling due to forest fire smoke, *Science*, *242*(4880), 911-913, doi:10.1126/science.242.4880.911.

Robock, A. (1991), Surface cooling due to forest fire smoke, *Journal of Geophysical Research*, *96*(D11), 20869-20878, doi:10.1029/91JD02043.

Robock, A. and Y. Liu (1994), The volcanic signal in Goddard Institute for Space Studies three-dimensional model simulations, *Journal of Climate*, *7*(1), 44-55, doi:10.1175/1520-0442(1994)007<0044;TVSIGI>2.0.CO;2.

Robock, A. (2000), Volcanic eruptions and climate, *Reviews of Geophysics*, *38*, 191-219, doi:10.1029/1998RG000054.

Robock, A., L. Oman, and G. L. Stenchikov (2007a), Nuclear winter revisited with a modern climate model and current nuclear arsenals: Still catastrophic

consequences, *Journal of Geophysical Research*, *112*, D13107, doi: 10.1029/2006JD008235.

Robock, A., L. Oman, G. L. Stenchikov, O. B. Toon, C. Bardeen, and R. P. Turco (2007b), Climatic consequences of regional nuclear conflicts, *Atmospheric Chemistry and Physics*, *7*, 2003-2012, doi:10.5194/acp-7-2003-2007.

Robock, A. (2008), 20 reasons why geoengineering may be a bad idea, *Bulletin of the Atomic Scientists*, *64*(2), 14-18, 59, doi:10.2968/064002006.

Robock, A., L. Oman, and G. L. Stenchikov (2008), Regional climate responses to geoengineering with tropical and Arctic SO_2 injections, *Journal of Geophysical Research*, *113*, D16101, doi:10.1029/2008JD010050.

Robock, A., A. Marquardt, B. Kravitz, and G. Stenchikov (2009), Benefits, risks, and costs of stratospheric geoengineering, *Geophysical Research Letters*, *36*, L19703, doi:10.1029/2009GL039209.

Robock, A., M. Bunzl, B. Kravitz, and G. Stenchikov (2010), A test for geoengineering?, *Science*, *327*(5965), 530-531, doi:10.1126/science.1186237.

Rohatschek, H. (1996), Levitation of stratospheric and mesospheric aerosols by gravitophoresis, *Journal of Aerosol Science*, *27*(3), 467-475, doi: 10.1016/0021-8502(95)00556-0.

Rose, D., B. Wehner, M. Ketzel, C. Engler, J. Voigtländer, T. Tuch, and A. Wiedensohler (2006), Atmospheric number size distributions of soot particles and estimation of emission factors, *Atmospheric Chemistry and Physics*, *6*, 1021-1031, doi:10.5194/acp-6-1021-2006.

Russell, P. B. and M. P. McCormick (1989), SAGE II aerosol data validation and initial data use: An introduction and overview, *Journal of Geophysical Research*, *94*(D6), 8335-8338, doi:10.1029/JD094iD06p08335.

Salter, S., G. Sortino, and J. Latham (2008), Sea-going hardware for the cloud albedo method of reversing global warming, *Philosophical Transactions of the Royal Society A*, *366*(1882), 3989-4006, doi:10.1098/rsta.2008.0136.

Salter, S. H. (2009), A 20 GW thermal 300-metre^3/sec wave-energised, surge-mode nutrient-pump for removing atmospheric carbon dioxide, increasing fish stocks and suppressing hurricanes, *Proceedings of the 8th European Wave and Tidal Energy Conference*, Uppsala, Sweden, 6 pp.

Santer, B. D., R. Sausen, T. M. L. Wigley, J. S. Boyle, K. AchutaRao, C. Doutriaux, J. E. Hansen, G. A. Meehl, E. Roeckner, R. Ruedy, G. Schmidt, and K. E. Taylor (2003), Behavior of tropopause height and atmospheric temperature in models, reanalyses, and observations: Decadal changes, *Journal of Geophysical Research*, *108*(D1), 4002, doi:10.1029/2002JD002258.

Schmidt, G. A., R. Ruedy, J. E. Hansen, I. Aleinov, N. Bell, M. Bauer, S. Bauer, B. cairns, V. Canuto, Y. Cheng, A. Del Genio, G. Faluvegi, A. D. Friend, T. M. Hall, Y. Hu, M. Kelley, N. Y. Kiang, D. Koch, A A. Lacis, J. Lerner, K. K. Lo, R. L. Miller, L. Nazarenko, V. Oinas, J. Perlwitz, J. Perlwitz, D. Rind, A. Romanou, G. L. Russell, M. Sato, D. T. Shindell, P. H. Stone, S. Sun, N. Tausnev, D. Thresher, and M.-S. Yao (2006), Present-day atmospheric simulations using GISS ModelE: Comparison to in situ, satellite and reanalysis data, *Journal of Climate*, *19*, 153–192, doi:10.1175/JCLI3612.1.

Schneider, S. and D. Keith (2001), Earth systems engineering and management, *Nature, 409*, 417-421, doi:10.1038/35053203.

Schwartz, S. E. and A. Slingo (1996), Enhanced shortwave cloud radiative forcing due to anthropogenic aerosols, In *Clouds, Chemistry and Climate--Proceedings of NATO Advanced Research Workshop*, Crutzen P. and V. Ramanathan, Eds., Springer, Heidelberg, 191-236.

Seinfeld, J. H. and S. N. Pandis (2006), Atmospheric Chemistry and Physics: From Air Pollution to Climate Change, John Wiley and Sons, Hoboken, New Jersey, 1203 pp.

Shepherd, J., K. Caldeira, P. Cox, J. Haigh, D. Keith, B. Launder, G. Mace, G. MacKerron, J. Pyle, S. Rayner, C. Redgwell, and A. Watson (2009), Geoengineering the climate: Science, governance and uncertainty, Royal Society Policy document 10/09, 82 pp.

Shindell, D. T., G. A. Schmidt, R. L. Miller, and D. Rind (2001), Northern Hemisphere winter climate response to greenhouse gas, ozone, solar, and volcanic forcing, *Journal of Geophysical Research*, *106*(D7), 7193-7210, doi: 10.1029/2000JD900547.

Simó, R., S. D. Archer, C. Pedrós-Alió, I. Gilpin, C. E. Stelfox-Widdiecombe (2002), Coupled dynamics of dimethylsulfoniopropionate and dimethylsulfide cycling and the microbial food web in surface waters of the North Atlantic, *Limnology and Oceanography*, *47*(1), 53-61.

Slingo, A. (1990), Sensitivity of the earth's radiation budget to changes in low clouds, *Nature, 343*, 49-51, doi:10.1038/343049a0.

Smith, D. M. and A. R. Chughtai (1997), Photochemical effects in the heterogeneous reaction of soot with ozone at low concentrations, *Journal of Atmospheric Chemistry*, *26*(1), 77-91, doi:10.1023/A:1005702818675.

Solomon, S. (1999), Stratospheric ozone depletion: A review of concepts and history, *Reviews of Geophysics*, *37*(3), 275-316, doi:10.1029/1999RG900008.

Solomon, et al. (2007), *Climate Change 2007: The Physical Science Basis, Contribution of Working Group I to the Fourth Assessment Report of the Intergovernmental Panel on Climate Change* (S. Solomon, D. Qin, M. Manning, Z. Chen, M. Marquis, K. B. Averyt, M. Tignor, and H. L. Miller, Eds.), Cambridge University Press, Cambridge, United Kingdom and New York, N. Y., 996 pp.

Solomon, S., G.-K. Plattner, R. Knutti, and P. Friedlingstein (2009), Irreversible climate change due to carbon dioxide emissions, *Proceedings of the National Academy of Sciences*, *106*(6), 1704-1709, doi:10.1073/pnas.0812721106.

SPARC CCMVal (2010), SPARC Report on the Evaluation of Chemistry-Climate Models, V. Eyring, T. G. Shepherd, D. W. Waugh (Eds.), SPARC Report No. 5, WCRP-132, WMO/TD-No. 1526, available online at http://www.atmosp.physics.utoronto.ca/SPARC.

Sprague (2006), Material safety data sheet: Jet A aviation fuel, 4 pp., available online at http://www.spragueenergy.com/documents/MSDS%20Jet%20A%20Aviation%20Fuel%2006.pdf.

Springmann, M., D. A. Knopf, and N. Riemer (2009), Detailed heterogeneous chemistry in an urban plume box model: Reversible co-adsoprtion of O_3, NO_2, and H_2O on soot coated with benzo[a]pyrene, *Atmospheric Chemistry and Physics*, *9*, 7461-7479, doi:10.5194/acp-9-7461-2009.

Stenchikov, G. L., I. Kirchner, A. Robock, H.-F. Graf, J. C. Antuña, R. G. Grainger, A. Lambert, and L. Thomason (1998), Radiative forcing from the 1991 Mount Pinatubo volcanic eruption, *Journal of Geophysical Research*, *103*, 13837-13857, doi:10.1029/98JD00693.

Stern, N. (2006), The economics of climate change: The Stern Review, Executive Summary, Her Majesty's Treasury, London, UK, 27 pp., available online at http://www.hm-treasury.gov.uk/d/Executive_Summary.pdf.

Stevens, B. and G. Feingold (2009), Untangling aerosol effects on clouds and precipitation in a buffered system, *Nature*, *461*, 607-613, doi:10.1038/nature08281.

Stevenson, D. S., R. M. Doherty, M. G. Sanderson, W. J. Collins, C. E. Johnson, and R. G. Derwent (2004), Radiative forcing from aircraft NO_x emissions: Mechanisms and seasonal dependence, *Journal of Geophysical Research*, *109*, D17307, doi:10.1029/2004JD004759.

Stolarski, R. S., S. L. Baughcum, W. H. Brune, A. R. Douglass, D. W. Fahey, R. R. Friedl, S. C. Liu, R. A. Plumb, L. R. Poole, H. L. Wesoky, and D. R. Worsnop (1995), 1995 scientific assessment of the atmospheric effects of stratospheric aircraft, NASA reference publication 1381, 105 pp.

T. W. Brown Oil Co., Inc. (1999), Material safety data sheet for #2 diesel, 2 pp., available online at http://www.mjmmasonry.com/safety/dieselfuelmsds.pdf.

Tang, I. N. (1996), Chemical and size effects of hygroscopic aerosols on light scattering coefficients, *J. Geophys. Res.*, *101*, D14, 19245-19250.

Teller, E., L. Wood, and R. Hyde (1997), Global warming and ice ages: I. Prospects for physics-based modulation of global change, U.S. Department of Energy, Lawrence Livermore National Laboratory, UCRL-JC-128715, 18 pp.

Teller, E., K. Caldeira, G. Canavan, B. Govindasamy, A. Grossman, R. Hyde, M. Ishikawa, A. Ledebuhr, C. Leith, C. Molenkamp, J. Nuckolls, and L. Wood (1999), Long-range weather prediction and prevention of climate catastrophes: A status report, U.S. Department of Energy, Lawrence Livermore National Laboratory, UCRL-JC-135414, 42 pp.

Teller, E., R. Hyde, and L. Wood (2002), Active climate stabilization: Practical physics-based approaches to prevention of climate change, U.S. Department of Energy, Lawrence Livermore National Laboratory, 8 pp.

Tilmes, S., R. Müller, and R. Salawitch (2008), The sensitivity of polar ozone depletion to proposed geoengineering schemes, *Science*, *320*, 1201-1204, doi:10.1126/science.1153966.

Tilmes, S., R. R. Garcia, D. E. Kinnison, A. Gettelman, and P. J. Rasch (2009), Impact of geoengineered aerosols on the troposphere and stratosphere, *Journal of Geophysical Research*, *114*, D12305, doi:10.1029/2008JD011420.

Toon, O. B., A. Robock, R. P. Turco, C. Bardeen, L. Oman, and G. L. Stenchikov (2007), Consequences of regional-scale nuclear conflicts, *Science*, *315*, 1224-1225, doi:10.1126/science.1137747.

Trenberth, K. E. and A. Dai (2007), Effects of Mount Pinatubo volcanic eruption on the hydrological cycle as an analog of geoengineering, *Geophysical Research Letters*, *34*, L15702, doi:10.1029/2007GL030524.

Turco, R. P., O. B. Toon, T. P. Ackerman, J. B. Pollack, and Carl Sagan (1983), Nuclear winter: Global consequences of multiple nuclear explosions, *Science*, *222*(4630), 1283-1292, doi:10.1126/science.222.4630.1283.

Turco, R. P., O. B. Toon, T. P. Ackerman, J. B. Pollack, and C. Sagan (1990), Climate and smoke: An appraisal of nuclear winter, *Science*, *247*, 166–176, doi:10.1126/science.11538069.

Turco, Richard P., Aerosol injection scenarios, unpublished.

Turco, Richard P., Geoengineering the stratospheric sulfate layer from aircraft platforms: Scale, engineering constraints, and estimated costs, unpublished.

Twomey, S. (1977), Influence of pollution on the short-wave albedo of clouds, *Journal of Atmospheric Science*, *34*(7), 1149-1162, doi:10.1175/1520-1469(1977) 034<1149:TIOPOT>2.0.CO;2.

USAF (2010a), Factsheets: KC-10 Extender, United States Air Force Air Mobility Command, available online at http://www.af.mil/information/factsheets/factsheet.asp?fsID=109.

USAF (2010b), Factsheets: KC-135 Stratotanker, United States Air Force Air Mobility Command, available online at http://www.af.mil/information/factsheets/factsheet.asp?fsID=110.

USP&E (2010), Why we recommend used diesel generators, U.S. Power and Environment, available online at http://www.uspowerco.com/articles/why_we_recommend_used_diesel_generators.

Vinnikov, K. Ya., A. Robock, N. A. Speranskaya, and C. A. Schlosser (1996), Scales of temporal and spatial variability of midlatitude soil moisture, *Journal of Geophysical Research*, *101*, 7163-7174.

Vogelmann, A. M., A. Robock, and R. G. Ellingson (1988), Effects of dirty snow in nuclear winter simulations, *Journal of Geophysical Research*, *93*(D5), 5319–5332, doi:10.1029/JD093iD05p05319.

von Neumann, J. (1955), Can we survive technology?, *Fortune*, June 1955, 106-108 & 151-152.

Wallace, J. M. and P. V. Hobbs (2006), Atmospheric science: An introductory survey, Academic Press, Burlington, Massachusetts, 504 pp.

Washington, W. M., R. Knutti, G. A. Meehl, H. Teng, C. Tebaldi, D. Lawrence, L. Buja, and W. G. Strand (2009), How much climate change can be avoided by mitigation?, *Geophysical Research Letters*, *36*, L08703, doi: 10.1029/2008GL037074.

Watson, A. Y. and P. A. Valberg (2001), Carbon black and soot: Two different substances, *AIHAJ - American Industrial Hygiene Association*, *62*(2), 218-228, doi:10.1080/15298660108984625.

Weinstock, B. and H. Niki (1972), Carbon monoxide balance in nature, *Science*, *176*(4032), 290-292, doi:10.1126/science.176.4032.290.

Wigley, T. M. L. (1989), Possible climate change due to SO_2-derived cloud condensation nuclei, *Nature*, *339*, 355-357, doi:10.1038/339365a0.

Wigley, T. M. L. (2006), A combined mitigation/geoengineering approach to climate stabilization, *Science*, *314*, 5798, 452-454, doi:10.1126/science.1131728.

Williamson, S. H. (2010), Seven Ways to Compute the Relative Value of a U.S. Dollar Amount, 1774 to present, MeasuringWorth, available online at http://www.measuringworth.com/uscompare/.

Wingenter, O. W., S. M. Elliot, and D. R. Blake (2007), New directions: Enhancing the natural sulfur cycle to slow global warming, *Atmospheric Environment*, *41*, 7373-7375, doi:10.1016/j.atmosenv.2007.07.021.

Zeman, F. S. and K. S. Lackner (2004), Capturing carbon dioxide directly from the atmosphere, *World Resource Review*, *16*(2), 157-172.

Zeman, F. (2007), Energy and material balance of CO_2 capture from ambient air, *Environmental Science and Technology*, *41*(21), 7558-7563, doi:10.1021/es070874m.

Zhisheng, A., J. E. Kutzbach, W. L. Prell, and S. C. Porter (2001), Evolution of Asian monsoons and phased uplift of the Himalaya-Tibetan plateau since Late Miocene times, *Nature*, *411*, 62-66, doi:10.1038/35075035.

CURRICULUM VITAE

EDUCATION

2007-2011	Rutgers University, Program in Atmospheric Science Doctor of Philosophy, Atmospheric Science, May 2011 Master of Science, Atmospheric Science, October 2009
2004-2007	Purdue University, Department of Mathematics Master of Science, Mathematics, May 2007
2000-2004	Northwestern University Bachelor of Arts with Departmental Honors, Mathematics, June 2004

POSITIONS HELD

2008-2011	Graduate assistant Rutgers University, Department of Environmental Sciences New Brunswick, New Jersey
2009	Part time lecturer Rutgers University, Department of Environmental Sciences New Brunswick, New Jersey
2008-2009	Teaching assistant Rutgers University, Department of Environmental Sciences New Brunswick, New Jersey
2007-2008	Excellence Fellow Rutgers University, School of Environmental and Biological Sciences New Brunswick, New Jersey
2004-2007	Teaching assistant Purdue University, Department of Mathematics West Lafayette, Indiana

PUBLICATIONS

Kravitz, B., A. Robock, O. Boucher, H. Schmidt, and K. E. Taylor (2011), Specifications for GeoMIP experiments G1 through G4, unpublished (working document).

Kravitz, B., A. Robock, and A. Marquardt (2011), Climate model simulations of geoengineering in the Arctic spring, manuscript in preparation.

Robock, A., B. Kravitz, and O. Boucher (2011), Report on Geoengineering Model Intercomparison (GeoMIP) Workshop held at Rutgers University, February 10-12, 2011, *Eos*, submitted.

Kravitz, B., A. Robock, A. Bourassa, T. Deshler, D. Wu, I. Mattis, F. Finger, A. Hoffmann, C. Ritter, L. Bitar, T. J. Duck, and J. E. Barnes (2011), Simulation and observations of stratospheric aerosols from the 2009 Sarychev volcanic eruption, *Journal of Geophysical Research*, submitted.

Kravitz, B., A. Robock, O. Boucher, H. Schmidt , K. Taylor, G. Stenchikov, and M. Schulz (2011), The Geoengineering Model Intercomparison Project (GeoMIP), *Atmospheric Science Letters*, doi:10.1002/asl.316.

Kravitz, B. and A. Robock (2011), The climate effects of high latitude eruptions: The role of the time of year, *Journal of Geophysical Research*, *116*, D01105, doi:10.1029/2010JD014448.

Kravitz, B., A. Robock, L. Oman, G. Stenchikov, and A. B. Marquardt (2010), Correction to "Sulfuric acid deposition from stratospheric geoengineering with sulfate aerosols", *Journal of Geophysical Research*, *115*, D16119, doi: 10.1029/2010JD014579.

Jones, A., J. Haywood, O. Boucher, B. Kravitz, and A. Robock (2010), Geoengineering by stratospheric SO_2 injection: Results from the Met Office HadGEM2 climate model and comparison with the Goddard Institute for Space Studies ModelE, *Atmospheric Chemistry and Physics, 10*, 5999-6006, doi:10.5194/acp-10-5999-2010.

Kravitz, B., A. Robock, A. Bourassa, and G. Stenchikov (2010), Negligible climatic effects from the 2008 Okmok and Kasatochi volcanic eruptions, *Journal of Geophysical Research*, *115*, D00L05, doi: 10.1029/2009JD013525.

Robock, A., M. Bunzl, B. Kravitz, and G. L. Stenchikov (2010), A Test for Geoengineering?, *Science, 327*(5965), 530-531, doi:10.1126/science. 1186237.

Robock, A., A. Marquardt, B. Kravitz, and G. Stenchikov (2009), Benefits, risks, and costs of stratospheric geoengineering, *Geophysical Research Letters*, *36*, L19703, doi:10.1029/2009GL039209.

Kravitz, B., A. Robock, L. Oman, G. Stenchikov, and A. B. Marquardt (2009), Acid deposition from stratospheric geoengineering with sulfate aerosols, *Journal of Geophysical Research*, *114*, D14109, doi: 10.1029/2009JD011918.

Abhyankar, S. S., and B. Kravitz (2007), Two counterexamples in normalization, *Proceedings of the American Mathematical Society*, *135* (11), 3521-3523.